

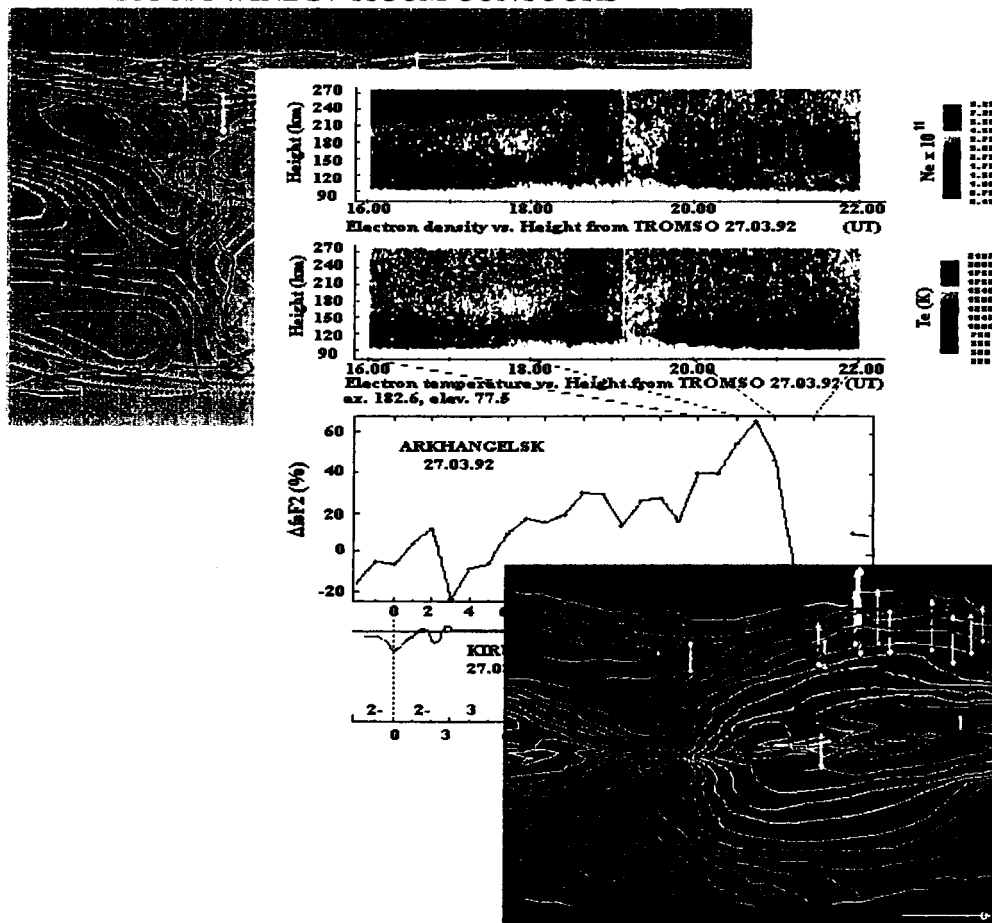
Final Report  
NASA Contract NASW-4755

FINAL  
IN-416-CR  
7CIT  
707523  
273 P.

# A SUNDIAL-ATLAS PRECURSOR TO THE TIMED MISSION: A Quick-Response Global Investigation into Coupled Lower Thermospheric, Ionospheric, and Mesospheric Physics

June 4, 1996

## TIGCM WINDS / TIGCM CONTOURS



## FLIP WINDS / FLIP CONTOURS

RPT-97-14

PUBLICLY AVAILABLE

**Final Report**  
**NASA Contract NASW-4755**

**A SUNDIAL-ATLAS PRECURSOR TO THE TIMED MISSION:  
A Quick-Response Global Investigation into Coupled Lower  
Thermospheric, Ionospheric, and Mesospheric Physics**

**June 4, 1996**

**Principal Investigator**  
**E.P. Szuszczewicz**  
**Applied Physics Operation**  
**Science Applications International Corporation**  
**McLean, VA**

## **Table of Contents**

<b>1. EXECUTIVE SUMMARY .....</b>	<b>1</b>
<b>2. THE INVESTIGATION .....</b>	<b>3</b>
<b>2.1 Relevance to Mainstream Efforts in Space Science.....</b>	<b>3</b>
<b>2.2 Investigative Components.....</b>	<b>4</b>
<b>3. RESULTS .....</b>	<b>5</b>
<b>4. REFERENCES.....</b>	<b>11</b>
<b>REPORT DOCUMENTATION PAGE (Standard Form 298).....</b>	<b>14</b>
<b>APPENDIX:</b>	
<b>A. F-Region Climatology During the SUNDIAL/ATLAS-1 Campaign of March 1992: Model-Measurement Comparisons and Cause-Effect Relationships</b>	
<b>B. High-Latitude Ionospheric Electrodynamics as Determined by the AMIE Procedure for the Conjunctive SUNDIAL/ATLAS-1/GEM Period of March 28-29, 1992</b>	
<b>C. AMIE-TIGCM Comparisons with Global Ionospheric and Thermospheric Observations During the GEM/SUNDIAL/ATLAS-1 Period of 28-29 March 1992</b>	
<b>D. High Latitude Hall and Pedersen Conductances during Substorm Activity in the SUNDIAL-ATLAS Campaign</b>	
<b>E. The Study of the Ionospheric Variability Within the Euro-Asian Sector During the SUNDIAL/ATLAS-1 Mission</b>	
<b>F. Zonal/Meridional Wind and Disturbance Dynamo Electric Field Control of the Low Latitude Ionosphere based on the SUNDIAL/ATLAS-1 Campaign</b>	
<b>G. Ionospheric Climatology and Weather in the Australian - Japanese Sector during the SUNDIAL/ATLAS-1 Campaign</b>	

## 1. EXECUTIVE SUMMARY

The SUNDIAL-ATLAS effort was a global-scale investigation which responded to the science priorities of the ITM Panel, the Integrated SPD Strategy Implementation Plan as a whole, and the need for potential cost-saving design criteria for the TIMED mission. The investigation focused on coupling processes in the ionospheric-thermospheric system, taking advantage of the timelines of the ATLAS-1 mission (March 1992), and the global-scale ground-based measurement and modeling activities of the SUNDIAL program. The collaborative SUNDIAL-ATLAS activity was the first opportunity for global measurements of the chemistry, kinetics, and electrodynamics which couple the E-, F<sub>1</sub>-, and F<sub>2</sub>-regions into a single interactive system. As such, the program represented an important first step in studying global issues; and accordingly, was an important proof of concept experiment relevant to the strategic mission plans for the ITM community and the upcoming intermediate class satellite program called TIMED.

To meet its projected goals, TIMED must perform a number of critical measurements and execute a number of correlations that were to be tried and tested for the first time in the SUNDIAL-ATLAS investigation. This was designed to include global correlations of thermospheric and ionospheric composition during quiet and disturbed conditions and the co-registration of global-scale ground-based measurements with along-track satellite diagnostics. The TIMED Science Team specifically stated that "because of the exploratory nature of the TIMED mission and limitations in instrumentation imposed by financial constraints of its intermediate-type mission, it is imperative that a coordinated collaborative program with ground-based investigations be initiated at an early date."

The SUNDIAL component of the current investigation addressed this need by acquiring, reducing, and analyzing a multi-sensor database that complemented and extended that which was generated in the ATLAS mission (Atmospheric Laboratory for Applications and Science). The SUNDIAL data defined the state and condition of the global-scale ionosphere in the altitude range from 100 km to the F<sub>2</sub>-peak. These data specified the peak heights and densities of the E-, F<sub>1</sub>-, and F<sub>2</sub>-regions, along with the global distributions of intermediate, descending, and sequential layers which play a critical role in the dynamo region of the lower ionospheric-thermospheric domain. The data were collected by the SUNDIAL network of more than 50 ground-based stations utilizing ionosondes, radars, photometers, Fabry-Perot interferometers, and total electron content measurements. The data were acquired during a three-week period centered on the eight-day ATLAS-1 mission, which provided image and photometric sensing of the altitude distributions of the major and minor ions and neutrals in the ITM system. This report focuses on the scientific contributions of the SUNDIAL



component of the overall investigation. That part concentrated on developing an integrated view of the dynamics of the ionospheric-thermospheric system during the ATLAS mission and improving the overall understanding of controlling terms. Special emphasis was placed on the roles of plasmaspheric fluxes and thermospheric winds in controlling the heights and densities of the F-region peak. In the process the investigation “re-discovered” the old but unsettled issue of maintaining of the nighttime ionosphere. Detailed analysis showed that the nighttime discrepancy between first-principle model predictions and observations is traceable in first order to model underestimates of prevailing meridional winds. Other SUNDIAL results focused on high-latitude dynamics, storm-time characterization of ionospheric-thermospheric responses as well as a quantitative test and validation of those models widely used in the scientific community: the IRI, FLIP and TIGCM (i.e., the International Reference Ionosphere, the Field Line Interhemispheric Plasma Model, and the Thermosphere-Ionosphere Global Circulation Model. Overall results are to be published in a special ATLAS/SUNDIAL issue of the Journal of Geophysical Research. The title of those papers and authorship are as follows:

- 1 F-Region Climatology During the SUNDIAL/ATLAS-1 Campaign of March 1992: Model-Measurement Comparisons and Cause-Effect Relationships, E.P. Szuszczewicz, D. Torr, P. Wilkinson, P. Richards, R. Roble, B. Emery, G. Lu, M. Abdu, D. Evans, R. Hanbaba, K. Igarashi, P. Jiao, M. Lester, S. Pulinets, B.M. Reddy, P. Blanchard, K. Miller, and J. Joselyn
2. High-Latitude Ionospheric Electrodynamics as Determined by the AMIE Procedure for the Conjunctive SUNDIAL/ATLAS-1/GEM Period of March 28-29, 1992, G. Lu, B.A. Emery, A. Rodger, M. Lester, J. Taylor, D.S. Evans, M. Ruohoniemi, W.F. Denig, O. de la Beaujardier, R.A. Frahm, J.D. Winningham, and D.L. Chenette
3. AMIE-TIGCM Comparisons with Global Ionospheric and Thermospheric Observations During the GEM/SUNDIAL/ATLAS-1 Period of 28-29 March 1992, B.A. Emery, G. Lu, E.P. Szuszczewicz, A.D. Richmond, R.G. Roble, P.G. Richards, K.L. Miller, R. Niciejewski, D.S. Evans, F.J. Rich, W.F. Denig, D.L. Chenette, P. Wilkinson, S. Pulinets, K.F.O'Loughlin, R. Hanbaba, M. Abdu, P. Jio, K. Igarashi, and B.M. Reddy
4. High Latitude Hall and Pedersen Conductances during Substorm Activity in the SUNDIAL-ATLAS Campaign, M. Lester and J.A. Davies
5. The Study of the Ionospheric Variability Within the Euro-Asian Sector During the SUNDIAL/ATLAS-1 Mission, S.A. Pulinets and K.F. Yudakhin
6. Zonal/Meridional Wind and Disturbance Dynamo Electric Field Control of the Low Latitude Ionosphere based on the SUNDIAL/ATLAS-1 Campaign,

M.A. Abdu, J.H.A. Sobral, P. Richards, Marta M. de Gonzalez, Y.N. Huang, B.M. Reddy, K. Cheng, and I.S. Batista

7. Ionospheric Climatology and Weather in the Australian - Japanese Sector during the SUNDIAL/ATLAS-1 Campaign, P.J. Wilkinson, P. Richards, K. Igarashi, and E.P. Szuszczewicz

## **2. THE INVESTIGATION**

### **2.1 Relevance to Mainstream Efforts in Space Science**

There are a number of trends evolving in experimental and theoretical aspects of solar-terrestrial physics. These may be considered to include: 1) The organization of characteristic responses within the framework of space weather and climatology; 2) An increased emphasis on remote sensing techniques; and 3) Dependence on large-scale numerical models for predictions or deductions about cause-effect relationships that are not readily measured.

Within the concept of "space weather and climatology" [Sime and Behnke, 1994; Siscoe et al., 1994; Szuszczewicz, 1995], climatology deals with "average" conditions that result under a set of large-scale slowly-changing (i.e., weeks, to months, to years) forcing functions. On the other hand weather addresses drivers and system responses framed within their hour-to-hour and day-to-day variability. Embodied in these concepts is the idea of "predictions" that encompasses the scientifically rigorous position that accurate predictions of weather and climatology are the ultimate test of understanding. As space science matures the logic of such a focus looms as increasingly important.

The trend toward an ever-increasing reliance on large-scale numerical models stems in part from the premise that no measurement program will ever be able to define completely the input and output parameters in a given cause-effect chain of geophysical events. Thus theory, and in particular comprehensive first-principle models, must be relied upon to make deductions where data are not available and to provide insight into the physical processes of importance. However, theoretical models are accurate only to the extent that the fundamental processes are adequately understood, mathematically represented, and empirically bounded. Therefore there is the need to use experimental data, in particular global-scale data, to validate individual models, quantify their accuracies, impose self-consistency, and identify regions for improvement.

The trend toward an increased emphasis on remote sensing techniques is motivated in part by the number of geophysical or solar-terrestrial domains that are difficult or impossible to routinely access with "in situ" techniques. This trend also appears to be motivated by a perspective that remote sensing techniques can provide more global views of phenomenological domains and therefore

perform (arguably) more effectively than satellite- or rocket-borne "in situ" diagnostics. Such has been the thrust of the ATLAS-1 mission [Torr et al., 1993; Fennelly et al., 1993], the current series of Shuttle-borne GLO investigations [Broadfoot et al., 1992, Gardner et al., 1995], and the planned NASA/TIMED satellite program. Many of the remote sensing techniques however are integrated line-of-sight measurements that require inversion procedures that are forced to make assumptions about the physical processes and local particle distributions giving rise to their respective observables. Therefore, there is often need for coincident ground-truth measurements that provide benchmarks for the remote sensing procedures as well as spatial and temporal continuity between and among the along-track remote-sensing database.

The investigation embodied all three trends. It addressed the issue of cause-effect terms as manifested in the global-scale climatology of the ionospheric-thermospheric system during the solar-maximum equinoctial period of the ATLAS-1 mission. It also addressed the issue of model testing and verification, with an emphasis on quantifying agreement and disagreement with observations as well as between and among various models. The approach also focused on remote sensing techniques and necessary elements of ground-truth with a global network of 53 SUNDIAL ionosondes operating around-the-clock for the entire period of the ATLAS-1 mission (23 March through 2 April 1992).

## **2.2 Investigative Components**

ATLAS-1 was launched on March 23, 1992 at 13:01 UT into a 57° inclination 297 km circular orbit with a complement of photometric devices covering atomic, molecular and ionic emissions over the wavelength regime from the EUV through the IR [Torr et al., 1993]. The intent was to measure the density and temperature distributions of the neutral and ion constituents from mesospheric altitudes up through the F-region. This was to be the first of a series of flights which would develop one of the first datasets dealing with the mesosphere and make available ionospheric and thermospheric results for the test and verification of developing large-scale models.

The ground-based SUNDIAL component had a separate but synergistic set of continuing objectives that supported the ATLAS-1 interests while developing a synoptic view of the global-scale ionospheric-thermospheric (I-T) system. Among those objectives has been the development of a worldwide database [Szuszczewicz et al., 1988, 1990, 1993] for an empirical specification of the state and condition of the I-T system and its weather and climatology as influenced by seasonal, solar-cycle, diurnal and storm-time controls. Working with that database the objectives also contributed to the development of a predictive capability through the test, verification and validation of empirical and first principle models. Past SUNDIAL efforts have included the empirically-derived International Reference Ionosphere (IRI) [Rawer, 1981; Rawer and

Ramanamurty, 1985; Schunk and Szuszcwicz, 1988] and the auroral oval models of Feldstein, NOAA/TIROS and DMSP [Szuszcwicz et al., 1993]. Test and validation efforts have also included a number of first-principle models: the time-dependent ionospheric model of Utah State [Wilkinson et al., 1988; Sica et al., 1990], the NCAR Thermospheric-Ionospheric General Circulation Model TIGCM [Wilkinson et al., 1992; Szuszcwicz et al., 1995] and the Rice Convection Model [Spiro et al., 1988; Fejer et al., 1990].

In this investigation we concentrated on the IRI, the NCAR/TIGCM, and the FLIP (FLIP = Field Line Interhemispheric Plasma [Richards et al., 1994a]) models. They represent a unique set of capabilities that reflect major differences in approaches to the representation of the prevailing physics along with a substantial difference in computer requirements. The IRI, FLIP, and TIGCM are PC, work station, and Cray based, respectively. The IRI is purely empirical in its approach. The FLIP code is a one-dimensional model which inputs thermospheric controls by incorporating composition from the MSIS model (Mass Spectrometer and Incoherent Radar, Hedin (1987)) and meridional winds from empirical models or from radars, ionosondes or Fabry-Perot interferometers. The NCAR/TIGCM might (arguably) be considered the closest to an all first-principles model since it self-consistently solves the system of equations which defines the coupled I-T domain. Rigorously speaking however, it is not entirely first principle since it invokes the empirically-defined electric field model of Richmond et al. [1980] and the AMIE specification [Richmond, 1992; Lu, 1995a] of particles, fields, and currents at high latitudes. This investigation presents the very first joint comparison of all three approaches against the global database with a perspective that highlights the differences in the approaches and the relative agreement with the data. We focused on climatology, drawing perspectives on diurnal variability, thermospheric wind controls, plasmaspheric fluxes, and phenomenological domains. We also included a perspective on the overall characteristics of the F-region ionosphere as manifested during the March 23 to April 2, 1992 SUNDIAL/ATLAS-1 period.

### 3. RESULTS

The results of this investigation will be published in a collection of 7 papers appearing in a special issue of the Journal of Geophysical Research. The titles, authors, and abstracts follow with the full manuscripts appearing in the Appendix:

**F-Region Climatology During the SUNDIAL/ATLAS-1 Campaign of March 1992: Model-Measurement Comparisons and Cause-Effect Relationships,** E.P. Szuszcwicz, D. Torr, P. Wilkinson, P. Richards, R. Roble, B. Emery, G. Lu, M. Abdu, D. Evans, R. Hanbaba, K. Igarashi, P. Jiao, M. Lester, S. Pulnits, B.M. Reddy, P. Blanchard, K. Miller, and J. Joselyn. *We present the first joint comparison of global measurements of F-region characteristics with three models used widely in the specification of the ionospheric-thermospheric system.*

The models, the IRI, FLIP and TIGCM, represent a unique set of capabilities with major differences in approaches to the prevailing physics and different levels of computational complexity. The database was developed by a global network of 53 ionosonde stations operating around-the-clock for the period 22 March through 4 April 1992 in collaboration with the ATLAS-1 mission. The emphasis is on the F-region characteristics of peak heights ( $h_m F_2$ ) and densities ( $f_o F_2$ ), their climatological (i.e., average) behavior during the ATLAS-1 period, and associated cause-effect relationships. We explore latitudinal and UT/LT variations with attention to the influences of meridional winds and plasmaspheric fluxes in the maintenance of different domains in the ionospheric-thermospheric system. We find that all three models tend to underestimate the values of  $h_m F_2$  and  $f_o F_2$  with the largest discrepancies in  $f_o F_2$  resulting in the FLIP and TIGCM representations at night. These discrepancies can grow to levels as large as 45% near 4 AM LT, a “rediscovery” of the old but unsettled issue of maintenance of the nighttime ionosphere. This nighttime discrepancy is traceable in first order to model underestimates of prevailing meridional winds. The contributions of plasmaspheric fluxes are also considered, with the conclusion that they are of secondary importance, but substantially more work is necessary to uniquely quantify their role. In contrast to their nighttime characteristics, the FLIP and TIGCM generally have excellent agreement (i.e.,  $\pm 3\%$ ) with daytime observations of  $f_o F_2$ , and the IRI tends to underestimate the observed values of  $f_o F_2$  by a nominally LT-insensitive level of  $13 \pm 3\%$ . We review other campaign results in this special issue, with a focus on regional responses to the prevailing conditions and their characterization in terms of latitudinal distributions of F-region heights and densities.

**High-Latitude Ionospheric Electrodynamics as Determined by the AMIE Procedure for the Conjunctive SUNDIAL/ATLAS-1/GEM Period of March 28-29, 1992,** G. Lu, B.A. Emery, A. Rodger, M. Lester, J. Taylor, D.S. Evans, M. Ruohoniemi, W.F. Denig, O. de la Beaujardier, R.A. Frahm, J.D. Winningham, and D.L. Chenette. During the conjunctive SUNDIAL/ATLAS-1/GEM campaign period of 28-29 March 1992, a set of comprehensive data has been collected both from space and from ground. The Assimilative Mapping of Ionospheric Electrodynamics (AMIE) procedure is used to derive the large-scale high-latitude ionospheric conductivity, convection, and other related quantities, by combining the various data sets. The period was characterized by several moderate substorm activities. Variations of different ionospheric electrodynamic fields are examined for one sub-storm interval. The cross-polar-cap potential drop, Joule heating, and field-aligned current are all enhanced during the expansion phase of substorms. The most dramatic changes of these fields are found to be associated with the development of the substorm electrojet in the post-midnight region. Variations of global electrodynamic quantities for this 2-day period have revealed a good correlation with the auroral electrojet (AE) index. Different energy dissipation channels have also been estimated. On the average over the two days, the total globally integrated Joule heating is about 102 GW and the

*total globally integrated auroral energy precipitation is about 52 GW. Using an empirical formula, the ring current energy injection is estimated to be 125 GW for a decay time of 3.5 hr, and 85 GW for a decay time of 20 hr. We also find an energy-coupling efficiency of 3% between the solar wind and the magnetosphere for a southward IMF condition.*

**AMIE-TIGCM Comparisons with Global Ionospheric and Thermospheric Observations During the GEM/SUNDIAL/ATLAS-1 Period of 28-29 March 1992,** B.A. Emery, G. Lu, E.P. Szuszczewicz, A.D. Richmond, R.G. Roble, P.G. Richards, K.L. Miller, R. Niecejewski, D.S. Evans, F.J. Rich, W.F. Denig, D.L. Chenette, P. Wilkinson, S. Pulnits, K.F.O'Loughlin, R. Hanbaba, M. Abdu, P. Jio, K. Igarashi, and B.M. Reddy. *Satellite and ground-based observations during the solar maximum period of 28-29 March 1992 were combined in the Assimilative Mapping of Ionospheric Electrodynamics (AMIE) procedure to derive realistic global distributions of the auroral precipitation and ionospheric convection. The total hemispheric Joule heating rate was found to be 5-20 GW greater in the hemisphere where the magnetic pole is tilted towards the sun. Comparisons with Fabry-Perot, horizontal winds were good, and improved when the emission altitude was lowered in the presence of auroral arcs. Comparisons with ionosonde meridional neutral winds showed the AMIE-TIGCM winds to be a little larger, with peak nighttime equatorward winds occurring 1-2 hours later than the derived observations. There was good agreement with the ionosonde winds and the height of the electron density maximum ( $h_m F_2$ ) in the timing of gravity waves launched from high latitude sources. Calculations from the AMIE-TIGCM run suggest that the propagation time of gravity waves to the equator is between 2 and 3 hours. Because Joule heating events are different in each hemisphere, the resulting gravity waves and  $O/N_2$  decreases are different in each hemisphere. Changes in the  $O/N_2$  ratio were strongly correlated with changes in the peak electron density ( $N_m F_2$ ) for middle and high latitudes. On a constant pressure surface for a particular latitude, differences in the  $O/N_2$  ratio showed minima about  $75^\circ$  which in longitude produced by Joule heating events at higher latitudes and more eastward longitudes. The equatorward movement of these minima is about  $10^\circ$  in 4-5 hours, while zonal winds move the minima westward at night. The observed  $N_m F_2$  longitudinal asymmetries near  $50^\circ$  magnetic latitude were generally reproduced by AMIE-TIGCM on the second day of the simulation. The good daytime  $N_m F_2$  agreement deteriorated at low and equatorial latitudes where dynamo electric fields are expected to be important. Agreement is also not very good in the polar cap where the daytime  $N_m F_2$  observations were low compared to the nighttime observations which were unusually high. The AMIE-TIGCM underestimated the electron density after midnight by up to a factor of two in mid-latitudes, while the height of  $N_m F_2$  layer was about 40 km lower than the observations at midnight. Field Line Interhemispheric Plasma (FLIP) model runs at 55 N showed that the  $N_m F_2$  could be doubled at 4 LT by shifting the model winds 2 hours earlier at night and this would also raise the  $h_m F_2$  up as much as 20 km around midnight. However, the*

TIGCM  $N_2$  density was found to be approximately a factor of 2 less than MSIS-86 at 300 km, so possible TIGCM increases in  $N_2$  and conquest decreases in the  $O/N_2$  ratio would reduce  $N_m F_2$  by at least a factor of two. To increase the  $N_m F_2$  at night, another AMIE-TIGCM run was made with nighttime downward fluxes of  $O^+$  increased between a factor of two and six at the upper boundary around 550 km to levels consistent with incoherent scatter radar observations of the  $O^+$  flux during solar maximum. The resulting  $N_m F_2$  at night is now between 0 and 20% higher than the observations, thereby eliminating the problem of low nighttime  $N_m F_2$  calculations.

**High Latitude Hall and Pedersen Conductances during Substorm Activity in the SUNDIAL-ATLAS Campaign**, M. Lester and J.A. Davies. Simultaneous high time resolution observations of the height integrated Hall and Pedersen conductivities,  $\Sigma_H$  and  $\Sigma_P$ , the ionospheric electric field and the ground magnetic field during a magnetospheric substorm are reported. The measurements discussed here were taken during the SUNDIAL/ATLAS-1 campaign of March 24-April 2, 1992. The EISCAT UHF special programme SP-UK-ATLAS which operated on March 27, 1992 provided continuous high time resolution, 10 s, measurements of the electron density and the ion vector velocity from which  $\Sigma_H$  and  $\Sigma_P$  and the ionospheric electric field were calculated. During the growth phase,  $\Sigma_P$  and  $\Sigma_H$  were less than 10 S and the ratio,  $R=\Sigma_H/\Sigma_P$ , was less than 1. Although both  $\Sigma_H$  and  $\Sigma_P$  increased at the onset of the expansion phase,  $R$  remained close to 1. This ratio provides information on the mean energy of the precipitating particles responsible for the enhanced conductances. A ratio of 1 implies a mean energy of the particles of 2 keV. Both  $\Sigma_H$  and  $\Sigma_P$  increased towards the end of the expansion phase with peak values of 71 S and 34 S respectively. The ratio  $R$  also increased to values exceeding 2, equivalent to mean energies of more than 6 keV. The largest value of  $R$  was 3.25 during the substorm recovery phase which is equivalent to mean energies of more than 10 keV. The maximum Hall current density during this interval was  $2.66 \text{ A m}^{-1}$  which occurred the early part of the recovery phase of the substorm. At a number of intensifications, peaks in the current density were observed, for which the electric field was responsible in some cases and the Hall conductance in others.

**The Study of the Ionospheric Variability Within the Euro-Asian Sector During the SUNDIAL/ATLAS-1 Mission**, S.A. Pulinets and K.F. Yudakhin. Data from ten ionospheric stations gathered during SUNDIAL/ATLAS-1 Mission which covered period March 24 through April 2, 1992 are analyzed. The study was concentrated on documenting and understanding the ionospheric variability that prevailed during the period of interest. The stations cover the  $10^\circ$ - $90^\circ$  E longitude sector and eight of the stations are within  $55^\circ \pm 5^\circ$  N latitudes. This opens the possibility for a study of longitudinal variations within Europe-Western Asia subauroral ionosphere. The period was moderately disturbed: the  $K_p$  and  $A_p$  did not exceeded 3+ and 26, respectively, for the considered period. It could

be regarded as recovery phase after the storm that took place near 2300 UT on 21 of March. But the period of interest was occupied by the sequence of substorms what makes difficult to look for a direct cause effect relations, and we put more attention to the different indices study from the point of view of their ability to describe the ionospheric variability. This variability was high in relation to the median values. The critical frequency variations had periodic character, and deviation from median exceeded 50% for both positive and negative variations within the given period for most of the stations. To reveal some systematic character in observed variations, the different techniques of visualization of the experimental data and correlation analysis were applied to the data. The quasiperiodic (~5 days) variations were revealed on the all longitudinal chain of the ionospheric stations. Different scales of the observed variability phenomena were regarded, what gave possibility to find the direct cause-effect relation for some of them. The applicability of two new indices for estimation of the ionosphere variability was studied. One of them, constructed from the ionospheric data themselves, shows high correlation with the averaged particle precipitation index based on the NOAA/TIROS satellite data. For the last one the cross-correlation analysis was carried out with the critical frequency deviations from the monthly median values for longitudinal chain of stations. The most striking fact is that the cross-correlation functions are symmetrical not in relation to the universal time (what one could expect regarding the development of the storm or substorm) but to the local time of the given station.

**Ionospheric Climatology and Weather in the Australian - Japanese Sector during the SUNDIAL/ATLAS-1 Campaign,** P.J. Wilkinson, P. Richards, K. Igarashi, and E.P. Szuszczewicz. The SUNDIAL/ATLAS-1 campaign took place during a period of high solar flux and moderate magnetic activity. For most days during the campaign the ionosphere over Australia and Japan was undisturbed. The International Reference Ionosphere (IRI), used with a suitable equivalent sunspot number, provided a good climatological description of the Australian and Japanese observations. The measured  $h_mF_2$  was employed in the field interhemispheric (FLIP) model to determine equivalent neutral winds and accurately reproduced the measured  $h_mF_2$ . With these winds, the daytime  $n_mF_2$  was well reproduced in most cases although the measured  $n_mF_2$  tended to peak before noon while the model  $n_mF_2$  peaked 2-3 hours later at some locations. At night, the model  $n_mF_2$  was typically lower than the measurements. The difference between the modeled and measured nighttime  $n_mF_2$  worsened as the latitude decreased suggesting that the problem is not principally due to inadequate plasmaspheric fluxes. The equivalent winds from  $h_mF_2$  were similar in amplitude to the winds from the HWM90 model but there were large differences in the phases. The two sets of winds show a similar decrease in amplitude with decreasing latitude. There appears to be a large longitudinal variation in the wind behaviour in the Australian sector. While the winds in eastern Australia show similar diurnal variations with daytime poleward winds and nighttime equatorward winds, the west coast winds were poleward most of



the time. The differences in poleward winds are reflected in the much smaller changes in  $h_m F_2$  in the west. The  $O^+$  fluxes to and from the plasmasphere are generally larger than the  $H^+$  fluxes for these solar maximum conditions. They show structure related to the neutral winds and  $h_m F_2$ . The  $O^+$  flux variations are similar at most stations with upward fluxes during the day and very large downward  $O^+$  fluxes at sunset followed by a rapid decay to small fluxes for most of the night. The  $H^+$  flux behaviour is more complex with the west coast station (Mundaring) showing a classical, strong diurnal variation, upward during the day and downward at night. On the other hand, the  $H^+$  fluxes are upward most of the time at Hobart on the east coast.

**Zonal/Meridional Wind and Disturbance Dynamo Electric Field Control of the Low Latitude Ionosphere based on the SUNDIAL/ATLAS-1 Campaign,** M.A. Abdu, J.H.A. Sobral, P. Richards, Marta M. de Gonzalez, Y.N. Huang, B.M. Reddy, K. Cheng, and I.S. Batista. We present an evaluation of global scale equatorial- and low- latitude ionospheric disturbances in response to the weak-to-moderate disturbed conditions that marked the SUNDIAL/ATLAS-1 12-day campaign of 22 March - 02 April 1992. Ionosonde data from South American and Indian-Asian longitudes are analyzed to examine first the climatological (the average) pattern of the critical F region parameters (the layer peak density and height) in comparison with the empirical International Reference Ionosphere (IRI) model, and then to characterize the day-to-day variabilities aiming at identifying potential causal contributions from either disturbance zonal and meridional winds or magnetospheric and disturbance dynamo electric fields. Included in this analysis are data from South American midlatitude locations which are used to determine meridional winds using an adaption of the servo analysis technique in the Field Line Integrated Plasma (FLIP) model. We have made an assessment of the causal mechanism of the day-to-day variabilities as arising from latitude dependent disturbance meridional winds, and from electric fields produced by disturbance zonal winds and disturbance dynamo. While the contribution from disturbance meridional winds decreases from mid- to equatorial latitude, that of the electric fields maximizes around the equator. It is found that there are two time intervals of maximum ionospheric variability resulting from the weak-moderate magnetospheric disturbance conditions that prevailed during the campaign: one near the evening/postsunset hours and the other in the post midnight-sunrise hours over low latitudes. At midlatitudes a broad maximum of the response occurs from pre midnight to morning hours. We provide a comparison of results for the South American and Indian-Asian longitudes and a discussion of the competing roles of the disturbance zonal and meridional winds, and magnetospheric and disturbance dynamo electric fields as a function of latitude.

#### 4. REFERENCES

- Broadfoot, A.L., B.R. Sandel, D.J. Knecht, R.R. Viereck and E. Murad, Panchromatic Spectrograph with Supporting Monochromatic Imagers, Applied Optics, 31, 3083, 1992
- Fejer, B.G., R.W. Spiro, R.A. Wolf, and J.C. Foster, Latitudinal Variation of Perturbation Electric Fields During Magnetically Disturbed Periods: 1986 SUNDIAL Observations and Model Results, Annales Geophysicae, 8, 441, 1990
- Fennelly, J.A., D.G. Torr, P.G. Richards, and M.R. Torr, Simultaneous Retrieval of the Solar EUV Flux and Neutral Thermospheric O, O<sub>2</sub>, N<sub>2</sub> and Temperature from Twilight Airglow, J. Geophys. Res., 99, 6483, 1993
- Gardner, A.G., R.A. Vierek, E. Murad, D.J. Knecht, C.P. Pike, A.L. Broadfoot, and E.R. Anderson, Simultaneous Observations of Neutral and Ionic Magnesium in the Thermosphere, Geophys. Res. L., (1995 in press)
- Hedin, A.E., MSIS-86 Thermosphere Model, J. Geophys. Res., 92, 4649, 1987
- Lu, G., A.D. Richmond, B.A. Emery, R.G. Roble, Magnetospheric-Ionospheric-Thermospheric Coupling, Effect of Neutral Winds on Energy Transfer and Field Aligned Current, J. Geophys. Res. (1995a, in press)
- Rawer, K., and Y.V. Ramanamurty, International Reference Ionosphere - Status 1985/1986, URSI COSPAR Workshop Proceedings, Wheaton and Co., Ltd., UK, 1985
- Rawer, K., International Reference Ionosphere - IRI-79, NOAA Rpt., UAG-82, U.S. Dept. of Commerce, Washington, DC, 1981
- Richards, P.G., D.G. Torr, B.W. Reinisch, R.R. Gamache, and P.J. Wilkinson, F<sub>2</sub> Peak Electron Density at Millstone Hill and Hobart: Comparison of Theory and Measurement at Solar Maximum, J. Geophys. Res., 99, 15,005, 1994a
- Richmond, A.D., Assimilative Mapping of Ionospheric Electrodynamics, Adv. Space Res., 12, 59, 1992
- Richmond, A.D., et al., An Empirical Model of Quiet-Day Ionospheric Electric Fields at Middle and Low Latitudes, J. Geophys. Res., 85, 4658-4664, 1980

- Schunk, R.W., and E.P. Szuszcwicz, First Principle and Empirical Modeling of the Global-Scale Ionosphere, Ann. Geophys. 5, 19, 1988
- Sica, R., R.W. Schunk, and P. Wilkinson, A Study of the Undisturbed Mid-Latitude Ionosphere Using Simultaneous, Multiple-Site Ionosonde Measurements Using the SUNDIAL '86 Campaign, J. Geophys. Res., 95, 8727, 1990
- Sime, D. and R. Behnke, The U.S. Space Weather Program, Part 1, STEP Int'l., 4, No. 11, November 1994
- Siscoe, G., E. Hildner, T.H. Killeen, L.J. Lanzerotti, and W. Lotko, Developing Service Promises Accurate Space Weather Forecasts in the Future, EOS: Trans. Am. Geophys. Union, 75, 353, 1994
- Spiro, R.W., R.A. Wolf, and B.G. Fejer, Penetration of High-Latitude-Electric-Field Effects to Low Latitudes During SUNDIAL 1984, Annales Geophysicae, 6, 39-50, 1988
- Szuszcwicz, E.P., Advances in Ionospheric Physics: Roles, Relevance and Predictions in the System of Solar-Terrestrial Plasmas, U.S. National Quadrennial Rpt. to the IUGG, Reviews of Geophysics, Supplement, 721, 1995
- Szuszcwicz, E.P., B. Fejer, E. Roelof, R. Schunk, R. Wolf, R. Leitingner, M. Abdu, B.M. Reddy, J. Joselyn, P. Wilkinson, and R. Woodman, SUNDIAL: A World-Wide Study of Interactive Ionospheric Processes and Their Roles in the Transfer of Energy and Mass in the Sun-Earth System, Annales Geophysicae, 6, 3-18, 1988
- Szuszcwicz, E.P., P. Wilkinson, M.A. Abdu, E. Roelof, R. Hanbaba, M. Sands, T. Kikuchi, R. Burnside, J. Joselyn, M. Lester, R. Leitingner, G.O. Walker, B.M. Reddy, and J. Sobral, Solar-Terrestrial Conditions During SUNDIAL '86 and Empirical Modeling of the Global-Scale Ionospheric Responses, Annales Geophysicae, 8, 387, 1990
- Szuszcwicz, E.P., P. Wilkinson, W. Swider, S. Pulints, M.A. Abdu, E. Roelof, T. Fuller-Rowell, T. Bateman, P. Blanchard, G. Gustafsson, R. Hanbaba, J. Joselyn, T. Kikuchi, R. Leitingner, M. Lester, B. Reddy, M. Ruohoniemi, M. Sands, J. Sobral, G.O. Walker, and V. Wickwar, Measurements and Empirical Model Comparisons of F-region Characteristics and Auroral Oval Boundaries During the Solstitial SUNDIAL Campaign of 1987, Annales Geophysicae, 11, 601-613, 1993

- Szuszczewicz, E.P., R.G. Roble, P.J. Wilkinson, and R. Hanbaba, Coupling Mechanisms in the Lower Ionospheric-Thermospheric System and Manifestations in the Formation and Dynamics of Intermediate and Descending Layers, J. Atm. Terr. Phys., 57, 1483, 1995
- Torr, D.G., M.R. Torr, and P.G. Richards, Thermospheric airglow emissions: a comparison of measurements from ATLAS-1 and Theory, Geophys. Res. Lett., 6, 519, 1993
- Torr, D.G., M.R. Torr, and P.G. Richards, Thermospheric Airglow Emissions: A Comparison of Measurements from ATLAS-1 and Theory, Geophys. Res. Lett., 6, 519, 1993
- Wilkinson, P., R.W. Schunk, R. Hanbaba, and H. Mori, Interhemispheric Comparison of SUNDIAL F-Region Data with Global-Scale Ionospheric Models, Ann. Geophys., 6, 31, 1988
- Wilkinson, P.J., E.P. Szuszczewicz, and R.G. Roble, Measurements and Modeling of Intermediate, Descending, and Sporadic Layers in the Lower Ionosphere: Results and Implications for Global-Scale Ionospheric-Thermospheric Studies, Geophys. Res. Lett., 19, 95-98, 1992

# REPORT DOCUMENTATION PAGE

Form Approved  
OMB No. 0704-0188

Public reporting burden for this collection of information is estimated to average 1 hour per response, including the time for reviewing instructions, searching existing data sources, gathering and maintaining the data needed, and completing and reviewing the collection of information. Send comments regarding this burden estimate or any other aspect of this collection of information, including suggestions for reducing this burden, to Washington Headquarters Services, Directorate for Information Operations and Reports, 1215 Jefferson Davis Highway, Suite 1204, Arlington, VA 22202-4302, and to the Office of Management and Budget, Paperwork Reduction Project (0704-0188), Washington, DC 20503.

1. AGENCY USE ONLY (Leave blank)		2. REPORT DATE June 4, 1996	3. REPORT TYPE AND DATES COVERED Final Report 01/05/93-09/30/95	
4. TITLE AND SUBTITLE A SUNDIAL/ATLAS PRECURSOR TO THE TIMED MISSION: A Quick-Response Global Investigation into Coupled Lower Thermospheric, Ionospheric & Mesospheric Physics			5. FUNDING NUMBERS NASW-4755	
6. AUTHOR(S) E.P. Szuszczewicz				
7. PERFORMING ORGANIZATION NAME(S) AND ADDRESS(ES) Science Applications International Corporation 1710 Goodridge Drive McLean, Virginia 22102			8. PERFORMING ORGANIZATION REPORT NUMBER  SAIC-96/1129 RPT-97-14	
9. SPONSORING/MONITORING AGENCY NAME(S) AND ADDRESS(ES) National Aeronautics and Space Administration Space Physics Division Washington, DC 20546			10. SPONSORING/MONITORING AGENCY REPORT NUMBER	
11. SUPPLEMENTARY NOTES Scientific findings to be published in a special issue of the Journal of Geophysical Research				
12a. DISTRIBUTION/AVAILABILITY STATEMENT Unlimited			12b. DISTRIBUTION CODE	
13. ABSTRACT (Maximum 200 words) The SUNDIAL-ATLAS effort was a global-scale investigation which responded to the science priorities of the ITM Panel, the Integrated SPD Strategy Implementation Plan as a whole, and the need for potential cost-saving design criteria for the TIMED mission. The investigation focused on coupling processes in the ionospheric-thermospheric system, taking advantage of the timelines of the ATLAS-1 mission (March 1992), and the global-scale ground-based measurement and modeling activities of the SUNDIAL program. The collaborative SUNDIAL-ATLAS activity was the first opportunity for global measurements of the chemistry, kinetics, and electrodynamics which couple the E-, F1-, and F2-regions into a single interactive system. As such, the program represented an important first step in studying global issues; and accordingly, was an important proof of concept experiment relevant to the strategic mission plans for the ITM community and the upcoming intermediate class satellite program called TIMED. This report highlights the scientific findings of the SUNDIAL component of the investigation - with those findings resulting in a special issue publication of 7 papers in the Journal of Geophysical Research.				
14. SUBJECT TERMS (a) Ionospheric Physics, (b) Thermospheric Physics, (c) Model Validation, (d) Ground Truth, (e) SUNDIAL			15. NUMBER OF PAGES 14	
			16. PRICE CODE	
17. SECURITY CLASSIFICATION OF REPORT Unclassified	18. SECURITY CLASSIFICATION OF THIS PAGE Unclassified	19. SECURITY CLASSIFICATION OF ABSTRACT Unclassified	20. LIMITATION OF ABSTRACT UL	

**F-Region Climatology During the  
SUNDIAL/ATLAS-1 Campaign of March 1992:  
Model-Measurement Comparisons and  
Cause-Effect Relationships**

**E.P. Szuszczewicz, D. Torr, P. Wilkinson, P. Richards, R. Roble, B. Emery,  
G. Lu, M. Abdu, D. Evans, R. Hanbaba, K. Igarashi, P. Jiao, M. Lester,  
S. Pulinets, B.M. Reddy, P. Blanchard, K. Miller, and J. Joselyn**

**F-Region Climatology During the SUNDIAL/ATLAS-1  
Campaign of March 1992: Model-Measurement Comparisons and  
Cause-Effect Relationships**

E. P. Szuszczewicz<sup>1</sup>, D. Torr<sup>2</sup>, P. Wilkinson<sup>3</sup>, P. Richards<sup>2</sup>, R. Roble<sup>4</sup>, B. Emery<sup>4</sup>,  
G. Lu<sup>4</sup>, M. Abdu<sup>5</sup>, D. Evans<sup>6</sup>, R. Hanbaba<sup>7</sup>, K. Igarashi<sup>8</sup>, P. Jiao<sup>9</sup>, M. Lester<sup>10</sup>,  
S. Pulinets<sup>11</sup>, B.M. Reddy<sup>12</sup>, P. Blanchard<sup>1</sup>, K. Miller<sup>13</sup>, J. Joselyn<sup>6</sup>

Short Title: F-Region Climatology During the SUNDIAL/ATLAS-1 Campaign

**ABSTRACT**

We present the first joint comparison of global measurements of F-region characteristics with three models used widely in the specification of the ionospheric-thermospheric system. The models, the IRI, FLIP and TIGCM, represent a unique set of capabilities with major differences in approaches to the prevailing physics and different levels of computational complexity. The database was developed by a global network of 53 ionosonde stations operating around-the-clock for the period 22 March through 4 April 1992 in collaboration with the ATLAS-1 mission. The emphasis is on the F-region characteristics of peak heights ( $h_m F_2$ ) and densities ( $f_o F_2$ ), their climatological (i.e., average) behavior during the ATLAS-1 period, and associated cause-effect relationships. We explore latitudinal and UT/LT variations with attention

---

<sup>1</sup>Science Applications International Corporation, McLean, Virginia

<sup>2</sup>University of Alabama, Huntsville, Alabama

<sup>3</sup>IPS Radio & Space Services, West Chatswood, Australia

<sup>4</sup>National Center for Atmospheric Research, Boulder, Colorado

<sup>5</sup>Instituto Nacional De Pesquisas Espaciais, Sao Paulo, Brazil

<sup>6</sup>NOAA, Boulder, Colorado

<sup>7</sup>CNET, Lannion, France

<sup>8</sup>Communications Research Lab, Tokyo, Japan

<sup>9</sup>China Research Institute of Radio Propagation

<sup>10</sup>University of Leicester, Leicester, United Kingdom

<sup>11</sup>IZMIRAN, Moscow, Russia

<sup>12</sup>National Physical Laboratory, New Delhi, India

<sup>13</sup>Utah State University, Logan, Utah

to the influences of meridional winds and plasmaspheric fluxes in the maintenance of different domains in the ionospheric-thermospheric system. We find that all three models tend to underestimate the values of  $h_m F_2$  and  $f_0 F_2$  with the largest discrepancies in  $f_0 F_2$  resulting in the FLIP and TIGCM representations at night. These discrepancies can grow to levels as large as 45% near 4 AM LT, a "rediscovery" of the old but unsettled issue of maintenance of the nighttime ionosphere. This nighttime discrepancy is traceable in first order to model underestimates of prevailing meridional winds. The contributions of plasmaspheric fluxes are also considered, with the conclusion that they are of secondary importance, but substantially more work is necessary to uniquely quantify their role. In contrast to their nighttime characteristics, the FLIP and TIGCM generally have excellent agreement (i.e.  $\pm 3\%$ ) with daytime observations of  $f_0 F_2$ , and the IRI tends to underestimate the observed values of  $f_0 F_2$  by a nominally LT-insensitive level of  $13 \pm 3\%$ . We review other campaign results in this special issue, with a focus on regional responses to the prevailing conditions and their characterization in terms of latitudinal distributions of F-region heights and densities.

## 1. INTRODUCTION

### 1.1 Perspectives on the Investigation

There are a number of trends evolving in experimental and theoretical aspects of solar-terrestrial physics. These may be considered to include: 1) The organization of characteristic responses within the framework of space weather and climatology; 2) An increased emphasis on remote sensing techniques; and 3) Dependence on large-scale numerical models for predictions or deductions about cause-effect relationships that are not readily measured.

Within the concept of "space weather and climatology" [Sime and Behnke, 1994; Siscoe et al., 1994; Szuszczewicz, 1995], climatology deals with



"average" conditions that result under a set of large-scale slowly-changing (i.e., weeks, to months, to years) forcing functions. On the other hand, weather addresses drivers and system responses framed within their hour-to-hour and day-to-day variability. Embodied in these concepts is the idea of "predictions" that encompasses the scientifically rigorous position that accurate predictions of weather and climatology are the ultimate test of understanding. As space science matures the logic of such a focus looms as increasingly important.

The trend toward an ever-increasing reliance on large-scale numerical models stems in part from the premise that no measurement program will ever be able to define completely the input and output parameters in a given cause-effect chain of geophysical events. Thus theory, and in particular comprehensive first-principle models, must be relied upon to make deductions where data are not available and to provide insight into the physical processes of importance. However, theoretical models are accurate only to the extent that the fundamental processes are adequately understood, mathematically represented, and empirically bounded. Therefore there is the need to use experimental data, in particular global-scale data, to validate individual models, quantify their accuracies, impose self-consistency, and identify regions for improvement.

The trend toward an increased emphasis on remote sensing techniques is motivated in part by the number of geophysical or solar-terrestrial domains that are difficult or impossible to routinely access with "in situ" techniques. This trend also appears to be motivated by a perspective that remote sensing techniques can provide more global views of phenomenological domains and therefore perform (arguably) more effectively than satellite- or rocket-borne "in situ" diagnostics. Such has been the thrust of the ATLAS-1 mission [Torr et al., 1993; Fennelly et al., 1993], the current series of Shuttle-borne GLO

investigations [Broadfoot et al., 1992; Gardner et al., 1995], and the planned NASA/TIMED satellite program. Many of the remote sensing techniques however are integrated line-of-sight measurements that require inversion procedures that are forced to make assumptions about the physical processes and local particle distributions giving rise to their respective observables. Therefore, there is often need for coincident ground-truth measurements that provide benchmarks for the remote sensing procedures as well as spatial and temporal continuity between and among the along-track remote-sensing database.

This investigation embodies all three trends. It addresses the issue of cause-effect terms as manifested in the global-scale climatology of the ionospheric-thermospheric system during the solar-maximum equinoctial period of the ATLAS-1 period. It also addresses the issue of model testing and verification, with an emphasis on quantifying agreement and disagreement with observations as well as between and among various models. The approach also focuses on remote sensing techniques and necessary elements of ground-truth with a global network of 53 SUNDIAL ionosondes operating around-the-clock for the entire period of the ATLAS-1 mission (23 March through 2 April 1992).

## **1.2 Investigative Components**

ATLAS-1 was launched on March 23, 1992 at 13:01 UT into a 57° inclination 297 km circular orbit with a complement of photometric devices covering atomic, molecular and ionic emissions over the wavelength regime from the EUV through the IR [Torr et al., 1993]. The intent was to measure the density and temperature distributions of the neutral and ion constituents from mesospheric altitudes up through the F-region. This was to be the first of a series of flights which would develop one of the first datasets dealing with the

mesosphere and make available ionospheric and thermospheric results for the test and verification of developing large-scale models.

The ground-based SUNDIAL component had a separate but synergistic set of continuing objectives that supported the ATLAS-1 interests while developing a synoptic view of the global-scale ionospheric-thermospheric (I-T) system. Among those objectives has been the development of a worldwide database [Szuszczewicz et al., 1988, 1990, 1993] for an empirical specification of the state and condition of the I-T system and its weather and climatology as influenced by seasonal, solar-cycle, diurnal and storm-time controls. Working with that database the objectives also contributed to the development of a predictive capability through the test, verification and validation of empirical and first principle models. Past SUNDIAL efforts have included the empirically-derived International Reference Ionosphere (IRI) [Rawer, 1981; Rawer and Ramanamurty, 1985; Schunk and Szuszczewicz, 1988] and the auroral oval models of Feldstein, NOAA/TIROS and DMSP [Szuszczewicz et al., 1993]. Test and validation efforts have also included a number of first-principle models: the time-dependent ionospheric model of Utah State [Wilkinson et al., 1988; Sica et al., 1990], the NCAR Thermospheric-Ionospheric General Circulation Model TIGCM [Wilkinson et al., 1992; Szuszczewicz et al., 1995] and the Rice Convection Model [Spiro et al., 1988; Fejer et al., 1990].

In this investigation we concentrate on the IRI, the NCAR/TIGCM, and the FLIP (FLIP = Field Line Interhemispheric Plasma [Richards et al., 1994a]) models. They represent a unique set of capabilities that reflect major differences in approaches to the representation of the prevailing physics along with a substantial difference in computer requirements. The IRI, FLIP, and TIGCM are PC, work station, and Cray based, respectively. The IRI is purely empirical in its approach. The FLIP code is a one-dimensional model which

inputs thermospheric controls by incorporating composition from the MSIS model (Mass Spectrometer and Incoherent Radar, Hedin (1987)) and meridional winds from empirical models or from radars, ionosondes or Fabry-Perot interferometers. The NCAR/TIGCM might (arguably) be considered the closest to an all first-principles model since it self-consistently solves the system of equations which defines the coupled I-T domain. Rigorously speaking however, it is not entirely first principle since it invokes the empirically-defined electric field model of Richmond et al. [1980] and the AMIE specification [Richmond, 1992; Lu, 1995a] of particles, fields, and currents at high latitudes. We present here the very first joint comparison of all three approaches against the global database with a perspective that highlights the differences in the approaches and the relative agreement with the data. We focus on climatology, drawing perspectives on diurnal variability, thermospheric wind controls, plasmaspheric fluxes, and phenomenological domains. We also include a perspective on the overall characteristics of the F-region ionosphere as manifested during the March 23 to April 2, 1992 SUNDIAL/ATLAS-1 period.

## **2. THE DATABASE AND THE MODELS**

### **2.1 The Data**

#### **2.1.1 Prevailing conditions**

The SUNDIAL/ATLAS-1 campaign was conducted during the first equinoctial period of the descending phase of solar cycle 22. The months of March and April showed a dramatic decrease in energetic solar events compared with previous months. While there were 49 energetic solar x-ray events (M-class or higher) in February, there were only four in March and eight in April. Four M-class events occurred during the ATLAS-1 period: one on March 31 at 1545 UT and three on April 1 at 0100, 1017 and 1748 UT. The

average uncorrected 10.7 cm flux for the ATLAS-1 period was 182, compared with averages of 171 and 158 for the entire months of March and April, respectively.

Solar wind observations for the campaign period were not available through the 26th of March, but observations for the remainder of the campaign showed rather steady behavior with the solar wind velocity in the 325-425 km/sec domain, and densities holding relatively steady near  $10/\text{cm}^3$ . There was a brief period in which the density was enhanced by a factor of three (around 21-24 UT on 31 March) but that was not accompanied by any increased velocity.

To develop a perspective on geomagnetic activity for the season and phase of the solar cycle in which the investigation took place, we present in Figure 1 the  $K_p$ ,  $A_p$  and  $-Dst$  indices. The three panels in that figure, top-to-bottom, show  $K_p$ ,  $A_p$ , and  $-Dst$ , respectively, for March and April 1992. The  $K_p$  and  $A_p$  values,  $3 \pm 2$  and  $20 \pm 15$ , respectively, for the ATLAS-1 period (March 23 - April 2) were generally typical for the entire month of March. Overall, the conditions can be described as moderately active.

In the bottom panel of Figure 1 it can be seen that  $-Dst$  values were generally depressed during the ATLAS-1 period with values less than -50 considered "stormy" [Taylor et al., 1994; Kamide, 1994]. These results show that the entire ATLAS-1 period occurred during the recovery phase of a storm that took place at about 2300 UT on 21 March. That recovery can be seen to be populated by a number of substorms [Lester et al., 1995] with  $Dst$  values gradually returning to zero on April 2, the quietest day of the entire campaign.

One final perspective on energy inputs and activity levels were provided by the interhemispheric power and activity indices determined by measurements on the NOAA/TIROS satellite [Foster et al., 1986]. Those results

corroborate the generally active nature of the ATLAS-1 period. The NOAA/TIROS activity indices were routinely between 4 and 8, with only two brief excursions to the maximum level of activity (i.e., 10) at about 17 UT on 24 March and 4 UT on 29 March.

In companion papers, substorm influences on high-latitude conductivities are investigated during the periods 27 and 30-31 March [Lester et al., 1995], while the overlapping GEM (Geophysical Environmental Modeling) campaign days of March 28 and 29 are studied from perspectives focused on high-latitude inputs and substorms [Lu et al., 1995b] and global-scale ionospheric-thermospheric variability [Emery et al., 1995]. These studies, along the investigations of Wilkinson et al. (1995), Abdu et al. (1995), and Pulinets et al. (1995), who focus on ionospheric weather and climatology in the 115°-165° longitude zone, at equatorial latitudes, and in the Russian sector, respectively, represent the ground-based measurement and modeling component of the campaign.

### **2.1.2 The ionosonde database**

The ground-based data were acquired by the global network of 53 ionosonde stations listed in Table 1, complemented by radar observations at EISCAT, Sondrestrom, Millstone Hill, Arecibo, and Jicamarca. While the radar observations operated only on a short schedule, the ionosonde measurements were carried out around-the-clock for the entire ATLAS-1 period with emphasis here on F-region characteristics ( $f_0F_2$  and  $M(3000)F_2$ ).  $f_0F_2$  is the critical frequency of the  $F_2$ -peak ( $f_0F_2$  [kHz] =  $8.9(10^3)[N_mF_2(\text{cm}^{-3})]^{1/2}$ ) and  $M(3000)F_2$  is the transmission factor from which the real height  $h_mF_2$  of the  $F_2$ -peak can be derived [Dudeney, 1983]. Accuracy in the values of  $f_0F_2$  and  $M(3000)F_2$  is discussed in Wilkinson [1978] and potential errors in the transformation of  $M(3000)F_2$  to  $h_mF_2$  are discussed in Wilkinson et al. (1996, this issue). These

references report that accuracy in  $f_0F_2$  is typically 0.1 MHz (or equivalently 125  $\text{cm}^{-3}$  in the density of the  $F_2$  peak,  $N_mF_2$ ) and inaccuracies in  $M(3000)F_2$  can amount to random errors in  $h_mF_2$  not in excess of  $\pm 10$  km.

Table 2 and Figure 2 provide an introductory perspective on observed ground-based responses of the ionosphere to the prevailing solar-terrestrial conditions. Table 2 presents a subset of "events" primarily observed in the northern hemisphere. These include a series of substorms, as identified in the European sector by the successor to the EISCAT magnetometer cross [Luhr et al., 1984], the midlatitude SAMNET magnetometer chain [Yeoman et al., 1990], and by positive and negative storm phases in the Russian and French ionosonde results.

In general, "stormy" ionospheric conditions were observed at high latitudes, while nominally-quiet characteristics were observed at mid- and equatorial latitudes. This can be seen to some extent in Figure 2 which displays diurnal plots of  $f_0F_2$  for pairs of stations in the Russian/East-African, the Asian/Australian, and the American sectors. ( $f_0F_2$  will be expressed in MHz throughout the paper. For readers preferring  $N_mF_2$  we note for reference that  $f_0F_2 = 5, 10$  and  $15$  MHz converts to  $N_mF_2 = 0.3, 1.3$  and  $2.8(10^6) \text{ cm}^{-3}$ , respectively.) These station pairs (each pair formed by a high-northern and low-southern latitude site in approximately the same longitude sector) are Moscow/La Reunion, Magadan/Townsville, and Ottawa/Buenos Aires, respectively. The plots present: 1) the hourly observations as solid dots, 2) the average diurnal characteristic determined for the entire campaign period as a solid line, and 3) the IRI specification as a dashed line. It can be seen in the figure that the high-latitude sites show irregular day-to-day behavior. Note, for example, the negative and positive storm phases at Moscow on the 25th and 27th, respectively. By contrast, the mid-latitude stations show very regular

behavior, with the day-to-day characteristics virtually identical with the campaign-period average

All ionosonde data were subjected to three levels of editing and quality control: the first by regional coordinators (e.g. Drs. Pulnits for Russian data, Dr. Abdu for South American data, etc.), the second at the initial staging center for data fusion (the Ionospheric Prediction Service, at Sydney, Australia), and the third at the SAIC Data Archive and Analysis Center where errors and inconsistencies were screened on regional and global bases using special-purpose data handling and visualization tools [Szuszcwicz et al., 1995c]. This process mitigated possible contamination of subsequent model-measurement comparisons by spurious or otherwise erroneous data.

## **2.2 The Models**

### **2.2.1 The IRI**

Currently the empirically-derived IRI model is the most used and widely-tested climatological specification of the global ionosphere [Rawer, 1981; Rawer and Ramanamurty, 1985; Schunk and Szuszcwicz, 1988]. It describes the E- and F-regions of the ionosphere in terms of location (geographic or geomagnetic), time, solar activity (sunspot number), and season (month). By definition it is based on accumulated data, including critical frequencies ( $f_oE$ ,  $f_oE_s$ ,  $f_oF_1$ , and  $f_oF_2$ ), altitudes of peak concentrations ( $h_mE$ ,  $h_mF_1$ , and  $h_mF_2$ ), half thicknesses of the individual layers, and ion composition and plasma temperatures. The database forming the foundation of the IRI was compiled from ionosondes, topside sounders, incoherent scatter radars, and *in situ* satellite and rocket profiles (wherever available). Averaged profiles were synthesized and analytical fits developed, with the end product representing an intelligent mix of empiricism, physics, extrapolation, and intuition. In general, the quality of the IRI representation of actual climatological conditions is directly



related to available data, its global distribution, parameter space coverage, time base, and accuracy. Obvious gaps in the database include ocean regions and ionogram definition of the *E-F* region valley.

Notwithstanding the limitations of the IRI, it can (and does) provide a valuable resource that includes a broad experience base in ionospheric profiling and data archiving. Its output provides a global specification not only on the macroscale features of electron density, but also on the ion and electron temperatures, and the ion composition. These additional features make the IRI an attractive model for comparison with satellite and ground-based data as well as first-principle codes.

The IRI is an evolutionary model, with its primary emphasis being an attempt at a global-scale representation of observations. In this regard the IRI makes its limitations clear, particularly with regard to the relative paucity of ion composition results. Work has continued in improving its specification of the topside domain [Bilitza, 1994], its specification of plasma temperatures and ion composition [Bilitza et al., 1992a], and its specification of global and mesoscale electron density distributions [Bilitza et al., 1992b; and Szuszczewicz et al., 1990 and 1993]; while its inaccuracies at high latitudes can be partially mitigated by inclusion of the NOAA/TIROS, DMSP, or Feldstein auroral oval models [Szuszczewicz, et al., 1993, and references therein].

For comparisons in this investigation the IRI was run with the observed smoothed sunspot number of 108 and a seasonal behavior equivalent to the end of March and beginning of April (i.e., month = 3.5), a period conforming closely to the SUNDIAL/ATLAS-1 campaign.

### **2.2.2 The FLIP Model**

The field line interhemispheric plasma model has been described previously by Richards and Torr [1988] and more recently by Torr et al. [1990]

and Richards et al [1994a]. The main component of this one-dimensional model calculates the plasma densities and temperatures along entire magnetic flux tubes from 80 km in the northern hemisphere through the plasmasphere to 80 km in the southern hemisphere using a tilted dipole approximation to the Earth's magnetic field. The FLIP model solves the continuity and momentum equations for  $O^+$ ,  $H^+$ ,  $N^+$ , and  $He^+$ .

The electron and ion temperatures are obtained by solving the energy equations [Schunk and Nagy, 1978] with electron heating due to photoelectrons provided by a solution of the two-stream photoelectron flux equations using the method of Nagy and Banks [1970]. The solutions have been extended to encompass the entire field line on the same spatial grid as the ion continuity and momentum equations.

Once all the interhemispheric solutions have been determined, densities of  $NO^+$ ,  $O_2^+$ ,  $N_2^+$  ( $v=0-6$ ),  $O^+(2D)$ , and  $O^+(2P)$  are obtained from local chemical equilibrium. Then diffusion equations are solved on separate vertical grids in both hemispheres to obtain the densities of the minor neutral species  $N(2D)$ ,  $N(4S)$ ,  $NO$ , and vibrationally excited  $N_2$  on vertical grids extending from 80 km to about 500 km in each hemisphere.

The FLIP model includes provisions to solve the continuity and momentum equations for the first six vibrational levels of  $N_2$  in order to take into account the strong dependence of the  $O^+ + N_2 \rightarrow NO^+ + N$  reaction rate on vibrational excitation of  $N_2$  [Richards et al., 1986; Richards and Torr, 1986a]. However, vibrationally excited  $N_2$  was not included in the present investigation, noting that in a recent study of ionospheric behavior at Millstone Hill and Hobart during 1990, the FLIP model was able to reproduce the observed daytime densities extremely well without the need for an accounting of vibrationally-excited  $N_2$  [Richards et al., 1994a].

Most important reaction rates and cross sections that are used in the FLIP model are now reasonably-well established [Torr et al., 1990], and some innovative algorithms have been developed in recent years to incorporate actual measurements (e.g. F-region heights or meridional winds) into the FLIP model when they are available [Richards et al., 1995].

The FLIP model requires three key inputs: 1) the neutral atmosphere, 2) either the meridional component of the neutral wind or  $h_m F_2$  (which is converted into a wind), 3) and the solar EUV flux. The neutral densities and temperatures are provided by the mass spectrometer and incoherent scatter (MSIS-86) model [Hedin, 1987]. Once the time and location of the required thermospheric parameters are specified, the only adjustable parameters in the MSIS model are the solar index (F10.7) and magnetic index ( $A_p$ .) Both the solar activity and magnetic activity indices were stable in late March 1992. Under these circumstances, there was little day-to-day variation in the model calculation and it was possible to simulate just one day as being representative of the whole period, with no adjustments made to the input parameters to obtain better agreement with the data.

For this investigation the FLIP model winds were obtained from the International Reference Ionosphere (IRI) model specifications for  $h_m F_2$  during March 1992 using the servo-analysis method of Richards [1991]. For climatological studies, this method is preferred over using winds from the HWM90 model of Hedin et al. [1991] because the IRI  $h_m F_2$  is based on a much larger database with greater global coverage.

For the EUV fluxes in FLIP we have used a new solar flux model called EUVAC [Richards et al., 1994b] which is based on the F74113 solar EUV reference spectrum and the relative variations of the EUV flux observed by the

Atmosphere Explorer E satellite. The EUVAC model produces 50-575 Å integrated fluxes that agree well with the most reliable rocket measurements.

Apart from the uncertainties in the neutral densities, winds, and EUV flux, there are uncertainties in the degree of particle and energy coupling between the ionosphere and plasmasphere. Although the FLIP model self-consistently includes coupling to the plasmasphere and the conjugate ionosphere, there can be large uncertainties in the plasma and heat content of the plasmasphere. There is currently no way of measuring or predicting the state of the plasmasphere as it recovers after magnetic storm depletions. These uncertainties in the plasmasphere have little effect on the daytime ionosphere, but there may be up to a factor of two difference in the calculated  $N_m F_2$  (or equivalently a factor of 1.4 in the calculated  $f_0 F_2$ ) at night for extremes of assumptions about the plasmaspheric conditions. In this paper, the flux tubes were moderately depleted at the beginning of the run but filled up during the simulation periods. Thus, flux tubes below  $L = 2$ , which fill up quickly, were close to full, while longer flux tubes were about half full during the simulation period.

The ionospheres in the auroral and equatorial regions are extremely difficult to model quantitatively with FLIP (and most other models). In the auroral zone there are electric fields, particle precipitation, and changes in neutral composition which are difficult to predict, while in the equatorial region the variation of the electric fields is the main cause of uncertainty. The FLIP model does not model the electron densities well in the equatorial and auroral zones primarily because it does not currently include convection electric fields. The model is now being modified to account for this.

### 2.2.3 The TIGCM

The NCAR TIGCM self-consistently calculates thermospheric and ionospheric structure, taking into account the dynamic coupling between the thermospheric neutral wind and the ionospheric plasma [Roble et al., 1988]. It is an outgrowth of the NCAR-TGCM (Thermospheric General Circulation Model) which included a non-reactive empirical ionosphere and solved the primitive equations of dynamic meteorology adapted to the physics appropriate to thermospheric heights. The basic TGCM and associated developments have been described in detail by Dickinson et al. [1981, 1984], Roble et al. [1987], Fesen et al. [1986], and Roble and Ridley [1987].

The TIGCM employs an Eulerian approach to modeling the ionosphere as an alternative to the Lagrangian approach used by Sojka and Schunk [1985] and Fuller-Rowell et al. [1987]. Equations describing the ionosphere and thermosphere are both solved on the TGCM geographic grid and ion drift for the ionospheric calculation is obtained from the empirical model of Richmond et al. [1980] for low- and mid-latitudes while the empirical model of Heelis et al. [1982] or the AMIE (Assimilative Mapping of Ionospheric Electrodynamics, Richmond, 1992) procedure is used for high latitudes. Therefore the model does not self-consistently solve for the naturally occurring electrodynamic coupling in the magnetospheric-ionospheric-thermospheric system. The TIGCM also employs a simple dipole magnetic field model with displaced geomagnetic and geographic poles. For inputs, the model requires specifications of several external sources. These include solar EUV and UV fluxes, auroral particle precipitation, the ionospheric convection pattern, and the amplitudes and phases of semi-diurnal tides at the mesopause boundary.

The odd nitrogen chemistry is the same as that discussed by Roble et al. [1987].  $N(^2D)$  is assumed to be in photochemical equilibrium throughout the

thermosphere and transport equations are solved for  $N(^4S)$  and NO. The model considers  $N(^4S)$  in photochemical equilibrium and specifies a constant number density of  $8 \times 10^6 \text{ cm}^{-3}$  for NO at the lower boundary.

The ion-chemistry scheme, rate coefficients, and calculation procedure for the ionosphere can be reviewed in Roble et al. [1987] and Roble and Ridley [1987], while the bulk motion includes both magnetic field-aligned diffusion and  $\underline{E} \times \underline{B}$  forces in solving transport equations.

The upper boundary condition is diffusive equilibrium. The upper altitude limit of the model is about 550 km where an analytical formulation is used as a boundary condition for positive and negative flux transfer. This flux, which contributes to the overall density-height profile and equilibrium values of  $f_0F_2$  and  $h_mF_2$ , results from normal topside dynamics (e.g., wind and electric-field induced transport) as well as inputs from the conjugate ionosphere and fluxtube-coupled regions of the outer plasmasphere. Under equinox conditions with full fluxtubes,  $O^+$  flows up from the ionosphere during the day, charge exchanges with neutral H to produce  $H^+$ , which in turn is stored in the outer plasmasphere. The process reverses at night, with the end result being an oversimplified diurnal characteristic which consists of an ebb and flow of plasma between the ionosphere and outer plasmasphere. This process is referred alternatively as plasmaspheric flux, magnetospheric flux, protonospheric flux, or ionospheric-plasmaspheric flux.

The lower boundary condition assumes photochemical equilibrium. Once the  $O^+$  density distribution is defined, the  $NO^+$ ,  $O_2^+$ ,  $N_2^+$  and  $N^+$  distributions are determined by assuming photochemical equilibrium [Roble and Ridley, 1987]. The temperature, dynamics, composition and the global ionosphere are calculated at each time step and the heating and cooling rates from chemical reactions, IR emissions, etc. are coupled into the thermodynamic

equation at the next time step. Likewise, neutral winds, temperature, composition, and ionization rates are updated at each time step for the ionospheric calculation.

The TIGCM output provides global distributions of the neutral gas temperature and winds, ion drift velocities, the heights of constant pressure surfaces, and the number densities of  $O_2$ ,  $N_2$ ,  $O$ ,  $N(^2D)$ ,  $N(^4S)$ ,  $NO$ ,  $He$ , and  $Ar$ . It also solves for the ionospheric structure, giving global distributions of  $O^+$ ,  $O_2^+$ ,  $NO^+$ ,  $N_2^+$ ,  $N^+$ , electron density, and ion and electron temperatures. The TIGCM has an effective  $5^\circ$  latitude-longitude geographic grid with 25 constant pressure levels in the altitude range from approximately 97 km to 500 km. The time step can be flexible, varying from 3-min to 6-min, depending on the inputs. The model was exercised in a "weather" mode with an emphasis on March 28 and 29 in studies of high-latitude electrodynamics [Lu et al., 1994; Emery et al., 1995]. It was also run in a "climatological" mode in order to specify the baseline conditions upon which to initiate the study of electrodynamics on the 28 and 29. The "climatological" run, described more fully in Emery et al. [1995], is the basis for the TIGCM model-measurement comparisons carried out in this investigation.

For March 28 and 29 the average solar radiation index  $S_a$  (i.e. the 10.7 cm flux) was  $188.5 \times 10^{-22} \text{ W/m}^2 \text{ Hz}$ . This was the fundamental input driving the specification of the solar EUV and UV fluxes. For energetic inputs at high latitudes, ionospheric convection and particle precipitation were derived from AMIE (Assimilative Mapping of Ionospheric Electrodynamics) with approximately 50-min resolution; while the low- and mid-latitude ionospheric convection was derived from the empirical model of Richmond et al. [1980].

The semidiurnal tide model, described by Fesen et al. (1991), was included at the lower boundary of the TIGCM, and the model was first run to

obtain a diurnally reproducible solution. For a "climatological" run, the patterns of the ionospheric convection and particle precipitation used in this investigation were an averaged AMIE prescription, derived from detailed data acquired during the 48-hour period 28-29 March 1992 and described in the companion paper by Emery et al. [1995]. The time-dependent AMIE patterns were then incorporated into the TIGCM for a simulation of high-latitude thermospheric dynamics.

### 3. MODEL-MEASUREMENT COMPARISONS

#### 3.1 Global Perspectives

Figures 3 and 4 provide global comparisons of the observed values of  $f_0F_2$  and  $h_mF_2$ , respectively, at UT=12 with the "predictions" of the IRI, the TIGCM, and the FLIP models (top, middle, and bottom panels, respectively). The observations at each station represent the value averaged over the campaign period for the UT (or LT) in question. The colored circles in the figures locate the stations, with the percent difference between the model predictions and the individual station observations defined by the color legend on the bottom left side of the figures. The bottom right hand color bar defines the range of values for the color-coded isocontours in the figure (for  $f_0F_2$  and  $h_mF_2$  in Figures 3 and 4, respectively) which correspond to the outputs of each of the models in their respective panels. The abscissa is longitude with  $0^\circ$  at the center. The ordinate is latitude, extending north and south to  $\pm 90^\circ$  from the geographic equator. The  $f_0F_2$  contours are color-coded from a low value of 3 MHz (dark blue,  $N_e = 1.1(10)^5 \text{ cm}^{-3}$ ) to a high value of 16 MHz (red,  $N_e = 3.2(10)^6 \text{ cm}^{-3}$ ).  $h_mF_2$  contours are also color-coded with a red-to-blue range extending from 500 to 250 km. The black curves at high northern/southern latitudes specify the boundaries of the auroral oval according to the Feldstein



model for a moderate activity level  $Q = 4$  [Feldstein, 1963; Holtzworth and Meng, 1975].

The  $f_0F_2$  features (e.g., in the IRI panel) which dominate the figure include: (1) the sunrise terminator in the American sector rising in a span of approximately one hour from 5 to 10 MHz (i.e.,  $N_mF_2$  from  $0.3$  to  $1.3 (10^6) \text{ cm}^{-3}$ ), and (2) the Appleton Anomaly with its peak densities somewhat symmetrically centered about the dip equator and extending in local time from 9 AM to midnight. These large-scale features, along with the auroral oval boundaries, help identify important phenomenological domains while providing visual aides to the local time.

The  $f_0F_2$  contours in Figure 3 show that the largest densities are at the daytime peaks of the Appleton Anomaly, with the highest value near 16 MHz ( $N_mF_2 = 3.2(10^6) \text{ cm}^{-3}$ ) at  $LT \approx 1400$  tapering off from the individual peaks to lower values equatorward and poleward. The lowest values are in the pre-dawn sector, with magnitudes near 5 MHz ( $N_mF_2 = 3(10^5) \text{ cm}^{-3}$ ).

A review of the IRI panel in Figure 4 reveals maximum values of  $h_mF_2$  at the daytime equator with magnitudes in 425 km range. F-region heights fall off poleward of the equatorial region and at all latitudes in evening and night time hours ( $LT \geq 8 \text{ PM}$ ). Lowest F-region heights are in the dawn sector at middle-to-high latitudes where values are near 275 km .

The FLIP and TIGCM panels in Figures 3 and 4 show characteristics similar to those described in the IRI panel with the exception that the FLIP model does not reproduce the well-known double peak of the Appleton Anomaly. This is primarily due to the fact that FLIP is designed for midlatitudes where it accounts for winds, chemistry, and plasmaspheric fluxes. It has no convection electric fields and therefore its results are compromised at low-to-equatorial latitudes where electric fields are important.

Each ionosonde site in Figures 3 and 4 is identified by a colored circle, with the color representing the percent difference between the observed value ( $f_0F_2$  or  $h_mF_2$ ) and the model prediction (i.e., % difference = 100 (Data - Model)/Data). The differences are presented on a scale of -40% to +40% in  $f_0F_2$  and -25% to +25% in  $h_mF_2$  (in both cases over the range blue to red as scaled in the legend).

We offer the following observations relative to Figure 3:

1) The IRI underestimates the values of  $f_0F_2$ , with the primary differences ranging from 0% (green) to 20% (yellow). There is no obvious LT dependence in the differences. Within a few percent this has been found to be true for all UT intervals.

2) Both the FLIP and TIGCM predictions demonstrate better agreement with the  $f_0F_2$  data in daytime (more greens), and both depart in major ways from the data in the post-sunset to pre-sunrise period. In the nighttime hours the FLIP model and TIGCM tend to underestimate the critical frequencies of the F-region peak by 20-40%. This is a consistent feature that prevailed for all UT intervals.

Reference to Figure 4 leads to the following observations regarding  $h_mF_2$ :

1) All three models either agree with the data (green) or underestimate the heights of the F-region peaks by as much as 20 - 25% (orange to red).

2) The level of agreement between data and model are comparable for both the FLIP and TIGCM, whereas the overall results suggest that the IRI has the poorest representation of  $h_mF_2$  among the three model comparisons displayed in the figure. This will be shown to be generally true but not by a large margin.

Before leaving the discussion of Figure 4 we note that the ionosonde values of  $h_m F_2$  were derived from the M(3000) $F_2$  algorithm of Dudeney [1983]. Had we used the  $h_m F_2$  formulism of Bilitza et al. [1979] instead, there would have been little-to-no difference at night and smaller ionosonde-derived values of  $h_m F_2$  during the day. But the daytime difference between the Dudeney and Bilitza et al. approaches would generally be less than 2.5%.

### **3.2 An integrated view of LT and latitudinal effects**

Figure 5 provides an integrated view of the model-measurement comparisons with a perspective that establishes quantitative figures of merit for each of the models. The results in Figure 5 also help develop an understanding of inaccuracies in the model predictions that might be identified with geophysical domains or LT dependence.

The top, middle, and bottom panels present comparisons of the campaign-averaged data with the IRI, FLIP and TIGCM climatological "predictions" in regions for which  $\text{abs}(\text{MLAT}) < 25^\circ$ ,  $\text{abs}(\text{MLAT}) > 25^\circ$ , and  $0^\circ \leq \text{abs}(\text{MLAT}) \leq 90^\circ$ , respectively. The latter case involves all stations, while  $\text{abs}(\text{MLAT}) < 25^\circ$  and  $>25^\circ$  refer to model comparisons with the equatorial-to-low latitude and mid-to-high latitude stations, respectively. The left column deals with  $f_0 F_2$  and the right panel deals with  $h_m F_2$ . The abscissa is LT while the ordinate is the percent difference between the data and the model. (Positive values occur when the magnitudes of the observations are greater than the predictions of the model, that is, when the models underestimate the observable.) Each LT plot has been integrated over all universal times with a sliding 3 hr LT window for each UT from 0 through 23 hrs.

Focusing first on the bottom panels of Figure 5 (comparisons with all stations) we offer the following conclusions:

1) The FLIP and TIGCM do very well in  $f_0F_2$  daytime comparisons ( $6 < LT[hrs] < 18$ ), underestimating and overestimating the data by  $+3\pm 3\%$  and  $-3\pm 3\%$ , respectively. (We note that positive percentages mean that the data values are in excess of the model values). In the same LT period the IRI underestimates the data by  $+12\pm 2\%$ , with an overall diurnal characteristic that is virtually LT-independent.

2) The FLIP and TIGCM predictions for  $f_0F_2$  show a marked departure from agreement with the observations in the post-sunset to pre-sunrise period (i.e.,  $18 \leq LT \leq 6$ ), rising sharply from excellent agreement at sunset to disagreements at levels near 45% and 28% for the FLIP and TIGCM models, respectively, near  $LT = 4$ . (We note that a 45% underestimate in  $f_0F_2$  is a 110% underestimate in  $N_mF_2$ ). An initial suggestion for the cause of this discrepancy is the "old unsolved problem" involving the maintenance of the nighttime ionosphere through plasmaspheric fluxes [see e.g., Evans, 1975; Sica et al, 1990]. We will discuss this issue more fully in subsequent sections, but first move on to other observations in Figure 5 including discrepancies in  $h_mF_2$  and their associated impact on  $f_0F_2$  values.

3) The bottom-right panel in Figure 3 compares the observed values of  $h_mF_2$  (all stations) with the model predictions. The results show that all models underestimate the observations by values less than 13%, with the IRI having the poorest and the TIGCM the best overall agreement with the data. In the post-sunset to pre-sunrise period the FLIP and TIGCM are nearly identical, generally underestimating  $h_mF_2$  by  $5\pm 2\%$ . At 300 km this is a 15 km underestimate, or equivalently a half scale height for  $N_2$ . If  $O^+ + N_2 \rightarrow NO^+ + N$  and  $NO^+ + e \rightarrow N + O$  were the primary loss channels for F-peak densities, a theoretical underestimate in  $h_mF_2$  by a half scale height in  $N_2$  (i.e., 15 km) would account

for a 50% increase in the loss rate of  $O^+$  ions. This is indeed a potential contribution to the observed discrepancies in  $f_0F_2$ .

4) Continuing to review the results in the bottom-right panel of Figure 5, it can be seen that the FLIP and TIGCM models also underestimate the values of  $h_mF_2$  during the daytime, with FLIP generally worse than the TIGCM. If all other physical processes in the two models are identical, one would expect (assuming the same principle loss mechanism discussed in item #3) that the FLIP model would predict lower values than the TIGCM for  $f_0F_2$ . On a relative scale this is consistent with the daytime findings in the bottom-left panel of Figure 5 where FLIP underestimates and the TIGCM overestimates the values of  $f_0F_2$ .

5) Turning attention to the middle and upper panels of Figure 5, it can be seen that the post-sunset to pre-sunrise discrepancy in  $f_0F_2$  exists at middle-to-high and low-to-equatorial latitudes, respectively. This would suggest that downward transport of  $H^+$  at night and subsequent charge exchange with  $O$  to form increased levels of  $O^+$  is not the cause for the  $f_0F_2$  model-measurement discrepancy. This is because such downward plasmaspheric transport of  $H^+$  is effectively zero at low-to-equatorial latitudes. This interpretation of results is not without counter and supporting arguments. Note for example that the pre-sunrise TIGCM results for  $f_0F_2$  are generally better at low latitudes than at mid-to-high latitudes, suggesting that flux is at least part of the problem. And while the FLIP results at night are worse at low-to-equatorial latitudes, the model includes no electric fields which have a dominant control of heights and densities at equatorial latitudes. At night these electric field controls tend to move  $h_mF_2$  to lower altitudes, thus reducing the plasma densities below those currently predicted by the FLIP model. This suggests that the problem is neither electric fields nor plasmaspheric fluxes.

6) Final observations in Figure 5 focus on  $h_m F_2$ , where the equatorial-to-low latitude results (top-right panel) are uniquely different from those at mid-to-high latitudes. The primary difference is at post-sunset and to a lesser degree at pre-sunrise. The post-sunset discrepancy is most likely the result of the well-known post-sunset pre-reversal enhancement in F-region heights at equatorial latitudes. This is a dynamo effect, not included in the simple electric field model of Richmond et. al (1980) that is employed in the TIGCM. It is interesting to note that it is also not accounted for in the empirically-based IRI, suggesting too little data during that period of the day or too much smoothing of the results. The pre-sunrise enhancement, if we allow ourselves to call it that, is a new observation, with causality most likely associated with ionospheric expansion due to heating at F-region sunrise. This issue will be taken up again in section 3.4.

### **3.3 Effects of thermospheric winds**

The results in Figure 5 suggest a consistency between the  $f_0 F_2$  and  $h_m F_2$  observations, in that model underestimates of  $f_0 F_2$  were correlated with underestimates of  $h_m F_2$ . And this correlation was supported by simple arguments of recombination chemistry. In this section, further analysis of the data allows causality to be traced to model representations of meridional winds, known to have strong influences on  $h_m F_2$  at mid-latitudes.

Figure 6 presents a global perspective of magnetic meridional winds as predicted by the TIGCM, HWM (Horizontal Wind Model, Hedin (1991)), and the FLIP models, as well as those measured by the SUNDIAL network of ionosondes using the  $h_m F_2$  servo-analysis procedures of Miller et al. (1993, 1995) with the Dudeney [1983] formulation for  $h_m F_2$ . With regard to the accuracy of this  $h_m F_2$  servo-analysis procedure we note that several comparisons have been made of winds derived from  $h_m F_2$  with meridional

winds derived from other methods. These have been primarily with incoherent scatter radars (see, e.g., Igi et al. [1995]), although Miller et al. [1986] and Miller [1989] also compared results with winds measured by Fabry-Perot interferometry. In each of these comparisons the winds derived from  $h_m F_2$  measurements were found to be consistent with the results of the other techniques, both in magnitude and in the pattern of variability. This  $h_m F_2$  servo-analysis technique was applied to all stations for such displays as presented in Figure 6 regardless of latitude, but their results are not expected to be realistic representations of meridional winds in regions for which  $\text{abs}(\text{MLAT}) < 20^\circ$ . The presentation in Figure 6 is at UT = 12 with  $f_o F_2$  contours and auroral oval boundaries as previously described. Wind magnitudes are depicted by scaled vector lengths and by color codes at each of the stations. The figure is useful in so far as it develops an appreciation for station distributions and general perspectives on variations with latitude and local time. A review of the figure shows marked differences between the findings of the TIGCM and the HWM and FLIP predictions; and the TIGCM appears to be in best agreement with the observed winds. This is in fact consistent with a general finding when an LT-dependence (integrated over all UTs) is developed for detailed comparisons between measured and modeled winds. Such a comparison is presented in Figure 7 where the abscissa is LT and the ordinate is the magnitude of meridional winds predicted by each of the models or measured by the ground-based network of ionosondes. Only stations in the region  $20^\circ < \text{abs}(\text{MLAT}) < 60^\circ$  were considered in this comparison since this is the general bound of applicability of the servo-analysis technique. Positive winds are poleward, while negative winds are equatorward.

Review of Figure 7 leads to the following observations:

1) There is a large spread in values in both daytime and nighttime sectors. The daytime spread is 0 to 40 meters/sec, while the nighttime spread is 30 to 90 meters/sec.

2) The model in best agreement with the data is the TIGCM.

3) At night the FLIP and TIGCM winds are both less than the observations, suggesting that their values of  $h_m F_2$  should be less than those observed. This is consistent with the findings in Figure 5 as well as with argument that weaker equatorward winds result in lower values of  $h_m F_2$ . Hence, we have established (at least in part) model underestimates of nighttime meridional winds as the cause for lower nighttime model predictions of  $h_m F_2$  and  $f_o F_2$ .

4) During the day the observations show very light winds, generally  $\pm 10$  meters/sec, whereas FLIP and HWM are typically in the 25 m/s range. Both FLIP and the TIGCM predict stronger daytime winds than those observed. FLIP winds are stronger than those of the TIGCM suggesting lower values of  $h_m F_2$  than those predicted by TIGCM. This is consistent with the comparisons discussed in Figure 5.

In closing the discussion of Figure 7 we note that the low ionosonde values for daytime winds are corroborated by the mid-latitude observations of IGI et al. [1995] during summer and equinox periods using both ionosonde and MU radar techniques. This corroboration, taken in concert with the global observations presented here and associated model comparisons, suggests that current wind models must be more carefully evaluated, not only under nighttime conditions (as discussed above in connection with maintenance of the nighttime ionosphere) but in the daytime as well.



### **3.4 Modeling the plasmaspheric flux**

The previous sections have established a cause-effect path which links model underestimates in nighttime values of  $f_0F_2$  to underestimates in  $h_mF_2$  and finally to underestimates in the meridional component of the prevailing thermospheric winds. Ancillary arguments have also suggested that the nighttime discrepancy in  $f_0F_2$  might be due in part to inaccurate model specification of plasmaspheric fluxes.

The issue of plasmaspheric fluxes and their contribution to the maintenance of the nighttime ionosphere has itself been somewhat of a controversy without definitive resolution. Part of the problem is the difficulty in the measurement itself. The early work of Evans (1975) suggested that the incoherent scatter radar technique was perhaps the best approach, but even it, according to Evans, has difficulty in uniquely and quantitatively determining the flux. Among the difficulties is the signal-to-noise ratio at night and the need to eliminate layer dynamics (i.e., induced by winds and electric fields) in order to determine the true plasmaspheric contributions. In his study of five nights (near local midnight at Millstone Hill) spanning four seasons, he found average fluxes at  $3(10)^7/\text{cm}^2 \cdot \text{s}$ . He also found that  $\text{H}^+$  was a minor ion (never greater than 25%) over the altitude range over which useful measurements were made (i.e.,  $<800$  km), and that the majority of the results exhibited a decrease in the  $\text{O}^+$  flux with altitude. This altitude dependence indicated that the layers were descending and corrections had to be made. The maximum flux values were at or near  $h_mF_2$  and approached  $2(10)^9/\text{cm}^2 \cdot \text{s}$ , a value clearly dominated by topside layer dynamics. In the end he concluded that large increases in plasmaspheric fluxes, that could give rise to nighttime increases in total electron content, did not appear to be seen. This conclusion was in keeping with that of

Jain and Williams (1974). We pursue this issue further with a discussion of these fluxes as specified within the TIGCM and the FLIP models.

The TIGCM invokes a sinusoidal latitudinal variation of this flux in which it is defined as zero at the magnetic equator and constant above  $60^\circ$  mlat. The flux model is discontinuous at  $60^\circ$ , with day/night values just equatorward set at  $+2(10)^8/-2(10)^8 \text{ cm}^2\cdot\text{s}$ , and values of  $3(10)^8/-1(10)^8 \text{ cm}^2\cdot\text{s}$  just poleward of that. The region above  $60^\circ$  is constant in latitude, while below  $60^\circ$  it goes to zero at the magnetic equator in a cosine fashion. There is no LT dependence in the flux model with the exception of an interpolation routine from the day/night levels between zenith angles of  $80^\circ$  and  $110^\circ$ . We note that the TIGCM includes no  $\text{H}^+$  transport or associated charge-exchange chemistry. This flux model is applied at the upper altitude limit of the TIGCM (approx. 550 km) and is intended to include all effects on  $\text{O}^+$  (i.e., topside layer dynamics and protonospheric fluxes).

By contrast, the FLIP model approaches the plasmaspheric flux issue self-consistently along fluxtubes from hemisphere to hemisphere. It has already been pointed out that uncertainties in the fluxes between the ionosphere and the plasmasphere have little effect on the daytime ionosphere, but there may be up to a factor of two difference in the calculated  $N_m F_2$  densities (or equivalently a factor of 1.4 in the calculated values of  $f_0 F_2$ ) at night for extremes in assumptions about the plasmaspheric conditions. In this work, the fluxtubes in the FLIP simulations were moderately depleted at the beginning of the run but filled up after several cycles of the simulation. The expectation therefore is that maximum plasmaspheric flux is already making its contribution to the nighttime FLIP values of  $f_0 F_2$ .

Figure 8 plots the flux levels derived in the FLIP model in the  $20^\circ$  meridian for  $30^\circ$ ,  $50^\circ$  and  $70^\circ$  northern geographic latitudes at the 550 km level.

These fluxes represent values that integrate the effects on  $O^+$  of layer movement due to winds and electric fields, photoproduction (in the daytime), heating and cooling of the plasma, and ionospheric-plasmaspheric exchange. The 550 km height is the approximate topside boundary for the TIGCM and has been selected for comparison with its analytical flux formulation.

The interpretation of the fluxes in Figure 8 is complicated by the fact that 550 km is in an altitude regime where measurements by Evans [1975] have indicated that the daytime flux changes sign from downwards at lower altitudes to upwards at higher altitudes. Below this "transition" level, excess ions flow down under the influence of gravity to regions of higher loss in reactions with  $N_2$  and  $O_2$ , while above this altitude  $O^+$  ions flow upwards, and through charge exchange with H, produce  $H^+$  ions. Some of the flux variation in Figure 8 is due to movement of the altitude of the transition between upward and downward flux. Figure 8 shows that there are 3 prominent features of the diurnal flux variation: the sunrise and midday upward flux maxima, and the post-sunset downward flux maximum. (The southern hemisphere  $O^+$  flux variation shows similar features to the northern hemisphere variation discussed here.) The sunrise peak in the  $O^+$  flux is principally a consequence of the thermal expansion of the ionospheric plasma. The low density in the morning allows the electron temperature to rise steeply, causing a large increase in scale height that is seen as a large flux in the topside ionosphere [Richards and Torr, 1986]. Because of the tilt of the magnetic field, the sun rises more than half an hour earlier in the southern hemisphere than in the northern hemisphere and this causes predawn heating which leads to the initial upward surge in flux. From the point of view of photoelectron heating, sunrise occurs at about 100 degrees solar zenith angle compared to about 90 degrees for photoionization. The upward flux receives an additional boost at local sunrise. The separation of

the two sunrises produces an inflection on the flux curves for 30°N and 50°N geographic latitudes. The sunrise effect is not as dramatic at 70°N because the changes in electron temperature are likewise not as dramatic. Heat from the plasmasphere keeps the ionospheric electron temperature high at night.

After the sunrise increase in flux there is an abatement until mid-morning due to a decrease in the electron temperature as the plasma density builds up and also because of a poleward wind which pushes ions down the field lines.

The flux increases after the morning low as a result of an abatement of the poleward wind and the substantial photoproduction of ions which peaks near noon. The decrease in the magnitude of the midday  $O^+$  upward flux with increasing latitude is partially due to the lowering of the layer as a result of a latitudinal increase in the poleward wind. The daytime upward  $O^+$  fluxes at 50 degrees latitude are comparable to the fluxes observed by Evans [1975].

The large downward flux after sunset is caused by the thermal collapse of the ionosphere. This collapse is exaggerated by the fact that the electron cooling is large because plasma density remains high while the heating is shut off. The effect decreases with latitude because the plasmaspheric heat reservoir reduces the severity of the thermal collapse. In addition, larger equatorward winds help to keep the ionization higher at high latitudes.

The flux characteristics in Figure 8 are clearly not like those in the analytical formulation of the TIGCM. For immediate purposes however we focus on the post-midnight to pre-sunrise period where we have documented the discrepancy between observed and modeled values of  $f_oF_2$  and where we seek to confirm or deny plasmaspheric flux as a causality. Remembering the cosine characterization of nighttime flux in the TIGCM with a maximum downward value of  $-2(10^8) \text{ cm}^2\cdot\text{s}$  at 60° MLAT, we focus on the FLIP values at 50°N ( $\approx 50$  MLAT at 20° E longitude). Those values vary from  $-1.5(10^8) \text{ cm}^2\cdot\text{s}$  at LT=0 to

zero at LT=4. If the FLIP results were to be the guide, and consistency with the observations of Evans (1975) an empirical boundary, we conclude: 1) that the filled-fluxtube fluxes of FLIP represent a maximized "saturated" plasmaspheric input to the post-midnight ionosphere, 2) the TIGCM fluxes, while requiring a more realistic LT and latitudinal dependence, need not have fluxes increased in the post-midnight period, and 3) that thermospheric winds, not plasmaspheric flux, is the primary cause for FLIP and TIGCM model underestimates of the densities and heights of the nighttime F-region.

#### 4. COMMENTS AND CONCLUSIONS

The overall comparison between the data and the models suggests that the physics of the daytime F-region climatology is reasonably well understood. This is based on the March-April 1992 period of the SUNDIAL/ATLAS-1 campaign and the accuracies between the  $f_0F_2$  predictions of the IRI, the FLIP and the TIGCM models, and the database of 53 ionosondes. Reference to Table 3 shows that the IRI, FLIP and TIGCM models agree with the full complement of stations by  $12 \pm 2\%$ ,  $+3 \pm 3\%$ , and  $-3 \pm 3\%$  respectively, with only minor variations in the percentages when the comparisons are restricted to equatorial-to-low latitudes (i.e.,  $\text{abs}(\text{MLAT}) < 25^\circ$ ) and middle-to-high latitudes (i.e.,  $\text{abs}(\text{MLAT}) > 25^\circ$ ).

There is a marked difference in the accuracies in the post-sunset to pre-sunrise period, with the maximum disagreements occurring in the post-midnight period at about 4 AM local time. Defining this post-midnight period as LT = 0 to 5 hrs, Table 3 shows that the inaccuracy in FLIP and the TIGCM can be as great as 45% and 26% respectively when the results are integrated over all stations. These results, in effect, re-discovered the old but unsettled issue of our understanding of the maintenance of the nighttime ionosphere and quantified it

in terms of relative and absolute accuracies among the three models and the observations.

Recently, Sica et al (1990) have drawn some attention to this problem in their inability to uniquely differentiate the relative influences of meridional winds and protonospheric fluxes on modeled values of  $f_0F_2$  and  $h_mF_2$ . They pointed out that any number of reasonable but non-unique admixtures of meridional wind speeds and protonospheric fluxes could give rise to identical values of  $f_0F_2$ . Their database was only that of a network of  $f_0F_2$  measurements from mid-latitude ionosondes.

Pursuing the issue further in this investigation, correlations were carried out that involved measurements of  $f_0F_2$ ,  $h_mF_2$ , and meridional winds. And these correlations were integrated over all stations as well as over stations restricted to equatorial-to-low and mid-to-high latitudes. The correlations also involved considerations of the physical assumptions within the FLIP and TIGCM models, wherein FLIP self-consistently solves for the plasmaspheric flux inputs while the TIGCM invokes a relatively simple analytical formalism. The correlations showed a cause-effect chain in which the low model values of  $f_0F_2$  were traceable to low model values for  $h_mF_2$  (and associated increases in recombination losses) and ultimately to low model values of nighttime meridional winds. The search for causality identified with nighttime protonospheric fluxes tended to suggest that they were of secondary concern. This was shown to be particularly true since the self-consistent solution of FLIP flux values was in general agreement with those in the post-midnight TIGCM flux formalism.

No consideration was given to electric field effects, where at least at mid-latitudes their influences are expected to be minimal. Nor was there any attention given to thermospheric densities and composition. It is possible that

thermospheric densities and composition played a role in the discrepancies, but the relatively good agreement between the models and the data in the daytime suggested some confidence in the individual model treatments of thermospheric densities and composition.

Current efforts are focusing on the addition of convection electric field formalisms to the FLIP and an improved representation of topside fluxes into the TIGCM. The intent is to include local time and latitudinal controls. This will represent a convergence of predictive methodologies and a closer scrutiny of cause-effect relationships.

**Acknowledgments.** The authors wish to thank the institutions and agencies in each of the countries which participated in this investigation. The overall effort was supported by the Space Physics Division of the National Aeronautics and Space Administration under contract NASW-4755.

## REFERENCES

- Abdu, M.A., J.A.H. Sobral, P. Richards, M.M. deGonzalez, Y.N. Huang, B.M. Reddy, K. Cheng, E.P. Szuszczewicz, and I.S. Batista, Zonal/Meridional winds and disturbance dynamo electric field control of the low-latitude ionosphere based on the SUNDIAL/ATLAS-1 campaign, J. Geophys. Res. [1996, this issue].
- Bilitza, D., R. Eyfrig, N.M. Sheikh, A global model for the height of the F2-peak using M3000 values from the CCIR numerical map, ITU Telecomm. J., **46**, 549-553, 1979.
- Bilitza, D., Topside Models: status and future improvements, Adv. Space Res., **12**, 17-27, 1994.
- Bilitza, D., K. Rawer, L. Bosny, and T. Gulyaeva, International reference ionosphere - past, present and future: II. Plasma temperatures, ion composition and ion drift, Adv. Space Res., **13**, (3)15-(3)23, 1992a.
- Bilitza, D., K. Rawer, L. Bosny, and T. Gulyaeva, International reference ionosphere - past, present, and future: I. Electron density, Adv. Space Res., **13**, (3)3-(3)-13, 1992b.
- Broadfoot, A.L., B.R. Sandel, D.J. Knecht, R.R. Viereck and E. Murad, Panchromatic spectrograph with supporting monochromatic imagers, Applied Optics, **31**, 3083, 1992.
- Dickinson, R.E., E.C. Ridley, and R.G. Roble, A three-dimensional, time-dependent general circulation model of the thermosphere, J. Geophys. Res., **86**, 1499-1512, 1981.
- Dickinson, R.E., E.C. Ridley, and R. G. Roble, Thermospheric general circulation with coupled dynamics and composition, J. Atmos. Sci., **41**, 205-219, 1984.



- Dudeney, J.R., The accuracy of simple methods for determining the height of the maximum electron concentration of the F2-layer from scaled ionospheric characteristics, J. Atm. Terr. Phys., **45**, 629, 1983.
- Emery, B., G. Lu, E.P. Szuszczewicz, A.D. Richmond, R.G. Roble, P.G. Richards, K. Miller, R. Niciejewski, D.S. Evans, F.J. Rich, W.F. Denig, D.L. Chenette, P. Wilkinson, S. Pulinets, R. Hanbaba, M. Abdu, P. Jiao, K. Igarashi, and B.M. Reddy, Ionospheric and thermospheric comparisons of the TIGCM using AMIE and parameterized high-latitude inputs with global observations during the GEM/SUNDIAL/ATLAS-1 period of March 28-29, 1992, J. Geophys. Res., (1996, this issue).
- Evans, J.V., A study of F2 region night-time vertical ionization fluxes at Millstone Hill, Planet. Space Sci., **23**, 1611 (1975);
- Fejer, B.G., R.W. Spiro, R.A. Wolf, and J.C. Foster, Latitudinal variation of perturbation electric fields during magnetically disturbed periods: 1986 SUNDIAL observations and model results, Annales Geophysicae, **8**, 441, 1990.
- Feldstein, Y.I., On morphology of auroral and magnetic disturbances at high latitudes, Geomagn. Aeron., **3**, 183, 1963.
- Fennelly, J.A., D.G. Torr, P.G. Richards, and M.R. Torr, Simultaneous retrieval of the solar EUV flux and neutral thermospheric O, O<sub>2</sub>, N<sub>2</sub> and Temperature from Twilight Airglow, J. Geophys. Res., **99**, 6483, 1993.
- Fesen, C.G., R.E. Dickinson, and R.G. Roble, Simulation of thermospheric tides at equinox with the National Center for Atmospheric Research thermospheric general circulation model, J. Geophys. Res., **91**, 4471-4489, 1986.

- Fesen, C.G., R.G. Roble, and E.C. Ridley, Thermospheric tides at equinox: Simulation with coupled composition and auroral forcings, 2. Semidiurnal component, J. Geophys. Res., 96, 3663, 1991.
- Foster, J.C., J.M. Hoit, R.G. Musgrove, and D.S. Evans, Ionospheric convection associated with discrete levels of particle precipitation, Geophys. Res. Lett., 13, 656, 1986.
- Fuller-Rowell, T.J., et al., Interactions between neutral thermospheric composition and the polar ionosphere using a coupled ionosphere-thermosphere model, J. Geophys. Res., 92, 7744-7748, 1987.
- Gardner, A.G., R.A. Vierek, E. Murad, D.J. Knecht, C.P. Pike, A.L. Broadfoot, and E.R. Andersen, Simultaneous observations of neutral and ionic magnesium in the thermosphere, Geophys. Res. L., (1995 in press).
- Hedin, A.E., MSIS-86 thermosphere model, J. Geophys. Res., 92, 4649, 1987.
- Hedin, A.E., M.A. Biondi, R.G. Burnside, G. Hernandez, R.M. Johnson, T.L. Killeen, C. Mazaudier, J.W. Meriwether, J.E. Salah, R.J. Sica, R.W. Smith, N.W. Spencer, V.B. Wickwar, and T.S. Viridi, Revised global model of thermospheric winds using satellite and ground-based observations, J. Geophys. Res., 96, 7657, 1991.
- Heelis, R.A., J.K. Lowell, and R.W. Spiro, A model of the high-latitude ionospheric convection pattern, J. Geophys. Res., 87, 6339-6345, 1982.
- Holtzworth, R.H., and C.I. Meng, Mathematical representation of the auroral oval, Geophys. Res. Lett., 2, 337, 1975.
- Ilg, S., W.L. Oliver, T. Ogawa, and S. Fukao, Thermospheric winds over Japan: Comparison of ionosonde and radar measurements, J. Geophys. Res., 100, 21323-21328, 1995.
- Jain, A.R. and P.J.S. Williams, J. Atm. Terr. Phys 36, 417, 1974

- Kamide, Y., Problems in studies of magnetic storms: An introductory remark, in Proceedings of the International Conference on Magnetic Storms, Hokkaido, Japan, Nagoya University Press, pp. 1-9, 1994.
- Lester, M., J.A. Davies, H. Luhr and T.S. Viridi, High Latitude Hall and Pedersen conductances during substorm activity in the SUNDIAL/ATLAS-1 campaign, J. Geophys. Res. (1996, this issue).
- Lu, G., A.D. Richmond, B.A. Emery, and R.G. Roble, Magnetospheric-ionospheric-thermospheric coupling, effect of neutral winds on energy transfer and field aligned current, J. Geophys. Res. (1995a, in press).
- Lu, G., B.A. Emery, A. Rodger, M. Lester, J. Taylor, D.S. Evans, M. Ruohoniemi, W.F. Denig, O. de la Beaujardiere, R.A. Frahm, J.D. Winningham, and D.L. Chenette, High-latitude ionospheric electrodynamics as determined by the AMIE procedure for the conjunctive SUNDIAL/ATLAS-1/GEM period, J. Geophys. Res. [1995b, this issue].
- Luhr, H., S. Thuurey and N. Klocker, The EISCAT magnetometer cross. Operational aspects - first results, Geophysics Surveys, 6, 305 - 315, 1984.
- Miller, K.L., P.G. Richards, and H.Y. Wu, A global-study of meridional winds and electron densities in the F-region during the SUNDIAL 1987 campaign, Ann. Geophys., 11, 572, 1993.
- Miller, K.L., M. Lemon, and P.G. Richards, A fast method for the derivation of meridional winds from the height of the ionospheric F<sub>2</sub> region, J. Geophys. Res. , 1995, submitted.
- Miller, K. L. , D.G. Torr, and P.G. Richards, Meridional winds in the thermosphere derived from measurements of F2 layer height, J. Geophys. Res., 91, 4531, 1986.

- Miller, K. L., P. Richards, and D. G. Torr, The derivation of meridional neutral winds in the thermosphere from F2 layer height, in World Ionosphere/Thermosphere Study, WITS Handbook, Vol. 2, C. H. Liu, editor, SCOSTEP Secretariat, University of Illinois, Urbana, Ill., 1989.
- Nagy, A.F., and P.M. Banks, Photoelectron fluxes in the ionosphere, J. Geophys., 75, 6269, 1970.
- Pulinets, S., D. Evans, and M. Lester, UT and LT variations in the development of ionospheric disturbances over Russian longitudes, J. Geophys. Res., (1996, this issue).
- Rawer, K., "International reference ionosphere - IRI 79, NOAA Rpt., UAG-82., U.S. Dept. of Commerce, Washington, D.C., 1981
- Rawer, K., and Y.V. Ramanamurty, International Reference Ionosphere-Status 1985/1986, URSI COSPAR Workshop Proceedings, Wheaton and Co., Ltd., UK, 1985.
- Richards, P.G., and D.G. Torr, A factor of 2 reduction in the theoretical F2 peak electron density due to enhanced vibrational excitation of N<sub>2</sub> in summer at solar maximum, J. Geophys. Res., 91, 11,331, 1986a.
- Richards, P. and D. Torr, Thermal coupling of conjugate ionospheres and the tilt of the Earth's magnetic field, J. Geophys. Res., 91, 9017, 1986b.
- Richards, P.G., D.G. Torr, and W.A. Abdon, Effects of vibrational enhancement of N<sub>2</sub> on the cooling rate of ionospheric thermal electrons, J. Geophys. Res., 91, 304, 1986.
- Richards, P.G., and D.G. Torr, Ratios of photoelectron to EUV ionization rates for aeronomic studies, J. Geophys. Res., 93, 4060, 1988.
- Richards, P.G., An improved algorithm for determining neutral winds from the height of the F<sub>2</sub> peak electron density, J. Geophys. Res., 96, 17,839, 1991.

- Richards, P.G., D.G. Torr, B.W. Reinisch, R.R. Gamache, and P.J. Wilkinson, F<sub>2</sub> peak electron density at Millstone Hill and Hobart: Comparison of theory and measurement at solar maximum, J. Geophys. Res., 99, 15,005, 1994a.
- Richards, P.G., J.A. Fennelly, and D.G. Torr, EUVAC: A solar EUV flux model for aeronomic calculations, J. Geophys. Res., 99, 8981, 1994b.
- Richards, P.G., M.P. Hickey, and D.G. Torr, New sources for the hot oxygen geocorona, Geophys. Res. Lett., 99, 657, 1994.
- Richards, P.G., D.G. Torr, M.E. Hagan, and M.J. Buonsanto, A new algorithm for improved ionospheric electron density modeling, J. Geophys. Res., 100, in press, January 1995.
- Richmond, A.D., Assimilative mapping of ionospheric electrodynamics, Adv. Space Res., 12, 59, 1992.
- Richmond, A.D., et al., An empirical model of quiet-day ionospheric electric fields at middle and low latitudes, J. Geophys. Res., 85, 4658-4664, 1980.
- Richmond, A.D. and Y. Kamide, Mapping electrodynamic features of the high-latitude ionosphere from localized observations: Combined incoherent scatter radar and magnetometer measurements for Jan 18-19, 1984, J. Geophys. Res., 93, 5741, 1988.
- Roble, R.G., and E.C. Ridley, An auroral model for the NCAR thermospheric general circulation model (TGCM), Annales Geophysicae, 5A, (6), 369-382, 1987.
- Roble, R.G., E.C. Ridley, and R.E. Dickinson, On the global mean structure of the thermosphere, J. Geophys. Res., 92, 8745-8758, 1987.
- Roble, R.G., E.C. Ridley, A.D. Richmond, and R.E. Dickinson, A coupled thermosphere/ionosphere general circulation model, Geophys. Res. Lett., 15, 1325, 1988.

- Schunk, R.W., and A.F. Nagy, Electron temperatures in the F region of the ionosphere: Theory and observations, Rev. Geophys., 16, 355, 1978.
- Schunk, R.W., and E. P. Szuszcwicz, "First principle and empirical modeling of the global-scale ionosphere", Ann. Geophys. 6, 19, 1988.
- Sica, R., R.W. Schunk, and P. Wilkinson, A Study of the Undisturbed Mid-Latitude Ionosphere Using Simultaneous, Multiple-Site Ionosonde Measurements Using the SUNDIAL '86 Campaign, J. Geophys. Res., 95, 8727, 1990.
- Sime, D. and R. Behnke, The U.S. space weather program, Part 1, STEP Int'l., 4, No. 11, November 1994.
- Siscoe, G., E. Hildner, T.H. Killeen, L.J. Lanzerotti, and W. Lotko, Developing service promises accurate space weather forecasts in the future, EOS: Trans. Am. Geophys. Union, 75, 353, 1994.
- Sojka, J.J., and R.W. Schunk, A theoretical study of the global F-region for June solstice, solar maximum, and low magnetic activity, J. Geophys. Res., 90, 5285-5298, 1985.
- Spiro, R.W., R.A. Wolf, and B.G. Fejer, Penetration of high-latitude-electric-field effects to low latitudes during SUNDIAL 1984, Annales Geophysicae, 6, 39-50, 1988.
- Szuszcwicz, E.P., B. Fejer, E. Roelof, R. Schunk, R. Wolf, R. Leitingner, M. Abdu, B.M. Reddy, J. Joselyn, P. Wilkinson, and R. Woodman, SUNDIAL: a world-wide study of interactive ionospheric processes and their roles in the transfer of energy and mass in the Sun-Earth system, Annales Geophysicae, 6, 3-18, 1988.

- Szuszczewicz, E.P., P. Wilkinson, M.A. Abdu, E. Roelof, R. Hanbaba, M. Sands, T. Kikuchi, R. Burnside, J. Joselyn, M. Lester, R. Leitingner, G.O. Walker, B.M. Reddy, and J. Sobral, Solar-terrestrial conditions during SUNDIAL '86 and empirical modeling of the global-scale ionospheric responses, Annales Geophysicae, **8**, 387, 1990.
- Szuszczewicz, E.P., P. Wilkinson, W. Swider, S. Pulinets, M.A. Abdu, E. Roelof, T. Fuller-Rowell, T. Bateman, P. Blanchard, G. Gustafsson, R. Hanbaba, J. Joselyn, T. Kikuchi, R. Leitingner, M. Lester, B. Reddy, M. Ruohoniemi, M. Sands, J. Sobral, G.O. Walker, and V. Wickwar, Measurements and empirical model comparisons of F-region characteristics and auroral oval boundaries during the solstitial SUNDIAL campaign of 1987, Annales Geophysicae, **11**, 601-613, 1993.
- Szuszczewicz, E.P., R.G. Roble, P.J. Wilkinson, and R. Hanbaba, Coupling Mechanisms in the Lower Ionospheric-Thermospheric System and Manifestations in the Formation and Dynamics of Intermediate and Descending Layers, J. Atm. Terr. Phys., **57**, 1483, 1995.
- Szuszczewicz, E.P., Advances in ionospheric physics: roles, relevance and predictions in the system of solar-terrestrial plasmas, U.S. National Quadrennial Rpt. to the IUGG, Reviews of Geophysics, Supplement, 721, 1995.
- Szuszczewicz, E.P., A. Mankofsky, P. Blanchard, C. Goodrich, D. McNabb, and D. Kamins, SAVS: A space and atmospheric visualization science system, in Visualization Techniques in Space and Atmospheric Sciences, E.P. Szuszczewicz and J.H. Bredekamp, editors, U.S. Gov't Printing Office (in press, 1995c).
- Taylor, J.R., M. Lester, and T.K. Yeoman, A superposed epoch analysis of geomagnetic storms, Annales Geophysicae, **12**, 612 - 624, 1994.

- Torr, M.R., D.G. Torr, P.G. Richards, and S.P. Yung, Mid- and low-latitude model of thermospheric emissions, 1,  $O^+(^2P)$  7320 Å and  $N_2(^2P)$  3371 Å, J. Geophys. Res., **95**, 21,147, 1990.
- Torr, D.G., M.R. Torr, and P.G. Richards, Thermospheric airglow emissions: a comparison of measurements from ATLAS-1 and Theory, Geophys. Res. Lett., **6**, 519, 1993.
- Wilkinson, P.J., Scaling errors in ionospheric characteristics, Ionosonde Network Advisory group Bulletin, 27, WDCA for STP, U.S. Dept. Commerce, NOAA, 20-25, 1978.
- Wilkinson, P.J., E.P. Szuszczewicz, and R.G. Roble, Measurements and Modeling of Intermediate, Descending, and Sporadic Layers in the Lower Ionosphere: Results and Implications for Global-Scale Ionospheric-Thermospheric Studies, Geophys. Res. Lett., **19**, 95-98, 1992.
- Wilkinson, P., P. Richards, K. Igarashi, Ionospheric climatology and weather in the Australian-Japanese sector during the SUNDIAL/ATLAS-1 campaign, J. Geophys. Res., (1996, this issue).
- Wilkinson, P., R.W. Schunk, R. Hanbaba, and H. Mori, Interhemispheric comparison of SUNDIAL F-region data with global-scale ionospheric models, Ann. Geophys., **6**, 31, 1988.
- Yeoman, T.K., D.K. Milling and D. Orr, Pi2 Polarization patterns on the U.K. Sub-auroral Magnetometer Network (SAMNET), Planetary and Space Science, **38**, 589 - 602, 1990.



## Figure Captions

Figure 1. Activity indices  $k_p$  (top panel),  $A_p$  (middle panel) and  $Dst$  (bottom panel) for March and April 1992. Note that  $-Dst$  is plotted.

Figure 2. Diurnal characteristics of measured values of  $f_oF_2$  (in MHz) at six of the ionosonde stations covering the period 24 March through April 4, 1992. Dots, solid curve, and dashed curve represent the data, the average diurnal behavior for the period, and the IRI "predictions", respectively.  $f_oF_2$  [Hz] =  $8.9(10^3) \sqrt{N_m F_2 [\text{cm}^{-3}]}$ , with the right-hand abscissa showing the conversion of  $f_oF_2 = 5, 10$  and  $15$  MHz to  $N_m F_2 = 0.3, 1.3$ , and  $2.8(10^6) \text{ cm}^{-3}$ , respectively.

Figure 3. Global representation (UT=12) of station locations and model-measurement comparisons of observed vs modeled values of  $f_oF_2$ . The color legend on the left presents the percent differences between the data at each station (colored circles in the figure) and the IRI (top panel), the TIGCM (middle panel) and the FLIP model (bottom panel) predictions. See text for other details in the figure. Extrema on the  $f_oF_2$  color scale for the isolines are 3 and 16 MHz corresponding to extrema in  $N_m F_2$  of  $1.1(10^5)$  and  $3.2(10^6) \text{ cm}^{-3}$ , respectively. The red-to-blue color scale for the percent differences of model vs measurements covers the +40% to -40% range. (Note that differences of 20% and 40% in model-measurement comparisons of  $f_oF_2$  are approximately equal to differences of 45% and 100%, respectively, in corresponding  $N_m F_2$  comparisons.)

Figure 4. Global representation (UT=12) of station locations and model-measurement comparisons of observed vs modeled values of hmF2. Color legend presents the percent differences between the data and the IRI (top panel), the TIGCM (middle panel) and the FLIP model (bottom panel). See text for other details in the figure.

Figure 5. Integrated presentation of LT dependence of percent differences (ordinate) between the observations of foF2 (left column) and hmF2 (right column) and the values from the IRI (solid curve), FLIP (dotted curve) and TIGCM (dashed curve) models. The right-hand axes of the foF2 panels show the scaling for percent differences corresponding to NmF2 model-measurement comparisons. The bottom panels integrate the results of all stations, while the middle and upper panels restrict the comparisons to middle-to-high latitude stations ( $\text{abs}(\text{MLAT}) > 25^\circ$ ) and low-to-equatorial stations ( $\text{abs}(\text{MLAT}) < 25^\circ$ ), respectively.

Figure 6. Global representation (UT=12) of measured and modeled meridional winds at 300 km (for the models) and at hmF2 for the observations. Magnitude and directions are shown by vectors and color code at each of the station locations. Each panel is identified, and the foF2 contours in the individual panels correspond to the model in question. In the data and HWM panels, the contours of foF2 are from the IRI model.

Figure 7. An integrated presentation of modeled and measured meridional winds over all stations for which  $20^\circ < \text{abs}(\text{MLAT}) < 60^\circ$ . Positive values are poleward, while negative values are equatorward.

Figure 8.  $O^+$  fluxes [units/cm<sup>2</sup>•sec] at 550 km from the FLIP model in the 20° east meridian at 30°N (solid curve), 50°N (dotted curve) and 70°N (dashed curve) geographic latitude.

TABLE 1

## SUNDIAL/ATLAS-1 STATIONS

Name	Lat	Long	Name	Lat	Long	Name	Lat	Long
Ahmedabad	23.0	72.6	Karaganda	49.8	73.1	Peiping	40.0	116.3
Akita	39.7	140.1	Khabarovsk	48.5	135.2	Poitiers	46.6	0.3
Arkhangelsk	64.6	40.5	Kiruna	67.8	20.4	Resolute Bay	74.7	265.1
Buenos Aires	-34.6	301.7	Kodaikanal	10.2	77.5	Rome	41.8	12.5
Cachoeira Paulista	-22.7	315.0	La Reunion	-21.2	55.6	Sverdlovsk	56.7	61.1
Canberra	-35.3	149.0	Lanchou	36.1	103.8	Tahiti	-17.7	210.7
Canton	23.1	113.3	Lannion	48.8	356.6	Tashkent	41.3	69.0
Chanchun	43.80	125.30	Leningrad	60.0	30.7	Townsville	-19.6	146.8
Chung-Li	25.0	121.2	Lycksele	64.6	18.8	Trivandrum	8.2	77.0
Chungking	29.6	106.5	Magadan	60.1	151.0	Tunguska	61.60	90.00
Churchill	58.7	265.8	Manchouli	48.6	117.4	Uppsala	59.8	17.6
Dakar	14.8	242.6	Moscow	55.5	37.3	Ushuaia	-54.8	291.7
Darwin	-12.3	130.9	Mundaring	-32.0	116.2	Vanimo	-2.7	141.3
Fortaleza	-3.7	321.0	Norfolk Is.	-29.0	168.0	Wakkanai	45.4	141.7
Hankou	30.7	114.3	Novosibirsk	54.60	83.20	Waltair	18.00	83.00
Hobart	-42.9	147.3	Okinawa	26.3	127.8	Wulumuqui	43.70	87.60
Irkutsk	52.5	104.0	Ottawa	45.4	284.1	Yamagawa	31.2	130.6
Kaliningrad	54.7	20.6	Ouagadougou	12.4	358.5			

**TABLE 2**

**SUNDIAL-ATLAS "EVENTS"**

	March								April		
	24	25	26	27	28	29	30	31	1	2	3
Northern European Sector Substorms (EISCAT Cross or Samnet Chain)	20-22	1930- 2130	1930- 2200	0130- 0300 19- 2230	00- 0130 2030- 2300	1930- 2400	00- 0430 1845- 2400*	00- 0300* 2030- 2330			1000- 1600 Very High Convec- tion at EISCAT
Only Quiet										1600-1600 Quiet	
French Sector							Daytime Pos. Phase	Day Neg			
Russian Sector	(2,3) Neg. Phase	(3,4) Pos. Phase				Intense Neg.	(2,3)	Rec.			
		(1)		(1)							
				Neg. Phase (4)	Rec. Phase						

- . Moscow
- . St. Petersburg
- . Arkhangelsk
- . Sverdlovsk
- . Novosibirsk

**TABLE 3. SUMMARY OF  $f_oF_2$  MODEL-MEASUREMENT COMPARISONS**

Model	Daytime ( $6 \leq LT \leq 18$ )			Post-Midnight ( $0 \leq LT \leq 5$ )		
	IMLATI<25°	IMLATI>25°	All	IMLATI<25°	IMLATI>25°	All
IRI	13±5%	+13±3%	+12±2%	+20±6%	+11±1%	+15±2%
FLIP	0(+40/-8%)	+6 ±3%	+3±3%	+48±13%	+30±8%	+35±10%
TIGCM	0±8%	-4±2%	-3±3%	+18±4%	+25±10%	+18±8%

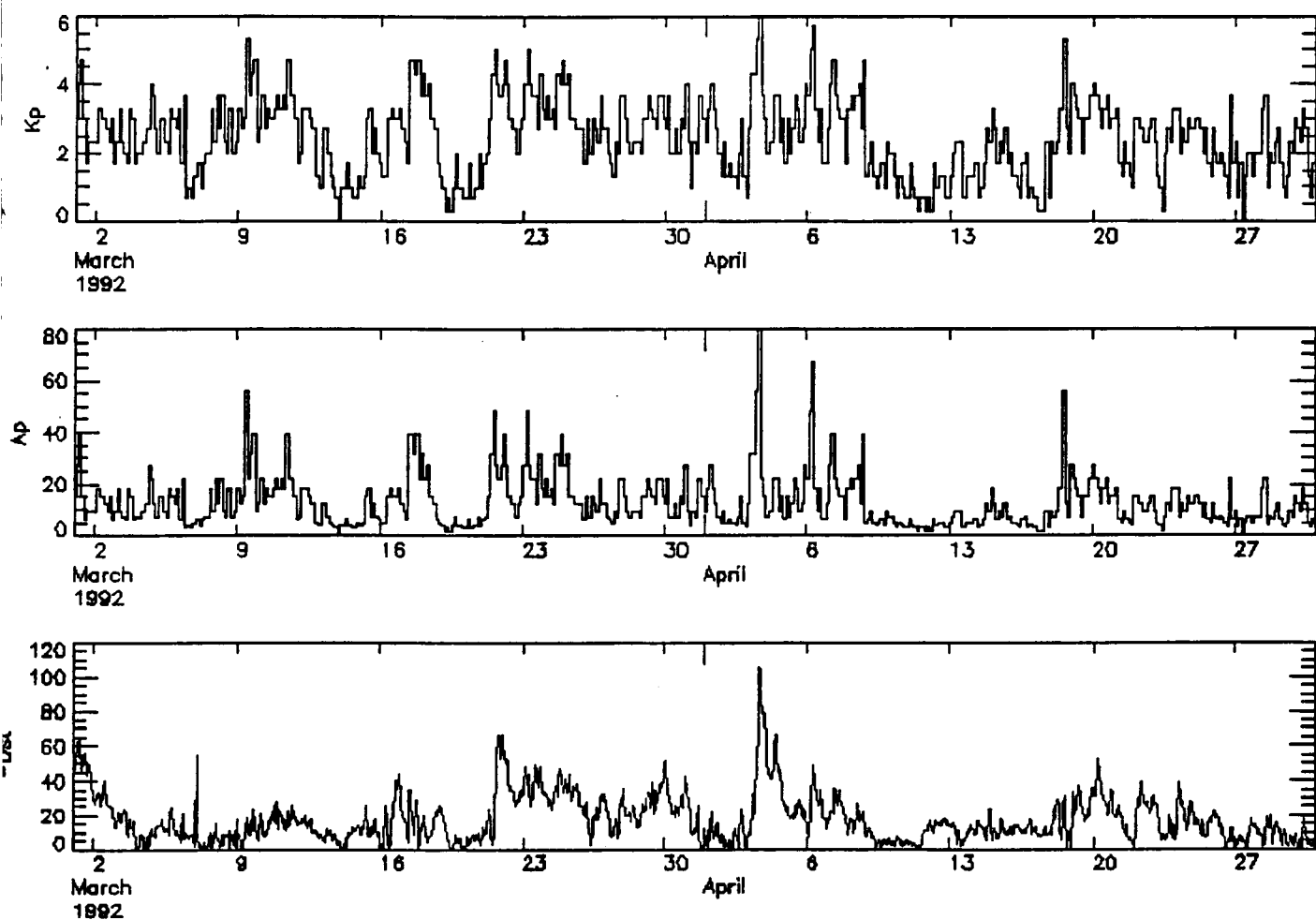


Figure 1

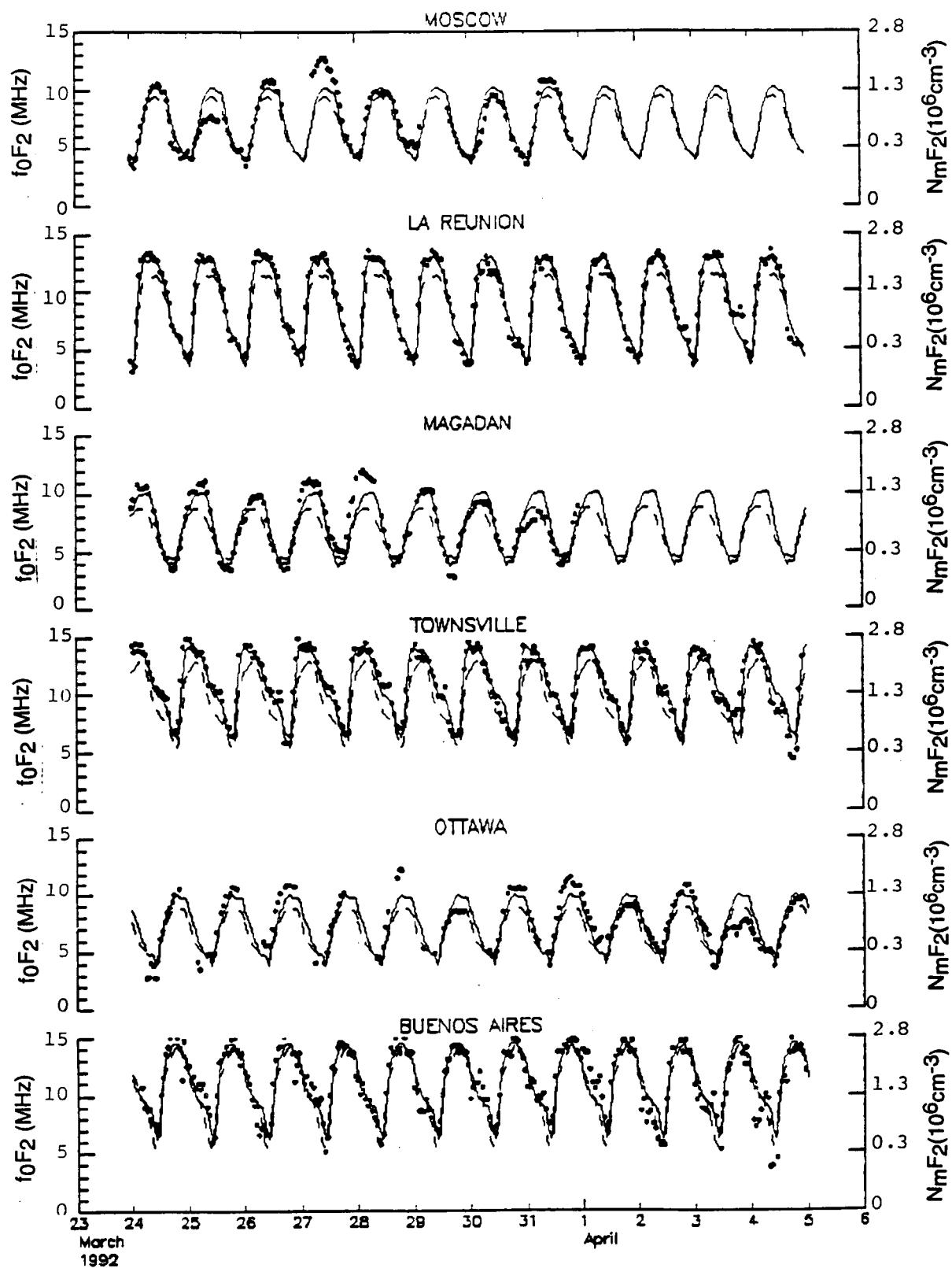
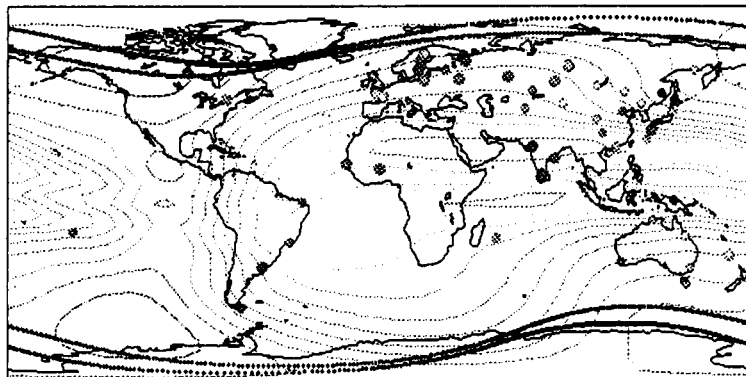


Figure 2

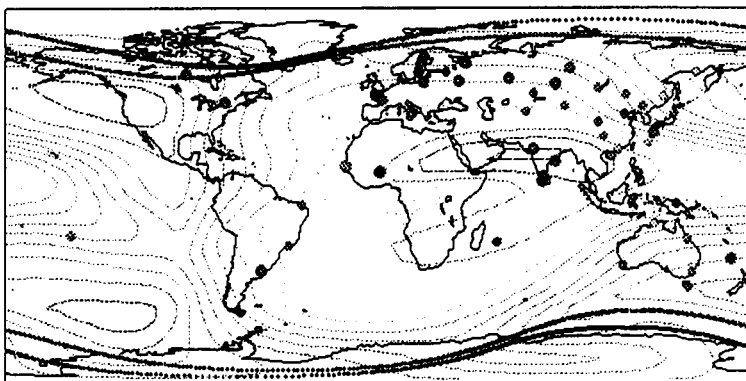


DATA (3.24.92 - 4.4.92) vs MODEL WITH foF2 CONTOURS UT = 12

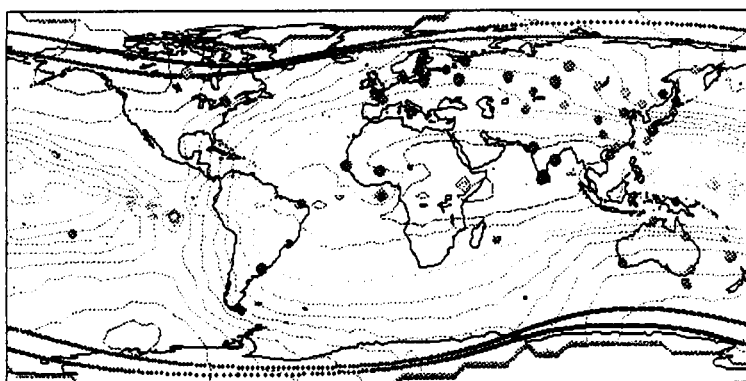
IRI



TIGCM



FLIP



% DIFFERENCES (AVG - MODEL)

-40 -20 0 20 40

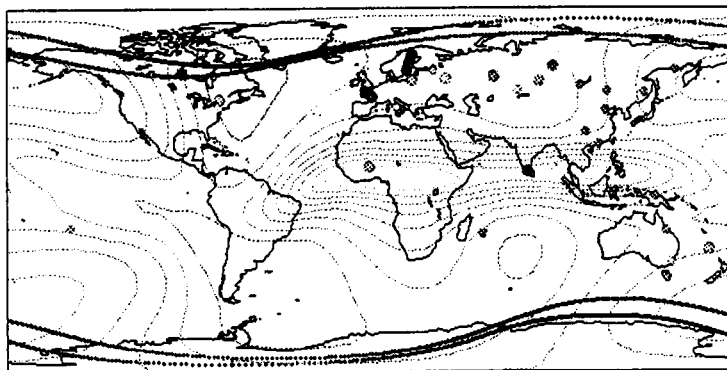
foF2 CONTOURS (MHz)

3.0 6.2 8.5 12.8 16.0

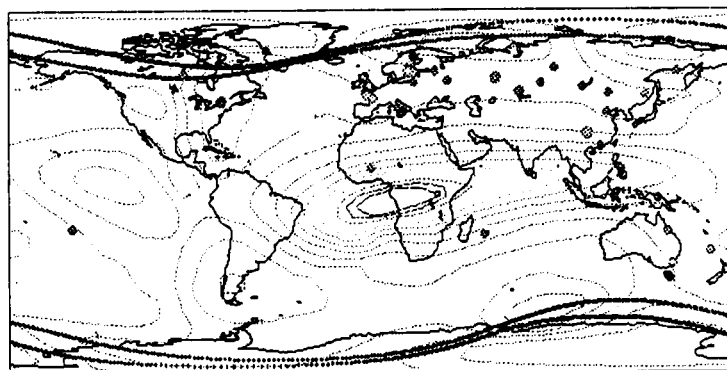
Figure 3

DATA (3.24.92 - 4.4.92) vs MODEL WITH hmF2 CONTOURS UT = 12

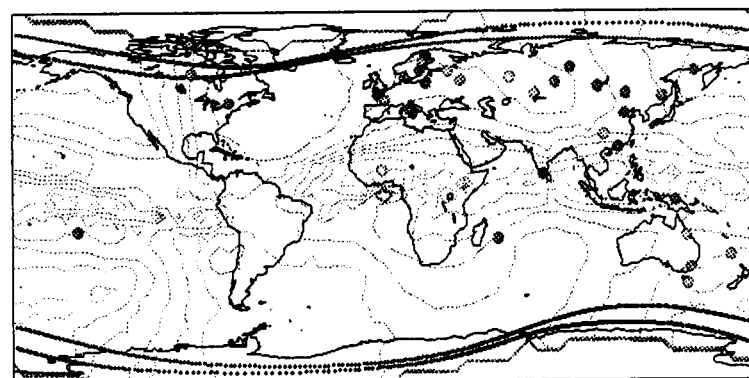
IFI



TIGCM



FLIP



% DIFFERENCES (AVG - MODEL)

-25.0 -12.5 0.0 12.5 25.0

hmF2 CONTOURS (Km)

250 300 350 400 450 500

Figure 4

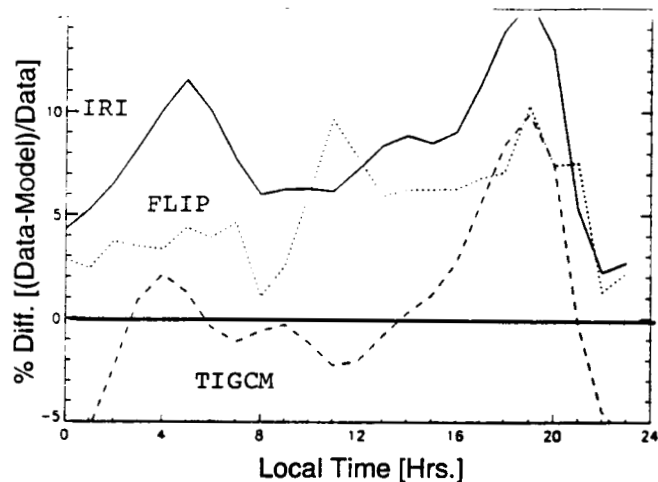
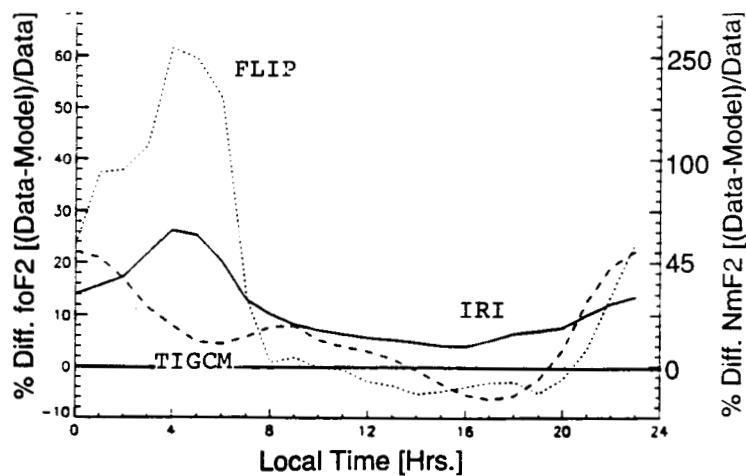
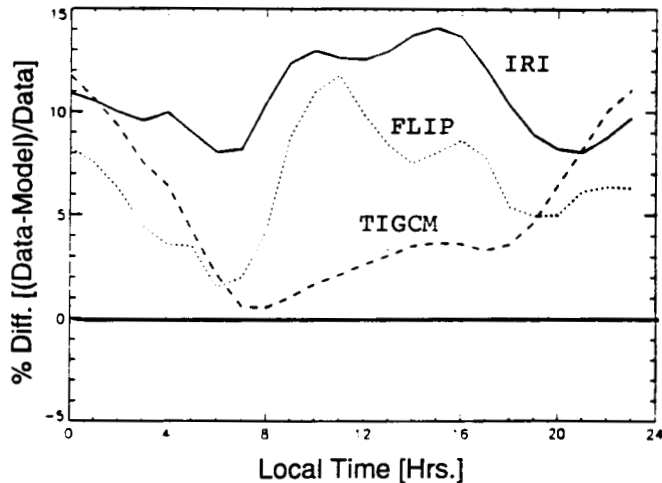
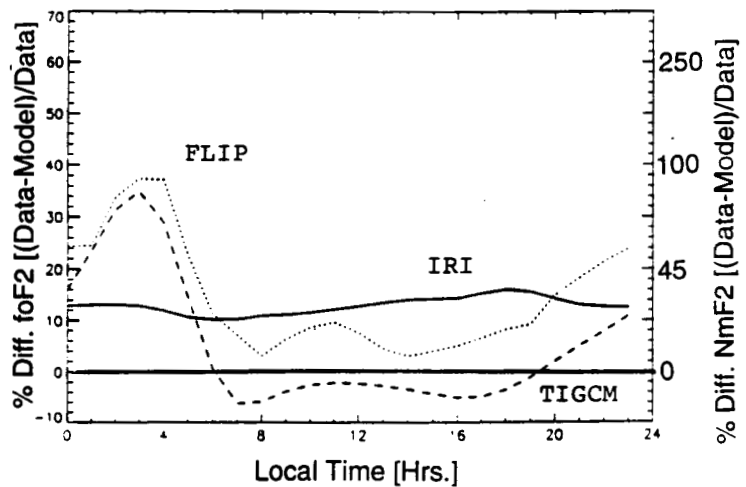
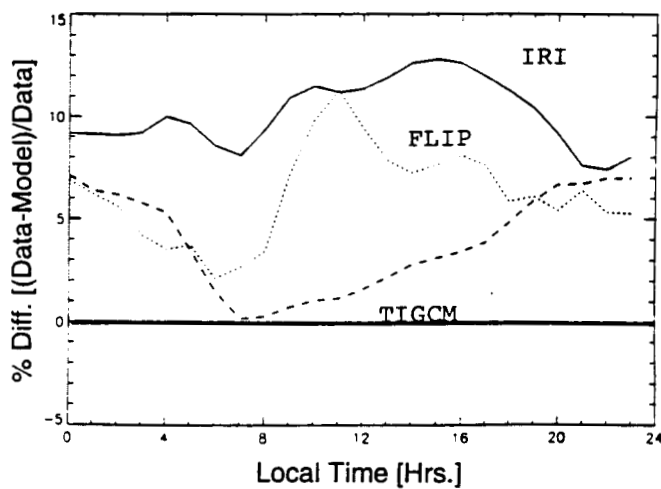
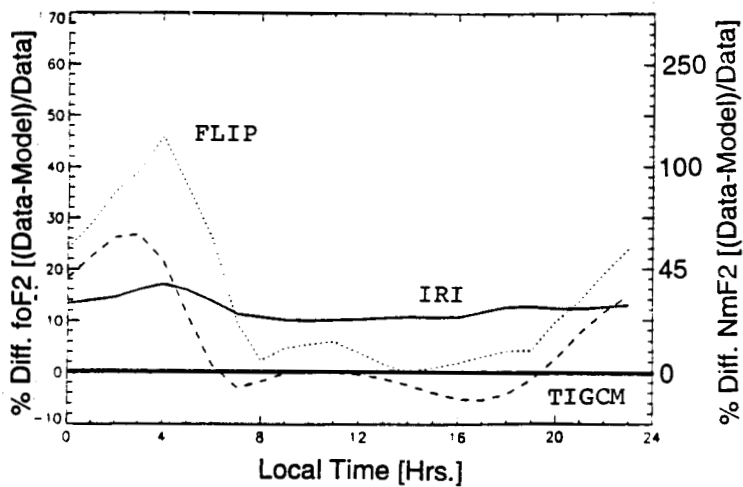
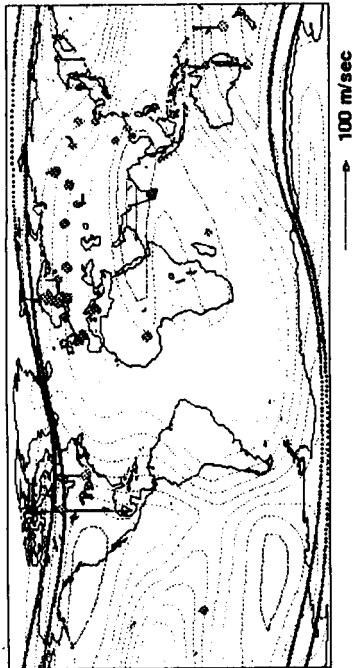
**f<sub>o</sub>F<sub>2</sub>****IMLATI < 25°****h<sub>m</sub>F<sub>2</sub>****IMLATI > 25°****ALL STATIONS**

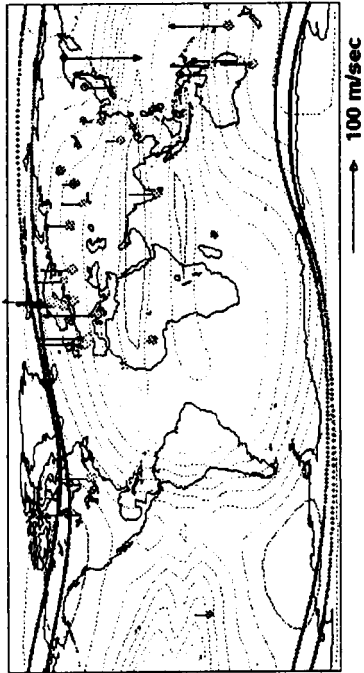
Figure 5

MERIDIONAL WINDS WITH foF2 CONTOURS UT = 12

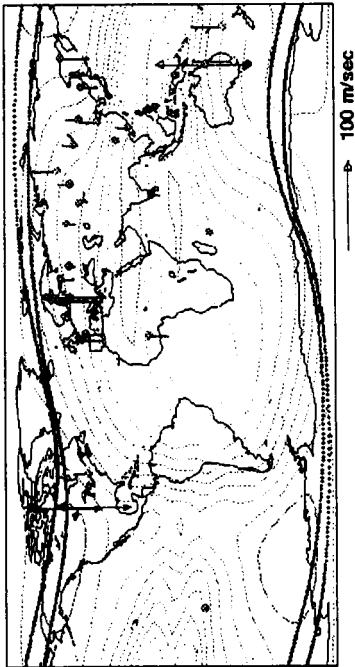
TIGCM WINDS / TIGCM COUNTOURS



HWM WINDS / IRI CONTOURS



DATA WINDS / IRI CONTOURS



FLIP WINDS / FLIP CONTOURS

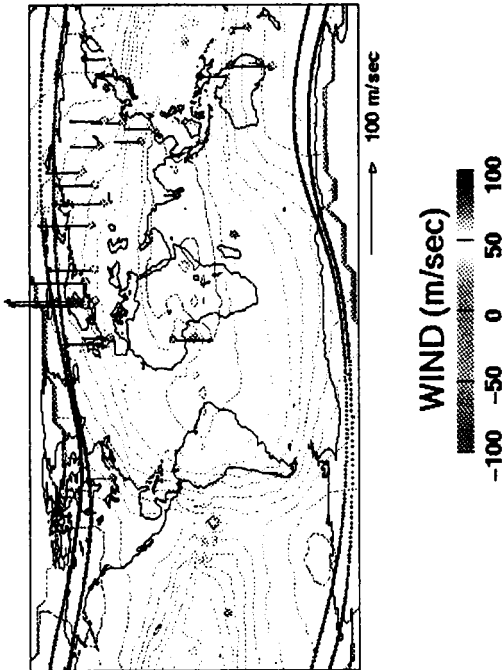


Figure 6

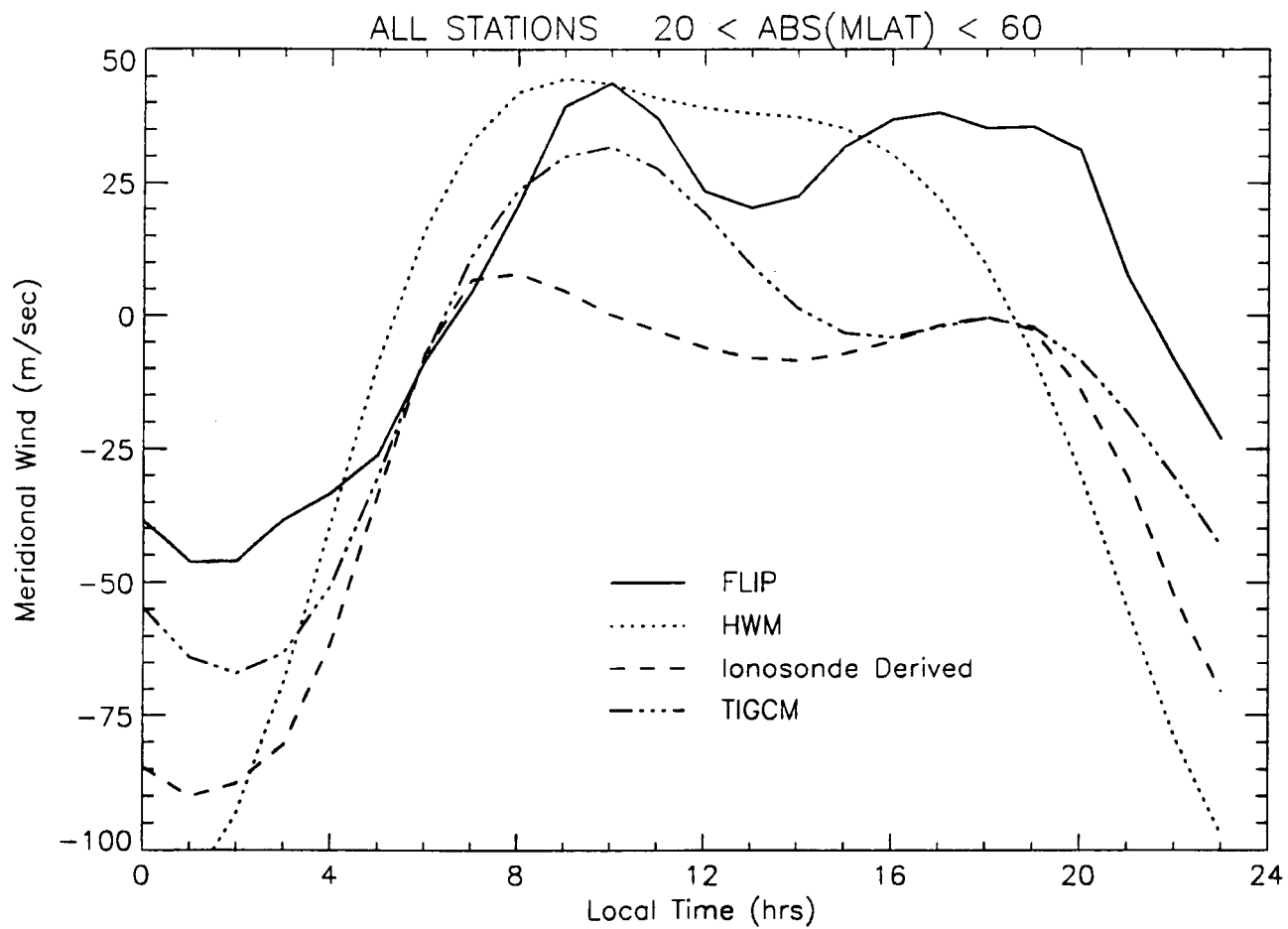


Figure 7

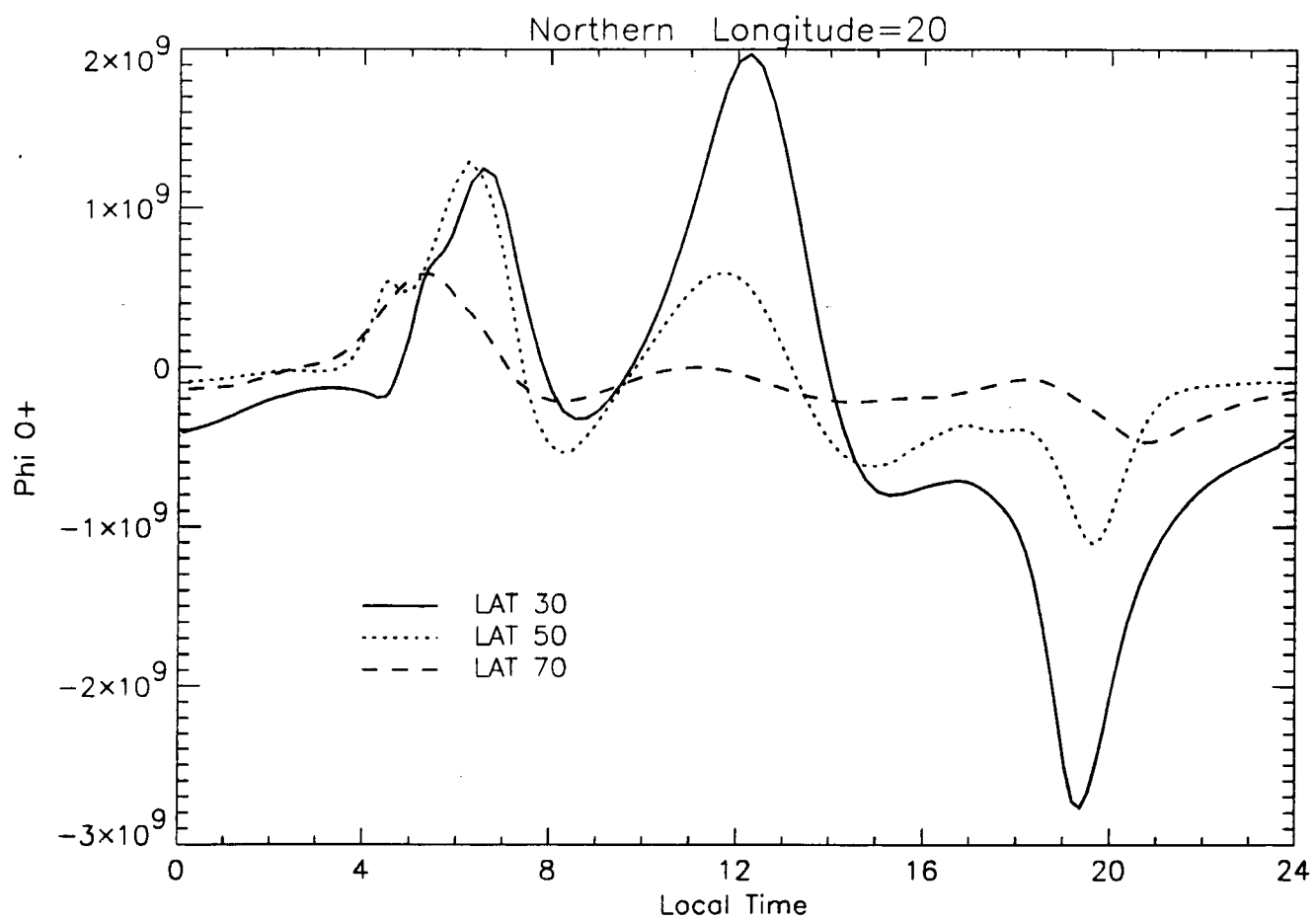


Figure 8

**High-Latitude Ionospheric Electrodynamics as  
Determined by the AMIE Procedure for the Conjunctive  
SUNDIAL/ATLAS-1/GEM Period of March 28-29, 1992**

**G. Lu, B.A. Emery, A. Rodger, M. Lester, J. Taylor, D.S. Evans, M. Ruohoniemi,  
W.F. Denig, O. de la Beaujardier, R.A. Frahm, J.D. Winningham,  
and D.L. Chenette**

**High-Latitude Ionospheric Electrodynamics as Determined by the AMIE  
Procedure for the Conjunctive SUNDIAL/ATLAS-1/GEM Period of  
March 28-29, 1992**

G. Lu<sup>1</sup>, B. A. Emery<sup>1</sup>, A. Rodger<sup>2</sup>, M. Lester<sup>3</sup>, J. Taylor<sup>3</sup>, D. S. Evans<sup>4</sup>, M. Ruohoniemi<sup>5</sup>,  
W. F. Denig<sup>6</sup>, O. de la Beaujardiere<sup>7</sup>, R. A. Frahm<sup>8</sup>, J. D. Winningham<sup>8</sup>, and D. L. Chenette<sup>9</sup>

<sup>1</sup> High Altitude Observatory, National Center for Atmospheric Research\*, Boulder, Colorado

<sup>2</sup> British Antarctic Survey, Cambridge, UK

<sup>3</sup> Department of Physics and Astronomy, University of Leicester, Leicester, UK

<sup>4</sup> Space Environment Laboratory, National Oceanic and Atmospheric Administration, Boulder, Colorado

<sup>5</sup> Applied Physics Laboratory, Johns Hopkins University, Laurel, Maryland

<sup>6</sup> Phillips Laboratory, Hanscom Air Force Base, Massachusetts

<sup>7</sup> SRI, Menlo Park, California

<sup>8</sup> Southwest Research Institute, San Antonio, Texas

<sup>9</sup> Lockheed Palo Alto Research Laboratory, Palo Alto, California

To be submitted to *Journal of Geophysical Research*

June 19, 1995

\* NCAR is sponsored by the National Science Foundation.



**Abstract.** During the conjunctive SUNDIAL/ATLAS-1/GEM campaign period of 28-29 March 1992, a set of comprehensive data has been collected both from space and from ground. The Assimilative Mapping of Ionospheric Electrodynamics (AMIE) procedure is used to derive the large-scale high-latitude ionospheric conductivity, convection, and other related quantities, by combining the various data sets. The period was characterized by several moderate substorm activities. Variations of different ionospheric electrodynamic fields are examined for one substorm interval. The cross-polar-cap potential drop, Joule heating, and field-aligned current are all enhanced during the expansion phase of substorms. The most dramatic changes of these fields are found to be associated with the development of the substorm electrojet in the post-midnight region. Variations of global electrodynamic quantities for this 2-day period have revealed a good correlation with the auroral electrojet (AE) index. Different energy dissipation channels have also been estimated. On the average over the two days, the total globally integrated Joule heating is about 102 GW and the total globally integrated auroral energy precipitation is about 52 GW. Using an empirical formula, the ring current energy injection is estimated to be 125 GW for a decay time of 3.5 hr, and 85 GW for a decay time of 20 hr. We also find an energy-coupling efficiency of 3% between the solar wind and the magnetosphere for a southward IMF condition.

## 1. Introduction

High-latitude ionospheric convection, auroral precipitation, and electric currents are the manifestations of solar wind and magnetospheric energy coupling into the ionospheric-thermospheric system. Therefore the high-latitude ionosphere provides an important linkage between the solar wind-magnetosphere environment and the dynamics of the Earth's upper atmosphere [e.g., Killeen *et al.*, 1984; Forbes and Harel, 1989; Crowley *et al.*, 1989. Thayer and Vickrey, 1992; Deng *et al.*, 1993; Lu *et al.*, 1995].

In a continuing effort to quantitatively understand and accurately model these coupling mechanisms and their manifestations in the ionospheric-thermospheric system, the first Atmospheric Laboratory for Applications and Science (ATLAS-1) mission was flown on the Atlantis space shuttle from March 24 to April 2, 1992. The mission focused on the chemistry, energetics, and electrodynamics of the ionospheric-thermospheric system through the comprehensive nature

of its own measurements combined with around-the-clock global observations of the SUNDIAL network of ionosondes and radars (see *Szuszczewicz et al.* [1995] for more information.) In conjunction with the SUNDIAL/ATLAS-1 mission, a Geospace Environment Modeling (GEM) campaign was taking place on March 28 and 29. The GEM campaigns are coordinated multi-instrument observations with the aim of understanding magnetospheric processes and their coupling with the solar wind and the ionosphere. A variety of data collected during the campaign is combined to construct large-scale instantaneous patterns of the high-latitude ionospheric conductivity, convection, and other related quantities, using the Assimilative Mapping of Ionospheric Electrodynamics (AMIE) procedure [*Richmond and Kamide*, 1988; *Richmond*, 1992]. The purpose of this paper is to examine the high-latitude ionospheric electrodynamic activity for this 2-day period. Distributions of the ionospheric convection and auroral precipitation are also important inputs to simulation models of ionospheric and thermospheric dynamics, such as the National Center for Atmospheric Research Thermosphere-Ionosphere General Circulation Model (NCAR-TIGCM) [*Roble et al.*, 1988]. In a companion paper, *Szuszczewicz et al.* [1995] compare the *F*-region measurements from a global network of ionosonde stations taken during the ATLAS-1 mission with the model predictions from TIGCM as well as two other models. Using realistic ionospheric inputs to the thermospheric simulation models allows meaningful comparison between observations and model predictions, especially during coordinated campaign studies.

In a previous study [*Lu et al.*, 1995], we have used realistic time-dependent high-latitude ionospheric convection and auroral precipitation patterns derived from AMIE as inputs to the TIGCM to investigate how the magnetospheric energy inputs affect the thermospheric dynamics as well as the feed-back of the thermospheric neutral wind dynamo onto magnetospheric electrodynamics. The focus of that study was mainly on the TIGCM results. In this paper, we present and discuss the AMIE results. Additional data sets have been added to improve the estimates of the high-latitude ionospheric electrodynamic fields since the previous study. A detailed description of all data that are incorporated into AMIE is given in the next section.

## 2. Data and Procedure

### 2.1 Data Inputs

**Satellite observations.** During this 2-day period, several satellites provided data to the assimilation of global electrodynamic fields. The IMP-8 satellite was located upstream of the

Earth at about (31,-16,-16)  $R_E$  in GSE coordinates at 1500 UT on March 29, 1992. Unfortunately, the interplanetary magnetic field (IMF) and solar-wind plasma data were only measured for about 6 hours during the two days under study. Plotted in Figure 1 is the IMP-8 data taken between 1320 and 1930 UT on March 29. The top three panels show the  $x$ ,  $y$  and  $z$  components (in GSM coordinates) of the IMF. During the interval,  $B_x$  oscillated in sign frequently and  $B_y$  and  $B_z$  were negative for most of the interval but the magnitudes of both components varied between about 0 nT and -6 nT. In spite of a few spikes due to instrumental noise, the solar-wind speed and density shown in the bottom two panels were almost steady, around 350 km/s and  $12 \text{ cm}^{-3}$ , respectively.

During the period of March 28-29, 1992, there were four Defense Meteorological Satellite Program (DMSP) spacecraft F8-F11 operating in Sun-synchronous polar circular orbits at altitudes of about 840 km, with orbital inclinations of  $98.7^\circ$  and orbital periods of 100 min. All four DMSP satellites measured the cross-track horizontal and vertical ion drift components, with F10 and F11 also measuring the along-track component. Because of some technical difficulties in reducing the along-track component, only the cross-track ion drifts or the along-track electric fields were incorporated into AMIE. The electric fields were mapped along the magnetic field lines to a reference altitude of 110 km and averaged to a 20-s time resolution before being fed into AMIE. The DMSP satellites also provided measurements of auroral precipitating particles within the 32 eV to 30 keV energy range. Since only high-energy particles penetrate into the lower thermosphere where the conductivity peaks, only those precipitating electrons with energies between 460 eV and 30 keV [Rich *et al.*, 1987] were considered in estimating the Pedersen and Hall conductances. The DMSP particle data were averaged in 30-s segments.

NOAA 12 is also a polar-orbiting satellite which has an altitude of 850 km and an orbital period of 100 min. The primary data provided by the NOAA 12 satellite were the fluxes of energetic particles in the 300 eV to 20 keV energy range averaged over about 40-s intervals.

The Upper Atmospheric Research Satellite (UARS) is in a near-circular orbit at about 585 km, with an inclination of  $57^\circ$ . The Atmospheric X-ray Imaging Spectrogram (AXIS) instrument of the Particle Environment Monitor (PEM) experiment on board the UARS measures 3- to 100-keV X-rays in 16 pixels covering 2000 km along the Earth's surface perpendicular to the satellite track every 8 seconds (for detailed instrumentation, see Chenette *et al.* [1993] and Winningham *et al.* [1993]). X-rays are generated by the energetic electrons as they are precipitating into the

atmosphere. The characteristic energy and energy flux of precipitating electrons are extracted from the X-ray spectrum [Chenette *et al.*, 1993] and the results are binned over neighboring pixels and averaged to 1-min resolution.

The Japanese satellite EXOS-D is in an orbital inclination of  $75^\circ$  and orbital period 212 min. The apogee and perigee of the satellite are 10,500 km and 270 km, respectively. During the March 1992 period, the satellite altitude varied from about 1100 km to 8500 km over the northern polar region. No data were obtained from the satellite when it was passing over the southern hemisphere because the ground receivers in the southern hemisphere were not operating during that period. EXOS-D measured the two components of the electric field perpendicular to the satellite spin axis, and the vector electric field was calculated with the assumption that the electric field is perpendicular to the main magnetic field (see Hayakawa *et al.* [1990] for further information). In addition, both UARS and EXOS-D provided measurements of magnetic perturbations [Winningham *et al.*, 1993, Fukunishi *et al.*, 1990] by subtracting the measured vector magnetic field from the IGRF 1990 model of the Earth's main field. The data from UARS and EXOS-D instruments were incorporated into AMIE for the first time.

**Radar measurements.** The Sondrestrom incoherent scatter radar was operating between 0440 and 2000 UT on March 29, 1992. Vector ion drift velocities were extracted from the line-of-sight components and binned over  $1^\circ$  intervals between  $72^\circ$  and  $76^\circ$  magnetic latitude every 5 min. The Wick VHF coherent scatter radar, originally part of the Sweden and Britain Radar Experiment (SABRE), measured *E*-region line-of-sight irregularity drifts from 0000 UT on March 28 until 0506 UT on March 29 with the data averaged every 5 min over  $1^\circ$  bins between  $60^\circ$  and  $68^\circ$  magnetic latitude. During this 2-day period, the Goose Bay HF coherent scatter radar provided vector ion drift velocities which were averaged every 10 min over  $2^\circ$  bins from  $65^\circ$  to  $81^\circ$  magnetic latitude. The Halley Bay HF coherent radar in Antarctica also provided vector velocities which were averaged each 10 min in  $1^\circ$  magnetic latitude bins ranging from  $-63^\circ$  to  $-83^\circ$ . The Goose Bay and Halley Bay radars are approximately magnetically conjugate.

**Ground magnetometers.** During this campaign period, the ground magnetic perturbations were measured by 93 magnetometer stations with 14 located in the southern hemisphere. Figure 2 shows the locations of the magnetometer stations poleward of  $40^\circ$  magnetic latitude in the northern and southern hemispheres as indicated by their 3-letter international codes. All three

components of the magnetometer data were used in the study. The magnetometer data were averaged to 5-min resolution. The effect of magnetospheric currents, such as the ring current and the magnetopause currents, is removed by subtracting  $D_{st} \cos|\theta|$  from the north-south component of the magnetic perturbations (where  $\theta$  is magnetic latitude).

## 2.2 AMIE Procedure

The AMIE procedure is an optimally constrained, weighted least squares fit of coefficients to the observed data. The procedure first estimates the height-integrated Pedersen and Hall conductivities by modifying statistical models. In this study statistical Pedersen and Hall conductivity models are obtained by combining the auroral conductivity model of *Fuller-Rowell and Evans* [1987] with the conductances produced by solar extreme ultraviolet (EUV) radiation. The auroral conductivity model is parameterized by the 10-level Hemispheric Power Index (HPI) [*Foster et al.*, 1986]. Energy fluxes and average energies of the auroral precipitating electrons measured by the DMSP and UARS satellites are used to calculate the height-integrated Pedersen and Hall conductivities, based on the empirical formulas of *Robinson et al.* [1987]. The estimates of the conductivities from the NOAA-12 data are based on an electron transport code under the full energy spectrum of the electron precipitation [*Fuller-Rowell and Evans*, 1987]. In addition the magnetic perturbations as measured by ground-based magnetometers are used to modify the ionospheric conductivities [*Ahn et al.*, 1983b] and provide an improved temporal and spatial resolution of high-latitude ionospheric conductances. The detailed fitting procedure has been described by *Richmond and Kamide* [1988] and *Richmond et al.* [1988]. We incorporate simultaneous observations from both hemispheres, assuming that the auroral precipitation is approximately conjugate. But observations from the opposite hemisphere are weighted 50% less in the fitting.

Ionospheric electric fields and currents are related by Ohm's law, through the Pedersen and Hall conductivities. Thus, once a reliable conductivity distribution is derived, the ionospheric convection pattern can be estimated from the direct ion drift observations by satellites and radars, and from the inversion of magnetic perturbations. Additionally, an *a priori* statistical potential model is often applied, which provides a first-order estimate of the ionospheric potentials where there are no *in situ* measurements. The statistical electric potential model used in this study is based on Millstone Hill radar observations [*Foster et al.*, 1986], and is also parameterized by the

HPI index. The different data sets are weighted by the inverse square of their effective errors so that less reliable data contribute less to the fitting. AMIE uses apex coordinates [VanZandt *et al.*, 1972; Richmond, 1995] with the apex latitude being similar to invariant latitude and corrected geomagnetic latitude in polar regions. All data are converted to apex coordinates before being incorporated into AMIE. The current grid size of AMIE is about  $1.7^\circ$  in latitude and  $10^\circ$  in longitude.

### 3. Results

#### 3.1 Examination of Large-Scale Electrodynamic Patterns

The period of March 28-29, 1992, is featured by a series of moderate substorms. In this subsection we examine the large-scale patterns of ionospheric convection, Joule heating, and field-aligned current density during a substorm interval between 0800 and 1200 UT on March 29. This is the third largest substorm during this 2-day period in terms of the magnitude of the *AE* index; the other two largest substorms are associated with either an ambiguous onset time (*AE* peaks at about 0510 UT on March 29) or a poor coverage of ground magnetometers over the Russian area near local midnight (*AE* peaks at 1550 UT on March 29). According to the distribution of the *AL* and *AE* indices (see Figure 7a), the substorm starts at about 0810 UT when the magnitudes of *AL* and *AE* start to increase abruptly. The substorm expansion phase exhibits a vibratory nature and lasts until about 1015 UT. After that, the substorm is in the recovery phase as *AL* and *AE* gradually diminish, until about 1200 UT. Ionospheric electrodynamic fields at six selected UT times within the substorm are examined in detail (described below in the text) and results are shown in Figures 3-6. The times of interest are 0810 UT when the onset of the expansion phase occurs; 0840 UT and 0910 UT in the expansion phase; 0940 UT and 1000 UT as peaks of the expansion phase when the derived *AE* index reaches maxima; and 1030 UT in the recovery phase. It is worth pointing out that this is not a case of a clear and isolated substorm event. This interval is more likely a superposition of two or more smaller substorms, which can be seen as *AL* and *AE* increase non-monotonically during the expansion phase. Therefore, identification of various substorm phases based on the *AL* and *AE* indices is rather crude. Nevertheless, our intention is to demonstrate the variations of the different electrodynamic parameters associated with geomagnetic activity.

The high-latitude electrodynamic fields shown in Figures 3-6 are derived from data sources described in the previous section. Precipitating particle observations from satellites and ion drift measurements from radars that are taken within  $\pm 5$  min of each analyzed time are utilized in the AMIE fitting procedure. The ground magnetometer data are averaged over 5-min in the vicinity of each given time. As we will discuss in the next section, the satellite ion drift or electric field measurements can have a significant influence on the cross-polar-cap potential drop. Therefore, in order to make a direct comparison between the patterns derived at different UT times during the substorm, we do not use the satellite ion drift data that are only available during a satellite overflight. However, we do utilize the satellite particle precipitation measurements to modify the ionospheric conductivities so that the inference of electric fields from the magnetometer data becomes more reliable.

Figure 3 shows consecutive patterns of ionospheric convection during the substorm. The convection or electric potential contours are in solid lines where the AMIE procedure infers an uncertainty of less than 50% in the large-scale electric field; otherwise the contours are in dashed lines. The total cross-polar-cap potential drop given at the upper right corner of each pattern is the difference between the most positive and most negative potentials. At 0810 UT, the onset of the expansion phase, the convection pattern consists of two cells that are nearly symmetric about the noon-midnight meridian, but the positive-potential dawn cell penetrates slightly into the pre-midnight region. The primary positive potential peak of the dawn cell is located at about 0200 magnetic local time (MLT) as indicated by the plus sign; in addition, there is a secondary positive potential peak at about 0630 MLT, which is not clearly visible with the 5-kV contour interval. At 0840 UT, the substorm expansion phase, the magnetic perturbations in midnight and early morning sectors have increased dramatically. The enhancement of magnetic perturbation also enhances the plasma convection, and the total cross-polar-cap potential drop rises from 42 kV to 65 kV. The double peaks on the dawnside are now both visible. The primary potential peak has moved to 0300 MLT while the secondary peak remains at the same location. The pattern at 0910 UT is nearly the same as that at 0840 UT, but the total potential drop is slightly smaller (61 kV). As mentioned above, this is not a typically isolated substorm event. A dip in the *AL* and *AE* indices is seen at about 0900 UT. At 0940 UT, the first peak of the expansion phase, the ground magnetic perturbations are most enhanced, and the cross-polar-cap potential drop reaches 78 kV. The nightside tip of the dawn cell has protruded into the premidnight region up to 2200 MLT. The pri-

mary potential peak now is located at 0400 MLT, and the secondary peak near dawn remains at the same location at about 0630 MLT. At 1000 UT, the second peak of the expansion phase, the magnetic perturbations are slightly weaker than at the previous peak in the midnight-to-early morning sector, but stronger near the dawn. At this time, the potential peak at 0630 MLT becomes the primary one, and the peak near 0400 MLT becomes secondary. At 1030 UT, the substorm recovery phase, the magnetic perturbations decrease further, and so does the cross-polar-cap potential drop. The potential peak in the morning sector becomes invisible as the substorm subsides.

Variations of the horizontal ionospheric currents are shown in Figure 4. At the onset of the substorm expansion phase (0810 UT), there are three distinct current jets or electrojets: (1) the eastward electrojet between 1200 and 2200 MLT; (2) the westward electrojet between 0600 and 1100 MLT; and (3) the westward electrojet between 2300 and 0300 MLT. These currents are primarily Hall currents. Spatial separation between the two westward current jets indicates that they may be associated with different processes in the different magnetospheric regions. The intensity of the eastward electrojet and the morning-side westward electrojet is mainly controlled by the direct energy input due to solar wind-magnetosphere interaction; whereas the enhancement of the electrojet near local midnight is the manifestation of substorms as a results of sporadic unloading of magnetotail energy [Clauer and Kamide, 1985; Kamide and Baumjohann, 1993]. The westward edge of the nightside westward electrojet is the location of the westward traveling surge (WTS) [Akasofu *et al.*, 1965; Kamide and Akasofu, 1975; Baumjohann, 1983]. During the expansion phase, the auroral electrojets on the dawnside and duskside are nearly unchanged. The electrojet near midnight, however, is not only enhanced in its strength but also expanded longitudinally to join with the westward electrojet from the dawnside, as well as to abut with the eastward electrojet from the duskside near 2300 MLT. At the peak of the expansion phase, the nightside electrojet is most intense and at the same time, the dawnside and duskside electrojets are also enhanced. During the recovery phase, all three electrojets gradually decay, and the nightside electrojet retreats to the morning sector.

The field-aligned current density  $j_{||}$  is found from the divergence of the horizontal current:

$$j_{||} = \nabla_{\perp} \cdot (\Sigma_P E) + \nabla_{\perp} \cdot (\Sigma_H \mathbf{b} \times E)$$

where  $\Sigma_P$  and  $\Sigma_H$  are the height-integrated Pedersen and Hall conductances, respectively,  $\mathbf{b}$  is a



unit vector of the magnetic field, and  $E$  is the ionospheric electric field. Thus the field-aligned current depends on the divergence of the electric field as well as the gradient of the conductances. In the AMIE procedure, we assume that the magnetic field is vertical and neglect the neutral wind dynamo effect. Figure 5 illustrates the field-aligned-currents response to the substorm. Solid (dashed) contours represent downward (upward) field-aligned currents with contour intervals of  $0.2 \mu\text{A}/\text{m}^2$  starting at  $\pm 0.1 \mu\text{A}/\text{m}^2$ . The total downward field-aligned current given at the upper right is defined as one-half the hemispheric integral of the absolute value of the current density over the area poleward of  $50^\circ$ . At 0810 UT, the large-scale distribution shows upward region 1 and downward region 2 currents on the duskside, and downward region 1 and upward region 2 currents on the dawnside, similar to the statistical patterns of *Iijima and Potemra* [1978]. However, unlike the statistical distribution of the field-aligned current which peaks at about 0900 MLT for downward region 1 current and at 1400 MLT for upward region 1 current [*Iijima and Potemra*, 1978], Figure 5a shows double peaks for both dawn and dusk region 1 currents at the onset of the substorm. The duskside upward current peaks at about 1600 and 2200 MLT, and the dawnside downward current peaks at 0800 and 0130 MLT, respectively. In addition, a weak upward current appears poleward of the dawnside region 1 current. Along with the upward region 2 current from the dawnside, they form triple current sheets in the post-midnight sector. However, the polarities of the triple current sheets are opposite to those associated with the Harang discontinuity in the midnight sector [*Iijima and Potemra*, 1978]. The field-aligned currents become more intense as the substorm progresses. The dayside peaks of current density appear relatively stable; whereas the nightside peaks tend to move counterclockwise. Between 0810 UT and 0840 UT, the nightside peak of the upward current has moved from pre-midnight to post-midnight at about 0200 MLT. It remains at about the same MLT as the downward region 1 current peak throughout the substorm expansion phase as well as at the substorm peaks. During the substorm recovery phase, the intensity of the field-aligned current decreases. The upward current that is poleward of the downward region 1 current in the early morning sector nearly disappears at 1030 UT.

Joule heating is attributed as the main dissipation channel of the magnetospheric energy into the ionosphere [*Lu et al.*, 1995]. However, estimating Joule heating is subjected to large uncertainties owing to variations of the electric field and conductivity from their average values.

Recently, theoretical calculations conducted by *Codrescu et al.* [1995] find a 30% increase in Joule heating due to a uniformly distributed E-field variability, or a 20% increase due to a uniformly distributed conductivity variability. As demonstrated by *Richmond and Kamide* [1988], a very important feature of AMIE is its ability to give quantitative information about the error  $\delta e$  associated with the estimated large-scale electric field  $E$  at each grid point. Thus the “correct” height-integrated Joule heating  $Q_J$  should be expressed by [*Richmond et al.*, 1990]:

$$Q_J = \sum_p E^2 + \sum_p \langle (\delta e)^2 \rangle$$

Here the second term represents the additional increase in Joule heating due to the E-field uncertainty. It should be pointed out that  $\delta e$  represents the errors associated with imperfect data (such as standard deviations in averaging the data) and incomplete spatial coverage of the observations. Smaller-scale electric fields and their contributions to the Joule heating have not been taken into account currently in the procedure. In addition, errors associated with ionospheric conductivity are also excluded from our calculations. Figure 6 shows the distribution of the “corrected” height-integrated Joule heating, where the correction represents the second term in the expression for  $Q_J$ . Note that the contour interval is 4 mW/m<sup>2</sup>, except for Figure 6a where the contour interval is 2 mW/m<sup>2</sup>. The total Joule heating integrated above 50° magnetic latitude is given at the upper right corner of each pattern. By examining these patterns, it is easy to see that Joule heating is concentrated in the regions of the duskside eastward electrojet, the dawnside westward electrojet, and the nightside westward electrojet. As the substorm progresses, Joule heating becomes more and more intense, especially in the early morning sector.

As a comparison, we also estimate Joule heating without taking into account the second term of the above equation for the same six UT times (the patterns are not shown). The “simple” Joule heating thus calculated is similar to the “corrected” Joule heating in terms of general distribution. However, the magnitude of the total hemisphere-integrated “simple” Joule heating is about 10-20% smaller than the “corrected” Joule heating. Although the conductivity variability will alter the local distribution of Joule heating, it is unlikely to affect the total hemisphere-integrated Joule heating significantly because of cancellations between localized enhancement and reduction in conductivity.

Figures 3-6 demonstrate the ability of the AMIE procedure to reproduce the large-scale

dynamics at high latitudes associated with substorms based on various observations. A distinctive feature of the ionospheric convection or electric potential during the substorm is the formation of double potential peaks within the dawnside positive-potential cell. As the substorm progresses, the potential peak in the post-midnight sector moves counterclockwise; whereas the peak near dawn remains nearly steady. A similar phenomenon was found by *Shue and Weimer* [1994] in their statistical study. As explained by *Kamide et al.* [1994], the peak near dawn represents the “normal” magnetospheric convection which is controlled mainly by the interaction between the solar wind and the magnetosphere; while the peak in the morning sector is primarily caused by substorm activity, and therefore its motion directly reflects systematic variations associated with substorms.

The nightside westward electrojet develops separately from the westward electrojet in the late morning sector following the onset of the expansion phase. As the substorm evolves, the nightside electrojet expands longitudinally as well as intensifies at a greater rate than the morning electrojet, which shows no obvious change until at the peak of the expansion phase. During the recovery phase, the nightside electrojet diminishes rapidly but the morning electrojet persists. Due to apparently different causes for the two westward electrojets, the former is called the substorm electrojet and the latter the convection electrojet [*Baumjohann*, 1983; *Kamide et al.*, 1994].

Compared with the horizontal ionospheric current, the field-aligned current distribution is more complicated. In the post-midnight region, the downward region 1 current from the morning side is surrounded by the upward field-aligned currents at the poleward and equatorward edges. Using the simultaneous imagery, high-resolution magnetic field, and precipitating particle measurements from the DMSP F7 satellites, *Bythrow and Potemra* [1987] have found that, near the head of the WTS, the most poleward upward field-aligned current corresponds to a narrow discrete auroral arc and the equatorward upward current corresponds to a broad and bright auroral emission. The downward field-aligned current in the middle separates the discrete arc at the poleward edge of the WTS from the bright auroral oval of the WTS. They attribute the WTS to the expansion of the central plasma sheet into the plasma-sheet boundary layer in the distant magnetotail. *Lyons et al.* [1990] have also related the poleward boundary of the WTS to the separatrix between the open and closed magnetic field lines. Because of the lack of a satellite observations in the midnight region during this substorm event, we are unable to examine the magnetospheric origins of the different field-aligned currents associated with the WTS. Furthermore, enhanced

upward field-aligned currents are often found at the westward edge of the WTS and the more wide-spread downward currents in the eastern part [e.g., *Baumjohann et al.*, 1981; *Opgenoorth et al.*, 1980;1983]. This east-west pair of field-aligned currents is fed by the westward substorm electrojet, which forms the substorm current wedge [*McPherron et al.*, 1973]. However, as shown in Figure 5, the pair of field-aligned currents in the post-midnight or early morning sector lines up in the north-south direction, instead of in the east-west direction. Because there was no satellite passing over the region near midnight during the substorm to provide valuable information about auroral precipitation, the ionospheric conductances in that region were mainly determined by the statistical models which tend to have a larger gradient in the north-south direction than in the east-west direction. During substorms, the field-aligned currents in the midnight region are influenced strongly by conductivity enhancements generated by energetic precipitating electrons associated with the WTS.

Joule heating represents the major magnetospheric energy dissipation in the ionosphere and thermosphere. During the substorm expansion phase, the WTS becomes the primary energy dissipation source because of the Cowling effect [*Baumjohann*, 1983]; it can account for about one half of the total hemisphere-integrated Joule heating during the substorm expansion phase.

### 3.2 Variations of Global Electrodynamic Quantities

Global ionospheric quantities, such as the cross-polar-cap potential drop, the hemisphere-integrated Joule heating, and the total field-aligned current, represent important features of the electrodynamic states associated with geomagnetic activity. In this section we examine these global quantities and their interrelationships.

Figure 7 shows variations of different parameters representing electrodynamic conditions at high latitudes over the period of March 28-29, 1992. The top panel shows the auroral electrojet indices *AU* (dash-dotted), *AL* (dashed), and *AE* (solid) calculated from the north-south component of the magnetic perturbations measured by 63 ground stations between 55° and 76° magnetic latitudes north and south. As a comparison, the dotted line in the top panel represents the *AE* index calculated from 10 out of the 12 standard *AE* stations that were available for this study. For these two days, the average value of the “standard” *AE* index (i.e., *AE*(10)) is about 28% smaller than the “true” *AE* index (i.e., *AE*(63)). *AL* and *AE* indicate that there are about 10 moderate substorms during this 2-day period. The second panel shows the distribution of the cross-polar-cap potential

drop in the northern (solid) and southern (dashed) hemispheres. The potential drops in the two hemispheres are generally comparable, indicating that the IMF is likely to be southward or weakly northward, as evident during the 1320 to 1945 UT interval on March 29. It should be noted that the accuracy of the ionospheric convection estimated from AMIE is determined by the underlying data coverage. The most reliable measurements of the cross-polar-cap potential are from the perpendicular-to-track ion drifts or along-track electric field measurements from near dawn-dusk polar orbiting satellites, such as the DMSP F8 and F11 spacecraft. AMIE tends to underestimate the potential drop when there is a lack of satellite electric field or ion drift measurements for periods of southward IMF. In fact, the peaks of potential drop shown in the second panel of Figure 7 correspond to the intervals of DMSP overflights. We find that, for this equinox period, the cross-polar-cap potential drop without the satellite data is usually about 20-30% lower than that with the satellite data. Since the ground magnetometer coverage is sparse in the southern hemisphere, on a few occasions, the difference in potential drops with and without the satellite data can be as high as 50%. Figure 8 shows one such case where Fig. 8a is the statistical pattern of Foster et al [1987] corresponding to a hemispheric power index of 6, Fig. 8b is the pattern derived from ground magnetometer data only, and Fig. 8c is the pattern derived from both ground and satellite data. With the ground magnetometer data only, the pattern tends to resemble the statistical model applied, and the resulting cross-polar-cap potential drop is 43 kV. By incorporating the satellite ion drift data into AMIE, both dawn and dusk cells are enhanced, and the potential drop increases to 79 kV.

The third panel in Figure 7 shows the hemispheric integrals of the “corrected” Joule heating in the northern and southern hemispheres as well as the incident auroral electron energy flux. The total auroral energy input due to precipitating electrons in the two hemispheres is about the same, because conjugate observations have been used in the fitting. Although energetic particle precipitation can become a locally dominant dissipation source, particularly within the auroral arcs [Evans et al., 1977; Vickrey et al., 1982; Kelley et al., 1991], it is globally less significant than Joule heating. During the 2 days, the average value of hemisphere-integrated Joule heating is 51 GW, and the average value of the hemisphere-integrated auroral precipitation is about 26 GW. So the hemispheric auroral energy dissipation is about one half of the hemispheric integrated Joule heating. It is noted that the Joule heating estimated from AMIE in this study is about 50% smaller than the “convection heating” (e.g., without taking into account the neutral winds) estimated from

the TIGCM in the previous study [Lu *et al.*, 1995]. One of the causes for the discrepancy is the way that ionospheric conductivity is calculated. The AMIE procedure adopts the empirical formulas of Robinson *et al.* [1987], whereas the TIGCM calculates ionospheric conductivities through the self-consistent estimates of electron and ion densities and temperatures within the model. It is found that, over the auroral regions, the height-integrated Pedersen conductivity from TIGCM is about 30% larger than that of AMIE, but the height-integrated Hall conductivity is about the same. It should be emphasized here that the AMIE procedure neglects the neutral wind dynamo. From the TIGCM simulations, Lu *et al.* [1995] found that the neutral winds can have a significant influence on the ionospheric electrodynamics by reducing the total Joule heating by approximately 28%.

Harel *et al.* [1981] have derived an empirical relation between the hemisphere-integrated Joule heating  $U_J$  and the cross-polar-cap potential drop  $\Phi$ :

$$U_J = \Sigma_{eff} \Phi^2$$

where  $\Sigma_{eff}$  is an effective ionospheric Pedersen conductance, which is about 30 Siemens (S) from their study. To follow this idea, Figure 9 is the plot of  $U_J$  versus  $\Phi^2$ , with a correlation coefficient of 0.83 in the northern hemisphere (top), and 0.75 in the southern hemisphere (bottom). The obtained effective conductance is 14.5 S in the northern hemisphere and 16.3 S in the southern hemisphere, which is about half of the magnitude derived by Harel *et al.* [1981].

The bottom panel of Figure 7 is the hemisphere-integrated field-aligned current  $J_{||}$  in the northern (solid) and southern (dashed) hemispheres. The field-aligned current in the southern hemisphere is larger than that in the northern hemisphere between about 0300 and 0500 UT on both days, when the south magnetic pole is toward the Sun. Between about 1300 and 2200 UT, the field-aligned current in the northern hemisphere is larger than that in the southern hemisphere. The difference in field-aligned current between the two hemispheres can be attributed to the asymmetry of the ionospheric conductivity due to the hemispheric asymmetry in deposition of solar irradiation. Figure 10 shows the height-integrated Pedersen conductivities in the northern (top) and southern (bottom) hemispheres derived at 0325 and 1730 UT on March 29, 1992. At 0325 UT, the terminator of the solar-induced conductivity is about  $10^\circ$  nightside of the dawn-dusk meridian in the northern hemisphere, and about  $30^\circ$  in the southern hemisphere. In contrast,

at 1730 UT, the northern magnetic pole is toward the Sun; the terminator is about  $30^\circ$  nightside of the dawn-dusk meridian in the northern hemisphere and about  $10^\circ$  dayside of the dawn-dusk meridian in the southern hemisphere. The offset of the magnetic pole from the geographic pole introduces a diurnal variation of ionospheric conductivity, even during equinoxes. In the auroral zone, the conductivities are produced by both auroral precipitation and solar irradiation. The auroral-produced conductivities are nearly the same in the two hemispheres because conjugate observations have been used; whereas the solar-EUV-produced conductivities in the auroral zones have a difference of about 30% between the two hemispheres at these two UT times. These differences are also apparent in the hemisphere-integrated Joule heating for the same reason.

As illustrated in Figure 7, the cross-polar-cap potential drop, the hemispheric integrated Joule heating, and the total field-aligned current are apparently correlated with  $AE$ . To further examine the interrelationships among the various global quantities, Figure 11 shows the scatter plots of the different quantities versus the  $AE$  index (i.e.,  $AE(63)$ ) in both northern and southern hemispheres. Each panel also lists the linear correlation coefficient, the average value, and the linear fitting of each quantity to  $AE$ . Overall, the correlation coefficient  $r$  in the southern hemisphere is smaller than that in the northern hemisphere. This is because only 3 of the 63 ground magnetometer stations contributing to the calculation of the auroral indices are in the southern hemisphere. Therefore, the auroral indices presented in this study mainly reflect geomagnetic activity in the northern hemisphere. Additionally, the ground data coverage in the southern hemisphere is poorer than that in the northern hemisphere. The average values of the three global quantities over the 2-day period are nearly comparable between the two hemispheres, and this is consistent with the fact that this period is in an equinox season. From the linear regression fit, the proportionality factor between  $\Phi$  and  $AE$  is 0.08 kV/nT in the northern hemisphere and 0.07 kV/nT in the southern hemisphere, while the proportionality factor between  $J_{\parallel}$  and  $AE$  is 0.005 MA/nT in the northern hemisphere and 0.004 MA/nT in the southern hemisphere. These proportionality factors are about 30% smaller than those given by *Richmond et al.* [1990]. Note that *Richmond et al.* [1990] adopted  $AE(12)$  in their study while we used  $AE(63)$ . If we had used the “standard”  $AE$  (i.e.,  $AE(10)$ ) which is about 28% smaller than  $AE(63)$ , our results would be nearly the same as *Richmond et al.* [1990]. Previous studies have resulted in a proportionality factor of  $U_J$  versus  $AE$  between 0.21 GW/nT and 0.33 GW/nT [*Richmond et al.*, 1990; *Ahn et al.*, 1983a;

*Baumjohann and Kamide, 1984*]. As a comparison, the proportionality factor derived from this study is somewhat smaller: 0.16 GW/nT in the northern hemisphere and 0.13 GW/nT in the southern hemisphere. The reason for such discrepancy between these independent studies is complicated, but it may be attributed to the fact that different *AE* index (for example, *AE*(12) in *Richmond et al.*; *AE*(71) in *Ahn et al.* and *Baumjohann and Kamide*; and *AE*(61) for this study) and different conductivities (empirical conductivity models in *Ahn et al.* and *Baumjohann and Kamide*, and AMIE-derived conductivities in *Richmond et al.* and this study) are used for different studies. Seasonal effect may also contribute to the discrepancy.

The solid line in Figure 12a is the standard 1-hour  $D_{st}$  (the provisional data from the World Data Center-C2 at Kyoto University, Japan) which has been linearly interpolated to 5-min resolution. As a comparison, the dashed line shows the 5-min  $D_{st}$  index from the measurements of 11 stations located equatorward of  $\pm 45^\circ$  magnetic latitude. The standard  $D_{st}$  represents well the low-frequency variation, while the measured  $D_{st}$  shows more high-frequency structures.

The ring current injection rate  $U_R$  (in cgs units) can be calculated according to *Akasofu* [1981]:

$$U_R = 4 \times 10^{20} \left( \frac{\partial \bar{D}_{st}}{\partial t} + \frac{\bar{D}_{st}}{\tau_R} \right)$$

where  $\tau_R$  in seconds is the ring current particle lifetime, and  $\bar{D}_{st}$  in nT is the pressure-corrected  $D_{st}$  index defined by [Zwickl *et al.*, 1987]

$$\bar{D}_{st} = |D_{st}| - D_{st}(P)$$

with  $D_{st}(P) = aP^{1/2} - b$ ,  $a = 0.2 \text{ nT}/(\text{eV cm}^{-3})^{1/2}$ ,  $b = 20 \text{ nT}$ , and  $P$  is defined as the solar-wind dynamic pressure. During the interval of 1320-1930 UT on March 29, the available solar-wind plasma data indicate a solar-wind pressure of  $16 \times 10^3 \text{ eV/cm}^3$ , corresponding to  $D_{st}(P)$  of 5 nT. We assume that the solar-wind pressure is constant for the entire 2-day period. The ring current energy injection rate depends on  $\tau_R$ , which is a highly uncertain parameter that varies from less than 1 hour to about 20 hours [e.g., *Akasofu, 1981; Zwickl et al., 1987*], depending on the solar-wind energy transfer rate  $\epsilon$ . In Figure 12b, the solid and dashed lines are the ring current injection rate  $U_R$  corresponding to  $\tau_R = 3.5 \text{ hr}$  and 20 hr, respectively, using the standard  $D_{st}$  values.



Choosing  $\tau_R = 3.5$  hr ensures that  $U_R$  is always larger than zero. Alternatively, since  $\epsilon$  is less than  $5 \times 10^{18}$  ergs/s during the interval when the solar-wind data are available (see Figure 13), one can also take  $\tau_R = 20$  hr [Akasofu, 1981]. Choosing  $\tau_R = 20$  hr, however, makes  $U_R$  become negative at several intervals. This implies that  $\tau_R$  should be a time-dependent parameter that varies between 3.5 and 20 hr, rather than a constant during this 2-day period, even though the  $D_{st}$  index is relatively steady. The average value of  $U_R$  is 124 GW (or  $1.24 \times 10^{18}$  ergs/s) for  $\tau_R = 3.5$  hr and 85 GW for  $\tau_R = 20$  hr. The dotted line represents the ring current injection rate corresponding to  $\tau_R = 20$  hr, using the measured  $D_{st}$ , which shows some superimposed fine structures. Figure 12c shows the total magnetospheric energy input  $U_T$ , which is the sum of Joule heating and auroral energy precipitation in both hemispheres and the ring current injection rate  $U_R$ . The solid line corresponds to  $\tau_R = 20$  hr and the dashed line for  $\tau_R = 3.5$  hr.

Plotted in Figure 13 are  $U_T$  and  $\epsilon$ .  $\epsilon$  is given in Gaussian units by [Perreault and Akasofu, 1978]

$$\epsilon = v B^2 \sin^4\left(\frac{\theta}{2}\right) l_0^2$$

where  $v$  is the solar-wind speed,  $B$  is the interplanetary magnetic field,  $\theta$  is the angle between the  $z$  direction and the projection of the IMF in the  $y$ - $z$  plane of the GSM coordinate system, and  $l_0 = 7 R_E$  corresponding to an effective magnetospheric width of  $10 R_E$  [Perreault and Akasofu, 1978]. During this 6-hr interval, the average  $\epsilon$  is slightly larger than  $U_T$  with  $\tau_R = 20$  hr, but about half of  $U_T$  with  $\tau_R = 3.5$  hr. Therefore, in order to match  $\epsilon$  with  $U_T$ , either  $\tau_R$  should be 20 hr or larger, or  $l_0$  should be increased from  $7 R_E$  to  $10 R_E$  (corresponding to an effective magnetospheric width of about  $14.3 R_E$ ). For this case, the latter condition seems more reasonable since it is consistent with the statistical magnetopause configuration of Sibeck *et al.* [1991] for the given IMF values. It should also be pointed out that, in addition to  $U_T$ , part of the solar-wind energy input  $\epsilon$  is stored in the magnetotail as well as contributing to plasma sheet heating. Unfortunately, we are unable to quantify this part of energy loss for this particular period. Previous studies [Weiss *et al.*, 1992, and references therein] indicate that the typical values of energy storage in the magnetotail and plasma sheet heating are about  $5 \times 10^{11}$  W and  $1 \times 10^{11}$  W, respectively.

The solar wind energies are transmitted to the magnetosphere and ionosphere through magnetic coupling. It is of interest to estimate the coupling efficiency between the solar wind and the magnetosphere by comparing the solar-wind energy input with the energy dissipation into the magnetosphere. During the 6-hr interval, the average  $B_z$  is about -4 nT, which implies a corresponding dawn meridian magnetopause distance of  $14.5 R_E$  [Sibeck *et al.*, 1991]. Thus the effective cross-sectional area of the magnetopause is about  $3 \times 10^{20} \text{ cm}^2$ . Given the average solar-wind speed of 350 km/s and density of  $12 \text{ amu/cm}^3$ , the solar-wind energy input  $U_{sw}$  is about  $1 \times 10^{20} \text{ erg/s}$  or  $1 \times 10^4 \text{ GW}$ . Therefore, the coupling efficiency, defined as the ratio of  $U_T$  over  $U_{sw}$  is about 0.03. This value is approximately one order larger than that during strong northward IMF conditions [e.g., Tsurutani and Gonzalez, 1995].

#### 4. Summary

We have presented in this paper the large-scale high-latitude ionospheric electrodynamics during the ATLAS/GEM period of March 28-29, 1992. The high-latitude auroral precipitation, plasma convection, and other related electrodynamic quantities are important to the thermospheric dynamics in terms of ion drag and Joule heating.

The 2-day campaign period is featured by several moderate substorms. We have examined the large-scale patterns of various electrodynamic fields associated with the different phases of a substorm. Distributions of the ionospheric convection show clearly the co-existence of double positive potential peaks during the expansion phase of the substorm: one peak is located near 0300 MLT, the other near dawn. During the recovery phase, the peak potential in the early morning sector gradually decreases. At the onset of the substorm, there are three distinctive ionospheric electrojets: the eastward electrojet on the duskside; the westward electrojet in the postdawn sector; and the westward electrojet in the post-midnight sector, i.e., the substorm electrojet. As the substorm progresses, the substorm electrojet not only is enhanced in its strength but also expands longitudinally toward both dawn and dusk. On the other hand, the dawn and dusk convection electrojets are much slower in response to the development of the substorm. No significant enhancement of these electrojets is seen until at the peak of the substorm. As the substorm subsides, the substorm electrojet gradually decays and eventually merges with the dawnside

convection electrojet. Variations of field-aligned currents during the course of the substorm are somewhat more complicated. During the expansion phase, the distribution of field-aligned current shows that the downward current sheet is surrounded by upward currents poleward and equatorward in the vicinity of the WTS, and the current density is intensified. During the recovery phase, the field-aligned currents tend to die away, especially the most poleward component. Ionospheric Joule heating is concentrated in the regions associated with auroral electrojets. During substorms, the WTS becomes the primary energy dissipation source due to the Cowling effect.

Variations of global ionospheric quantities, such as the cross-polar-cap potential drop, the hemisphere-integrated Joule heating, and the total field-aligned current, represent important electrodynamic features associated with geomagnetic activity. A reasonably good correlation has been found between the various global quantities and the *AE* index (i.e., *AE*(63)), with a correlation coefficient between 0.5 and 0.8. On the average over this 2-day period, the total globally integrated Joule heating (corrected), sum over the two hemispheres, is about 102 GW, and the total globally integrated auroral energy precipitation is about 52 GW. Using an empirical formula, the ring current energy injection is estimated to be 125 GW for a decay time of 3.5 hr, and 85 GW for a decay time of 20 hr. In this study, we also estimate an energy-coupling efficiency of 3% between the solar wind and the magnetosphere when the IMF  $B_z$  is southward.

**Acknowledgments.** We wish to acknowledge the CEDAR (Coupling, Energetics and Dynamics of Atmospheric Regions) Data Base at the National Center for Atmospheric Research (NCAR) for providing the Sondrestrom incoherent scatter radar data. Both facilities are supported by the National Science Foundation (NSF). The Johns Hopkins University Applied Physics Laboratory HF radar at Goose Bay, Labrador, is supported in part by the NSF Division of Atmospheric Sciences under NSF grant ATM-9003860 and in part by the National Aeronautics and Space Administration (NASA) under grant NAG5-1099. The Wick radar was operated and maintained by the Department of Physics and Astronomy at University of Leicester in United Kingdom. We thank L. Morris at the World Data Center for selecting the ground magnetometer data, the Canadian Space Agency and T. Hughes at the National Research Council of Canada for providing data from the CANOPUS magnetometer array, E. Friis-Christensen at Danish Meteorological Institute for distributing the Greenland magnetometer network data, O. Troshichev for delivering the Russian

Arctic and Antarctic analog data, the Technical University of Braunschweig and the Finnish Meteorological Institute for supplying IMAGE magnetometer network data, the Auroral Observatory at the University of Tromsø, Norway for contributing data from the Norwegian Arctic Stations, P. Sutcliffe at the Hermanus Magnetic Observatory in South Africa for submitting the Hermanus magnetometer data, C. G. MacLennan at AT&T Bell Laboratories for providing data from their ground stations at Iqaluit (FRB) in Canada, and at McMurdo (MCM) and South Pole (SPA) in the Antarctic. We are grateful to F. Rich for providing us the DMSP data, the IMP-8 magnetometer data processing team at the Laboratory for Extraterrestrial Physics of GSFC for the use of the IMP-8 IMF data, and A. Lazarus at MIT for the IMP-8 plasma data. The EXOS-D satellite data were provided by A. Mutsuoka and H. Hayakawa at the Institute of Space and Astronautical Science, and by T. Nagatsuma and H. Fukunishi at the Upper Atmosphere and Space Research Laboratory of Tohoku University, Japan. We thank S. Nguyen and C. A. Gonzalez for their efforts with the UARS data. We also thank A. Richmond and E. Szuszcwics for many helpful comments and fruitful discussions. This study was supported in part by NSF under grant 93-SFA.1 and by NASA contract NAS5-27753 with SWRI.

## References

- Ahn, B. -H., S. -I. Akasofu, and Y. Kamide, The Joule heat production rate and the particle energy injection rate as a function of the geomagnetic indices *AE* and *AL*, *J. Geophys. Res.*, **88**, 6275, 1983a.
- Ahn, B. -H., R. M. Robinson, Y. Kamide, and S. -I. Akasofu, Electric conductivities, electric fields and auroral energy injection rate in the auroral ionosphere and their empirical relations to the horizontal magnetic disturbances, *Planet. Space Sci.*, **31**, 641, 1983b.
- Akasofu, S.-I., Energy coupling between the solar wind and the magnetosphere, *Space Sci. Rev.*, **28**, 121, 1981.
- Akasofu, S.-I., D. S. Kimball, and C.-I. Meng, The dynamics of the aurora II. Westward traveling surges, *J. Atmos. Terr. Phys.*, **27**, 173, 1965.
- Baumjohann, W., Ionospheric and field-aligned current system in the auroral zone: A concise review, *Adv. Space Res.*, **2**, 55, 1983.
- Baumjohann, W., and Y. Kamide, Hemispherical Joule heating and the *AE* indices, *J. Geophys.*

*Res.*, 89, 383, 1984.

- Baumjohann, W., R. J. Pellinen, H. J. Opgenoorth, and E. Nielsen, Joint two-dimensional observations of ground magnetic and ionospheric electric fields associated with auroral zone currents: Current systems associated with local auroral break-ups, *Planet. Space Sci.*, 29, 431, 1981.
- Bythrow, P. F., and T. A. Potemra, Birkeland currents and energetic particles associated with optical auroral signatures of a westward traveling surge, *J. Geophys. Res.*, 92, 8691, 1987.
- Chenette, D. L., D. W. Datlowe, R. M. Robinson, T. L. Schumaker, R. R. Vondrak, and J. D. Winningham, Atmospheric energy input and ionization by energetic electrons during the geomagnetic storm of 8-9 November 1991, *Geophys. Res. Lett.*, 20, 1323, 1993.
- Clauer, C. R., and Y. Kamide, DP 1 and DP 2 current systems for March 22, 1979 substorm, *J. Geophys. Res.*, 90, 1343, 1985.
- Codrescu, M. V., T. J. Fuller-Rowell, and J. C. Foster, On the importance of E-field variability for Joule heating in the high-latitude thermosphere, *Geophys. Res. Lett.*, submitted, 1995.
- Crowley, G., B. A. Emery, R. G. Roble, H. C. Carlson, Jr., D. J. Knipp, Thermospheric dynamics during September 18-19, 1984, 1. Model simulations, *J. Geophys. Res.*, 94, 16,925, 1989.
- Deng, W., T. L. Killeen, A. G. Burns, R. G. Roble, J. A. Slavin, and L. E. Wharton, The effects of Neutral inertia on ionospheric currents in the high-latitude thermosphere following a geomagnetic storm, *J. Geophys. Res.*, 98, 7775, 1993.
- Evans, D. S., N. C. Maynard, J. Troim, T. Jacobsen, and A. Egeland, Auroral vector electric field and particle comparisons, 2. Electrodynamics of an arc, *J. Geophys. Res.*, 82, 2235, 1977.
- Forbes, J. M., and M. Harel, Magnetosphere-thermosphere coupling: An experiment in interactive modeling, *J. Geophys. Res.*, 94, 2631, 1989.
- Foster, J. C., J. M. Holt, R. G. Musgrove, and D. S. Evans, Ionospheric convection associated with discrete levels of particle precipitation, *Geophys. Res. Lett.*, 13, 656, 1986.
- Fukunishi, H., et al., Magnetic field observations of Akebono (EXOS-D) satellite, *J. Geomagn. Geoelectr.*, 42, 385, 1990.
- Fuller-Rowell, T. J., and D. S. Evans, Height-integrated Pedersen and Hall conductivity patterns inferred from the TIROS-NOAA satellite data, *J. Geophys. Res.*, 92, 7606, 1987.
- Harel, M., R. A. Wolf, R. W. Spiro, P. H. Reiff, and C.-K. Chen, Quantitative simulation of a magnetospheric substorm 2. Comparison with observations, *J. Geophys. Res.*, 86, 2242, 1981.

- Hayakawa, H., et al., Electric field measurement on the Akebono (EXOS-D) satellite, *J. Geomag. Geoelectr.*, 42, 371, 1990.
- Iijima, T., and T. A. Potemra, Large-scale characteristics of field-aligned currents associated with substorms, *J. Geophys. Res.*, 83, 599, 1978.
- Kamide, Y., R. D. Richmond, B. A. Emery, C. F. Hutchins, B. -H. Ahn, O. de la Beaujardiere, J. C. Foster, R. A. Heelis, H. W. Kroehl, F. J. Rich, and J. A. Slavin, Ground-based studies of ionospheric convection associated with substorm expansion, *J. Geophys. Res.*, 99, 19,451, 1994.
- Kamide, Y., and S.-I. Akasofu, The auroral electrojet and global auroral features, *J. Geophys. Res.*, 25, 3585, 1975.
- Kamide, Y., and W. Baumjohann, *Magnetosphere-ionosphere coupling*, Springer-Verlag, New York, 1993.
- Kelley, M. C., D. J. Knudsen, and J. F. Vickrey, Poynting flux measurements on a satellite: A diagnostic tool for space research, *J. Geophys. Res.*, 96, 201, 1991.
- Killeen, T. L., P. B. Hays, G. R. Carignan, R. A. Heelis, W. B. Hanson, N. W. Spencer, and L. H. Brace, Ion-neutral Coupling in the high-latitude *F* region: Evaluation of ion heating terms from Dynamics Explorer 2, *J. Geophys. Res.*, 89, 7495, 1984.
- Lu, G., A. D. Richmond, B. A. Emery, and R. G. Roble, Magnetosphere-ionosphere-thermosphere coupling: Effect of neutral winds on Joule heating and field-aligned current, *J. Geophys. Res.*, in press, 1995.
- Lyons, L. R., O. de la Beaujardiere, G. Rostoker, and E. Friis-Christensen, Analysis of substorm expansion and surge development, *J. Geophys. Res.*, 95, 10575, 1990.
- McPherron, R. L., C. T. Russell, and M. P. Aubry, Satellite studies of magnetospheric substorms on August 15, 1968, *J. Geophys. Res.*, 78, 3131, 1973.
- Oppeorth, H. J., R. J. Pellinen, H. Maurer, F. Kuppers, W. J. Heikkila, K. U. Kaila, and P. Tanskanen, Ground-based observations of an onset of localized field-aligned currents during auroral breakup around magnetic midnight, *J. Geophys. Res.*, 48, 101, 1980.
- Oppeorth, H. J., R. J. Pellinen, W. Baumjohann, E. Nielsen, G. Marklund, and L. Eliasson, Three-dimensional current flow and particle precipitation in a westward traveling surge (observed during the Barium-GEOS rocket experiment), *J. Geophys. Res.*, 88, 3138, 1983.
- Perreault, P., and S. -I. Akasofu, A study of geomagnetic storms, *Geophys. J. Roy. Astron. Soc.*,

54, 547, 1978.

- Rich, F. J., M. S. Gussenhoven, and M. E. Greenspan, Using simultaneous particle and field observations on a low altitude satellite to estimate Joule heat energy flow into the high latitude ionosphere, *Ann. Geophysicae*, 5A, 527, 1987.
- Richmond, A. D., Assimilative mapping of ionospheric electrodynamics, *Adv. Space Res.*, 12, 59, 1992.
- Richmond, A. D., Ionospheric electrodynamics using magnetic apex coordinates, *J. Geomag. Geoelectr.*, in press, 1995.
- Richmond, A. D., and Y. Kamide, Mapping electrodynamic features of the high-latitude ionosphere from localized observations: Technique, *J. Geophys. Res.*, 93, 5741, 1988.
- Richmond, A. D., et al., Mapping electrodynamic features of the high-latitude ionosphere from localized observations: Combined incoherent scatter radar and magnetometer measurements for January 18-19, 1984, *J. Geophys. Res.*, 93, 5760, 1988.
- Richmond, A. D., et al., Global measures of ionospheric electrodynamic activity inferred from combined incoherent-scatter radar and ground magnetometer observations, *J. Geophys. Res.*, 95, 1061, 1990.
- Roble, R. G., E. C. Ridley, A. D. Richmond, and R. E. Dickinson, A coupled thermosphere/ionosphere general circulation model, *Geophys. Res. Lett.*, 15, 1325, 1988.
- Robinson, R. M., R. R. Vondrak, K. Miller, T. Dabbs, and D. Hardy, On calculating ionospheric conductances from the flux and energy of precipitating electrons, *J. Geophys. Res.*, 92, 2565, 1987.
- Shue, J.-H., and D. R. Weimer, The relationship between ionospheric convection and magnetic activity, *J. Geophys. Res.*, 99, 401, 1994.
- Sibeck, D. G., R. E. Lopez, and E. C. Roelof, Solar wind control of the magnetosphere shape, location, and motion, *J. Geophys. Res.*, 96, 5489, 1991.
- Szuszczewicz, E. P., D. Torr, P. Wilkinson, P. Richards, R. Roble, G. Lu, B. A. Emery, D. Evans, S. Pulinets, B. M. Reddy, M. Abdu, M. Lester, K. Igarashi, P. Jiao, P. Blanchard, and J. Joselyn, F-region climatology during the SUNDIAL/ATLAS-1 campaign of March 1992: Prevailing conditions and model-measurement comparisons, *J. Geophys. Res.*, submitted, 1995.
- Thayer, J. P., and J. F. Vickrey, On the contribution of the thermospheric neutral wind to high-lat-

- itude energetics, *Geophys. Res. Lett.*, 19, 265, 1992.
- Tsurutani, B. T., and W. D. Gonzalez, The efficiency of "viscous interaction" between the solar wind and the magnetosphere during intense northward IMF events, *Geophys. Res. Lett.*, 22, 663, 1995.
- VanZandt, T. E., W. L. Clark, and J. M. Warnock, Magnetic Apex Coordinates: A magnetic coordinate system for the ionospheric  $F_2$  layer, *J. Geophys. Res.*, 77, 2406, 1972.
- Vickrey, J. F., R. R. Vondrak, and S. J. Matthews, Energy deposition by precipitating particles and Joule dissipation in the auroral ionosphere. *J. Geophys. Res.*, 87, 5184, 1982.
- Weiss, L. A., P.H. Reiff, J. J. Moses, and B. D. Moore, Energy dissipation in substorms, *Eur. Space Agency Spec. Publ. ESA-SP-335*, 309, 1992.
- Winningham, J. D., et al., The UARS particle environment monitor, *J. Geophys. Res.*, 98, 10,649, 1993.
- Zwickl, R. D., L. F. Bargatze, D. N. Baker, C. R. Clauer, and R. L. McPherron, An evaluation of the total magnetospheric energy output parameter, UT, in *Magnetotail Physics*, p. 155, edited by A. T. Y. Lui, the Johns Hopkins University Press, Baltimore, 1987.



## Figure Captions

**Figure 1.** 1-min interplanetary magnetic fields (in GSM coordinates) and solar-wind plasma measured by the IMP-8 satellite between 1300 UT and 2000 UT on March 29, 1992.

**Figure 2.** Ground magnetometer locations at 0000 UT in the northern (top) and southern (bottom) hemispheres in apex magnetic coordinates. Only those stations poleward of  $\pm 40^\circ$  magnetic latitude are shown.

**Figure 3.** Consecutive northern hemispheric convection patterns derived between 0810 UT and 1030 UT. The patterns have a contour interval of 5 kV. The cross-polar-cap potential drop given at the upper right of each pattern is defined as the difference between the most positive and negative potential. Overlain are the horizontal magnetic perturbations which have been rotated  $90^\circ$  clockwise to indicate the direction of overhead equivalent current.

**Figure 4.** Patterns of ionospheric horizontal currents for the same time interval as Figure 3.

**Figure 5.** Distribution of field-aligned current for the same selected times as Figure 3. The contour interval is  $0.2 \mu\text{A}/\text{m}^2$ , starting at  $\pm 0.1 \mu\text{A}/\text{m}^2$ . Solid contours represent downward current and dashed contours upward current. The total downward current integrated poleward of  $50^\circ$  is given at the upper right of each pattern.

**Figure 6.** Distribution of height-integrated "corrected" Joule heating during the same substorm period as Figure 3 (see text for detail). The total Joule heating integrated poleward of  $50^\circ$  is given in the upper right of each pattern.

**Figure 7.** Distribution of various global electrodynamic quantities for the 2-day period of March 28-29, 1992.

**Figure 8.** (a) The statistical convection pattern corresponding to HPI=6 at 1710 UT on March

29, 1992. (b) The AMIE convection pattern derived from ground magnetometer data only. (c) The convection pattern derived from both ground and satellite data.

**Figure 9.** Scatter plots of hemisphere-integrated Joule heating  $U_J$  versus the cross-polar-cap potential  $\Phi$  squared in the northern (top) and southern (bottom) hemispheres. The solid line shows a linear regression fit.

**Figure 10.** Height-integrated Pedersen conductances derived at 0325 UT and 1730 UT on March 29, respectively. The northern hemispheric patterns are on the top, and the southern hemispheric patterns on the bottom. The contour intervals are 2 S.

**Figure 11.** Scatter plots of the cross-polar-cap potential drop, the hemisphere-integrated Joule heating, and the hemisphere-integrated field-aligned current versus  $AE$  (from top to bottom). The northern hemisphere is on the left, and the southern hemisphere on the right.

**Figure 12.** (a) The solid line shows the standard 1-hr  $D_{st}$  (previsional data), and the dashed line shows the measured  $D_{st}$  derived from 5-min averaged data from 11 station located between  $\pm 40^\circ$  magnetic latitude. (b) The solid and dashed lines are the ring current injection rates corresponding to  $\tau_R = 3.5$  hr and  $\tau_R = 20$  hr, respectively, using the standard  $D_{st}$ . The dotted line is the ring current injection corresponding to  $\tau_R = 20$  hr, using the measured  $D_{st}$ . (c) The total magnetospheric energy inputs corresponding to  $\tau_R = 3.5$  hr (dashed line) and  $\tau_R = 20$  hr (solid line).

**Figure 13.** Comparison of the solar-wind energy transfer rate  $\epsilon$  (dotted line) and the total magnetospheric energy input  $U_T$  for  $\tau_R = 3.5$  hr (dashed line) and  $\tau_R = 20$  hr (solid line).

IMP-8 Data for March 29, 1992

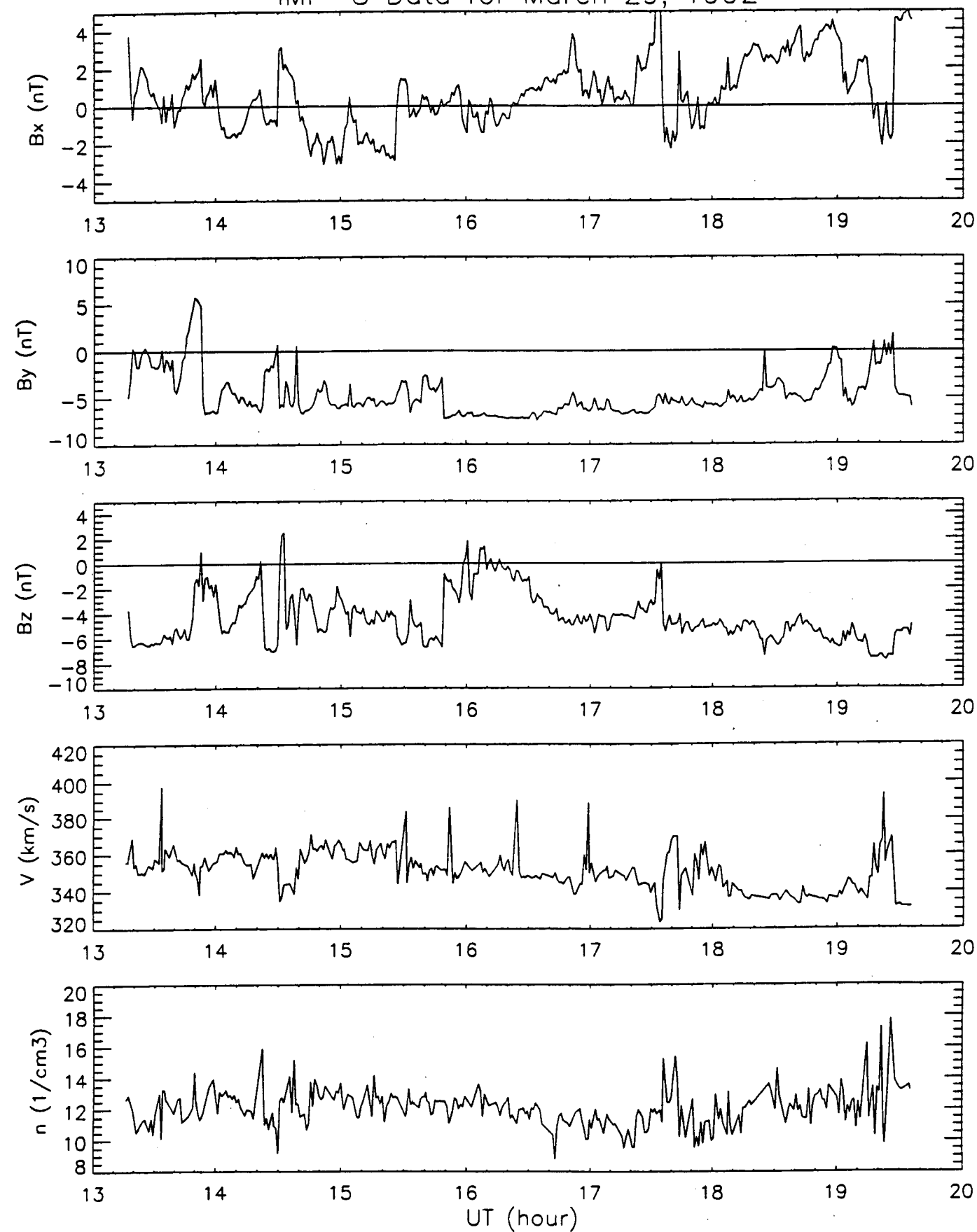
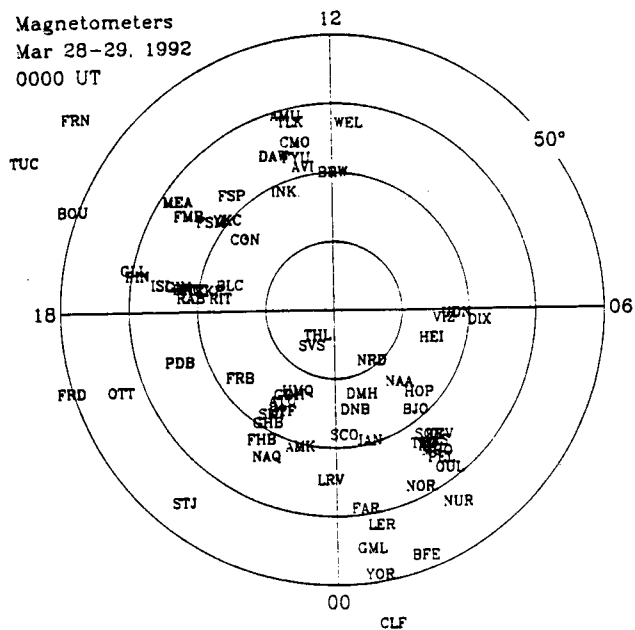


Fig. 1

Magnetometers  
Mar 28-29, 1992  
0000 UT



Magnetometers  
Mar 28-29, 1992  
0000 UT

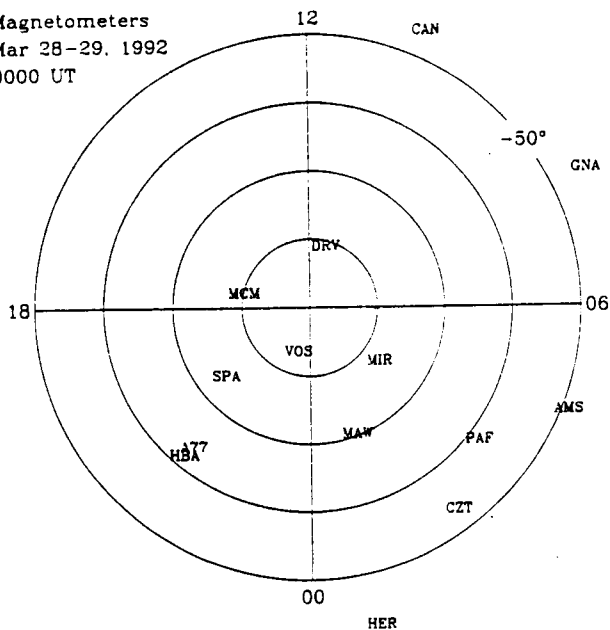


Fig. 2

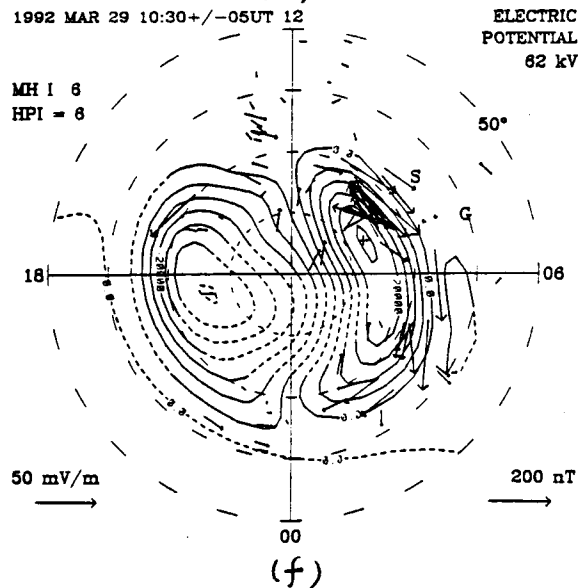
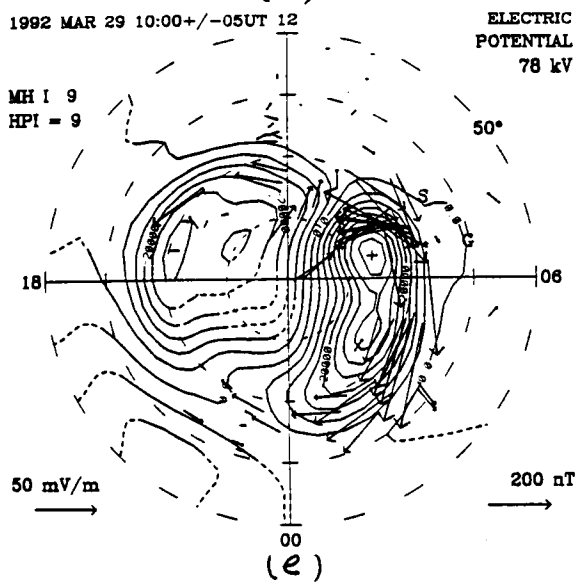
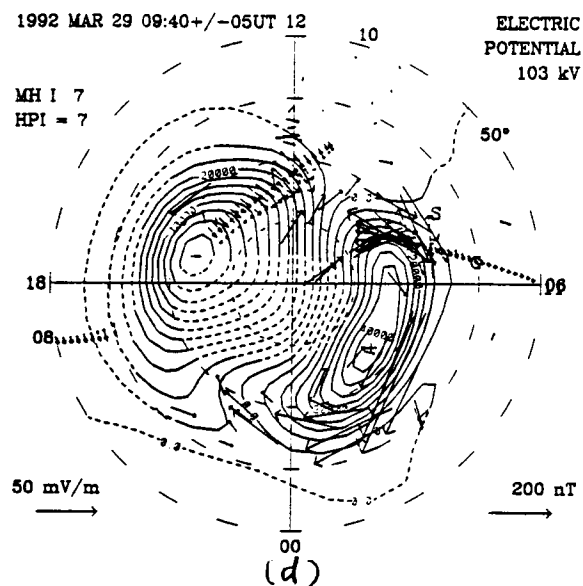
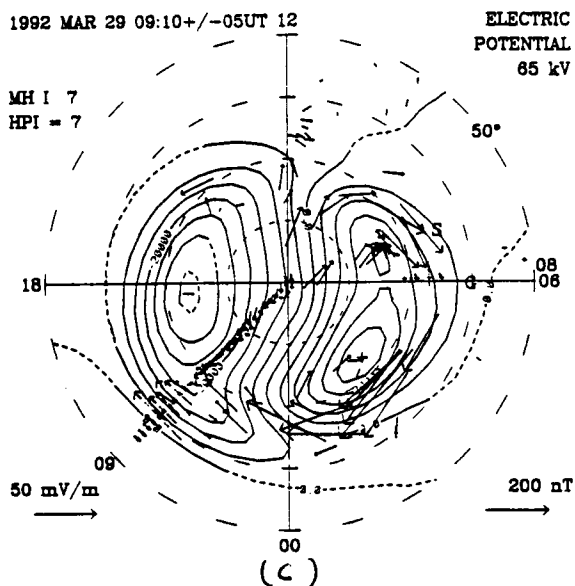
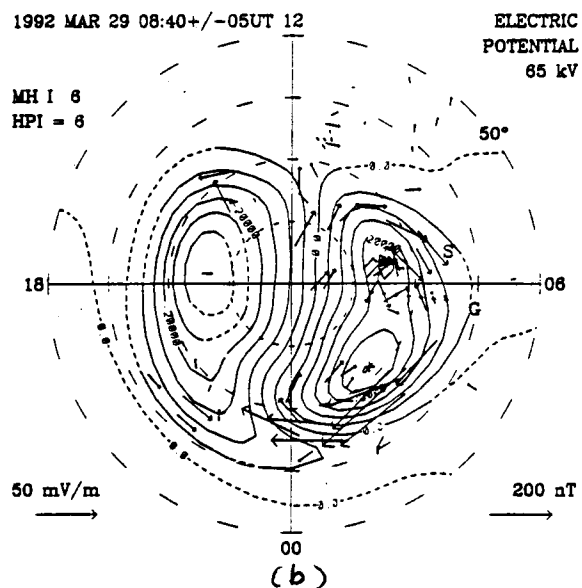
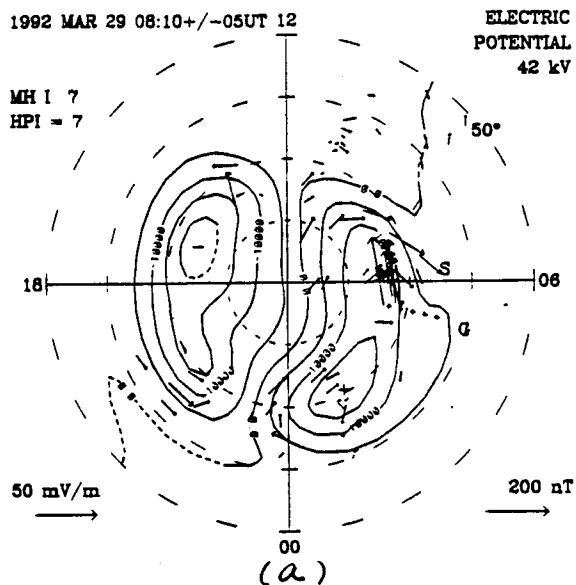


Fig. 3

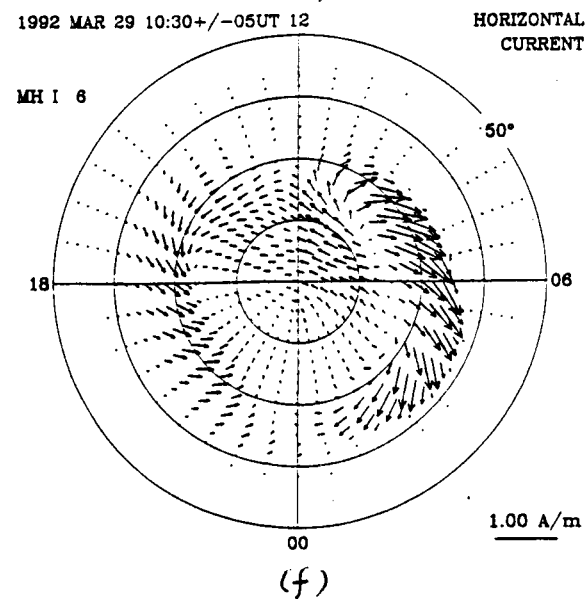
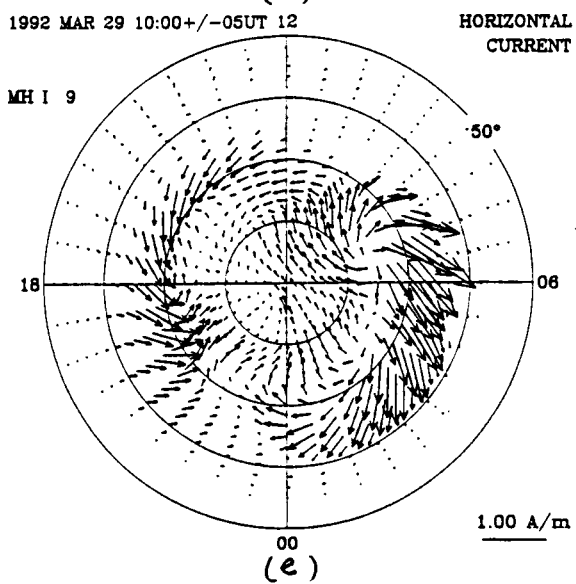
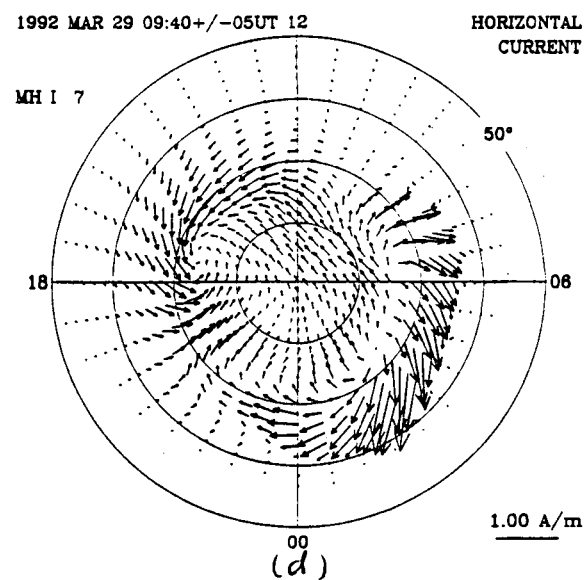
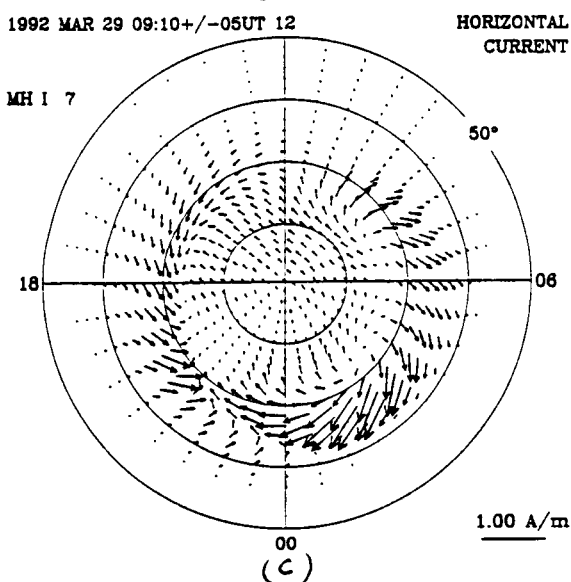
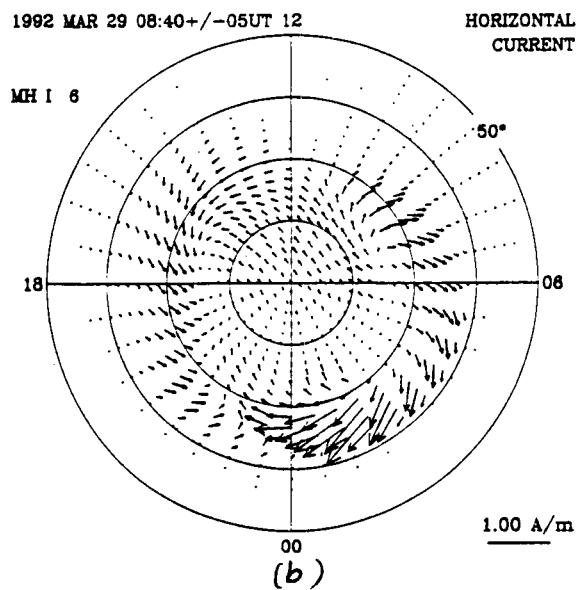
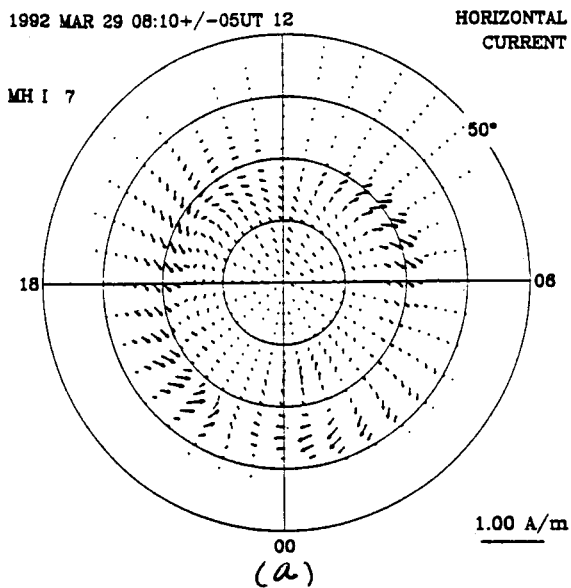


Fig. 4

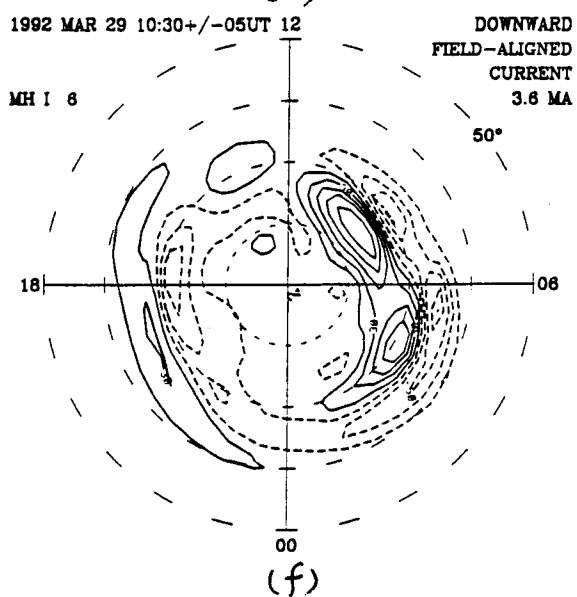
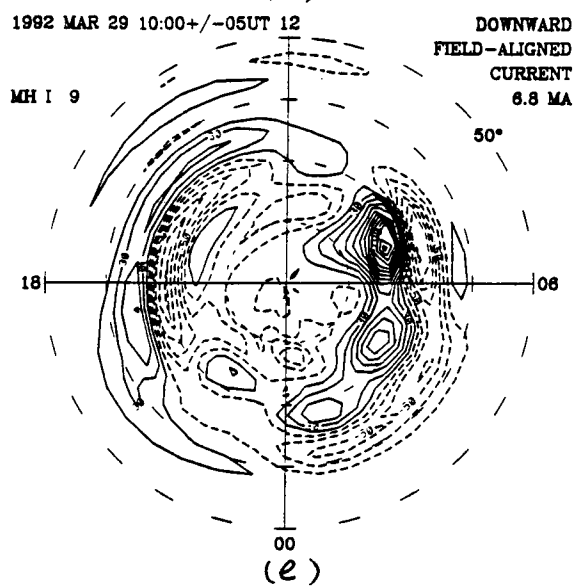
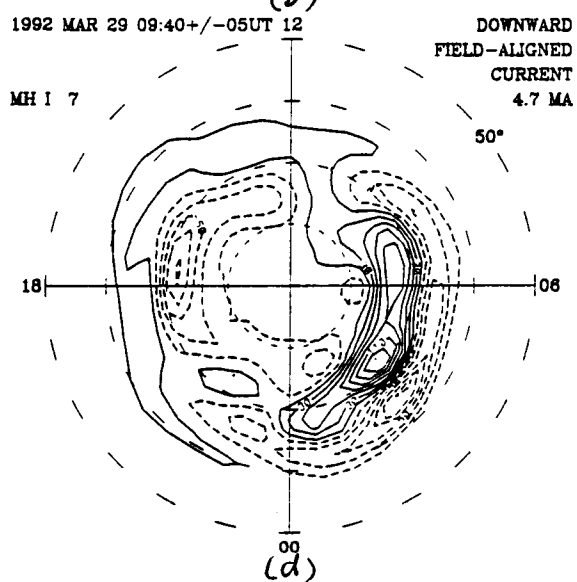
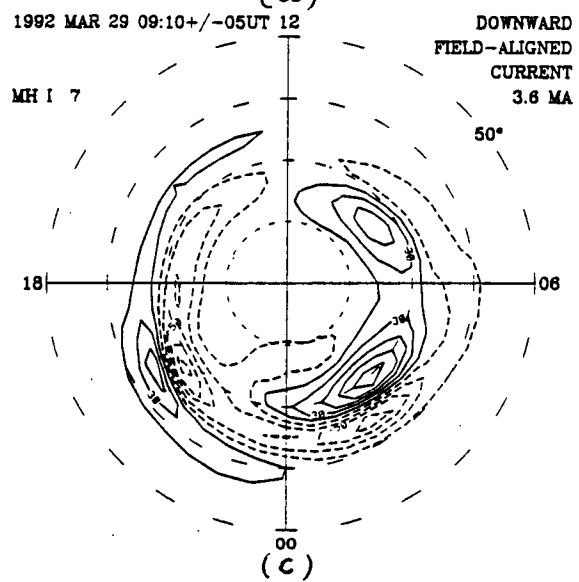
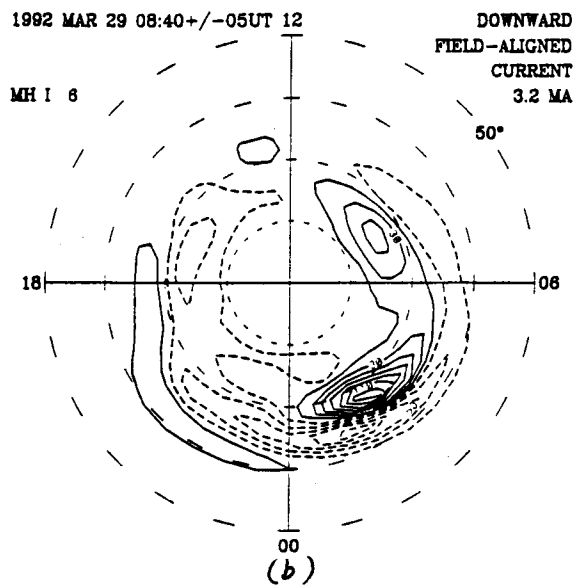
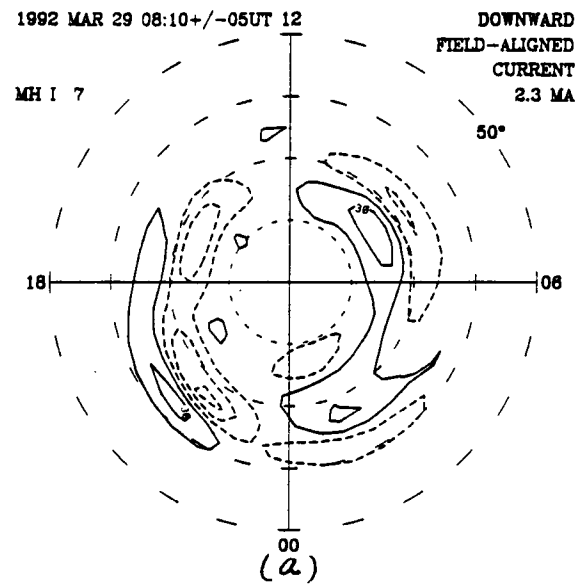
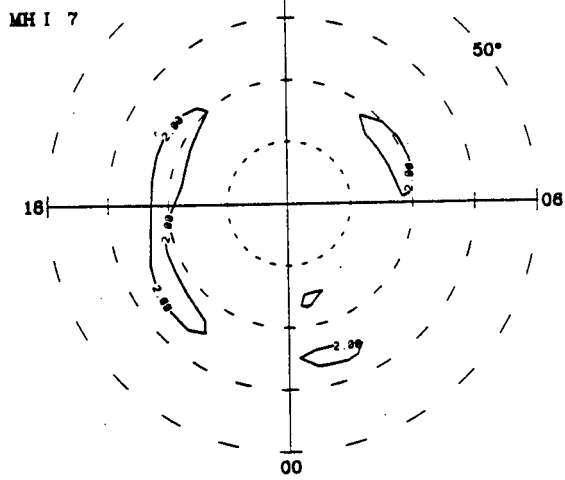


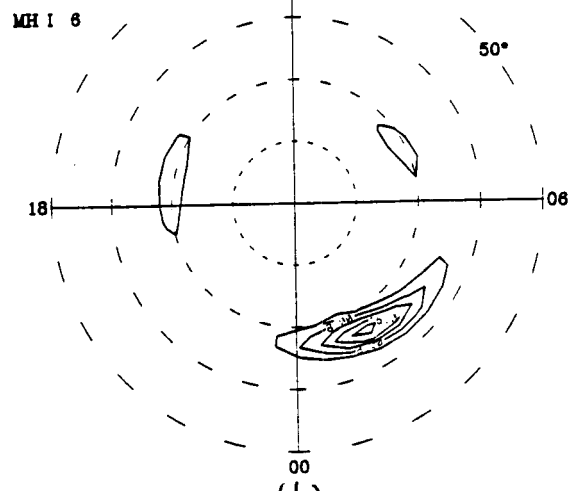
Fig. 5

1992 MAR 29 08:10+/-05UT 12  
CORRECTED JOULE  
HEATING  
27.1 GW



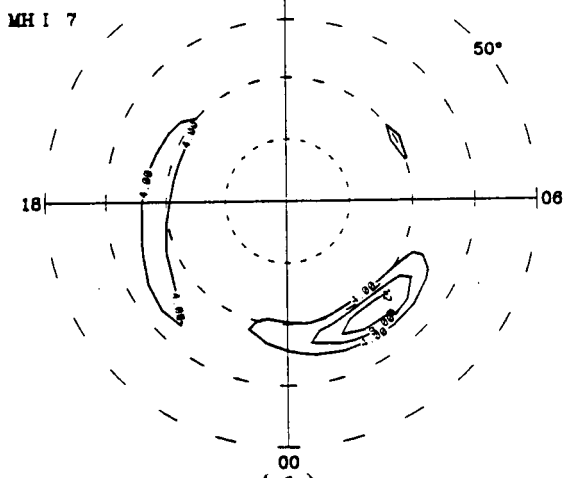
(a)

1992 MAR 29 08:40+/-05UT 12  
CORRECTED JOULE  
HEATING  
67.4 GW



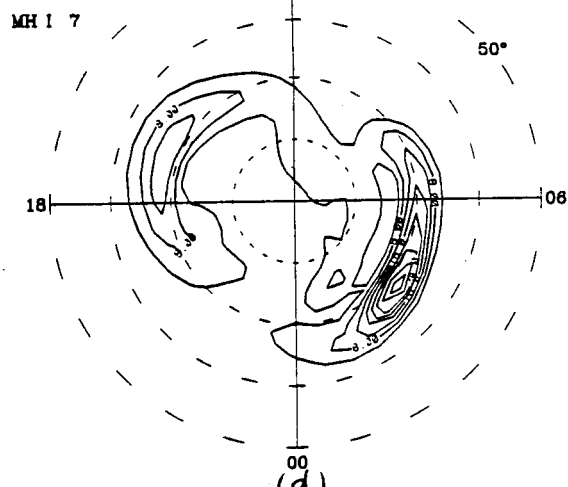
(b)

1992 MAR 29 09:10+/-05UT 12  
CORRECTED JOULE  
HEATING  
67.8 GW



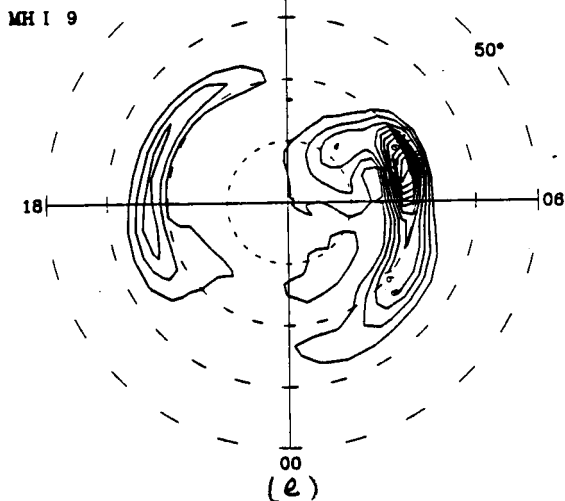
(c)

1992 MAR 29 09:40+/-05UT 12  
CORRECTED JOULE  
HEATING  
156.8 GW



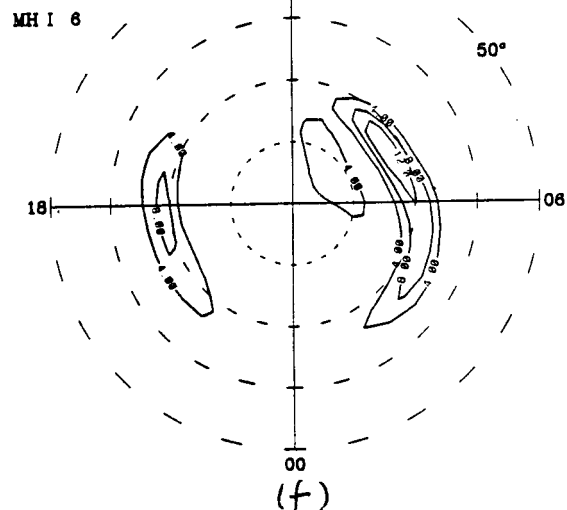
(d)

1992 MAR 29 10:00+/-05UT 12  
CORRECTED JOULE  
HEATING  
158.7 GW



(e)

1992 MAR 29 10:30+/-05UT 12  
CORRECTED JOULE  
HEATING  
82.4 GW



(f)

Fig. 6



March 28–29, 1992

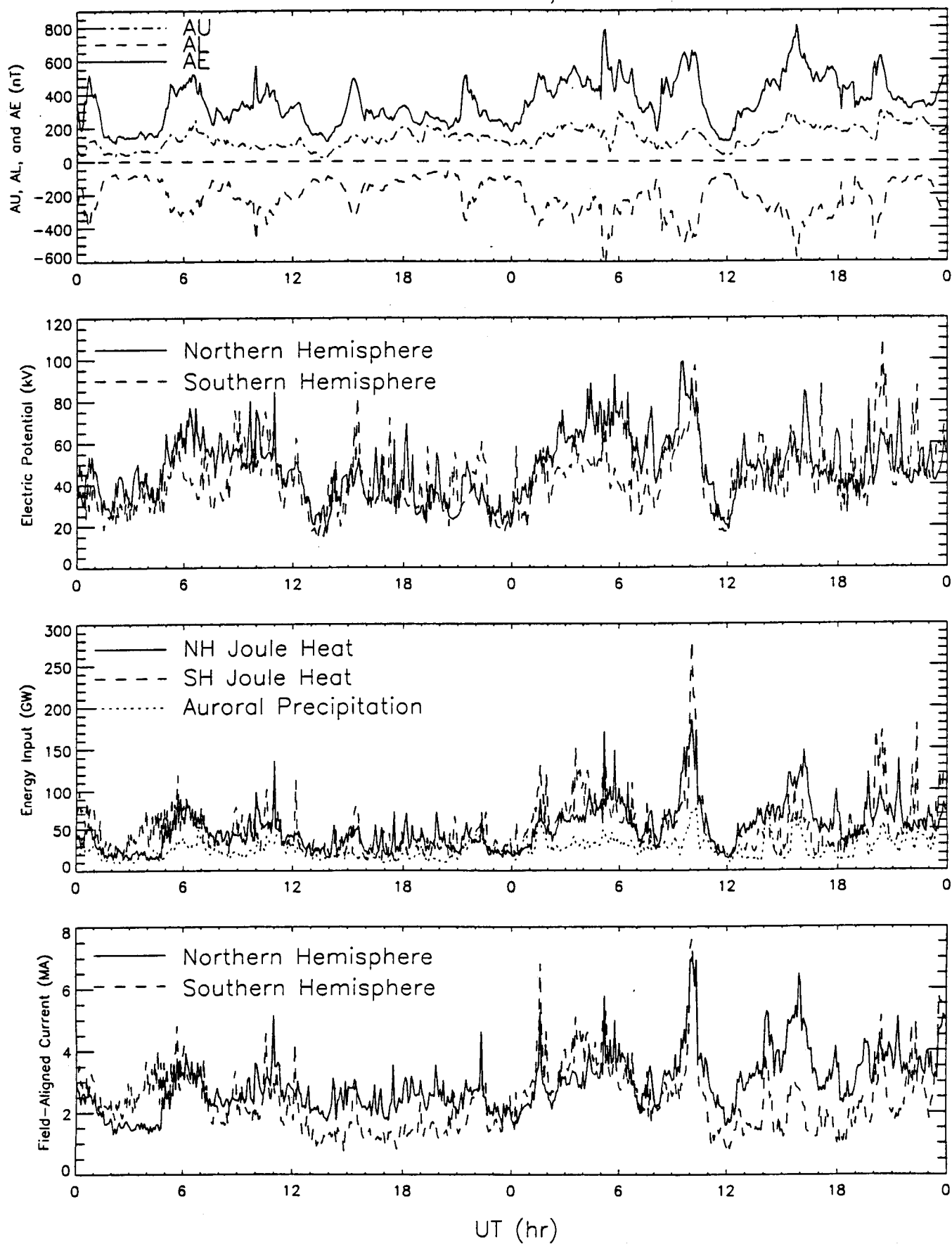
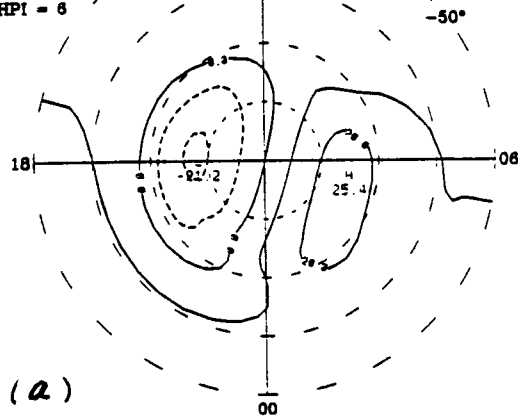


Fig. 7

1992 MAR 29 17:10 UT  
 $B_{xy} = 0.9, -6.0$   
 $B_z = -4.6$   
 $MH I = 6$   
 $HPI = 6$

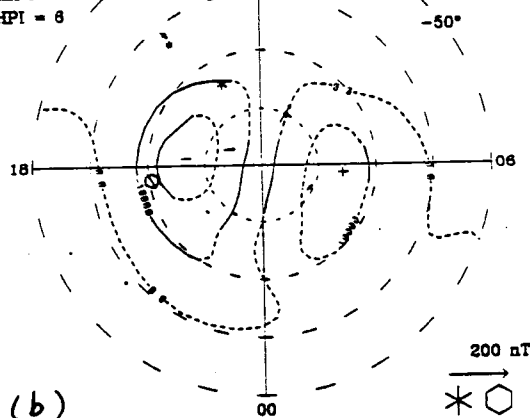
ELECTRIC  
 POTENTIAL



(a)

1992 MAR 29 17:10 UT  
 $B_{xy} = 0.9, -6.0$   
 $B_z = -4.6$   
 $MH I = 6$   
 $HPI = 6$

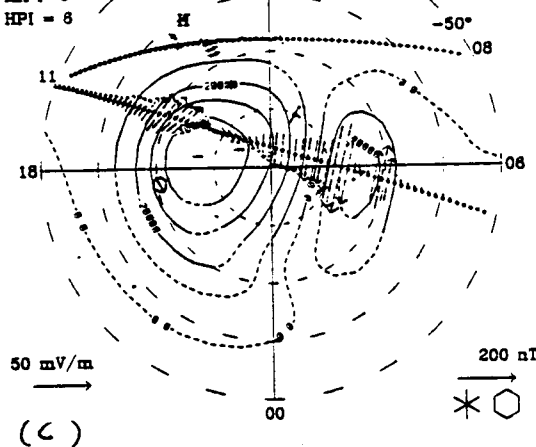
ELECTRIC  
 POTENTIAL  
 43 kV



(b)

1992 MAR 29 17:10 UT  
 $B_{xy} = 0.9, -6.0$   
 $B_z = -4.6$   
 $MH I = 6$   
 $HPI = 6$

ELECTRIC  
 POTENTIAL  
 79 kV



(c)

Fig. 8

March 28–29, 1992

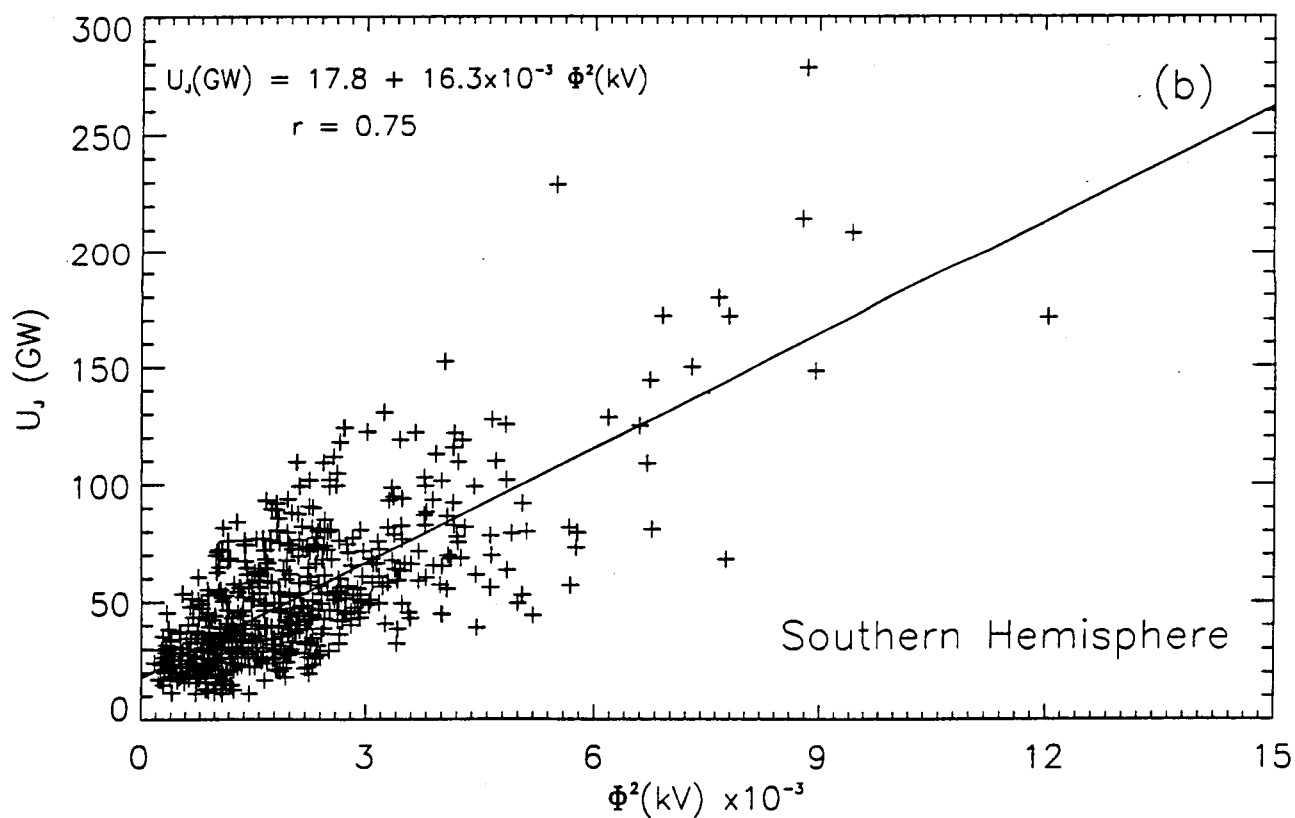
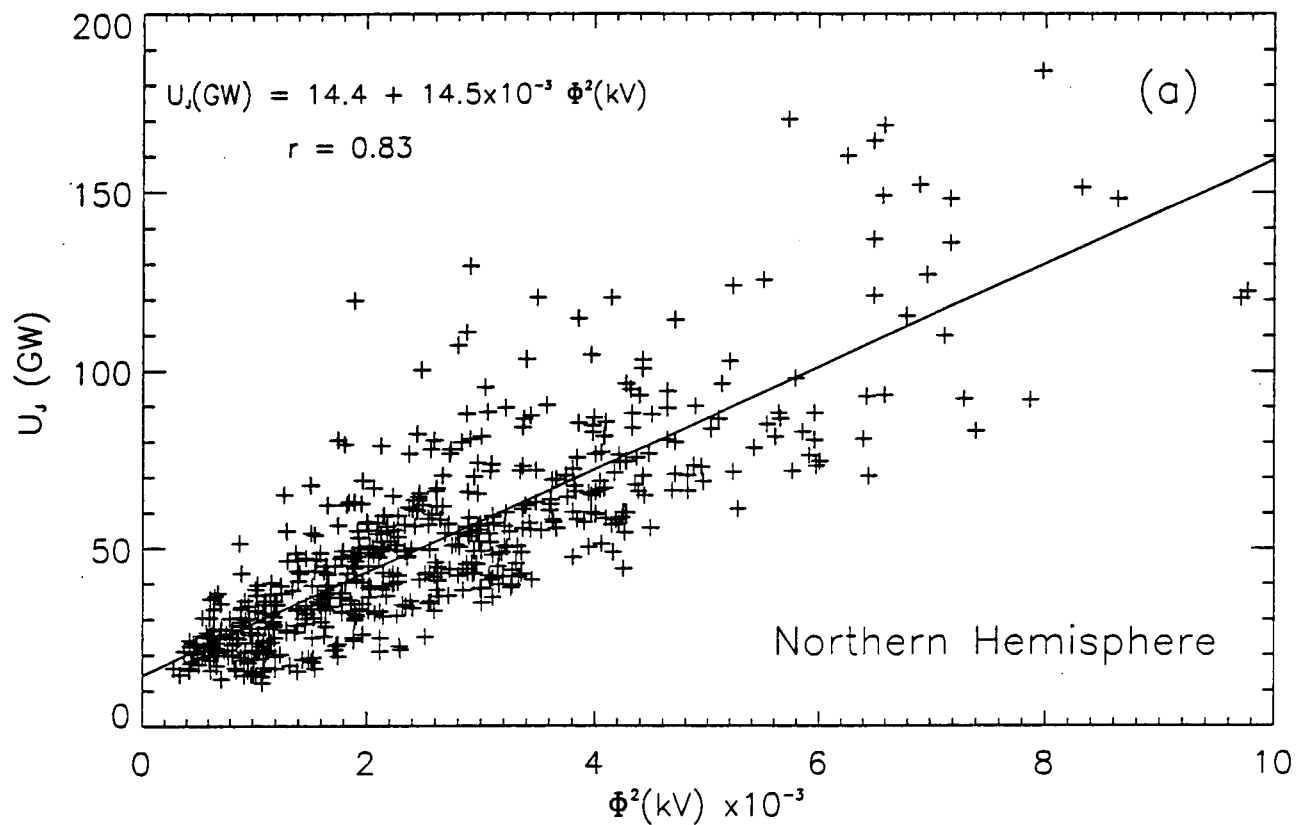
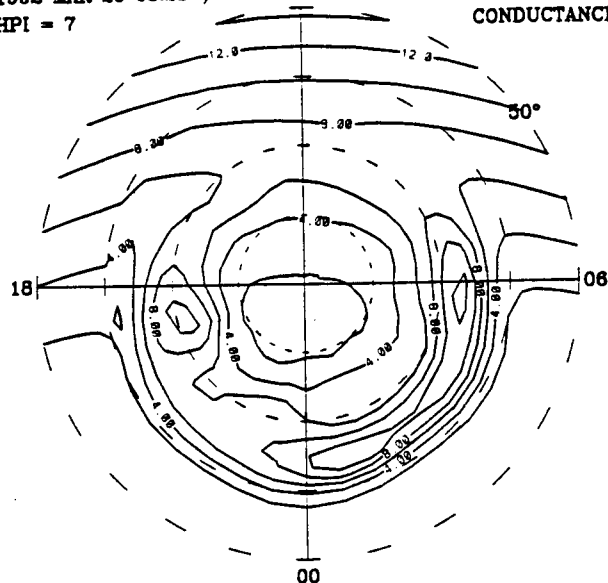


Fig. 9

# Northern Hemisphere

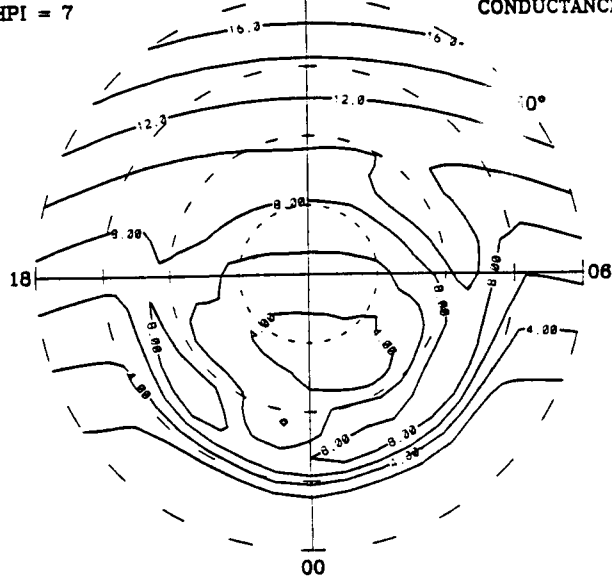
1992 MAR 29 03:25+/-03UT 12  
HPI = 7

PEDERSEN  
CONDUCTANCE



1992 MAR 29 17:30+/-03UT 12  
HPI = 7

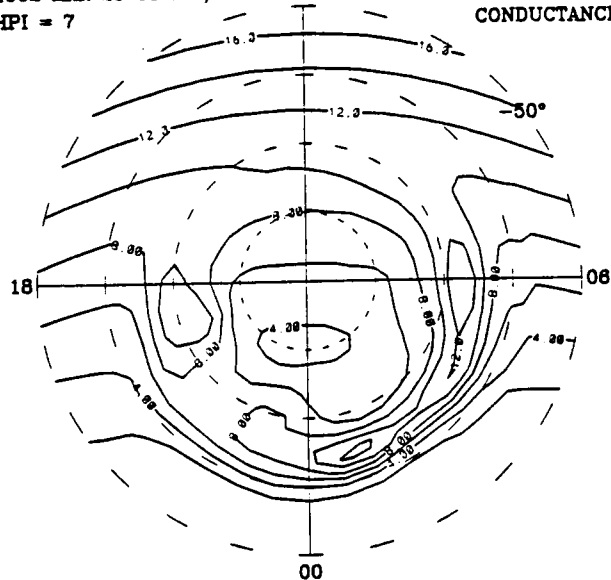
PEDERSEN  
CONDUCTANCE



# Southern Hemisphere

1992 MAR 29 03:25+/-03UT 12  
HPI = 7

PEDERSEN  
CONDUCTANCE



1992 MAR 29 17:30+/-03UT 12  
HPI = 7

PEDERSEN  
CONDUCTANCE

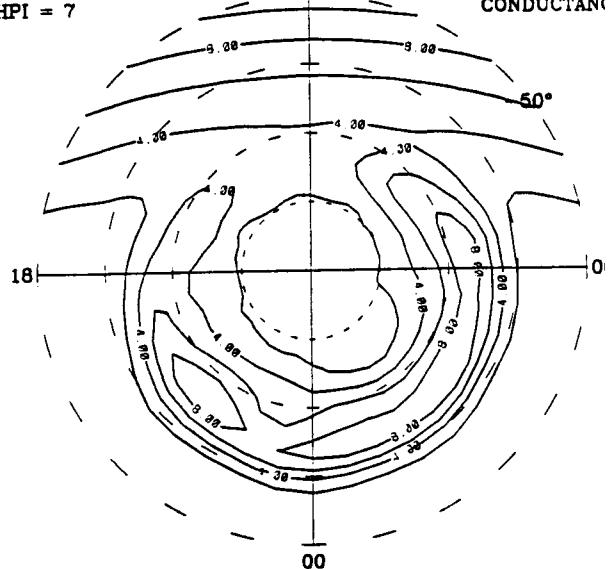


Fig. 10

# Nothern Hemisphere

# Southern Hemisphere

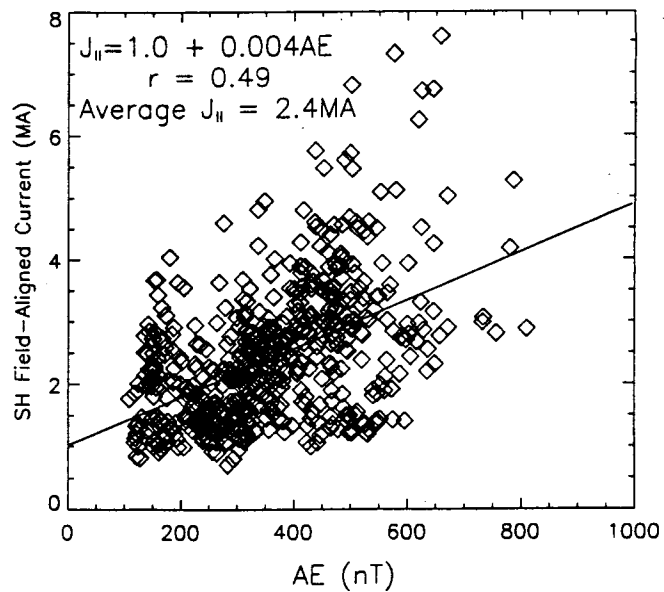
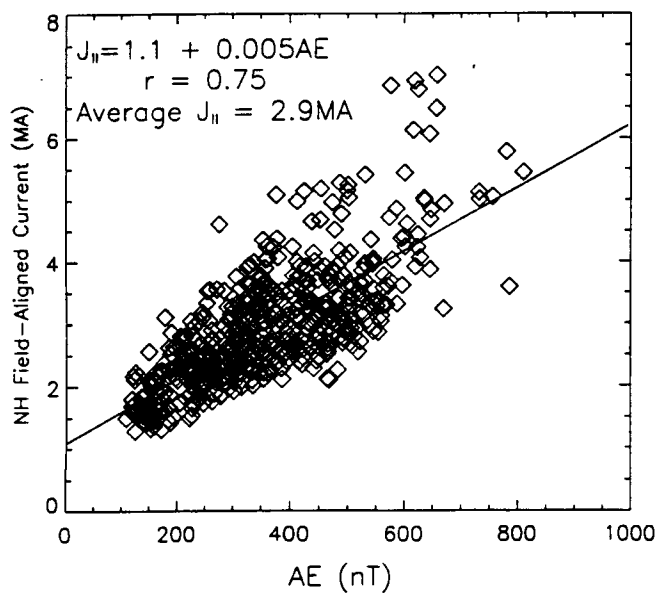
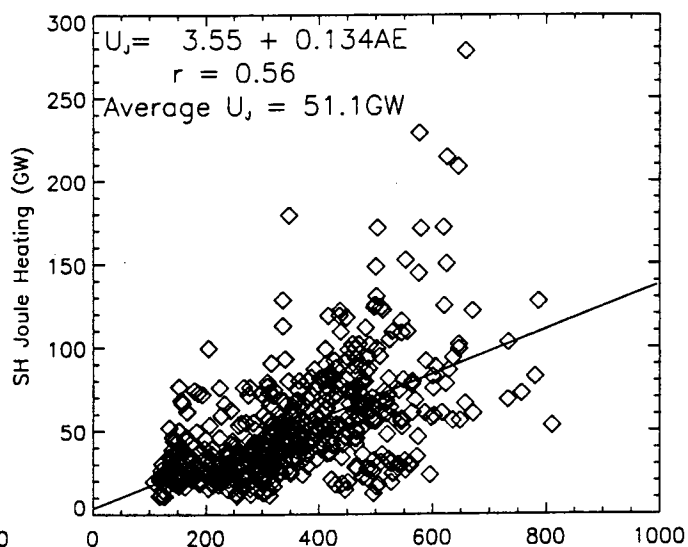
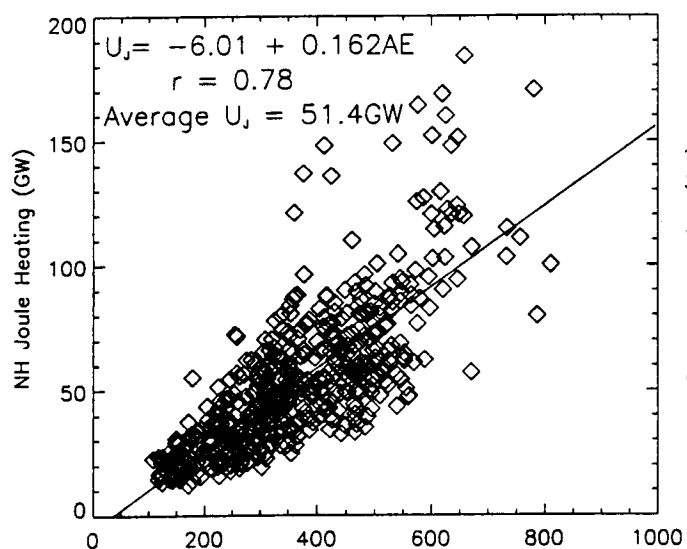
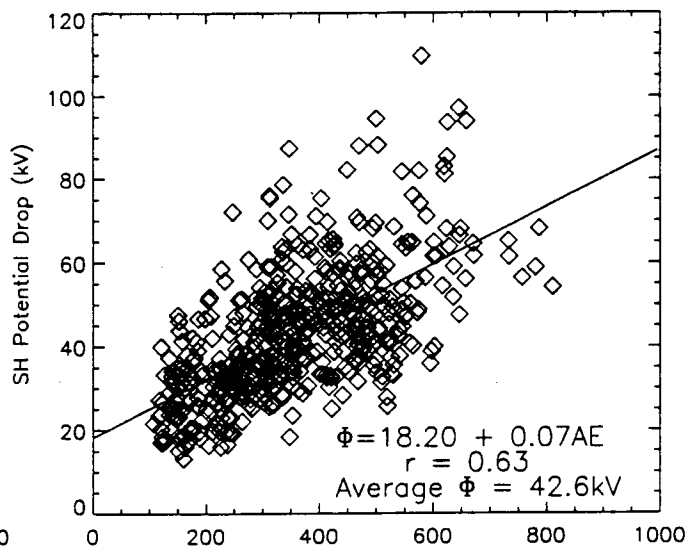
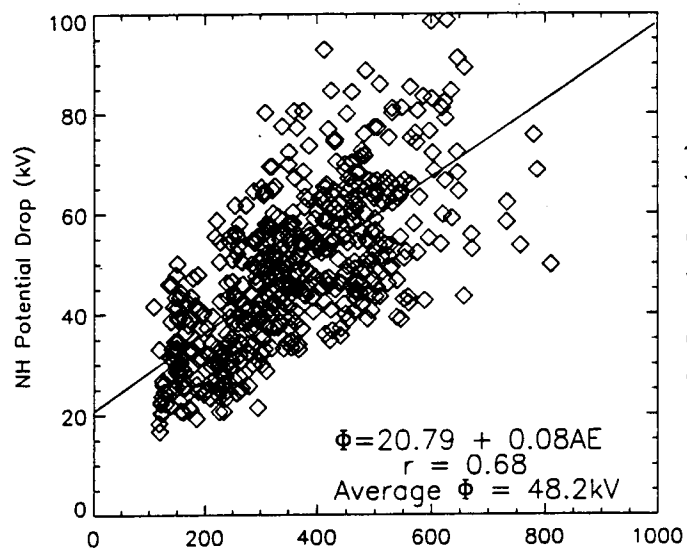


Fig. 11

March 28–29, 1992

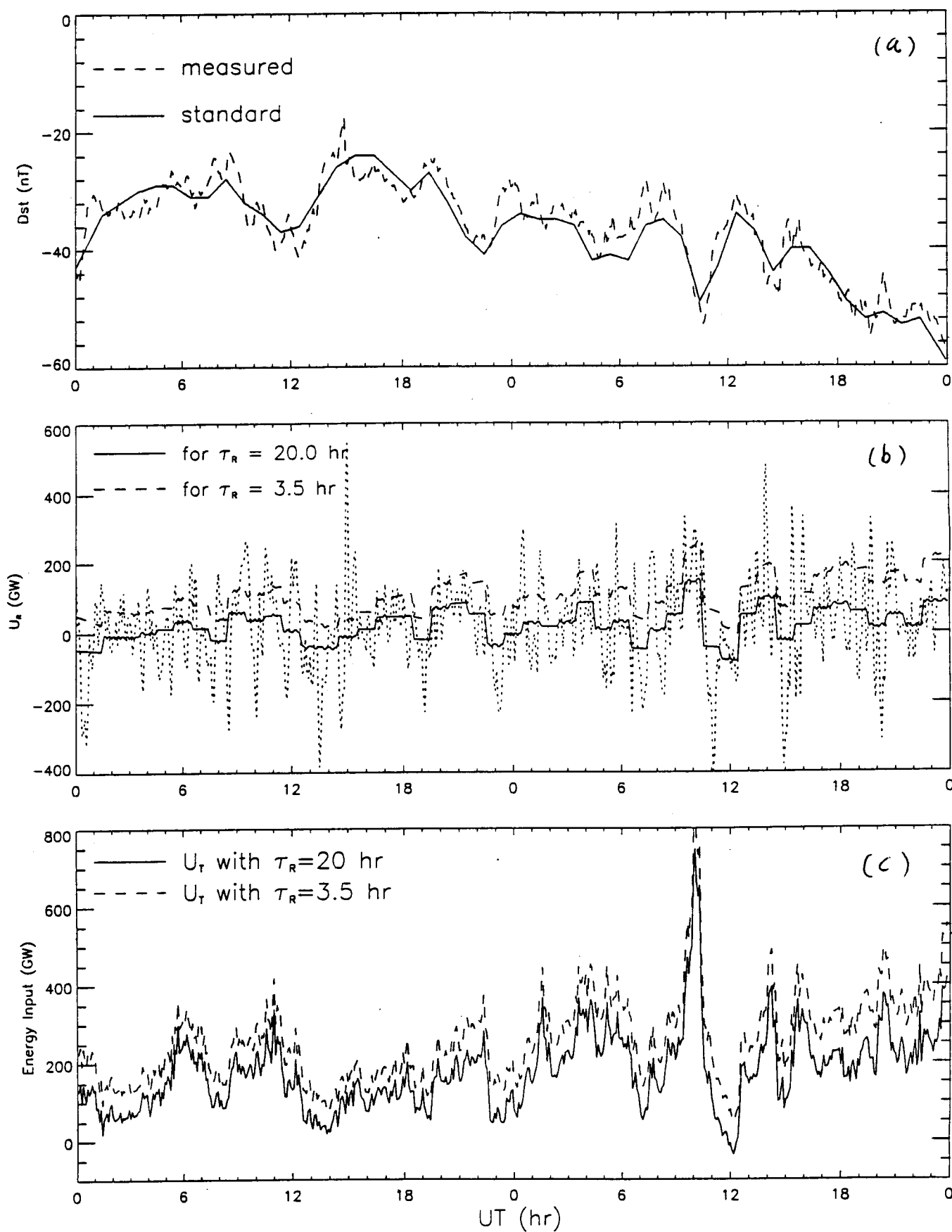


Fig. 12

March 29, 1992

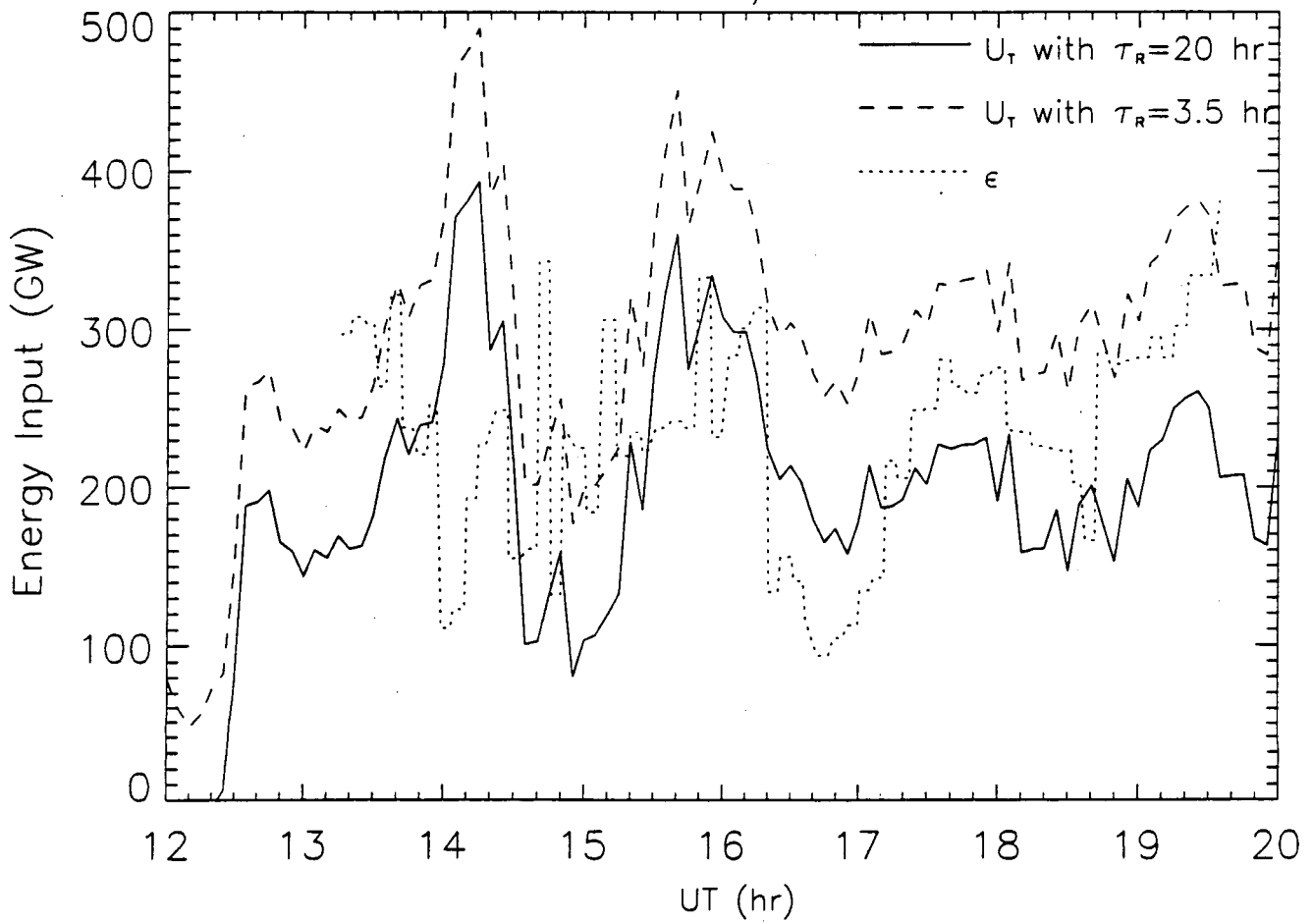
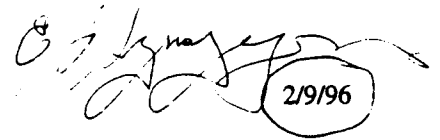


Fig. 13

**AMIE-TIGCM Comparisons with Global Ionospheric and  
Thermospheric Observations During the  
GEM/SUNDIAL/ATLAS-1 Period of 28-29 March 1992**

B.A. Emery, G. Lu, E.P. Szuszczewicz, A.D. Richmond, R.G. Roble,  
P.G. Richards, K.L. Miller, R. Niciejewski, D.S. Evans, F.J. Rich, W.F. Denig,  
D.L. Chenette, P. Wilkinson, S. Pulinets, K.F.O'Loughlin, R. Hanbaba, M. Abdu,  
P. Jio, K. Igarashi, and B.M. Reddy



 2/9/96

# AMIE-TIGCM Comparisons with Global Ionospheric and Thermospheric Observations During the GEM/SUNDIAL/ATLAS-1 Period of 28-29 March 1992

B. A. Emery<sup>1</sup>, G. Lu<sup>1</sup>, E. P. Szuszczewicz<sup>2</sup>, A. D. Richmond<sup>1</sup>, R. G. Roble<sup>1</sup>, P. G. Richards<sup>3</sup>, K. L. Miller<sup>4</sup>, R. Niciejewski<sup>5</sup>, D. S. Evans<sup>6</sup>, F. J. Rich<sup>7</sup>, W. F. Denig<sup>7</sup>, D. L. Chenette<sup>8</sup>, P. Wilkinson<sup>9</sup>, S. Pulinets<sup>10</sup>, K. F. O'Loughlin<sup>11</sup>, R. Hanbaba<sup>12</sup>, M. Abdu<sup>13</sup>, P. Jiao<sup>14</sup>, K. Igarashi<sup>15</sup> and B. M. Reddy<sup>16</sup>

<sup>1</sup>High Altitude Observatory, National Center for Atmospheric Research\*, Boulder, Colorado

<sup>2</sup>Science Applications International Corporation, McLean, Virginia

<sup>3</sup>University of Alabama, Huntsville, Alabama

<sup>4</sup>Utah State University, Logan, Utah

<sup>5</sup>University of Michigan, Ann Arbor, Michigan

<sup>6</sup>Space Environment Center, National Oceanic and Atmospheric Administration, Boulder, Colorado

<sup>7</sup>Geophysics Directorate, Phillips Laboratory, Hanscom Air Force Base, Massachusetts

<sup>8</sup>Lockheed Palo Alto Research Laboratory, Palo Alto, California

<sup>9</sup>IPS Radio and Space Services, West Chatswood, Australia

<sup>10</sup>IZMIRAN, Moscow, Russia

<sup>11</sup>National Geophysical Data Center, Boulder, Colorado

<sup>12</sup>CNET, Lannion, France,

<sup>13</sup>Instituto Nacional de Pesquisas Espaciais, Sao Paulo, Brazil

<sup>14</sup>China Research Institute of Radio Propagation, Beijing, China

<sup>15</sup>Communications Research Laboratory, Tokyo, Japan

<sup>16</sup>National Physical Laboratory, New Delhi, India

To be submitted to the Journal of Geophysical Research as part of a special ATLAS-1/SUNDIAL-92 Issue

\*NCAR is sponsored by the National Science Foundation

## Abstract

Satellite and ground-based observations during the solar maximum period of 28-29 March 1992 were combined in the Assimilative Mapping of Ionospheric Electrodynamics (AMIE) procedure to derive realistic global distributions of the auroral precipitation and ionospheric convection. The total hemispheric Joule heating rate was found to be 5-20 GW greater in the hemisphere where the magnetic pole is tilted towards the sun. Comparisons with Fabry-Perot horizontal winds were good, and improved when the emission altitude was lowered in the presence of auroral arcs. Comparisons with ionosonde meridional neutral winds showed the AMIE-TIGCM winds to be a little larger, with peak nighttime equatorward winds occurring 1-2 hours later than the derived observations. There was good agreement with the ionosonde winds and the height of the electron density maximum (hmF2) in the timing of gravity waves launched from high latitude sources. Calculations from the AMIE-TIGCM run suggest that the propagation time of gravity waves to the equator is between 2 and 3 hours. Because Joule heating events are different in each hemisphere, the resulting gravity waves and  $O/N_2$  decreases are different in each hemisphere. Changes in the  $O/N_2$  ratio were strongly correlated with changes in the peak electron density (NmF2) for middle and high latitudes. On a constant pressure surface for a particular latitude, differences in the  $O/N_2$  ratio showed minima about  $75^\circ$  wide in longitude produced by Joule heating events at higher latitudes and more eastward longitudes. The equatorward movement of these minima is about  $10^\circ$  in 4-5 hours, while zonal winds move the minima westward at night. The observed NmF2 longitudinal asymmetries near  $50^\circ$  magnetic latitude were generally reproduced by AMIE-TIGCM on the second day of the simulation. The good daytime NmF2 agreement deteriorated at low and equatorial latitudes where dynamo electric fields are expected to be important. Agreement is also not very good in the polar cap where the daytime NmF2 observations were low compared to the nighttime observations which were unusually high. The AMIE-TIGCM underestimated the electron density after midnight by up to a factor of two in mid-latitudes, while the height of the NmF2 layer was about 40 km lower than the observations at midnight. Field Line Interhemispheric Plasma (FLIP) model runs at 55 N showed that the NmF2 could be doubled at 4 LT by shifting the model winds 2 hours earlier at night and this would also raise the hmF2 up as much as 20 km around midnight. However, the TIGCM  $N_2$  density was found to be approximately a factor of 2 less than MSIS-86 at 300 km, so possible TIGCM increases in  $N_2$  and conse-

quent decreases in the  $O/N_2$  ratio would reduce NmF2 by at least a factor of two. To increase the NmF2 at night, another AMIE-TIGCM run was made with nighttime downward fluxes of  $O^+$  increased between a factor of two and six at the upper boundary around 550 km to levels consistent with incoherent scatter radar observations of the  $O^+$  flux during solar maximum. The resulting NmF2 at night is now between 0 and 20% higher than the observations, thereby eliminating the problem of low nighttime NmF2 calculations.

## Introduction

Many observations were collected during the solar maximum period of 28-29 March 1992 as one of the Geospace Environment Modelling (GEM) observational campaigns. A major goal of the GEM program is to understand the solar/magnetosphere/ionosphere coupling processes well enough so that models can be built for use in space weather applications. This GEM campaign was a part of the 12-day SUNDIAL/Atlas-1 period of 24 March to 4 April. A goal of the SUNDIAL program is to develop a synoptic view of the global ionosphere/thermosphere system using empirical and first principle models and a world-wide database of primarily ionosonde measurements. The mission of ATLAS-1 was to measure the density and temperature distributions of the neutral and ion constituents from the mesosphere to F region heights using remote sensing photometric instruments. High latitude global observations were used as inputs to the AMIE (Assimilative Mapping of Ionospheric Electrodynamics) model to define the ion convection (e.g. Richmond et al., 1988; Knipp et al., 1993). The AMIE technique also includes fitting the height-integrated Hall and Pedersen conductance in order to utilize ground magnetometer data (Richmond and Kamide, 1988). This paper will discuss the expansion of the AMIE fitting procedure to include separate fits for the auroral energy flux and mean energy, which have only been lightly touched upon in the literature (Knipp et al., 1993; Lu et al., 1995). These auroral parameters are essential inputs to the Thermosphere-Ionosphere General Circulation Model (TIGCM). Other global observations in this period will then be compared to the AMIE-TIGCM calculations.

In a companion paper, Lu et al. [1996] describe the high-latitude electrodynamics as determined by the AMIE procedure using data every 5 minutes for 28-29 March 1992. A previous paper (Lu et al., 1995) used a reduced data set in AMIE and put the 5 minute results into the TIGCM. The present paper uses the expanded data set but concentrates on UT times with the

maximum data coverage and averages all data for those periods over  $\pm 17.5$  minutes (or 35 minutes). This results in smoother patterns and less variability on small time scales, much of which is due to intermittent data coverage by satellites. All variability of this nature produces gravity waves in the high latitude regions of the TIGCM that propagate equatorward (e.g. Roble et al., 1987; Fesen et al., 1989; Crowley et al., 1989a). It is thus desirable to eliminate as many spurious gravity wave sources as possible in the TIGCM, especially when gravity waves are part of the study.

The resulting AMIE patterns were in turn averaged in order to provide "climatological" southern and northern hemisphere average patterns that were used to initialize the TIGCM run. The companion paper by Szuszczewicz et al. [1996] used a 24 hour TIGCM run of this climatological average to compare against other models and ionosonde data averaged over the 12-day campaign period. The present study concentrates on the daily variations for March 28-29 only, and compares the daily variability to the averages.

March 28-29, 1992 was in the declining phase of the solar cycle, with 10.7 cm solar fluxes of 185 and 192, respectively. Magnetic activity began on March 21 with a sudden storm commencement followed by a sequence of smaller storms. The only quiet day was April 2, with March 28 being the next quietest period with a daily Ap of 10. March 29 was the third most disturbed day of the period with a daily Ap of 18. Therefore, the 12-day average ionosonde data could be considered to be a disturbed average. Such continual activity makes it difficult to predict ionospheric storm effects.

Following a single isolated storm, the peak electron density NmF2 is reduced in mid-latitudes due to an increase in the  $N_2/O$  ratio (or a decrease in the  $O/N_2$  ratio), while it is usually increased at the magnetic equator due to meridional winds, although electric field effects can have a negative or positive effect (e.g. Prölss, 1995 and references therein). Individual magnetic storms can be either "positive" or "negative" according to whether NmF2 is increased or decreased from mean quiet day values. The negative storm effects caused by decreases in the  $O/N_2$  ratio can lag the storm by nearly a day and are sensitive to the local time at which the main phase of the magnetic storm begins. A study of a 10-day period by Codrescu et al. [1992] showed that the negative effects on NmF2 at  $45^\circ$  magnetic latitude can last at least 6 days after an initial storm. There are positive and negative variations in the disturbed period embedded within the

context of the general negative response. Since our period is shorter and does not cover the beginning of the magnetic activity, we will only be looking at these relative positive and negative variations within the larger context of a disturbed period.

We will compare neutral winds, first with Fabry-Perot measurements, and second with ionosonde hmF2 derived winds, noting evidence of gravity waves. We will look at NmF2 variations from the polar cap to the equator, and concentrate on the higher mid-latitude region where O/N<sub>2</sub> differences can make large changes in the daytime peak electron density. The question of the maintenance of the nighttime density will be examined with another AMIE-TIGCM run with realistic increased downward fluxes of O<sup>+</sup> at the upper boundary at night.

## Specifying the Auroral Inputs

The auroral inputs of the mean Maxwellian energy and the energy flux of precipitating electrons are necessary components to the TIGCM. They are normally parameterized in a circular aurora as described by Roble and Ridley [1987], where the characteristics of this simple oval are defined by the Hemispheric Power Index [Fuller-Rowell and Evans, 1987]. However, it is better to include a more realistic pattern of the auroral inputs from the AMIE results for campaign studies.

The first attempt to use AMIE inputs into the TIGCM was described in Crowley et al. [1989a], where patterns of the electric potential were put in, but the aurora was still based on the simple parameterization of Roble and Ridley [1987] modified by the available electron precipitation data. The present AMIE procedure now solves the auroral energy flux and mean electron energy explicitly. The AMIE data-fitting algorithms we use for energy flux and mean energy are entirely analogous to those described by Richmond and Kamide [1988] for fitting conductance observations. That is, for both the flux and the mean energy we determine a modifying function needed to multiply an empirical model in order to make the empirical model agree more closely with actual point observations. The modifying function is obtained by performing an optimal linear estimation fit to logarithms of ratios of observations to empirical model values, using constraints to obtain a smooth fit consistent with general properties of observed electron precipitation. The empirical energy flux model is that of Fuller-Rowell and Evans [1987], parameterized by the 10-level Hemispheric Power Index. The empirical mean energy model is obtained

from the Hall-to-Pedersen ratio of the Fuller-Rowell and Evans [1987] auroral conductance models, by finding a Maxwellian distribution that produces the same ratio [Fuller-Rowell, private communication]. The initial estimates of the Hemispheric Power Index are taken in this study from estimates of the hemispheric power in GW provided by four Defense Meteorological Satellite Program (DMSP) satellites: F08, F09, F10, and F11.

The conductance sources for this period [see Lu et al., 1996] came from electron precipitation measurements from four DMSP satellites and NOAA-12, plus X-ray measurements from the Upper Atmospheric Research Satellite (UARS). Ground magnetometer stations in auroral regions also contribute to conductance estimates (Ahn et al., 1983) which contain both auroral and solar ultraviolet (UV) influences. If the model UV component is less than the model auroral component, the solar UV component is subtracted from the observation, and the inverse of the formulas in Robinson et al. [1987] are used to convert the remaining Hall and Pedersen auroral conductance to auroral electron energy flux and mean energy.

The satellite observations are more direct observations of the auroral energy flux and electron mean energy. The Maxwellian energy and energy flux of precipitating electrons are extracted from the X-ray spectrum for energies above about 3 keV [Chenette et al., 1993]. For NOAA-12, auroral energy fluxes are integrated over the instrument span of 300 eV to 20 keV [Fuller-Rowell and Evans, 1987], while for DMSP, these are integrated over 460 eV to 30 keV [Rich et al., 1987]. The mean electron energy is the simple ratio of the energy flux over the number flux in this energy range for DMSP satellites, and this distribution function is assumed to be Maxwellian. The characteristic energy from the NOAA satellite is related to a particular Hall-to-Pedersen ratio, which in turn is assigned to a Maxwellian distribution that produces the same peak ionization.

Conjugacy is usually assumed for fitting the auroral parameters or conductance since this is a fairly good assumption for large-scale features of the aurora (e.g. Mizera and Evans, 1986). However, the error bar in the conjugate hemisphere is increased by 50%. Figure 1 illustrates the procedure for the northern hemisphere for 0755 UT on March 28, 1992. The hemispheric power determined from the DMSP-F09 and F08 passes centered at 0747 and 0800 UT are 34.6 and 23.9 GW, respectively, leading to an average of 28 GW at 0755, which corresponds to a Hemispheric Power Index of 7. Figure 1a shows the statistical model distribution of energy flux obtained from Fuller-Rowell and Evans [1987] for this level of auroral precipitation. The hemispheric integration of this flux is 28 GW, which is coincidentally the same hemispheric power as the original

estimate. Figure 1d is the mean Maxwellian energy derived from the conductance ratio at level 7. Figures 1b and 1e show the observations, where the mean energies are only plotted if the associated energy flux is greater than 0.3 mW/m. The orbits for NOAA and DMSP are marked, while the UARS track samples between 0100 and 0800 LT and between 60 and 70 degrees. The dashed lines on the F10 orbit indicate that it was in the southern hemisphere at the time. Figures 1c and 1f show the AMIE-fitted distributions, where the average hemispheric power estimated from the energy flux in Figure 1c is 31 GW. The estimated patterns derived in Figures 1c and 1f clearly reflect the influence of the data and are different from the initial statistical patterns of Figures 1a and 1d.

## Putting AMIE Outputs into the TIGCM

The original NCAR Thermosphere General Circulation Model (TGCM) described by Dickinson et al. [1981, 1984] calculates the thermospheric neutral dynamics, temperature and composition. This model has been used extensively in data comparisons (e.g. Hernandez and Roble, 1976; Forbes et al., 1987; Crowley et al., 1989b; Fesen et al., 1986). The TGCM was also used by Fesen et al. [1989] along with an equatorial model of the ionosphere to show that most of the storm time variations in the equatorial anomaly could be explained by the neutral winds that exhibited waves that propagated from high latitudes to the equator. The TIGCM is an extension of the TGCM that self-consistently solves for the ionospheric composition and temperatures (Roble et al., 1988). The updated metastable chemistry is described by Roble [1995]. Comparisons of the TIGCM have been used to study descending ionization layers (Wilkinson et al., 1992), and O/N<sub>2</sub> ratios related to magnetic storms (Burns et al., 1995a and 1995b). Codrescu et al. [1992] used the TIGCM along with northern hemisphere ionosondes between 15 and 50 degrees magnetic latitude near 130 E geographic longitude to look at relative differences during a solar maximum storm period in March 1979. The relative changes in the height and peak electron density following the initial storm on March 22 were in fairly good agreement at 45° magnetic latitude, but the agreement degraded further equatorward. However, in conjunction with the companion paper of Szuszczewicz et al. (1996), the present study is the first attempt to make direct, rather than relative, comparisons with ionosonde data using the TIGCM.

The required inputs for the TIGCM are specified semi-diurnal tides at the bottom bound-

ary,  $O^+$  fluxes at the top boundary (near 550 km for this period), solar EUV and UV fluxes, electric fields, and the auroral electron precipitation flux and Maxwellian energy. The mid- and low-latitude electric fields are specified by the empirical model of Richmond et al. [1980], while the high-latitude electric fields and the auroral parameters are specified in this study with the AMIE outputs. The time-averaged AMIE patterns over March 28-29 were used in the Szuszczyk et al. [1996] study. The present study uses the output of that simulation at 24 UT as the initial conditions for our simulation with time-varying AMIE inputs. Because the averages are similar to the conditions at 0 UT on March 28, the transition from the initial state to the campaign period is relatively smooth.

The two day period of March 28-29, 1992 was simulated in the TIGCM using 66 northern hemisphere and 53 southern hemisphere AMIE patterns of auroral energy flux, mean electron energy, and electric potential (i.e. convection). Figure 2 shows the hemispheric power estimated from the auroral energy flux fits as described in the previous section along with the AMIE polar cap potential drops. These curves roughly track the outer envelop of values shown in Figures 7b and c of the companion paper of Lu et al. [1996]. The time-averaged AMIE used as the initialization period are shown as straight lines on day 27 and do not represent the real conditions for this day. The average pattern of precipitating electron flux is similar to the statistical model plotted in Figure 1a, except for less flux near midnight as shown in Figure 1c. The time-averaged mean energy was also similar to the statistical model plotted in Figure 1d, apart from lower energies of about 3.5 keV in the pre-midnight sector compared to the model. The average hemisphere power on day 27 is about 31-33 GW, which is about the same as the average over March 28-29.

The time-averaged convection pattern in the southern hemisphere for day 27 exhibited a large, round negative electric potential cell in the evening with a small crescent-shaped dayside positive potential cell consistent with a negative IMF  $B_y$  such as was measured during the period of available IMF on March 29 (Lu et al., 1996). In the northern hemisphere, the two cells were more symmetric. The polar cap potential drop of the averaged patterns was 46 kV in both hemispheres. This is less than the daily potential drop averages of about 50 kV on March 28 and 70 kV on March 29, since averaging different convection patterns has the effect of smoothing them and reducing the extrema. As a comparison, the polar cap potential drop determined from the hourly IMF and solar wind velocity according to the formula of Reiff and Luhmann [1986] is plotted as a dotted line in Figure 2b between 13 and 20 UT on March 29. The IMF is not avail-



able at other times, so the polar cap potential drop is estimated from Kp (Reiff et al., 1981; Reiff, private communication) which varies between 2 and 4- over the two days. In the absence of AMIE inputs, this is the potential drop that would be used in the TIGCM along with the IMF  $B_y$  to specify convection parameters from Heelis et al. [1982]. However, as can be seen in Figure 2b, the temporal variations of the potential drop are quite different from the AMIE results even during the period of available IMF. This has profound consequences for the timing and location of Joule heating events since the Joule heating hemispheric averages calculated in the TIGCM and plotted in Figure 2c generally follow the polar cap potential drops in Figure 2b.

The cross-tail potential drop for the time-averaged convection in Figure 2b for day 27 is nearly identical for both hemispheres, but in Figure 2c, it is apparent that the TIGCM Joule heating rate is up to 10 GW larger in the southern hemisphere between 19 and 5 UT and up to 5 GW larger in the northern hemisphere between 6 and 18 UT. A TIGCM run made with the parameterized IMF and Kp potential drop shown in Figure 2b for March 28-29 showed similar results, with up to 15-20 GW larger Joule heating rates in one or the other hemisphere, with the largest differences at times of the largest potential drops on March 29. The north magnetic pole is tilted toward the sun around 16 UT, thus increasing the area of the convection exposed to sunlight. This UT difference is similar to the same finding by Lu et al. [1996] using the Joule heating estimates from AMIE with no neutral winds. A previous study by Lu et al. [1995] showed that the effect of adding the neutral winds for this period in the TIGCM results in a reduction of the Joule heating by an average of 28%. The UT effect is not as apparent in the AMIE-TIGCM Joule heat averages in Figure 2c for March 28-29 since the electric field differences are larger. However, at 1705 UT on March 29, the southern hemisphere potential drop is approximately the same as the northern hemisphere potential drop, but the Joule heating is greater in the northern hemisphere because the magnetic pole is tilted towards the sun.

## **Data/Model Comparisons with Fabry-Perot Observations**

There have been many previous comparisons of Fabry-Perot Interferometer (FPI) measurements of nighttime neutral winds and temperatures using the 630 nm emission of atomic oxygen with the TGCM and TIGCM (e.g. Hernandez and Roble, 1976, 1995). The nominal height of the emission layer is 250 km, but it can be lower in the presence of aurora. Figure 3 shows the

observations and comparisons with both model runs for Watson Lake (60.1N, 231.4E) which is located at a magnetic latitude of  $64^\circ$ . Inspection of the AMIE plots of the auroral electron energy flux show that Watson Lake is generally in or close to the equatorward part of the fitted auroral oval all night.

The brightness measurements plotted in Figure 3a were in relative units and so have been multiplied by 30 to be approximately the same as the AMIE-TIGCM pre-dawn levels in Rayleighs. These observations show enhancements at 10 UT on the 28th, and between 4-5 UT and 8-10 UT on the 29th. The AMIE-TIGCM run shows modest increases in brightness especially between 8 and 10 UT on the 29th. The AMIE model has a relatively coarse grid of 1.7 degrees in magnetic latitude by 10 degrees in magnetic longitude, while the TIGCM grid is 5 degrees in geographic latitude and 5 degrees in geographic longitude. Neither model can be expected to reproduce small scale local auroral features such as may be involved here, although the increased calculated brightness indicates that Watson Lake was fairly close to the auroral oval in the TIGCM simulation.

The increased brightness observations in Figure 3a correlate with decreases in the neutral temperature shown in Figure 3b, and are a reflection of nearby auroral emissions which come from lower altitudes than do the airglow emissions. The TIGCM temperatures are "Doppler" temperatures that are averages based on the calculated emission as a function of height (Hernandez and Roble, 1995), but they are close to the temperatures at 250 km. The observations show decreases of about 300 K in the regions of enhanced brightness. The average observed temperature in the enhanced brightness regions is about 800 K, compared to values about 1100 K before and afterwards. A nighttime temperature of 800 K above Watson Lake in the AMIE-TIGCM corresponds roughly to a height of 160 km. The peak altitude of 630 nm emission is 170 km for a Maxwellian spectra with mean electron energy of 4 keV (Rees and Roble, 1986). The peak mean electron energy from the average AMIE fit is nearly 4 keV near midnight around  $70^\circ$  magnetic latitude.

Figure 3c shows the vertical wind observations against the AMIE-TIGCM calculations. The observations are much larger than the model at all times because the global grid scale of the TIGCM does not allow large divergences and convergences in the horizontal winds to develop. However, large vertical winds are a common feature of FPI observations (e.g. Sipler et al., 1995;

Price et al., 1995; Smith and Hernandez, 1995). The vertical velocity appears to oscillate with a periodicity of about an hour, where upward velocity peaks correspond to mostly minor peaks in the temperature as shown by the dotted vertical lines in Figures 3b and c. This is especially true on March 28 and may be an indication of gravity waves.

The overhead neutral zonal and meridional winds above Watson Lake obtained from the AMIE-TIGCM run are plotted in Figures 3d and e as well as observations at Watson Lake from the look directions to the east and west, and to the north and south, at an elevation angle of 45 degrees. For an emission layer at 250 km, this corresponds to a horizontal distance of 250 km. The goodness of the comparison between the observations and AMIE-TIGCM results can usually be improved by adjusting the emission height at the UTs of the strongest brightness observations in Figure 3a. The revised AMIE-TIGCM velocities are shown as '+'s in Figures 3d and e. The equatorward wind observations peak between 10 and 12 UT (1:26 and 3:26 LT) in Figure 3e while the AMIE-TIGCM equatorward winds peak between 10 and 14 UT.

## **Data/Model Comparisons with Ionosonde Observations**

In the excellent review of ionospheric F-region storms by Prölss (1995), only a few mechanisms are important and explain most storm effects on the electron density. Most midlatitude effects are negative with density losses due to decreases in the  $O/N_2$  ratio on both constant altitude and pressure surfaces. Burns et al. (1995a,b) studied this extensively using the TIGCM and DE-2 satellite data. The decrease is usually due both to increases in  $N_2$  which increases the loss of  $O^+$ , and decreases in  $O$  which decreases the daytime production of  $O^+$ . According to Prölss [1995], positive storm effects could be related to composition changes, but are attributed mainly to upward drifts due to equatorward winds usually associated with gravity waves that show as increases in  $hmF2$ . The positive storm effects from this mechanism are day time only when there is significant solar ionization. Also important in both positive and negative storm effects are electric fields which are either external (of magnetospheric origin) or created by dynamo winds (e. g. Blanc and Richmond, 1980).

There have been several studies that have compared first principle models with ionosonde observations. Wilkinson et al. [1988] used the Utah State model with model auroral inputs and neutral composition and found, along with the companion study of Szuszczewicz et al. [1996],

that the agreement between model and observations is usually worst at night, with the model electron densities much lower than the observations. Another study by Sica et al. [1990] showed that agreement between the Utah State model and ionosonde NmF2 measurements at night could be achieved either with equatorward winds or with a reasonable downward flux of O<sup>+</sup> at 1000 km, or both. The present study will show that variations in the O/N<sub>2</sub> ratio are strongly correlated with variations in NmF2 both day and night. It will also show evidence of gravity waves and show that a reasonable downward flux of O<sup>+</sup> at night will increase the modelled NmF2 to observational levels.

Comparisons were made with data from the 53 ionosonde stations listed in Table 1 of Szuszczewicz et al. [1996] plus the American stations of Boulder and Wallops Island. All stations provided hourly foF2 data, which is the critical frequency of the ordinary ionosonde trace with typical error bars of 0.1 MHz (Wilkinson, 1978). This is related to the peak electron density (NmF2) by the following relationship:

$$foF2 \text{ (Hz)} = 9.0 \times \sqrt{NmF2 (m - 3)}$$

Thirty-six stations also provided values of the transmission factor M(3000)F2, making it possible to determine the height (hmF2) of NmF2 using the method of Dudeney [1983], where typical error bars are about  $\pm 20$  km. Neutral meridional winds positive towards magnetic north were then derived from the height of the peak electron density, hmF2, using the servo-analysis technique of Miller et al. [1986, 1993]. The servo-analysis of hmF2 produces an effective wind which is composed of the neutral wind plus electric field effects. Hence, the meridional wind estimates are not used above 60° magnetic or below 20° since electric fields are expected to be important in high and low latitudes. A  $\pm 20$  km error in hmF2 will result in  $\pm 25$  m/s errors in the ionosonde winds at night, and  $\pm 50$  m/s errors during the afternoon.

#### *High and Low Latitudes*

Figure 4 shows the electron density peak and the hmF2 for several stations at high and low latitudes where electric fields are expected to be important. The AMIE technique estimates the

high latitude electric fields, while low latitude electric fields are specified by the empirical model of Richmond et al. [1980]. Vertical lines mark local midnight. Both observations and AMIE-TIGCM calculations are plotted every UT hour for values at that hour. Also plotted are the 12-day average of the observations and the time-averaged AMIE-TIGCM simulation in order to tell what is different on March 28-29 compared to the averages.

The only polar cap station in this set is Resolute Bay at  $83^\circ$  magnetic latitude. Modelling high latitude stations is very difficult due to the presence of such features as polar holes, tongues of ionization brought in by convection from the dayside that can later break into patches, high-latitude troughs, and auroral ionization (Sojka et al., 1992; Prölss, 1995). In addition, the polar cap is in a region of open field lines so plasma can continuously escape. The most striking thing about the electron density peak for Resolute Bay shown in Figure 4a is the fact that it is greater at night than during the day. The dashed line average between March 24 and April 4 reveals that while the daytime values are about average on March 28-29, the nighttime values for this period are much larger than usual. In fact, the nighttime values of March 28 and 29 are the largest of the entire month of March. The normal behavior at Resolute Bay for the month of March 1992 (not shown) puts the peak electron density near 15 LT, which is more consistent with the model calculations. The model predicts the nighttime values fairly well in Figure 4a, but overestimates the daytime values by a factor of 2 to 3. Considering that these nighttime values are unusually large, it appears that the simulation overestimates the peak electron density in this polar cap location by about a factor of 2 for all times. The most likely cause for this discrepancy is incorrect specification of composition in the polar cap since the hmF2 observations in Figure 4b are approximated by the model calculations.

Lycksele in Figures 4c and d is close to the aurora. The NmF2 is modelled well by the AMIE-TIGCM on both days and nights, although the calculated hmF2 is lower than the observations. The drop in hmF2 at 21 UT on March 28 in the AMIE-TIGCM model is an indicator of auroral ionization at that time. The calculated daytime NmF2 is lower on March 29 than on March 28 and is lower than the time-averaged dotted line calculation. This decrease on March 29 is due to a smaller ratio of  $O/N_2$ .

Tahiti is in the equatorial anomaly and shows a maximum in the electron density in the pre-midnight region in Figure 4e. A pre-midnight maximum in NmF2 is observed for at least one day for all the stations that lie between 10 and 16 degrees magnetic north or south. The pre-mid-

night peak in electron density is a consistent feature of the anomaly crest during solar maximum conditions, although the peak is just after noon in solar minimum. The present model runs do not reproduce this peak, possibly because the electric field model of Richmond et al. [1980] used in the simulations is an average model based mostly on solar minimum data.

Ouagadougou lies near the magnetic equator, and like the other stations within a few degrees of the equator, Figure 4g shows a peak electron density around 9 LT, followed by a noon bite-out and relatively flat values the rest of the afternoon. The noon bite-out of electron density is a common feature at these latitudes (e.g. Prölss, 1995). All of the stations between  $\pm 10^\circ$  magnetic latitude show much lower densities during the remainder of the day compared to the simulation. The observed hmF2's are also much higher than those predicted by the model as shown in Figure 4h. At low latitudes, there is an anti-correlation of hmF2 and NmF2 (e.g. Fesen et al., 1989; Codrescu et al., 1992; Prölss, 1995). The discrepancies between the model calculations and the observations could be the result of incorrect electric fields in the model.

### *Gravity Waves*

Figure 5 is a plot of the observations on March 28-29 of NmF2, hmF2 and the servo-model ionosonde winds for Norfolk Island (29S, 168E) which is at a magnetic apex latitude (VanZandt et al., 1972) of  $-35.7^\circ$ . The winds are positive towards the north, or equatorward in the southern hemisphere. Figures 5b and c show clear evidence of gravity waves in the observations and calculations at night, especially on March 29. This is consistent with the calculations of Fuller-Rowell and Rees [1981] and Roble et al. [1987] who showed that the largest effects on the neutral wind were at night. The gravity waves are also evident at other southern hemisphere stations in this longitude sector from Hobart at  $-53.9^\circ$  magnetic latitude to Darwin at  $-22.2^\circ$ . The correspondence between the observed gravity waves and the calculated gravity waves is fairly close. By definition, the servo model gives no lag between the ionosonde winds and hmF2, but the model shows lags of between 0 and 1 hours between an initial gravity wave in the equatorward wind and the corresponding gravity wave in hmF2. This is consistent with estimates of the lag to be between 15 and 30 minutes (Richards, 1991). Shifting the equatorward peaks in the ionosonde meridional wind earlier improves the comparison with the AMIE-TIGCM results. The gravity wave peaks and valleys in hmF2 are larger in the observations compared to the simula-

tions.

On both nights, there is a relative increase in NmF2 compared to the 12-day average values. The increases appear to follow increases in hmF2, but there are no relative increases in the simulated NmF2 following relative increases in hmF2. This is in agreement with Prölss [1995] who states that increases due to gravity waves at night are ineffective in raising the NmF2. However, NmF2 should increase at night if the  $O^+$  downward flux is large for an hour or so. Evidence that this can happen will be discussed later. However, for now, the post-midnight increase of NmF2 at Norfolk Island cannot be explained by the present gravity waves in the AMIE-TIGCM calculations. In addition, no positive NmF2 effects during the day were identified that could be attributed to gravity waves and increased equatorward winds raising the layer up because the obvious gravity waves were confined to the nightside.

Figure 6 illustrates the waves in the neutral and ionized parameters as differences between the calculations from the AMIE-TIGCM run on March 29 compared to the time-averaged AMIE-TIGCM run. The plots cover the nighttime region for the longitude of 140 E around 380 km as a function of geographic latitude. Figure 6a shows the temperature differences which maximize in high latitudes. Dusk is located around 9 UT, which happens to be the start of a large Joule heating event that maximizes at 10 UT in Figure 2c in both hemispheres and which produces the neutral difference temperature maxima at 11 UT in Figure 6a. In the southern hemisphere, there is also a definite change in the  $O/N_2$  ratio with decreases after 11 UT for latitudes between 70S and 40S. The AMIE calculations of Joule heating place the location of maximum Joule heating in both hemispheres in the dusk sector around  $67^\circ$  magnetic latitude (57S and 77 N), although there is an additional large Joule heating source in the northern hemisphere on the day-side. The Joule heating in the dusk sector triggers equatorward difference winds at 9 UT in the southern hemisphere which show in Figure 6c as a maximum positive (equatorward) difference around 60S and as a maximum negative (equatorward) difference at 10 UT near 75N. These equatorward difference winds clearly propagate to the equator, arriving around 12 UT for propagation times of between 2 and 3 hours. These propagation times from high latitudes to the equator are consistent with the calculation of 2 hours by Roble et al. [1987] and of 2.5 hours by Richmond and Matsushita [1975].

Figures 6b and c show that the converging difference winds at the equator between 11-12

UT are associated with downward difference vertical winds. These results are in agreement with similar difference plots for the TGCM analysis of the storm on March 22, 1979 described by Roble et al. [1987]. The converging winds at 12 UT in Figure 6c are also associated with relative increases in the hmF2 on either side of the equator around 25° magnetic latitude (35N, 15S) shown in Figure 6d. Differences in foF2 are generally positive at low latitudes and negative at high latitudes, but the peaks in hmF2 near 25° magnetic latitude at 12 UT are co-located with relative minima in foF2. There is then a relative increase in foF2 at the magnetic equator (10N), while there is a relative decrease in hmF2. Diverging difference winds at 14 UT at the equator in Figure 6c are associated with upwelling in Figure 6b, relative decreases in hmF2 near 25° magnetic latitude in Figure 6d and relative increases in foF2 in Figure 6f. The anti-correlation of NmF2 and hmF2 in the lower latitudes is in agreement with observations and models (e.g. Fesen et al., 1989; Codrescu et al., 1992; Prölss, 1995). However, the major variations of foF2 in mid and high latitudes are strongly correlated with variations in the O/N<sub>2</sub> ratio plotted in Figure 6e which will be discussed in the next section.

#### *Positive and Negative N<sub>m</sub>F<sub>2</sub> Variations and O/N<sub>2</sub>*

The upper mid-latitude stations shown in Figure 7 illustrate distinct longitudinal differences in the changes in the daytime NmF2 between March 28 and 29, and different deviations from their 12 or 2-day averages. We will look at the relative variations of NmF2 within this 12-day disturbed period and explain them in terms of O/N<sub>2</sub> variations. Of particular interest are the variations in the same longitude sector where the observed NmF2 of Wallops Island in Figure 7b is only slightly larger on March 28 than its average while Ottawa further north is much larger. In comparing the northern and southern hemisphere stations of Magadan and Hobart in Figures 7g and h, the observations for both days are different in each hemisphere with respect to their averages. In all cases where the AMIE-TIGCM time-averaged NmF2 is different from the calculated NmF2 on March 29, the higher values are the result of higher O/N<sub>2</sub> values on the constant pressure surface around 380 km. This is consistent with the difference results of Figures 6e and f, where changes in foF2 correlate well with variations in O/N<sub>2</sub>. At 6 UT on March 29 in Figure 6e, the difference in the O/N<sub>2</sub> ratio at Hobart (42.9S, 147.3E) is positive, which results in the larger foF2 in Figure 6f, and the larger NmF2 in Figure 7h. Similarly, Magadan (60.1N, 151.0E) shows



an increase in  $O/N_2$  at 6 UT on March 29 in Figure 6e, and a corresponding increase in foF2 in Figure 6f and in NmF2 in Figure 7g. If Magadan were just slightly poleward, the difference would be negative instead of positive.

Prölss [1993] states that most sub-auroral storm effects are negative with ionization losses due to decreases in the  $O/N_2$  ratio pushed away from the auroral regions in storm surges in the post-midnight sector that then rotate in time before dissipating. Negative effects usually show up the next day in regions of decreased  $O/N_2$ . In Figure 6e, the storm decrease in  $O/N_2$  in the southern hemisphere occurs after 11 UT (20 LT) on March 29 and expands equatorward towards the dayside at the rate of about 10 degrees every 4 to 5 hours. Figure 8 is a plot of the difference in the  $O/N_2$  ratio on March 29 compared to the time-averaged calculations as a function of UT for the magnetic latitude of 52 N. The local times of midnight and noon are shown as slanting dash-dot and dotted lines, respectively. The minima are about 5 hours or  $75^\circ$  wide in longitude, and tend to die away in the evening before being replaced with other minima. The minima in  $O/N_2$  differences also drift westward with the zonal winds at night, and eastward with the zonal winds in the afternoon. The westward shift can be quite significant at night as shown by the shift around 6 UT near midnight around 100 W.

From Figure 7, at all longitudes except 75 W, the AMIE-TIGCM calculates the NmF2 better on March 29 compared to March 28. This may be due to the long residence times associated with  $O/N_2$  decreases. Because the Joule heat impulses are not correctly modeled for March 27, the  $O/N_2$  longitudinal asymmetries shown in Figure 8 will not be set up correctly. Excluding Ottawa, for the 12 stations between 47 and 57 degrees magnetic latitude, the average NmF2 values for five hours around local noon are overestimated by AMIE-TIGCM by 15.3% on the first day, and by 8.6% on the second day. This demonstrates the superiority of using AMIE high latitude inputs which in general improve the calculation of daytime NmF2 values on March 29 compared to March 28 in response to realistic LT and UT placement of Joule heating events.

### *Maintenance of the Nighttime Ionosphere*

The companion study by Szuszczewicz et al. [1996] showed that the major disagreement between the climatological AMIE-TIGCM model run and the observations was the failure of the model to maintain the observed level of peak ionization at night. They attribute this failure to

smaller model equatorward winds at night that lead to lower hmF2 heights, which in turn put the peak electron density in a region of higher loss rate. Sica et al. [1990] addressed the problem of the nighttime maintenance of the electron density in mid-latitudes for the solar minimum, quiet day of September 28, 1986, and concluded it could be maintained either with strong equatorward winds or downward  $O^+$  flux. In order to quantify the differences between the AMIE-TIGCM calculations and the observations for March 28-29 and to compare more easily with the companion paper of Szuszczewicz et al. [1996], averages and differences were taken of foF2, NmF2, hmF2, and the meridional winds as a function of local time. In particular, differences were averages of differences, not differences of averages. Figure 9 is a plot of these differences and averages where the differences and averages shown in Figures 5 and 7 from Szuszczewicz et al. [1996] have been re-calculated and plotted in a different format.

From Figure 9a, the time-averaged run underestimates foF2 for the 37 stations above  $25^\circ$  magnetic latitude by about 25% at 3 LT, while the underestimate is about 30% for March 28-29. This corresponds to underestimates in NmF2 in Figure 9b of about 40% and 50% (a factor of 2 less), respectively. The model overestimates NmF2 during the day by between 10 and 20%.

Similarly, for 27 stations poleward of  $25^\circ$  magnetic latitude, the model underestimates hmF2 by 5 to 10 km in the afternoon in Figure 9d, and by up to 40 km around midnight, which is more than the error bar of  $\pm 20$  km. Figure 9c shows that the hmF2 peaks between 3 and 4 LT in the AMIE-TIGCM calculations, compared to between 0 and 1 LT in the observations. This is the same as the meridional winds shown in Figure 9e for 34 stations between 20 and 60 degrees magnetic latitude, where the model winds peak about 2 hours later than the ionosonde winds. There is a suggestion in the Fabry-Perot comparisons of the meridional winds in Figure 3e that the AMIE-TIGCM winds peak 1-2 hours later than the observations as well. The study by Miller et al. [1986] showed that the peak equatorward ionosonde winds usually followed peaks in the winds derived from the Millstone Hill and Arecibo incoherent scatter radars, although the ionosonde winds could be up to 50 m/s less equatorward before midnight. The differences between the model and ionosonde winds are plotted in Figure 9f, where the model winds on March 28-29 are more poleward during the day and more equatorward at night, while the time-averaged model winds were also less equatorward at night as in the Szuszczewicz et al. [1996] study. It appears from Figure 9e that the problem is not so much a problem of magnitude as deduced by the Szuszc-

zewicz et al. [1996] study, but a matter of shifting the AMIE-TIGCM winds 2 hours earlier at night.

To find out what the effect of shifting the peak equatorward winds earlier would be, several Field Line Interhemispheric Plasma (FLIP) model (Richards and Torr, 1988) runs were done at 55 N using the observed hmF2 and the model hmF2 averaged over the stations located between 47 and 57 degrees magnetic latitude. The earlier peak in hmF2 is related to stronger equatorward winds earlier in the night which can increase the NmF2 values by a factor of two at 4 LT and increase hmF2 by up to 20 km around midnight. The FLIP model winds derived from the model hmF2 values were less equatorward before 1 LT and more equatorward afterwards than the actual model calculated winds, which indicated that the composition was different in the two models. The FLIP model uses the MSIS-86 (Mass Spectrometer Incoherent Scatter) model described by Hedin [1987]. A brief check showed that the atomic oxygen densities were within 15%, but that the TIGCM neutral temperature, O<sub>2</sub> and N<sub>2</sub> densities were less than those of MSIS by about 100 K, a factor of four, and a factor of two at 300 km, respectively. A test run decreasing the O<sub>2</sub> and N<sub>2</sub> in FLIP resulted in better agreement in the magnitude of the winds and approximately doubled the NmF2 values during the day and increased them even more at night compared to the control run. The electron density decreases exponentially at night, so losses in NmF2 can be larger than changes in the composition by the end of the night. If N<sub>2</sub> were increased in the TIGCM, the O/N<sub>2</sub> ratio would decrease and the NmF2 would drop. If N<sub>2</sub> and temperature differences are at the heart of the model-observation discrepancies, then there must be another means of raising the NmF2 besides shifting the winds 2 hours earlier, since the decreases in NmF2 due to N<sub>2</sub> increases outweigh the increases due to the wind shift. We therefore look at the effect of the O<sup>+</sup> flux at night.

Plasma flows to and from the plasmasphere are known to have a marked effect on NmF2 and a small effect on hmF2 (e.g. Sica et al, 1990). The effects are greatest at night when there is no competing solar ionization. During magnetic storms, the plasma in the outer plasmasphere is stripped away by convection electric fields leaving depleted or empty flux tubes (e.g. Sica et al., 1990). The difference between full and empty flux tubes can be a factor of two in NmF2, with full flux tubes producing more NmF2 and larger O<sup>+</sup> fluxes. The O<sup>+</sup> flux is also a strong function of solar cycle.

Figure 10 is a plot of the day and night  $O^+$  flux used in the TIGCM at the upper boundary, which is approximately at 550 km for this period. There is no LT dependence in the model except for interpolation between day and night values between zenith angles of 80 and 100 degrees. The day/night fluxes are equal and opposite except for the region of the polar cap which is defined to be greater than  $60^\circ$  magnetic latitude for this purpose. These fluxes are based on 1969 solar maximum measurements at Millstone Hill described by Evans [1974] and summarized in Evans [1975a, 1975b].

Millstone is located at a magnetic latitude of  $53^\circ$  and the  $O^+$  flux at 650 km shows a strong upward flux around sunrise and a strong downward flux around sunset [Evans, 1975a]. Figures 18e and f in Evans [1974] show the flux at 650 km for March 21-22 and March 25-26, 1969. From previous figures in Evans [1974], the downward nighttime flux at 650 km is about 5% smaller than the downward flux at 550 km, while the daytime upward flux at 650 km can transition to a downward flux at 550 km. For March 25-26, 1969 the flux is upward for 8 hours at 650 km and downward for 16 hours with approximately equal average magnitudes. Compressing the 16-hour downward flux into 12 hours results in a downward nighttime flux of  $-2.0 \times 10^8$  ions/cm<sup>2</sup>-s that is double the similarly expanded 12-hour upward daytime flux of  $0.9 \times 10^8$  ions/cm<sup>2</sup>-s. These are plotted as x's in Figure 10. The average nighttime flux for March 21-22, 1969 (daytime observations are missing) is even larger, with gravity waves in the  $O^+$  flux and in the electron density in Figure 3f of Evans [1974] with a periodicity of about an hour. The average, 12-hour value of  $-3.3 \times 10^8$  ions/cm<sup>2</sup>-s is shown as a '+' in Figure 10. Figure 18f in Evans [1974] for March 25-26, 1969 showed a large downward  $O^+$  flux at 650 km around 22 LT that was almost as large as the sunset peak and was related to an increase in the downward vertical drift since the electron density shown in his Figure 3h was relatively flat. However, there was a perceptible increase in hmF2 and NmF2 at this time. Such an increase could be similar to the increases found in hmF2 and NmF2 at Norfolk Island in Figure 5. The AMIE-TIGCM calculations would not show an increase in NmF2 since the  $O^+$  flux is kept constant throughout the night.

Arecibo is located at a magnetic latitude of  $29^\circ$ . The  $O^+$  flux for four altitudes between 517 and 586 km was calculated for the solar maximum period of March and April 1982. The  $O^+$  flux decreases between 517 and 586 km by about 25-30% during the day and between 5-50% dur-

ing the night, with downward fluxes occurring over 13 to 15 hours starting in the afternoon. The average 12-hour fluxes for an average altitude of 551 km are plotted in Figure 10 with '+'s and an 'x' and are approximately double the Millstone observations at 650 km.

In Figure 8 of Szuszczewicz et al. [1996], the  $O^+$  flux at 550 km from the FLIP model is plotted for 20 E longitude. The fluxes are large upwards around 6 LT and large downwards around 19 LT. The details of the FLIP LT variations in the flux change considerably in longitude because of differences in interhemispheric flow, although all longitudes retain the sunrise upward peak and sunset downward peak. For magnetic latitudes close to 30, 50 and 70 degrees, the fluxes are downwards for 17, 16 and 19 hours, respectively. Like the Millstone Hill measurements, the average day/night fluxes are approximately equal, but when spread and compressed over 12 hours, the nighttime downward flux is approximately twice the daytime upward flux. Figure 10 plots the 12-hour day/night  $O^+$  flux averages from the FLIP model at 20 E as asterisks, which are larger than the Millstone or Arecibo observations. The dash-dot line in Figure 10 shows the day/night  $O^+$  fluxes we chose for a revised AMIE-TIGCM run. The polar cap is defined to be above  $75^\circ$  magnetic latitude with large daytime upward fluxes along open field lines. The day/night ratio of the flux magnitude at lower latitudes is about 1/3.

Increasing the downward  $O^+$  flux at the upper boundary increases the electron density and so increases the ion drag at night and in the early morning. This has the effect of decreasing the equatorward nighttime velocities by about 10 m/s and decreasing the poleward velocities after sunrise by as much as 10 m/s. The reduced winds in turn lead to hmF2s which are about 8 km lower around 4 LT and about 16 km higher around 7 LT. The effects are much larger at night in the NmF2 densities. Figure 11 shows the NmF2 differences between the observations and the AMIE-TIGCM calculations for six magnetic latitude regions, where the dash-dot lines show the effect of the revised  $O^+$  flux. In Figure 11a, it is apparent that the biggest discrepancy is in the polar cap where the electron density peak during the day is up to 3 times too large in the model. However, the increased outflow during the day along open field lines did not reduce the density by much since solar ionization effects are much stronger than  $O^+$  flux effects during the day. In the auroral region of Figure 11b, the AMIE-TIGCM NmF2 is a little low at 3 LT and up to a factor of 2 high in the evening sector. The evening excess may be related to the auroral ionization in the model. Increasing the downward flux at night reduces the underestimate at 3 LT, but increases the

evening overestimates. Between 22 and 57 degrees magnetic latitude, the NmF2 is underestimated by a factor of two (i.e. 50%) in the post-midnight region. With the revised fluxes, the calculated NmF2 is now too large at night by at least 20%. The model NmF2 is also low in the equatorial anomaly by 30% near midnight in Figure 11e, and is improved with the new fluxes. Finally, in the magnetic equatorial region, the model NmF2 is low before 10 LT and high thereafter by about 60%. The new fluxes improve the NmF2 before 10 LT, but have minimal effect otherwise. Apart from the magnetic equator and the polar cap, the comparisons during the day are excellent. The revised  $O^+$  flux produces little change during the day, but has substantially increased the nighttime estimates of NmF2 at all latitudes below the polar cap. A more realistic LT dependence of the  $O^+$  flux would have very large downward values for a couple of hours around sunset, and much smaller values up until sunrise, when the flux would be large upwards. It is therefore possible that the post-midnight increases in NmF2 would not be as pronounced with a more realistic LT dependence as they are now.

Increasing the downward  $O^+$  flux at night to solar maximum levels can raise the NmF2 above the observations at night. Shifting the model peak equatorward winds and thus hmF2 2-3 hours earlier at night can also raise the NmF2 to observational levels, but increases in the neutral temperature and molecular composition to values consistent with MSIS will decrease the NmF2 day and night. Changes in the composition will also effect the neutral winds, and may or may not cause the peak equatorward winds to shift earlier at night. Therefore, most of the discrepancies between the model and observations can be rectified by a better physical description of magnetosphere/ionosphere interactions within the TIGCM.

## Summary and Conclusions

This study has described how the auroral inputs are derived in the AMIE technique, which are essential inputs to the TIGCM. Using AMIE high latitude inputs in the TIGCM improves the UT and LT placement of Joule heating events and ion drag momentum sources which launch gravity waves and change the  $O/N_2$  ratio within a local longitude sector. The total hemispheric Joule heating from the TIGCM is 15-20 GW larger in the hemisphere where the magnetic pole is tilted towards the sun.

The AMIE-TIGCM temperature calculations help to interpret the Fabry-Perot observa-

tions at Watson Lake within auroral arcs which move the emission peak to lower altitudes. Lowering the altitude of comparison improves the correspondance with the horizontal neutral winds. There is a suggestion that the observed equatorward winds peak 1-2 hours earlier than the model calculations. Also, the AMIE-TIGCM vertical winds are unable to reproduce the rapid variations and large magnitudes in the observations because of the large grid spacing used.

Many gravity waves were calculated by the AMIE-TIGCM, some of which were found in nighttime observations of the hmF2 and ionosonde meridional winds. The post-midnight increases in NmF2 observed at Norfolk Island and other locations were not replicated by calculations of the AMIE-TIGCM, although the earlier gravity-wave induced increases in hmF2 were partially reproduced. However, a strong downward O<sup>+</sup> flux at night over approximately an hour or so could raise the NmF2. Such LT variations in the flux are not at present in the TIGCM.

Gravity waves in NmF2 were visible in the AMIE-TIGCM calculations at lower latitudes which were anti-correlated with peaks in the hmF2 around  $\pm 25^\circ$  magnetic latitude. The relative variations at the magnetic equator were out of phase with the variations at  $\pm 25^\circ$  magnetic latitude. The difference hmF2 peaks at  $\pm 25^\circ$  magnetic latitude were related to the converging difference equatorwards winds that produced relative subsidence, and the NmF2 peaks were related to the diverging difference winds at the equator (i.e. relatively poleward) and concurrent relative upwelling. Above about  $40^\circ$  latitude, the major influence on variations in NmF2 were changes in the O/N<sub>2</sub> ratio produced by Joule heating events that remain in the same longitude sector and affect NmF2 variations for hours. Gravity wave and O/N<sub>2</sub> changes were different in the two hemispheres at similar longitudes.

The AMIE-TIGCM calculations of NmF2 were compared with observations as a function of latitude. The single polar station of Resolute Bay showed much larger model NmF2s during the day, and also at night on the average. Comparisons at mid-latitudes showed underestimates of NmF2 of a factor of two at 3 LT. These underestimates were converted to overestimates of at least 20% at mid-latitudes between 22 and 7 LT by increasing the downward nighttime O<sup>+</sup> flux by factors of two to six, values that are consistent with incoherent scatter radar observations during solar maximum. However, a realistic LT variation in the O<sup>+</sup> flux would produce different results, especially later at night when the flux values are reduced. Agreement was not complete at the low latitude stations where electric fields are expected to be important and where the empirical

model of Richmond et al. [1980] that was used may be inadequate.

Comparisons of the ionosonde-derived winds between 20-60 degrees magnetic latitude showed that the AMIE-TIGCM winds were more poleward during the day and more equatorward at night. The differences could be reduced if the AMIE-TIGCM winds were shifted 2 hours earlier, especially at night. Such a shift in the timing of the winds would also improve the 40 km discrepancy in the hmF2 at midnight, and raise the NmF2 by up to a factor of 2 after midnight. Comparisons with MSIS-86 at 55 N showed TIGCM neutral temperatures and molecular composition to be about 100 K and about a factor of two lower at 300 km. Raising  $N_2$  would decrease the  $O/N_2$  ratio and hence decrease NmF2 a factor of two during the day and more at night. The 2-3 hour discrepancy in the hmF2 and equatorward winds at night may or may not be related to differences in the model neutral temperature and molecular composition compared to MSIS. Shifting the equatorward model winds earlier can increase the NmF2 in the post-midnight sector, but increases in the model  $N_2$  will lower NmF2. A combination of composition and LT dependant  $O^+$  flux changes could result in better agreement in NmF2, hmF2 and winds.

This study has pointed out successes and failures in the model that require improvement in the modeling of aeronomic processes. Further campaign studies of this type should help improve the model performance for space weather studies. The present correspondence between data and model calculations for March 28-29, 1992 is remarkably good, but future studies can be carried out using the more advanced electrodynamics TIE-GCM model described by Richmond et al. [1992] which is being validated against climatological models and observations.

## Acknowledgements

The Arecibo incoherent scatter radar measurements and the Watson Lake Fabry-Perot measurements were taken from the CEDAR (Coupling, Energetics and Dynamics of Atmospheric Region) Data Base at the National Center for Atmospheric Research (NCAR) which is supported by the National Science Foundation (NSF). The Arecibo Observatory is operated by Cornell University under cooperative agreement with NSF. The Watson Lake Fabry Perot is operated by the University of Michigan with support from NSF and the US Air Force. We also thank all the institutions and agencies in each of the countries that participated in this investigation. This study was supported in part by the Space Physics Division of the National Aeronautics and Space Adminis-



tration (NASA) under contract NASW-4755 with the Science Applications International Corporation (SAIC).

## References

- Ahn, B.-H., R. M. Robinson, Y. Kamide, and S.-I. Akasofu, Electric conductivities, electric fields and auroral energy injection rate in the auroral ionosphere and their empirical relations to the horizontal magnetic disturbances, *Planet. Space Sci.*, **31**, 641-653, 1983.
- Blanc, M. and A. D. Richmond, The ionospheric disturbance dynamo, *J. Geophys. Res.*, **85**, 1669-1686, 1980.
- Burns, A. G., T. L. Killeen, G. R. Carignan and R. G. Roble, Large enhancements in the O/N<sub>2</sub> ratio in the evening sector of the winter hemisphere during geomagnetic storms, *J. Geophys. Res.*, **100**, 14,661-14,671, 1995a.
- Burns, A. G., T. L. Killeen, W. Deng, G. R. Carignan and R. G. Roble, Geomagnetic storm effects in the low- to middle-latitude upper thermosphere, *J. Geophys. Res.*, **100**, 14,673-14,691, 1995b.
- Chenette, D. L., D. W. Datlowe, R. M. Robinson, T. L. Schumaker, R. R. Vondrak, and J. D. Winningham, Atmospheric energy input and ionization by energetic electrons during the geomagnetic storm of 8-9 November 1991, *Geophys. Res. Lett.*, **20**, 1323-1326, 1993.
- Codrescu, M. V., R. G. Roble and J. M. Forbes, Interactive ionosphere modeling: A comparison between TIGCM and ionosonde data, *J. Geophys. Res.*, **97**, 8591-8600, 1992.
- Crowley, G., B. A. Emery, R. G. Roble, H. C. Carlson, D. J. Knipp, Thermospheric dynamics during September 18-19, 1984, 1. Model simulations, *J. Geophys. Res.*, **94**, 16,925-16,944, 1989a.
- Crowley, G., B. A. Emery, R. G. Roble, H. C. Carlson, J. E. Salah, V. B. Wickwar, K. L. Miller, W. L. Oliver, R. G. Burnside, and F. A. Marcos, Thermospheric dynamics during September 18-19, 1984, 2. Validation of the NCAR thermospheric general circulation model, *J. Geophys. Res.*, **94**, 16,945-16,959, 1989b.
- Dickinson, R. E., E. C. Ridley and R. G. Roble, A three-dimensional, time-dependant general circulation model of the thermosphere, *J. Geophys. Res.*, **86**, 1499-1512, 1981.
- Dickinson, R. E., E. C. Ridley and R. G. Roble, Thermospheric general circulation with coupled

- dynamics and composition, *J. Atmos. Sci.*, *41*, 205-219, 1984.
- Dudeney, J. R., The accuracy of simple methods for determining the height of the maximum electron concentration of the F2-layer from scaled ionospheric characteristics, *J. Atmos. Terr. Phys.*, *45*, 629-640, 1983.
- Evans, J. V., *Millstone Hill Thomson Scatter Results for 1969*, Lincoln Laboratory Technical Report 513, Massachusetts Institute of Technology, 139 pp, July 1974.
- Evans, J. V., A study of F2 region daytime vertical ionization fluxes at Millstone Hill during 1969, *Planet. Space Sci.*, *23*, 1461-1482, 1975a.
- Evans, J. V., A study of F2 region night-time vertical ionization fluxes at Millstone Hill, *Planet. Space Sci.*, *23*, 1611-1619, 1975b.
- Fesen, C. G., G. Crowley and R. G. Roble, Ionospheric effects at low latitudes during the March 22, 1979, geomagnetic storm, *J. Geophys. Res.*, *94*, 5405-5417, 1989.
- Fesen, C. G., R. E. Dickinson and R. G. Roble, Simulation of the thermospheric tides at equinox with the National Center for Atmospheric Research Thermospheric General Circulation Model, *J. Geophys. Res.*, *91*, 4471-4489, 1986.
- Forbes, J. M., R. G. Roble, F. A. Marcos, Thermospheric dynamics during the March 22, 1979, magnetic storm, 2. Comparisons of model predictions with observations, *J. Geophys. Res.*, *92*, 6069-6081, 1987.
- Fuller-Rowell, T. J. and D. S. Evans, Height-integrated Pedersen and Hall conductivity patterns inferred from the TIROS-NOAA satellite data, *J. Geophys. Res.*, *92*, 7606-7618, 1987.
- Fuller-Rowell, T. J. and D. Rees, A three-dimensional, time-dependent simulation of the global dynamical response of the thermosphere to a geomagnetic substorm, *J. Atmos. Terr. Phys.*, *43*, 701-721, 1981.
- Hedin, A. E., MSIS-86 thermosphere model, *J. Geophys. Res.*, *92*, 4649-4662, 1987.
- Heelis, R. A., J. K. Lowell, and R. W. Spiro, A model of the high-latitude ionospheric convection pattern, *J. Geophys. Res.*, *87*, 6339-6345, 1982.
- Hernandez, G. and R. G. Roble, Direct measurements of nighttime thermospheric winds and temperatures, 2, Geomagnetic storms, *J. Geophys. Res.*, *81*, 5173-5181, 1976.
- Hernandez, G. and R. G. Roble, Thermospheric nighttime neutral temperature and winds over Fritz Peak Observatory: Observed and calculated solar cycle variation, *J. Geophys. Res.*, *100*, 14,647-14,659, 1995.

- Knipp, D. J., B. A. Emery, A. D. Richmond, N. U. Crooker, M. R. Hairston, J. A. Cumnock, W. F. Denig, F. J. Rich, O. de la Beaujardiere, J. M. Ruohoniemi, A. S. Rodger, G. Crowley, B.-H. Ahn, D. S. Evans, T. J. Fuller-Rowell, E. Friis-Christensen, M. Lockwood, H. W. Kroehl, C. G. MacLennan, A. McEwin, R. J. Pellinen, R. J. Morris, G. B. Burns, V. Papitashvili, A. Zaitzev, O. Troshichev, N. Sato, P. Sutcliffe, and L. Tomlinson, Ionospheric convection response to slow, strong variations in a northward Interplanetary Magnetic Field: A case study for January 14, 1988, *J. Geophys. Res.*, **98**, 19,273-19,292, 1993.
- Lu, G., A. D. Richmond, B. A. Emery, and R. G. Roble, Magnetosphere-ionosphere-thermosphere coupling: Effect of neutral winds on energy transfer and field-aligned current, *J. Geophys. Res.*, **100**, 19,643-19,659, 1995.
- Lu, G., B. A. Emery, A. Rodger, M. Lester, J. Taylor, D. S. Evans, M. Ruohoniemi, W. F. Denig, O. de la Beaujardiere, R. A. Frahm, J. D. Winningham, and D. L. Chenette, High-latitude ionospheric electrodynamics as determined by the AMIE procedure for the conjunctive SUNDIAL/ATLAS-1/GEM period of March 28-29, 1992, *J. Geophys. Res.*, this issue, 1996.
- Miller, K. L., P. G. Richards and H. Y. Wu, A global-scale study of meridional winds and electron densities in the F-region during the SUNDIAL 1987 campaign, *Ann. Geophys.*, **11**, 572-584, 1993.
- Miller, K. L., D. G. Torr and P. G. Richards, Meridional winds in the thermosphere derived from measurement of F2 layer height, *J. Geophys. Res.*, **91**, 4531-4535, 1986.
- Mizera, P. F. and D. S. Evans, Simultaneous measurements of polar cap electron distributions in opposite hemispheres, *J. Geophys. Res.*, **91**, 9007-9011, 1986.
- Price, G. D., R. W. Smith and G. Hernandez, Simultaneous measurements of large vertical winds in the upper and lower thermosphere, *J. Atmos. Terr. Phys.*, **57**, 631-643, 1995.
- Prölss, G. W., On explaining the local time variation of ionospheric storm effects, *Ann. Geophys.*, **11**, 1-9, 1993.
- Prölss, G. W., Ionospheric F-region storms, Handbook of Atmospheric Electrodynamics, Vol II, editor Hans Volland, CRC Press, 195-248, 1995.
- Rees, M. H. and R. G. Roble, Excitation of O(<sup>1</sup>D) atoms in aurorae and emission of the [OI] 6300-A line, *Can., J. Phys.*, **64**, 1608-1613, 1986.
- Reiff, P. H. and J. G. Luhmann, Solar wind control of the polar-cap voltage, Solar Wind-Magneto-

- sphere Coupling, editors Y. Kamide and J. A. Slavin, Terra Scientific Publishing Company, 453-476, 1986.
- Reiff, P. H. R. W. Spiro, and T. W. Hill, Dependence of polar cap potential drop on interplanetary parameters, *J. Geophys. Res.*, **86**, 7639-7648, 1981.
- Rich, F. J., M. S. Gussenhoven and M. E. Greenspan, Using simultaneous, particle and field observations on a low altitude satellite to estimate Joule heat energy flow into the high-latitude ionosphere, *Ann. Geophys.*, **5**, 527-534, 1987.
- Richards, P. G., An improved algorithm for determining neutral winds from the height of the F<sub>2</sub> peak electron density, *J. Geophys. Res.*, **96**, 17,839-17,846, 1991.
- Richards, P. G. and D. G. Torr, Ratios of photoelectron to EUV ionization rates for aeronomic studies, *J. Geophys. Res.*, **93**, 4060-4066, 1988.
- Richmond, A. D., M. Blanc, B. A. Emery, R. H. Wand, B. G. Fejer, R. F. Woodman, S. Ganguly, P. Amayenc, R. A. Behnke, C. Calderon, and J. V. Evans, An empirical model of quiet day ionospheric electric fields at middle and low latitudes, *J. Geophys. Res.*, **85**, 4658-4664, 1980.
- Richmond, A. D. and Y. Kamide, Mapping electrodynamic features of the high-latitude ionosphere from localized observations: Technique, *J. Geophys. Res.*, **93**, 5741-5759, 1988.
- Richmond, A. D., Y. Kamide, B.-H. Ahn, S.-I. Akasofu, D. Alcayde, M. Blanc, O. de la Beaujardiere, D. S. Evans, J. C. Foster, E. Friis-Christensen, T. J. Fuller-Rowell, J. M. Holt, D. Knipp, H. W. Kroehl, R. P. Lepping, R. J. Pellinen, C. Senior, and A. N. Zaitzev, Mapping electrodynamic features of the high-latitude ionosphere from localized observations: Combined incoherent scatter radar and magnetometer measurements for January 18-19, 1984, *J. Geophys. Res.*, **93**, 5760-5776, 1988.
- Richmond, A. D. and S. Matsushita, Thermospheric response to a magnetic substorm, *J. Geophys. Res.*, **80**, 2839-2850, 1975.
- Richmond, A. D., E. C. Ridley and R. G. Roble, A thermosphere/ionosphere general circulation model with coupled electrodynamics, *Geophys. Res. Lett.*, **19**, 601-604, 1992.
- Robinson, R. M., R. R. Vondrak, K. Miller, T. Dabbs, and D. Hardy, On calculating ionospheric conductances from the flux and energy of precipitating electrons, *J. Geophys. Res.*, **92**, 2565-2569, 1987.
- Roble, R. G., A. D. Richmond, W. L. Oliver and R. M. Harper, Ionospheric effects of the gravity

- wave launched by the September 18, 1974, sudden commencement, *J. Geophys. Res.*, 83, 999-1009, 1978.
- Roble, R. G., J. M. Forbes and F. A. Marcos, Thermospheric dynamics during the March 22, 1979, magnetic storm, 1, Model simulations, *J. Geophys. Res.*, 92, 6045-6068, 1987.
- Roble, R. G. and E. C. Ridley, An auroral model for the NCAR thermospheric general circulation model (TGCM), *Ann. Geophys.*, 5, 369-382, 1987.
- Roble, R. G., E. C. Ridley, A. D. Richmond, and R. E. Dickinson, A coupled thermosphere/ionosphere general circulation model, *Geophys. Res. Lett.*, 15, 1325-1328, 1988.
- Roble, R. G., Energetics of the mesosphere and thermosphere, *The Upper Mesosphere and Lower Thermosphere: A Review of Experiment and Theory, Geophysical Monograph 87*, American Geophysical Union, 1-21, 1995.
- Sica, R. J., R. W. Schunk and P. J. Wilkinson, A study of the undisturbed mid-latitude ionosphere using simultaneous multiple site ionosonde measurements during the Sundial-86 campaign, *J. Geophys. Res.*, 95, 8271-8279, 1990.
- Sipler, D. P. M. A. Biondi and M. E. Zipf, Vertical winds in the midlatitude thermosphere from Fabry-Perot Interferometer measurements, *J. Atmos. Terr. Phys.*, 57, 621-629, 1995.
- Smith, R. W. and G. Hernandez, Vertical winds in the thermosphere within the polar cap, *J. Atmos. Terr. Phys.*, 57, 611-620, 1995.
- Sojka, J. J., R. W. Schunk, D. Rees, T. J. Fuller-Rowell, R. J. Moffett and S. Quegan, Comparison of the USU ionospheric model with the UCL-Sheffield coupled thermospheric-ionospheric model, *Adv. Space Res.*, 12, No. 6, 89-92, 1992.
- Szuszczewicz, E. P., D. Torr, P. Wilkinson, P. Richards, R. Roble, B. Emery, G. Lu, M. Abdu, D. Evans, K. Igarashi, P. Jiao, M. Lester, S. Pulinets, B. M. Reddy, P. Blanchard, K. Miller, and J. Joselyn, F-Region climatology during the SUNDIAL/ATLAS-1 campaign of March 1992: Model-measurement comparisons and cause-effect relationships, *J. Geophys. Res.*, this issue, 1996.
- VanZandt, T. E., W. L. Clark and J. M. Warnock, Magnetic apex coordinates: A magnetic coordinate system for the ionospheric F2 layer, *J. Geophys. Res.*, 77, 2406-2411, 1972.
- Wilkinson, P. J., Scaling errors in ionospheric characteristics, *Ionosonde Network Advisory Group Bulletin*, 27, World Data Center A for Solar Terrestrial Physics, US Dept. of Commerce, NOAA, 20-??, 1978.

Wilkinson, P. J., R. Schunk, R. Hanbaba and H. Mori, Interhemispheric comparison of SUNDIAL F-region data with global scale ionospheric models, *Ann. Geophys.*, 6, 31-38, 1988.

## Figure Captions

Figure 1: (a) Electron energy flux in  $\text{mW/m}^2$  from the Fuller-Rowell and Evans [1987] pattern for a hemispheric power index of 7 as a function of magnetic latitude and local time. (b) Observations of the energy flux in  $\text{mW/m}^2$  between 0738 and 0812 UT on March 28, 1992 from the DMSP-F08, F09, F10, and F11 satellites (marked with '8', '9', '10', '11'), the NOAA-12 satellite ('N'), the UARS AXIS X-ray imager ('X'), and ground magnetometers ('x'). The satellite estimates are marked with a 'o' if they are before 0755 UT, and marked with a '+' if they are after 0755 UT. (c) Fitted electron energy flux in  $\text{mW/m}^2$  from the AMIE procedure for 0755 UT on March 28, 1992. (d) Mean Maxwellian energy of the auroral electrons based on the Hall-to-Pedersen ratio at the hemispheric power level of 7 in keV. (e) Same as (b) except for the mean electron energy. (f) Same as (c) except for the mean electron energy.

Figure 2: (a) Hemispheric power in GW derived from the AMIE procedure for 66 northern hemisphere (\_\_\_) patterns and 53 southern hemisphere (\_\_\_) patterns for March 28-29, 1992. The first 24 hours is the average of these patterns used as the 24-hour initialization run in the TIGCM. (b) Like (a) except this is the cross-tail potential drop in kV derived from the AMIE procedure. The dotted line is the cross-tail potential drop determined from the solar wind speed and the IMF from Reiff and Luhmann [1986] between 13 and 20 UT on March 29. At other UTs, it is estimated from Kp (Reiff, private communication) for March 28-29. (c) Hemispheric Joule heating rate estimates in GW calculated from the TIGCM at every hour for the northern (\_\_\_) and southern (\_\_\_) hemispheres when using the AMIE patterns for March 28-29, 1992 and the time-averaged AMIE patterns for the first 24 hours. The effects of the neutral winds are included.

Figure 3: Fabry-Perot 930nm observations March 28-29, 1992 above Watson Lake, Canada. The AMIE-TIGCM results are plotted as a dot-dash line. (a) Brightness in R from observations overhead compared to model results. The observations in arbitrary units of relative brightness were multiplied by 30. (b) Neutral temperature in K from overhead compared

to model results. (c) Vertical wind looking directly above the station positive upwards in m/s compared to AMIE-TIGCM results. (d) Zonal neutral wind in m/s positive towards geographic east looking east (\_\_\_\_) and west(...) compared to model values. The '+'s are model values at 160 km. (e) Meridional neutral wind in m/s positive towards geographic north looking north (\_\_\_\_) and south (...) compared to model results.

Figure 4: Ionosonde station observations for March 28-29, 1992 ordered in apex latitude, which is the number after the station name. The vertical lines show the location of local midnight and the asterisks are observations. The dashed line is the observational average between March 24 and April 4, 1992. The solid line is the calculations from the TIGCM using time-varying AMIE inputs while the dotted line uses time-averaged AMIE inputs. (a) NmF2 at Resolute Bay in  $10^{-6}$  electrons/cm<sup>3</sup>. (b) hmF2 at Resolute Bay in km. (c) Same as (a) except for Lycksele. (d) Same as (b) except for Lycksele. (e) Same as (a) except for Tahiti. (f) Same as (b) except for Tahiti. (g) Same as (a) except for Ouagadougou. (h) Same as (b) except for Ouagadougou.

Figure 5: Same as Figure 4 except for Norfolk Island observations for March 28-29, 1992. (a) NmF2 in  $10^{-6}$  electrons/cm<sup>3</sup>, (b) hmF2 in km and (c) neutral wind positive towards magnetic north in m/s.

Figure 6: Plots of the differences at the +2 pressure surface near 380 km for the longitude of 140 E as a function of geographic latitude on March 29, 1992 between 6 and 18 UT. The differences are between the AMIE-TIGCM calculations for March 29 versus the time-averaged simulation. (a) Neutral temperature in K, (b) neutral vertical wind in m/s, (c) neutral meridional wind in m/s, (d) height of the F2 peak electron density, hmF2, in km, (e) O/N<sub>2</sub> ratio, and (f) critical frequency of the F2 peak electron density, foF2, in MHz.

Figure 7: Same as Figure 4 except for NmF2 in  $10^{-6}$  electrons/cm<sup>3</sup> for March 28-29, 1992 for stations between 46 and 56 degrees apex latitude north or south. The stations are ordered in geographic longitude. (a) Boulder, (b) Wallops Island, (c) Ottawa, (d) Kaliningrad, (e) Sverdlovsk, (f) Irkutsk, (g) Magadan and (h) Hobart.

Figure 8: Differences in the O/N<sub>2</sub> ratio at the constant pressure level +2 near 380 km for the magnetic latitude of 52 N as a function of UT and geographic longitude. The differences are between the AMIE-TIGCM calculations for March 29 versus the time-averaged simula-

tion. The numbers on the right axis correspond to the geographic latitude.

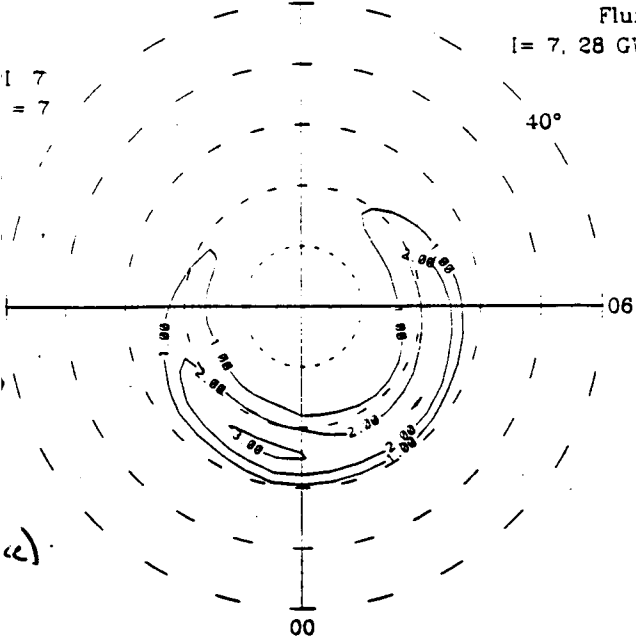
Figure 9: Differences between the AMIE-TIGCM calculations and the observations for March 28-29, 1992 as a function of LT are shown as a solid line, while differences between the time-averaged AMIE-TIGCM simulation and the 12-day ionosonde observations are the dotted line. Percentage differences are  $(\text{model-data})/\text{data}$ , while absolute differences are  $(\text{model-data})$ . Average values for the models are solid and dotted, while average values for the observations are dashed for March 28-29, and dash-dot for 12-day averages. (a) foF2 percentage differences for magnetic latitudes poleward of  $25^\circ$ . (b) NmF2 percentage differences for magnetic latitudes poleward of  $25^\circ$ . (c) Average hmF2 in km for magnetic latitudes poleward of  $25^\circ$ . (d) Same as (c) except are absolute differences. (e) Average meridional neutral winds positive polewards in m/s for magnetic latitudes between  $20^\circ$  and  $60^\circ$ . (f) Same as (e) except are absolute differences.

Figure 10: The day/night  $O^+$  flux in units of  $\text{ions}/\text{cm}^2\text{-s}$  at the upper boundary of the TIGCM near 550 km. The asterisks are approximate 12-hour values of the flux from the FLIP model from Figure 8 of Szuszczewicz et al. [1996]. These are fluxes at 550 km at 20E for the conditions of March 1992 ( $S_a=180$ ) using effective winds from the M3000 values of the International Reference Ionosphere. Millstone Hill measurements at 650 km evenly divided over 12 hours of upward and downward flux are marked as x's for March 25-26, 1969 ( $S_a=180$ ) and as a '+' for March 21-22, 1969 ( $S_a=230$ ). Arecibo measurements at 551 km approximated over 12 hours are marked as +s for March 16-17, 1982 ( $S_a=228$ ) and as an 'x' for April 20, 1982 ( $S_a=145$ ). The dash-dot line is the revised TIGCM  $O^+$  flux specification.

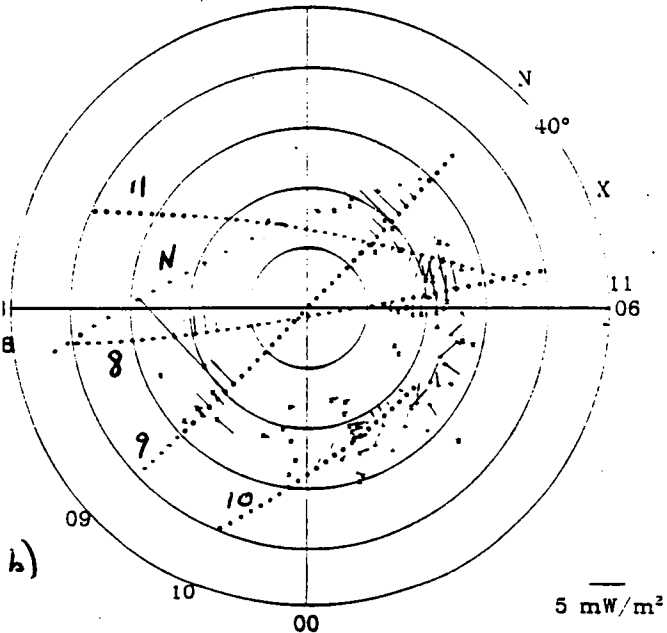
Figure 11: Percent differences  $(\text{model-data}/\text{data})$  between the NmF2 AMIE-TIGCM calculations and the observations for March 28-29, 1992 as a function of LT. The solid line is the original AMIE-TIGCM calculations and the dash-dot line is the AMIE-TIGCM calculations with the revised  $O^+$  flux of Figure 10. (a) 1 ionosonde station at magnetic latitudes over  $75^\circ$  north or south. (b) 4 stations between  $60^\circ$  and  $69^\circ$ . (c) 13 stations between  $47^\circ$  and  $57^\circ$ . (d) 23 stations between  $22^\circ$  and  $46^\circ$ . (e) 8 stations between  $10^\circ$  and  $19^\circ$ . (f) 4 stations between  $0^\circ$  and  $7^\circ$ .



Electron Energy  
Flux  
[ = 7.28 GW

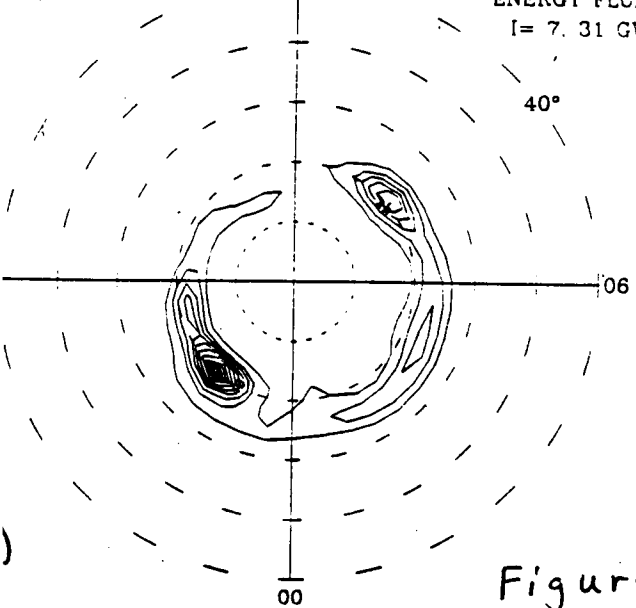


Eflx obs



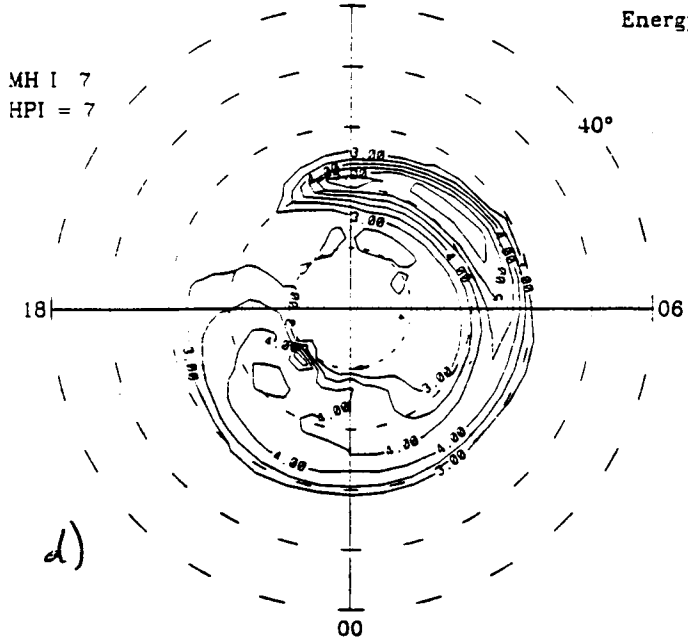
2 MAR 28 07:55+/-17UT 12  
= 7 - T

PARTICLE  
ENERGY FLUX  
I = 7.31 GW



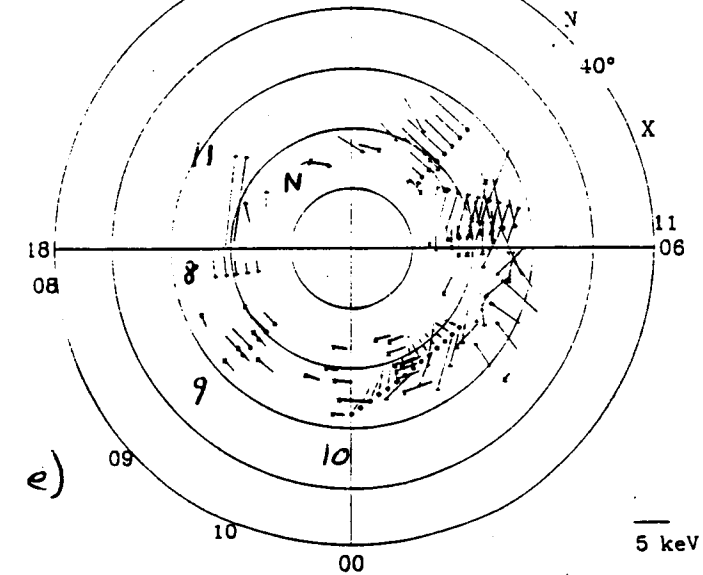
1992 MAR 28 07:55+/-17UT 12

Mean Electron  
Energy



1992 MAR 28 07:55+/-17UT 12

EkeV obs



1992 MAR 28 07:55+/-17UT 12  
HPI = 7

MEAN PARTICLE  
ENERGY

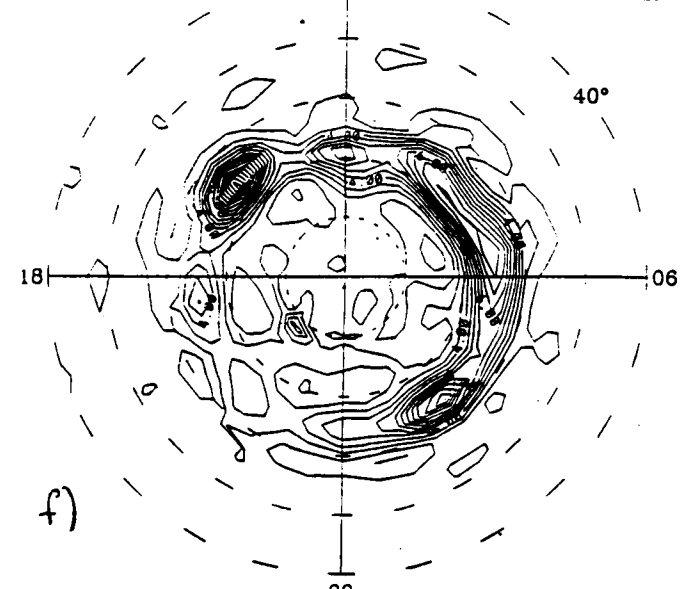


Figure 1

1992 March 28-29, AMIE(—N,—S),param(...)

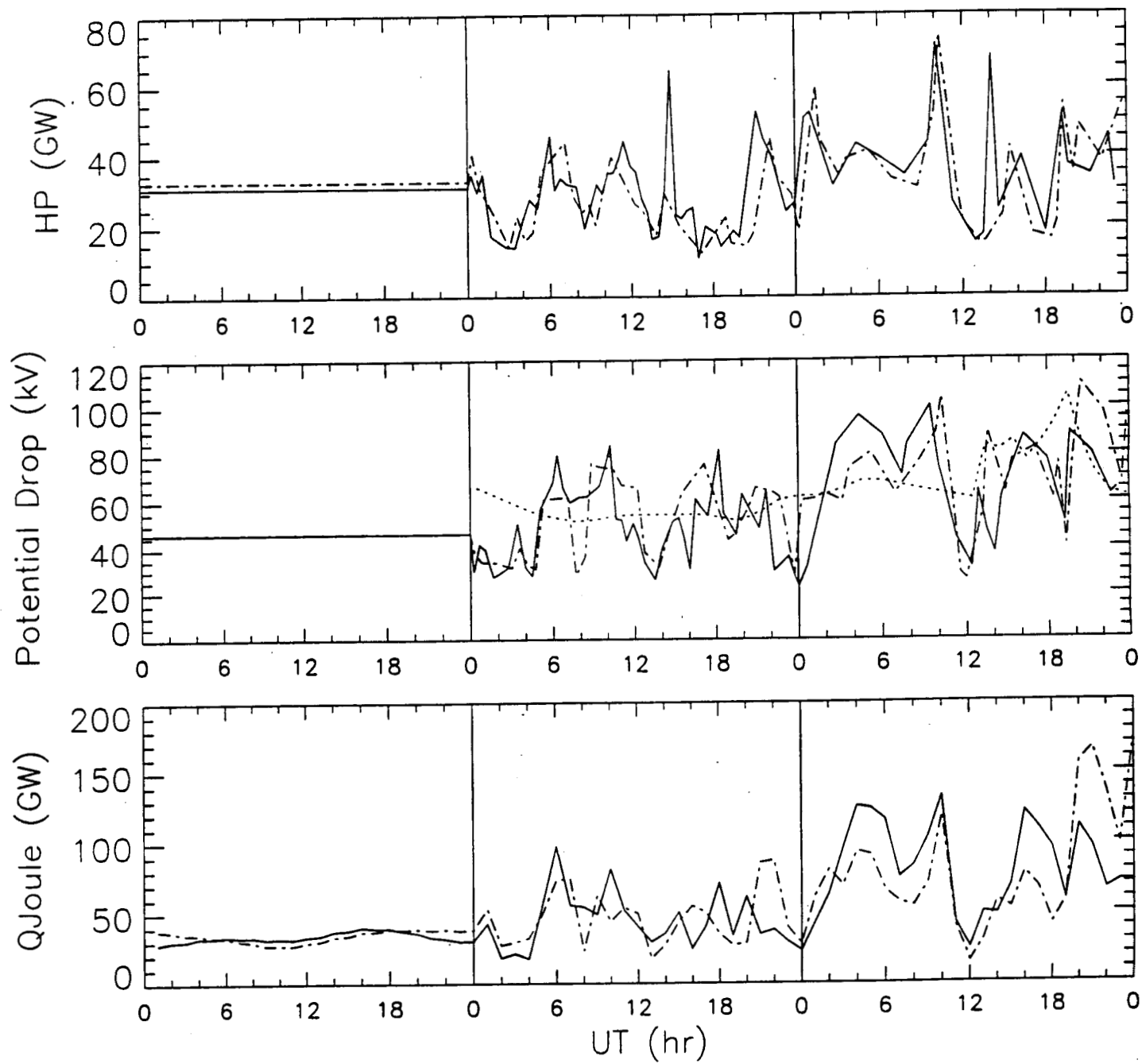


Figure 2

1992 March 28-29 Watson Lake FPI(—,...), AMIE/TIGCM(—.,+)

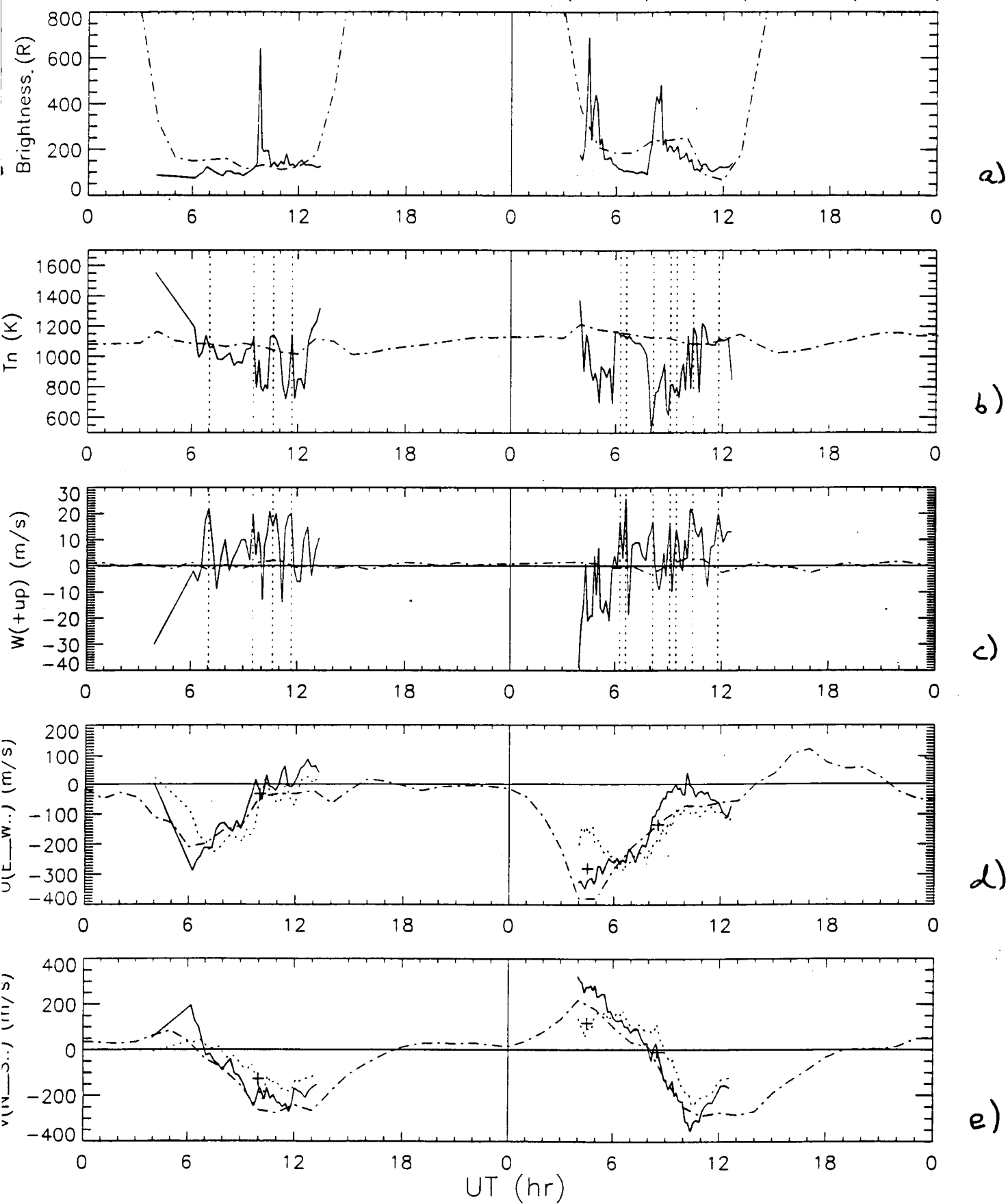


Figure 3

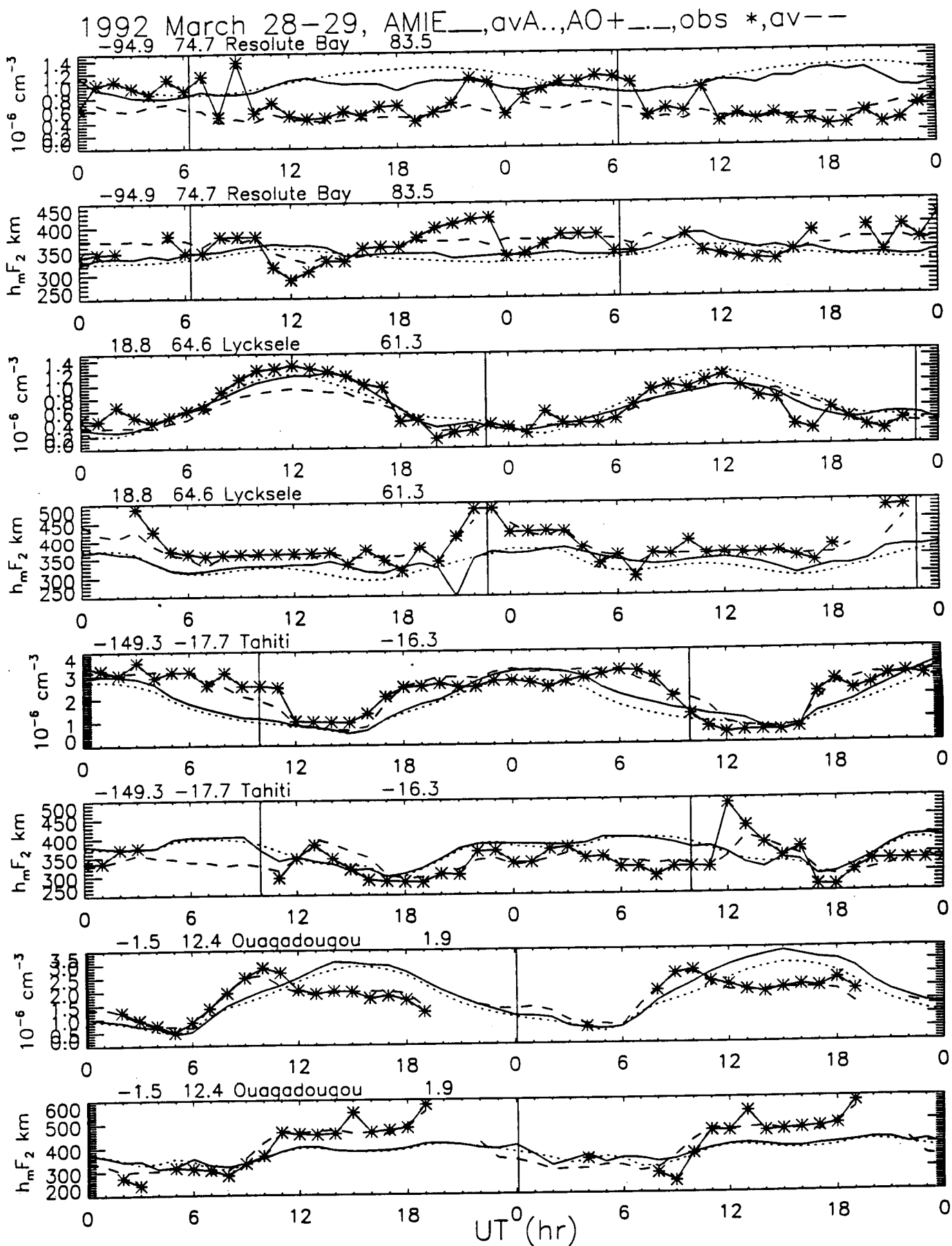


Figure 4

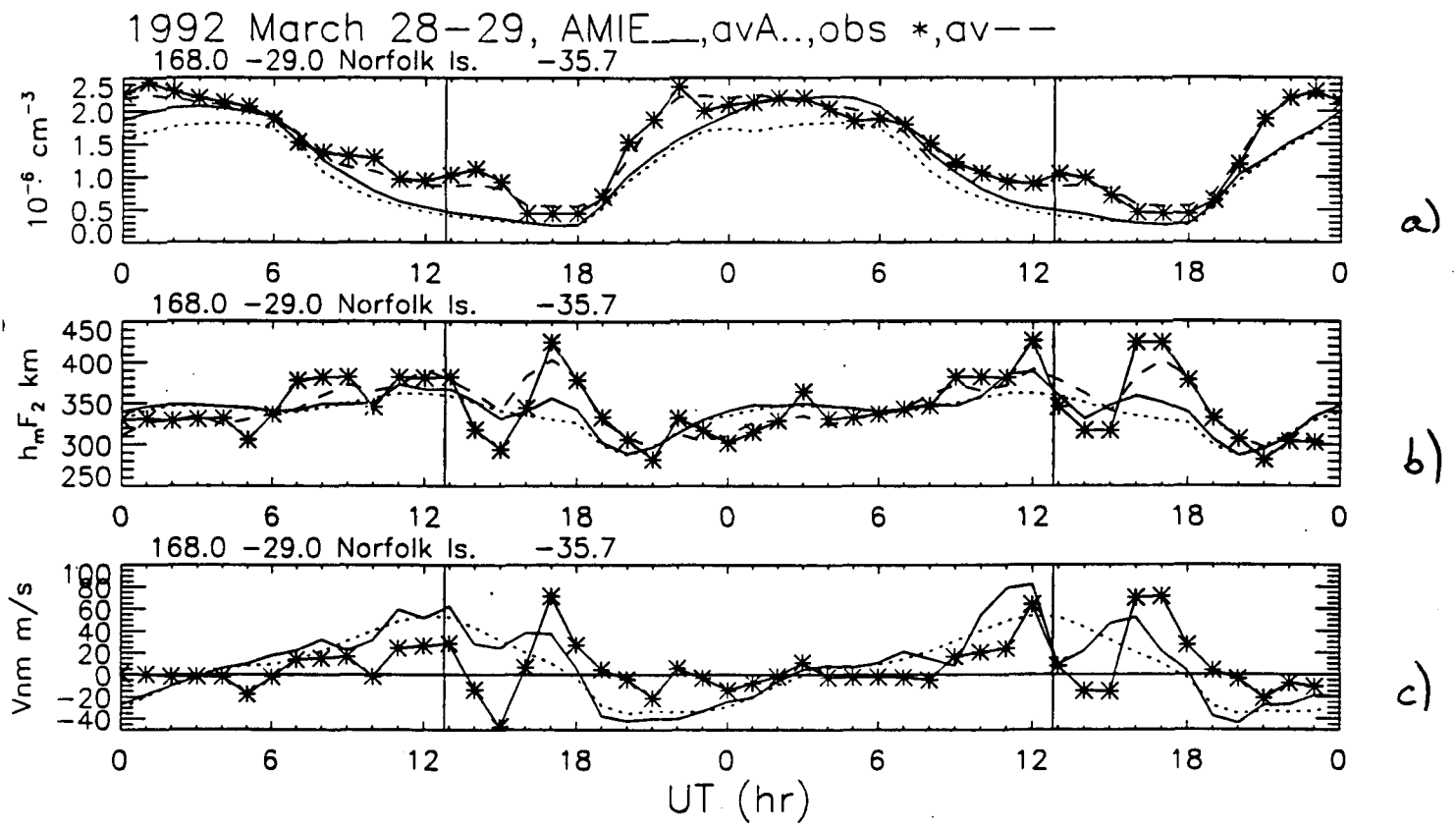
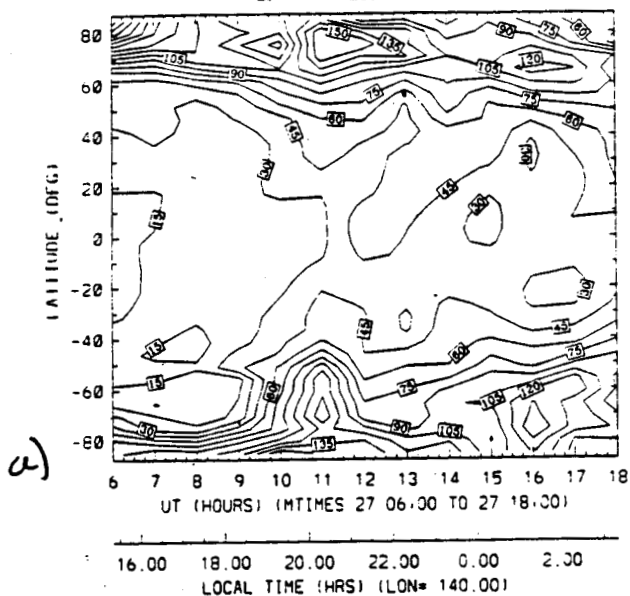
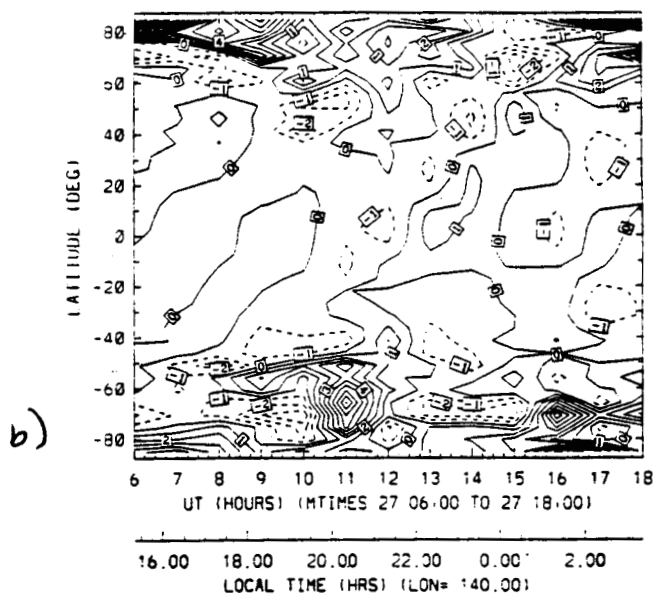


Figure 5

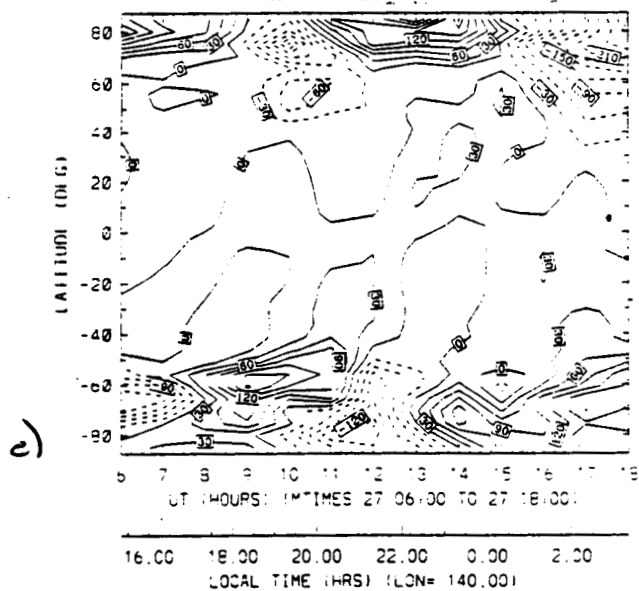
TIGCM NEUTRAL TEMPERATURE (DEG K) (DIFFERENCE)  
ZP= 2.0 LON= 140.00



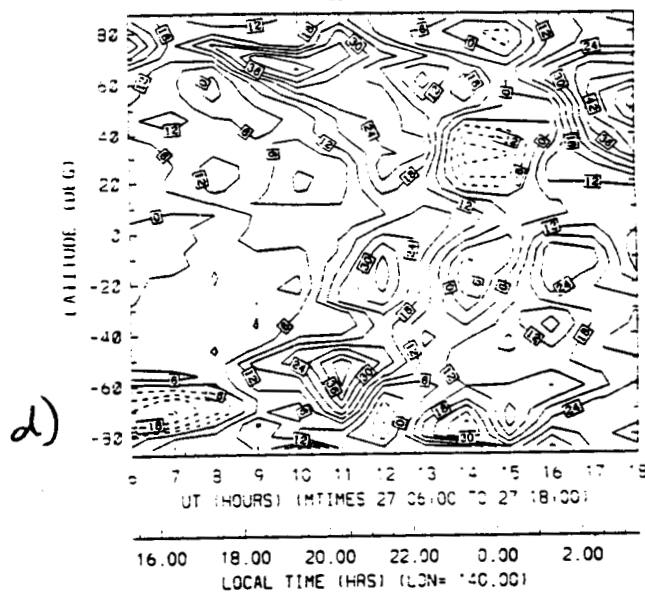
TIGCM VERTICAL WIND (PLUS UP) (M/S) (DIFFERENCE)  
ZP= 2.0 LON= 140.00



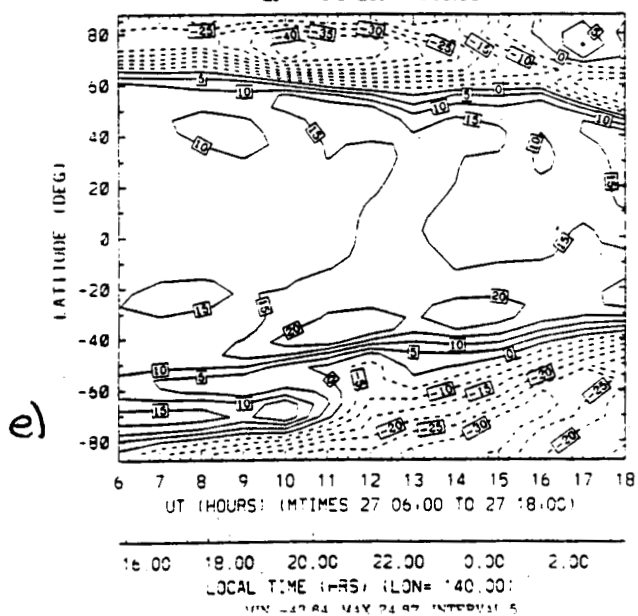
TIGCM NEUTRAL MERIDIONAL WIND (M/S) (DIFFERENCE)  
ZP= 2.0 LON= 140.00



TIGCM HMF2 (KM) (DIFFERENCE)  
LON= 140.00



TIGCM O/N2 (NUMBER DENSITY CM-3) (DIFFERENCE)  
ZP= 2.0 LON= 140.00



TIGCM FOF2 (MHz) (DIFFERENCE)  
LON= 140.00

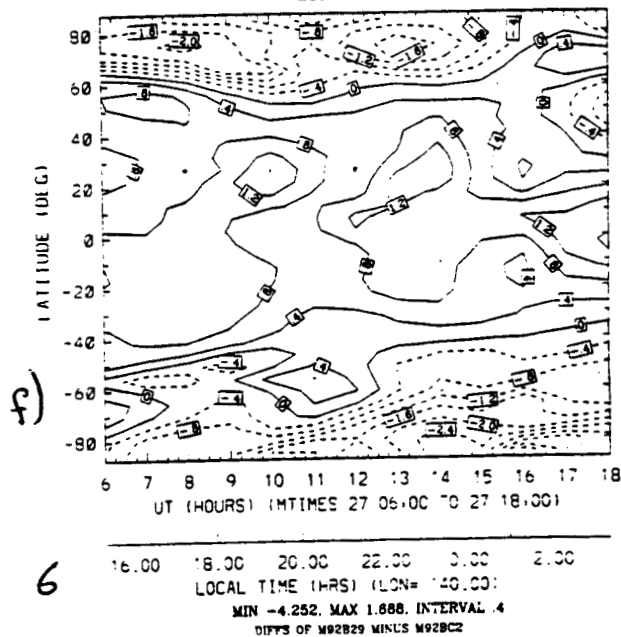


Figure 6

1992 March 28-29, AMIE\_\_\_, avA..., obs \*, av--,  $N_m F_2$

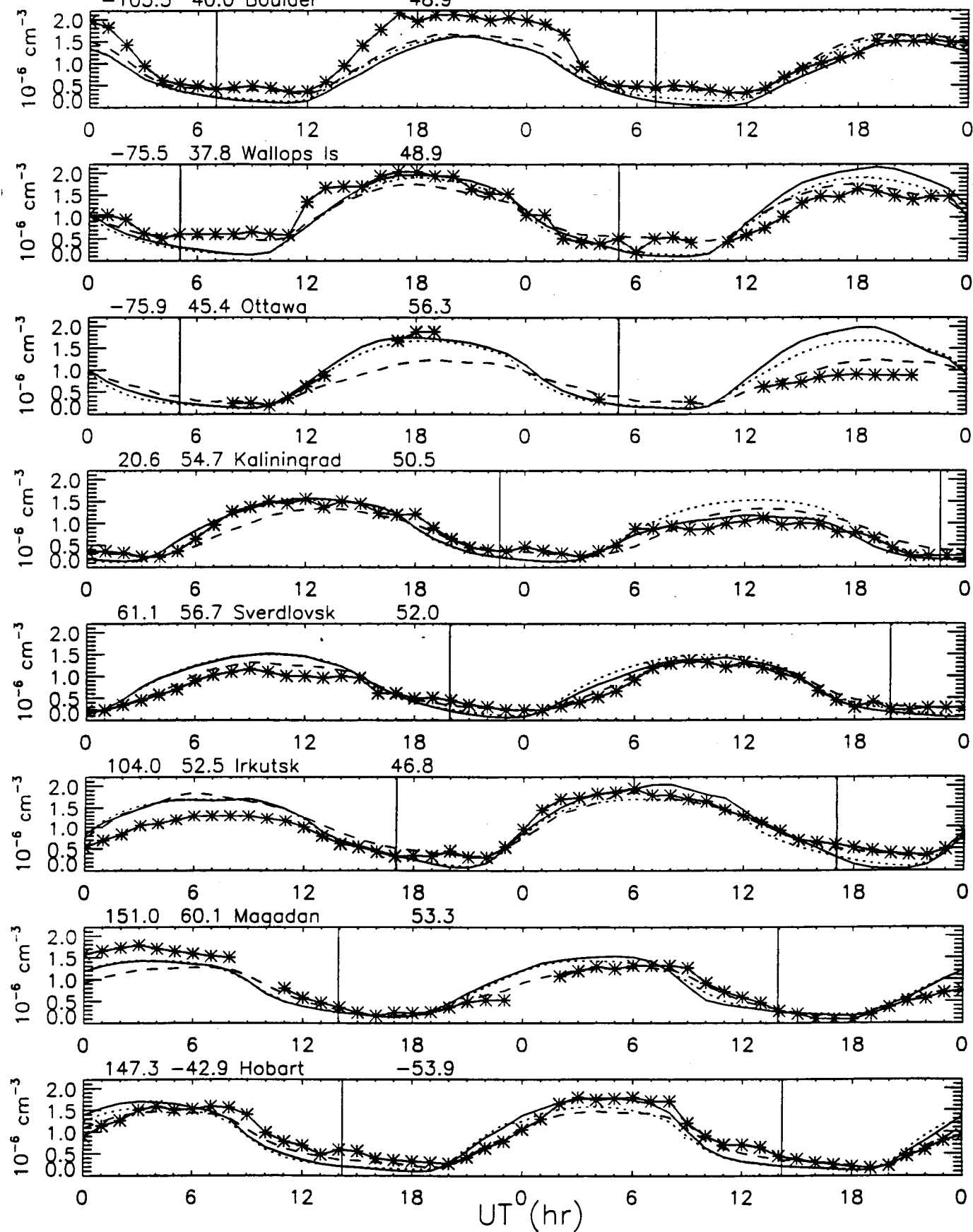


Figure 7

$\text{del}(\text{O}/\text{N}_2)$  at 52 N mag on  $Z=+2$

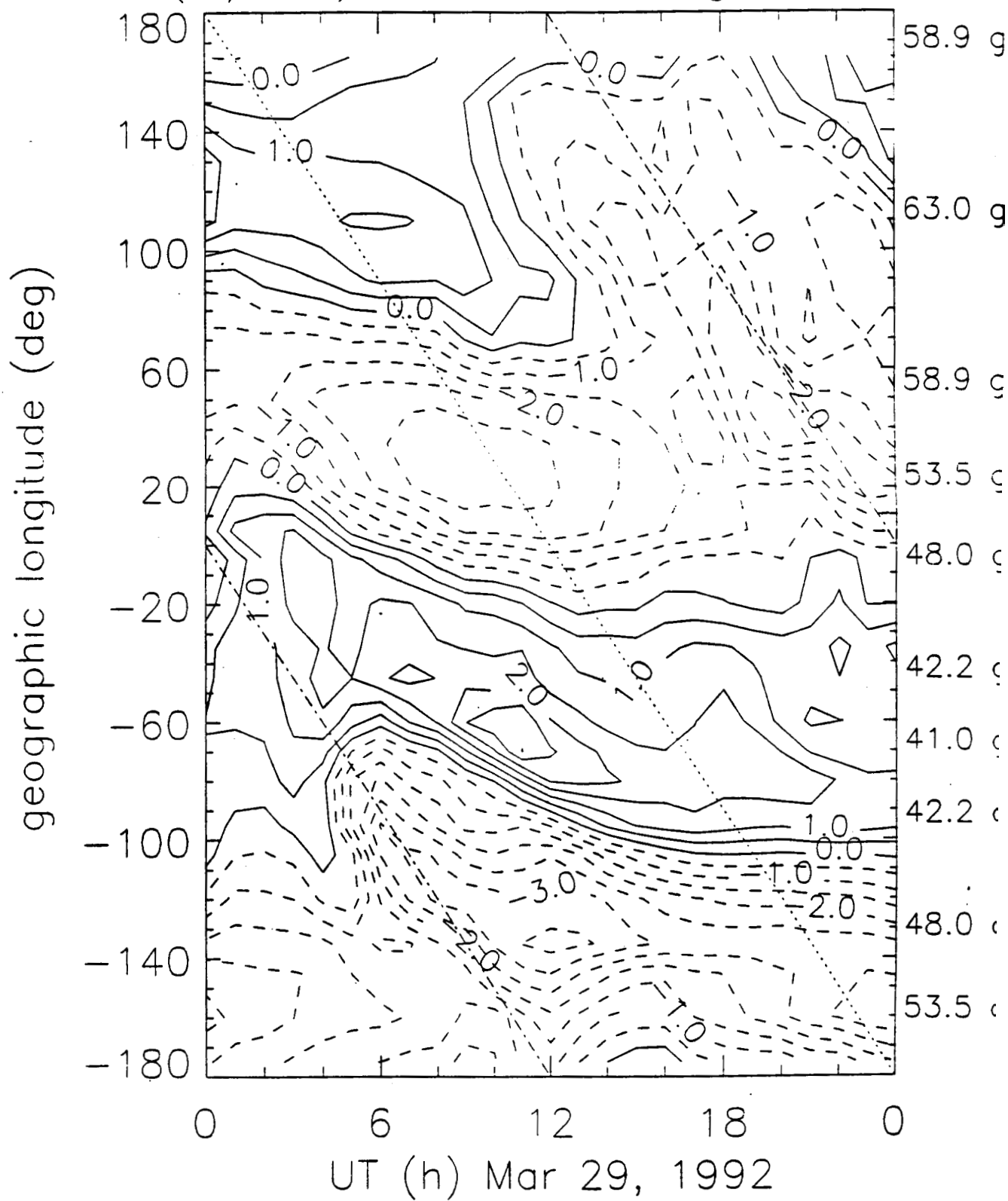


Figure 8



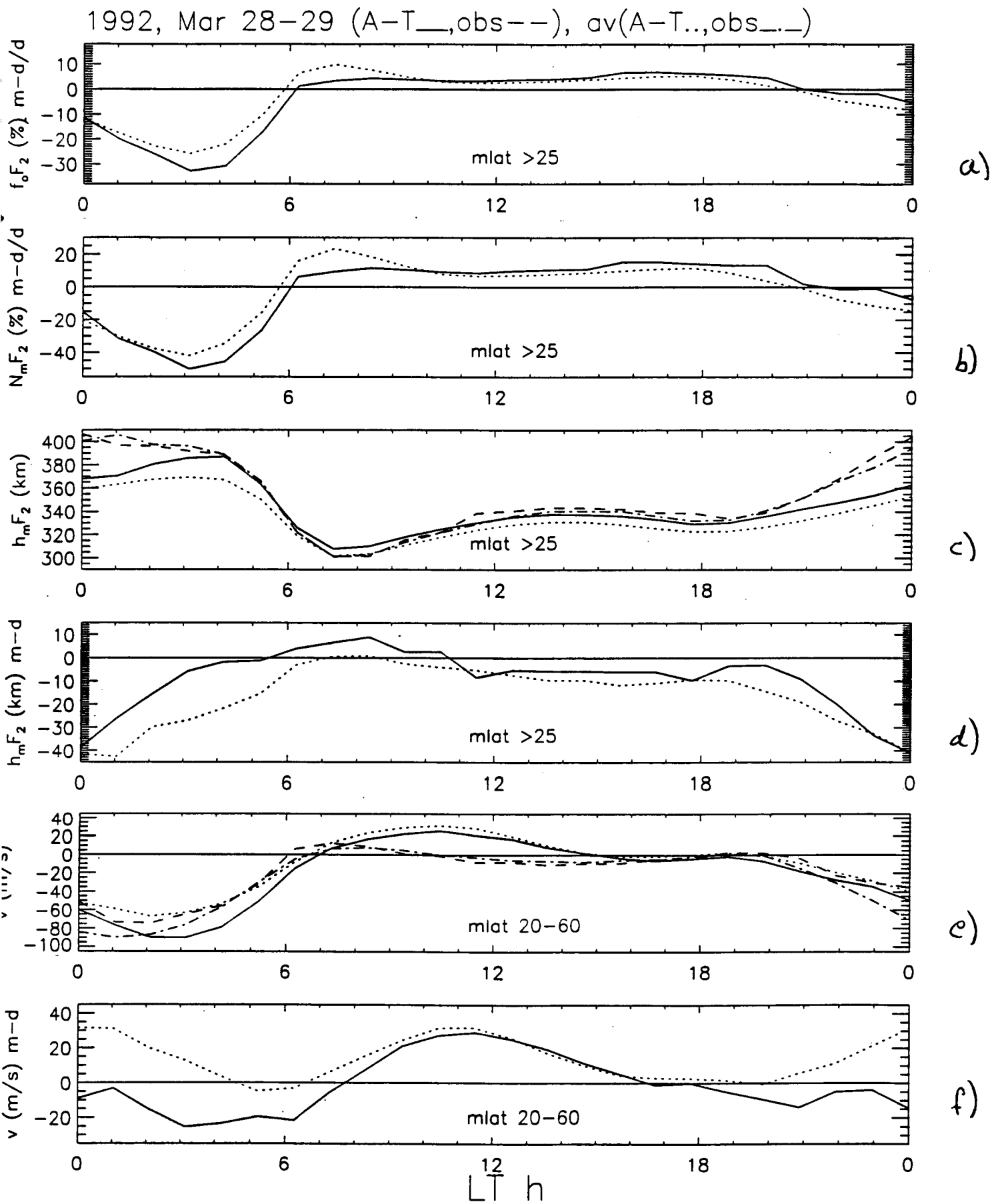


Figure 9

TIGCM  $O^+$  Flux at 550 km (—regular, - - - revised)

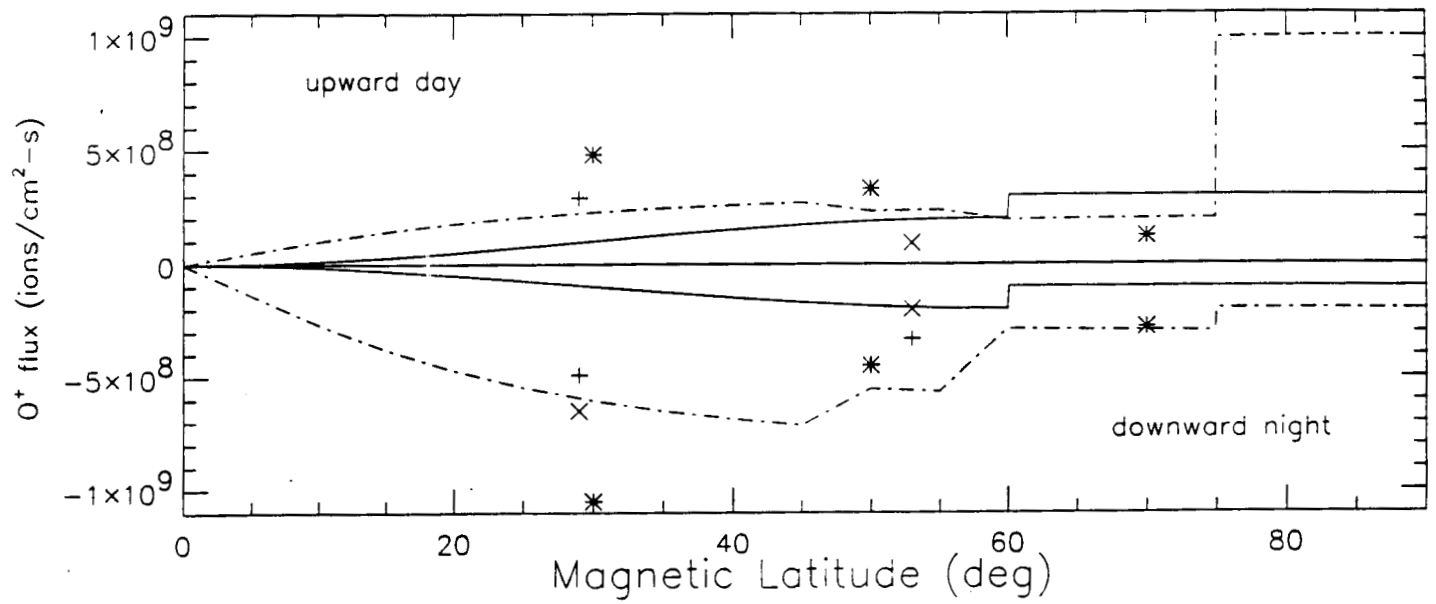


Figure 10

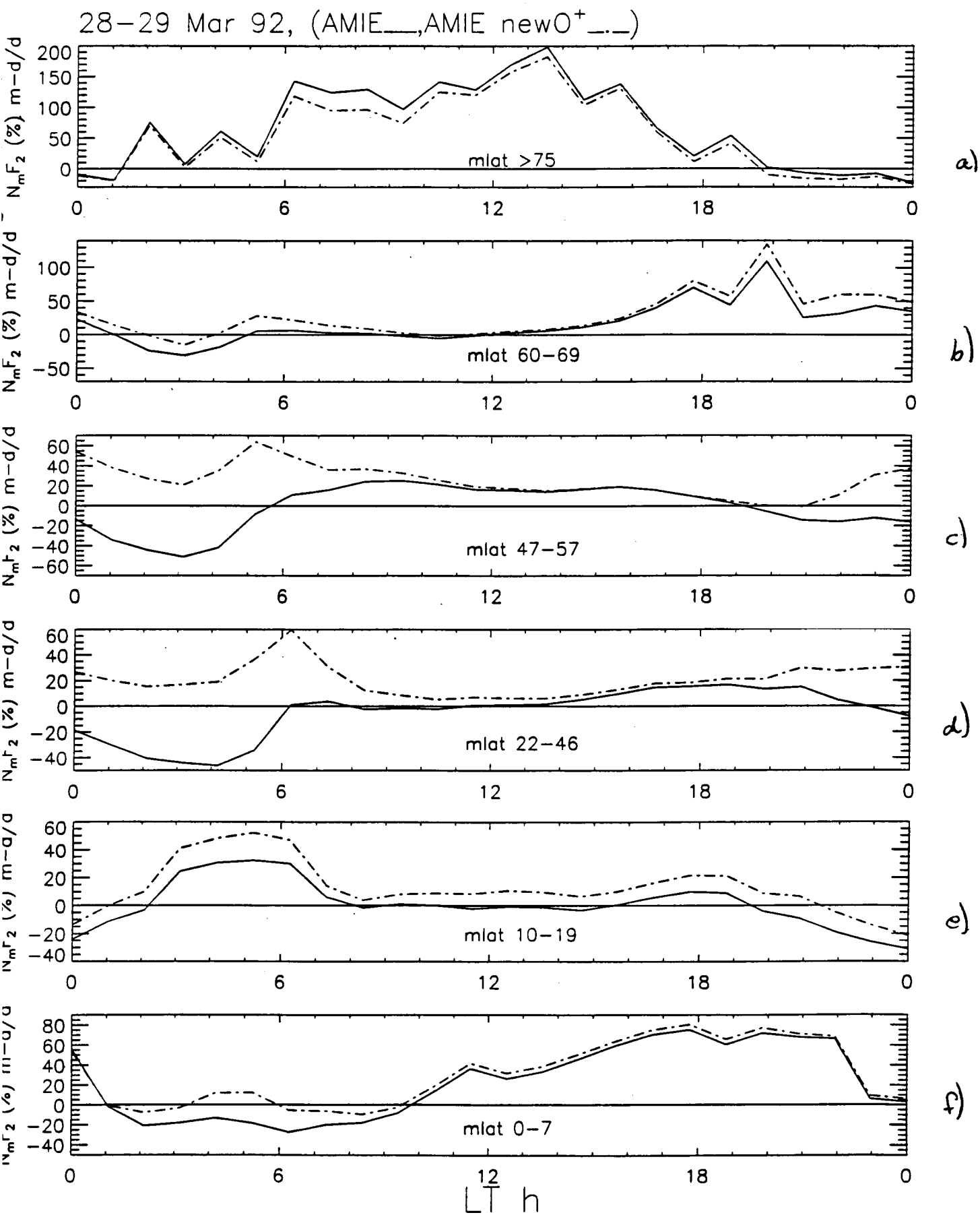


Figure 11

# **High Latitude Hall and Pedersen Conductances during Substorm Activity in the SUNDIAL-ATLAS Campaign**

**M. Lester and J.A. Davies**

*Ed, for your information. Note the  
author list now will change. Best  
wishes, Mark.*

**High Latitude Hall and Pedersen Conductances during Substorm  
Activity in the SUNDIAL-ATLAS Campaign.**

M. Lester and J.A. Davies

(Radio and Space Plasma Physics Group, Department of Physics and  
Astronomy, University of Leicester, Leicester, LE1 7RH, U.K.)

Submitted to Journal of Geophysical Research  
September 1995

## Abstract.

Simultaneous high time resolution observations of the height integrated Hall and Pedersen conductivities,  $\Sigma_H$  and  $\Sigma_P$ , the ionospheric electric field and the ground magnetic field during a magnetospheric substorm are reported. The measurements discussed here were taken during the SUNDIAL/ATLAS-1 campaign of March 24 - April 2 1992. The EISCAT UHF special programme SP-UK-ATLAS which operated on March 27 1992 provided continuous high time resolution, 10 s, measurements of the electron density and the ion vector velocity from which  $\Sigma_H$  and  $\Sigma_P$  and the ionospheric electric field were calculated. During the growth phase,  $\Sigma_P$  and  $\Sigma_H$  were less than 10 S and the ratio,  $R = \Sigma_H/\Sigma_P$ , was less than 1. Although both  $\Sigma_H$  and  $\Sigma_P$  increased at the onset of the expansion phase,  $R$  remained close to 1. This ratio provides information on the mean energy of the precipitating particles responsible for the enhanced conductances. A ratio of 1 implies a mean energy of the particles of 2 keV. Both  $\Sigma_H$  and  $\Sigma_P$  increased towards the end of the expansion phase with peak values of 71 S and 34 S respectively. The ratio  $R$  also increased to values exceeding 2, equivalent to mean energies of more than 6 keV. The largest value of  $R$  was 3.25 during the substorm recovery phase which is equivalent to mean energies of more than 10 keV. The maximum Hall current density during this interval was  $2.66 \text{ A m}^{-1}$  which occurred the early part of the recovery phase of the substorm. At a number of intensifications, peaks in the current density were observed, for which the electric field was responsible in some cases and the Hall conductance in others.

## 1. Introduction.

Modelling of the large-scale three dimensional current systems associated with the coupling of the ionosphere and magnetosphere has developed considerably in recent years (e.g. *Richmond and Kamide, 1988; Emery et al., 1990; Lu et al., 1995*). In particular, the technique of Assimilative Mapping of Ionospheric Electrodynamics (AMIE) can be employed to derive the distribution of the ionospheric conductances, electric fields, currents and other related quantities at high latitudes. Inputs to the model include radar and spacecraft measurements of electric fields or plasma velocities. The main input to the model, however, is magnetometer data and the results are dependent upon the ionospheric conductance. Usually, models of conductance (e.g. *Spiro et al., 1982; Fuller-Rowell and Evans, 1987*) are employed in this technique, although radar and satellite estimates of conductance can be included (e.g. *Knipp et al., 1989*). The height integrated Pedersen and Hall conductivities,  $\Sigma_P$  and  $\Sigma_H$  respectively, can be inferred from spacecraft measurements of precipitating electrons (e.g. *Spiro et al., 1982; Fuller-Rowell and Evans, 1987*). Incoherent scatter radar measurements of plasma density can also provide estimates of  $\Sigma_P$  and  $\Sigma_H$  (e.g. *Brekke et al., 1974, 1989; Kirkwood et al., 1988*). Spacecraft measurements can be made over a large spatial scale but cannot provide information of the temporal evolution of the measurements. Conversely, the ground based incoherent scatter measurements have a limited spatial coverage but the temporal coverage is excellent. The AMIE modelling provides a global coverage with improved temporal resolution but is reliant on data inputs.

Perturbations of the ground magnetic field can arise due to enhancements in conductivity, enhancements in electric field or some combination of both. The high-latitude nightside region is particularly susceptible to large scale magnetic perturbations, especially during magnetospheric substorms. The large scale auroral disturbances during substorms as well as potentially large electric fields associated with the destruction of open magnetic flux in the magnetotail can result in excursions of the horizontal and vertical magnetic field which can be greater than 500 nT. For the purposes of modelling the ionospheric electrodynamics in this region it is necessary to have a complete picture of the behaviour of the conductivity and electric field. Unfortunately, there have been relatively few attempts to undertake simultaneous measurements of the ionospheric electric field and conductivity during substorms. The Chatanika incoherent scatter radar provided the first results of such simultaneous measurements (see for example *Kamide and Vickrey, 1983* and references therein). *Kamide and Vickrey (1983)* noted that in the eastward electrojet in the evening sector, the magnitude of the northward electric field increased when the magnitude of the electrojet increased. Furthermore,

$\Sigma_H$  remained at  $\sim 10$  S even when the current density became as large as  $1 \text{ A m}^{-1}$ . The westward electrojet, on the other hand, appeared to have two separate components. In the 00 - 03 MLT sector, the electrojet intensity was maintained by a weak southward electric field and a high  $\Sigma_H$ . After 03 MLT, however, the electrojet was dominated by a strong southward electric field.

Whilst these results provide an important insight into the behaviour of  $\Sigma_H$  and electric fields, *Kamide and Vickrey (1983)* pointed out a number of caveats that needed to be considered because of limitations with the experiment. One of these was the large uncertainties in the north-south electric field. It has become apparent from tri-static measurements of ion velocity by EISCAT that the F-region electric field perpendicular to the magnetic field can vary on short ( $\sim 1$  minute) time scales (*Williams et al., 1990, 1992*). Furthermore, bi-static coherent radar measurements by STARE and SABRE demonstrate that the electric field can vary on horizontal spatial scales of tens of kilometres (e.g. *Baumjohann et al., 1981; Lester et al., 1990*). It is important, therefore, that simultaneous measurements of electric field and conductance be made to confirm these earlier results and EISCAT is well suited to this task.

Such an EISCAT study, employing continuous high time resolution measurements along the magnetic field of  $\Sigma_H$  and  $\Sigma_P$  in conjunction with electric field measurements made at 300 km on the same field line for part of the time, was reported by *Kirkwood et al., (1988)*. In addition, these authors utilised auroral images from the Viking spacecraft in order to place the observations of  $\Sigma_H$ ,  $\Sigma_P$  and electric field in a spatial context as well as in relation to substorm phases. Concentrating on conductances associated with the substorm westward electrojet, *Kirkwood et al. (1988)* found that  $\Sigma_H$  varied between 15 S and 30 S and the ratio,  $R$ , of  $\Sigma_H$  and  $\Sigma_P$  between 2 and 2.5, with little variation from one substorm to another. These observations were made within the diffuse aurora. Conductances in the discrete aurora leading the westward travelling surge (WTS) and the auroral bulge were much higher. In these locations  $\Sigma_H$  varied between 60 S and 100 S and  $R$  between 2 and 4. The highest observed values of  $\Sigma_H$  and  $\Sigma_P$  were 120 S and 48 S respectively at the equatorward edge of the WTS.

Previous estimates of conductances during substorms had also been made by modelling ground magnetometer data and STARE estimates of the electric fields. During auroral break-ups at the substorm expansion phase onset, *Baumjohann et al. (1981)* estimated peak values of 30 S for  $\Sigma_H$  and 10 S for  $\Sigma_P$  close to the western edge of the auroral active region. In the higher conducting region behind the head of the WTS, *Opgenoorth et al. (1983)* suggested values of 25 S and 20 S for the Hall and Pedersen conductances respectively.



The first ATLAS mission (*Torr, 1993*) of March 24 1992 - April 2 1992 was the focus for a co-ordinated ground based campaign involving the SUNDIAL experimenters (*Szuscszewicz et al., 1995*). As part of this ground-based campaign, the EISCAT UHF radar was operated for a short, 6 hour, interval on March 27 1992 in a special mode, SP-UK-ATLAS. An extended CP-1-J run of the EISCAT UHF radar also took place during the latter part of the ATLAS mission. This paper presents estimates of  $\Sigma_p$  and  $\Sigma_H$  and associated electric fields during substorm activity from the interval on March 27 1992.

## 2. Overview of 18 - 22 UT March 27 1992.

The run of the EISCAT UHF special programme SP-UK-ATLAS took place between 1600 UT and 2200 UT on March 27 1992. This experiment was effectively the CP-1-J experiment (see for example *Davies et al., 1995*) in which the Tromsø beam is pointed parallel to the magnetic field at an altitude near the F-region peak. The one significant difference, however, is that in the SP-UK-ATLAS experiment the two remote site antennas, at Sodankylä and Kiruna, intersect the Tromsø beam at a fixed height of 275 km. In CP-1-J, the remote sites intersect the Tromsø beam at 278 km for only 90 s in every 5 minutes, with the remaining time being spent in the E-region. Both experiments transmit the same pulse schemes, a long pulse for observations between 150 km and 550 km, two power profiles and an alternating code for measurements between 80 and 270 km. The SP-UK-ATLAS experiment provides continuous high time resolution estimates of the electric field in the F-region which, therefore, allows us to make simultaneous high time resolution measurements of conductance and electric fields. We concentrate on the interval 1800 - 2200 UT and summarise the EISCAT observations below.

The electron density and electron temperature were highly variable between 1800 and 2200 UT. The peak value of electron density varied between  $5 \times 10^{11} \text{ m}^{-3}$  and  $9 \times 10^{11} \text{ m}^{-3}$  and the altitude of the peak between about 250 km and 450 km, generally increasing towards the end of the interval. The electron temperature was enhanced between 1830 UT and 1900 UT and this was followed after 1930 UT by shorter lived periods of enhanced electron temperature. The ion temperature exhibited several short intervals of enhanced values which are due to ion frictional heating (e.g. *McCrea et al., 1991*). At 1800 UT the ion velocity perpendicular to the magnetic field was westward and southward, becoming eastward from about 1900 UT until 1930 UT. Variable flow followed with values reaching  $1 \text{ km s}^{-1}$ . After 2015 UT the ion velocity remained eastward, apart from two 2 minute intervals starting at 2044 UT and 2141 UT.

The alternating code measurements of enhanced levels of E-region ionisation provide evidence that particle precipitation occurred over much of the interval. Between 1830 and 1900 UT there were strong levels of particle precipitation with values of electron density of order  $1 \times 10^{12} \text{ cm}^{-3}$  at 120 km altitude. The precipitation however did not penetrate to altitudes much lower than 118 km. After 1930 UT there were several bursts of precipitation again only penetrating to about 118 km. After about 2040 UT stronger and more continuous precipitation occurred and penetrated to about 100 km.

In summary, the SP-UK-ATLAS observations between 1800 and 2200 UT on 27 March 1992 can be divided into four separate periods: 1800 - 1823 UT when there is no electron or ion heating and the ion velocity is westward with a magnitude of  $< 400 \text{ m s}^{-1}$ ; 1823 - 1855 UT when there were intervals of precipitation into the E and F regions, continuous electron heating prefaced by a short-lived ion heating event and a high ion velocity peaking at 1827 UT; 1855 - 1935 UT during which there was precipitation but only into the F-region and some intervals of electron and ion heating with variable westward/eastward ion velocity; 1935 - 2200 UT when there was precipitation initially to 118 km and then to 100 km, variable eastward flow initially and then eastward flow between  $400 - 800 \text{ m s}^{-1}$  from 2015 UT.

Investigation of magnetometer data from the IMAGE network (*Lühr, 1994*), which was based upon the EISCAT magnetometer cross (*Lühr et al., 1984*) demonstrates that the interval 1800 - 2200 UT contains substorm activity (Figure 1). One sensitive indicator of the substorm expansion phase and subsequent intensifications is the Pi2 pulsation (*Rostoker et al., 1980*) and the first Pi2 identified in the SAMNET data (*Yeoman et al., 1990*) was at 1936 UT. This was followed by Pi2 pulsations at 2006 UT, 2018 UT, 2042 UT, 2051 UT, 2100 UT and 2118 UT, where all times are accurate to within one minute. These times are identified in Figure 1 by the vertical lines. The first of these was associated with a weak negative X (North-South) component bay at SOR of approximately 100 nT, which is indicative of a weak westward electrojet. Subsequent Pi2 pulsations were also associated with negative excursions of the X component at MUO and PEL (2006 UT), SOR and MAS (2018 UT and 2042 UT), MAS and MUO (2051 UT), PEL (2100 UT) and BJO (at 2110 UT following the event at 2100 UT). The magnitudes of the bays associated with the pulsations were low to start ( $\sim 100 \text{ nT}$ ), but larger at the times of the later pulsations ( $-200 \text{ nT}$  to  $-300 \text{ nT}$ ). The integral effect was negative bays of up to  $-800 \text{ nT}$  at MUO and  $-500 \text{ nT}$  at SOR compared with the quiet time magnetic variation. After the last Pi2 pulsation, there was a general recovery of the magnetic field at all of the stations, although the minimum value of the X component occurred at different times at different stations. Further discussion of the electrojets and substorm current wedge associated with the substorm intensifications will follow in section 4.

Substorm identification can be difficult and often a single characteristic phenomenon may not be sufficient to identify all substorm expansion phases and intensifications (*Yeoman et al., 1994*). Another often used indicator of magnetospheric substorms is the particle injection at geosynchronous orbit (e.g. *Lanzerotti et al., 1971; Belian et al., 1981*). Such particle injections can either be dispersionless in energy which generally indicates that the spacecraft is close to the field lines which map to the auroral breakup region or dispersed in energy which indicates that the particles, once injected into the near earth tail, have undergone curvature and gradient drift (*Reeves et al., 1991*). Electron fluxes in the 30 - 500 keV range from 4 geosynchronous spacecraft operated by Los Alamos indicate only one large scale dispersionless injection, at 2009 UT at spacecraft 1991-030 which was located at a local time of ~0051 MLT. This was followed by a series of 4 increases in the particle flux at the same spacecraft at 2018 UT, 2030 UT, 2045 UT and 2106 UT which were also all dispersionless and are indicative of subsequent substorm intensifications. There followed at the three other spacecraft dispersed injections where the higher energy particles peaked before the lower energy particles. These dispersed injections could in general be related to the dispersionless injections observed by spacecraft 1991-030. One event, at 1848 UT, was observed by spacecraft 1989-046 at a time of 0746 MLT, and could not be related to a dispersionless injection at any of the 4 spacecraft or to any other evidence of substorm activity, although particle precipitation into the E-region occurred at EISCAT between 1823 and 1855 UT.

In summary, separate substorm expansion phases occurred at 1936 UT and 2006 UT. An earlier expansion phase may have occurred before 1848 UT although this is difficult to confirm. The expansion phase at 2006 UT involved a Pi2 pulsation, an enhanced westward electrojet and particle injection in the near earth tail and consisted of a number of intensifications. We argue that this is a separate expansion phase from the one at 1936 UT on the basis of the time difference from the first event of more than 20 minutes, a similar time difference to that employed by *Farrugia et al. (1993)* in their study of substorm activity during the passage of an interplanetary magnetic cloud. This second expansion phase lasted until at least 2118 UT, the time of the final Pi2 pulsation. During each expansion phase there were intervals of particle precipitation into the lower ionosphere which modified the Pedersen and Hall conductivities. No solar wind plasma or IMF measurements are available for this interval.

### 3. Conductances.

The height integrated Pedersen and Hall conductivities, or Pedersen ( $\Sigma_P$ ) and Hall ( $\Sigma_H$ ) conductances (Figure 2) have been calculated between 1800 to 2200 UT from the EISCAT SP-

UK-ATLAS alternating code measurements of electron density, analysed at an integration time of 60 seconds. The conductances were calculated over the altitude range 86 - 200 km along the magnetic field direction. The ion-neutral and electron-neutral collision frequencies were calculated using the MSIS-86 model (*Hedin, 1987*) to provide estimates of the neutral atmospheric composition and temperature within the altitude range of interest. Estimates of the ion and electron gyrofrequencies were based on values of the magnetic field from the IGRF model. The magnetic latitude of the Tromsø is between that of SOR and MAS, but its longitude is some 3° to the west of these stations.

The conductances were typically a few Siemens at the start of the interval (Figure 2, upper panel). Between 1828 UT and 1855 UT, both Hall (dotted line) and Pedersen (full line) conductances increased above 10 Siemens, reaching peak values for  $\Sigma_P$  of 40 S at 1851 UT and 27 S at 1850 UT in the case of  $\Sigma_H$ . The ratio of the two conductances,  $R = \Sigma_H/\Sigma_P$ , (Figure 2, lower panel) remained, in general, less than one. Following 1855 UT, both  $\Sigma_P$  and  $\Sigma_H$  decreased to below 10 S and remained so until about 2015 UT apart from three brief intervals centred at 1944 UT, 1956 UT and 2005 UT. Between 1855 UT and 2015 UT the ratio of the two conductances remained close to 1. Both  $\Sigma_P$  and  $\Sigma_H$  were higher following 2016 UT, with the former peaking at values of between 22 and 27 S and the latter peaking at values between 30 and 45. Higher conductances continued until 2036 UT, during which time  $R$  was between 1 and 1.5. After 2036 UT,  $\Sigma_P$  and  $\Sigma_H$  increased again, with  $\Sigma_P$  peaking at values between 20 and 33 S, while  $\Sigma_H$  now peaked at values above 50 S, and was well above 20S until 2153 UT. Between 2016 UT and 2100 UT the ratio of the two conductances was typically between 1.5 and 3.

The variation of  $R$  as a function of time (Figure 2, lower panel) demonstrates that the interval can on average be divided into two parts. The first from 1800 UT to 2000 UT where  $R$  was typically of order 1 and the second from 2000 UT to 2200 UT where  $R$  was typically larger than 1 and often of order 2 or more. The zonal component of the ion velocity was typically eastward during the first interval and westward during the second. Figure 3 further demonstrates the relationship between  $\Sigma_H$  and  $\Sigma_P$  for the two parts of the interval. Between 1800 and 2000 UT (Figure 3, upper panel), the two conductances were similar, although  $\Sigma_P$  was typically larger than  $\Sigma_H$ , with most values below 10S. Between 2000 and 2200 UT (Figure 3, lower panel)  $\Sigma_H$  had a much wider distribution of values and was closer to twice the value of  $\Sigma_P$ . This variation illustrates that the particle spectrum during the second interval was much harder with more particles penetrating to lower altitudes (*Robinson et al., 1987*). Thus, not only did the level of precipitation increase but also the particle spectrum changed from the

first to the second interval. Discussion of the conductances and their relationship to substorm phase is given in section 4.

The electric field measurements by EISCAT, were made at a height of 275 km, compared with the conductances which were measured between 86 km and 200 km. Although the EISCAT beam was parallel to the magnetic field at 275 km, the nature of the magnetic field is such that the measurements at lower altitudes were not exactly on the same field line. The differences were, however, small and we assume that measurements of  $E$ ,  $\Sigma_P$  and  $\Sigma_H$  are effectively along the same field line. Finally, before discussing in detail the electric field variation we note that the integration period of 1 minute is not short enough to cope with extremely short lived (a few seconds) variations in the electric field recently measured by EISCAT (*Lanchester et al., 1995*). For the purposes of this study, however, the time resolution of 1 minute is more than adequate. The electric field has been calculated from the ion velocity perpendicular to the magnetic field only.

The electric field (Figure 4, upper panel) varied between  $5 \text{ mV m}^{-1}$  and  $60 \text{ mV m}^{-1}$  during this interval. The field generally varied between  $15$  and  $25 \text{ mV m}^{-1}$  until 2000 UT and between  $20$  and  $40 \text{ mV m}^{-1}$  after 2000 UT. The electric field was near  $20 \text{ mV m}^{-1}$  until 1842 UT when it decreased to typically less than  $10 \text{ mV m}^{-1}$ . Initially,  $\Sigma_H$  (Figure 4, lower panel) was between  $2$  and  $3 \text{ S}$  and then increased to about  $20 \text{ S}$  at 1835 UT.  $\Sigma_H$  decreased at about 1855 UT, coincident with an increase in the electric field. Just before the first Pi2 pulsation at 1936 UT, there was a large spike in the electric field approaching nearly  $50 \text{ mV m}^{-1}$  and this was followed by a general increase in both the electric field and  $\Sigma_H$ . The electric field then was typically larger than  $20 \text{ mV m}^{-1}$  until the end of the interval. The subsequent Pi2 pulsations were associated with increases in the electric field, although only the events at 2018 UT and 2042 UT had simultaneous increases in  $\Sigma_H$ . The electric field in the last two hours of the interval was generally more structured than  $\Sigma_H$ .

#### 4. Discussion.

It is instructive to consider how the conductances varied as a function of substorm phase. As there were no IMF data, it is not possible to identify the time of any southward turning which is normally expected to be the initiation of the substorm growth phase (*Lester et al., 1993*). Since the growth phase is normally expected to last between 30 and 60 minutes (*Lui, 1991*), we have selected the interval 1900 - 1935 UT as representative of the growth phase in this case. Taking a longer interval may have included the response to the possible expansion phase

identified by the geosynchronous spacecraft 1989-046, which observed an energy dispersed particle injection at 1848 UT. During the growth phase,  $\Sigma_H$  was typically less than 2 S,  $\Sigma_P$  less than 3 S and their ratio  $R$  less than 1.0. The average values of  $\Sigma_P$  and  $\Sigma_H$  between 1900 and 1935 UT were 2.39 S and 2.65 S respectively and the mean value of  $R$  was 0.88.

The interval following the first Pi2 pulsation, 1936 UT to 2005 UT, is taken to represent the first expansion phase. The mean values and ranges for  $\Sigma_H$ ,  $\Sigma_P$  and  $R$  for this interval are given in Table 1. There was a clear increase in both  $\Sigma_H$  and  $\Sigma_P$  in the expansion phase, although  $R$  was only marginally larger than in the growth phase. The second expansion phase interval, which followed the first of the dispersionless injections, can be divided into three intervals, 2006 - 2017 UT, 2018 - 2042 UT and 2043 - 2130 UT. Mean values and ranges of the conductances and their ratio are found in Table 1. During the first of these intervals (2006 - 2017 UT),  $\Sigma_P$ ,  $\Sigma_H$  and  $R$  were similar to the earlier expansion phase. During the second (2018 - 2042 UT), however, there was a significant increase in all three parameters with three major peaks, at 2020 UT ( $\Sigma_H$  was 45 S and  $\Sigma_P$  22 S), at 2026 UT ( $\Sigma_H$  was 37 S and  $\Sigma_P$  25 S), and 2031 UT ( $\Sigma_H$  was 30 S and  $\Sigma_P$  25 S). In the third interval (2043 - 2130 UT), all three parameters again increased.  $\Sigma_H$  and  $\Sigma_P$  peaked at 71 S and 34 S respectively at 2045 UT after which both then tended to decline with  $\Sigma_H$  showing the highest variability.

The recovery phase of the substorm followed the last of the Pi2 pulsations. The onset for the recovery phase is difficult to identify but we have chosen the interval 2130 to 2200 UT (the end of the data) as representative of the initial part of the recovery phase if not the full interval. During the first ten minutes of the recovery phase,  $\Sigma_H$  was larger than 40 S with peaks of 65 S and 77 S at 2134 UT and 2139 UT respectively. Following this last peak,  $\Sigma_H$  decreased in an almost monotonic fashion to 20 S at 2200 UT. The corresponding peaks in  $\Sigma_P$  were 26 S and 24 S, and  $\Sigma_P$  decreased to 10 S at 2200 UT. The ratio  $R$  was larger than 2 until 2145 UT, with a peak value of 3.25 at 2139 UT. During the last 15 minutes,  $R$  was between 1.6 and 2.4. The mean value of  $\Sigma_H$  was 36.3 S,  $\Sigma_P$  was 15.8 and  $R$  was 2.22.

In summary, we find that the Pedersen conductance was dominant during the growth phase, the first expansion phase and the initial part of the second expansion phase. The Hall conductance eventually became dominant in the latter part of the expansion phase and continued to be so well into the recovery phase. Indeed, the ratio  $R$  was largest in the earliest stages of the recovery phase. The largest value of  $\Sigma_P$  was 34 S which occurred late in the expansion phase, although a higher value had occurred as part of the possible expansion phase before

1848 UT. The largest value of  $\Sigma_H$  of 76 S occurred in the early recovery phase.

Before comparing these observations with previous results, it is helpful to determine the location of the substorm currents relative to Tromsø. The substorm current wedge (McPherron *et al.*, 1973) provides a simple representation of the large scale currents associated with substorm expansion phase onset. At the time of the first Pi2 pulsation, the current wedge was located east of the SAMNET array and hence east of Tromsø. The X component at SOR was indicative of a westward electrojet whereas at Tromsø the direction of the ion velocity in the F region became westward immediately after the Pi2 pulsation. The westward ion velocity is equivalent to an eastward electrojet implying that a shear in the current existed between Tromsø and SOR. For the next three Pi2 pulsations, at 2006 UT, 2018 UT and 2043 UT, the centre of the current wedge was east of NUR ( $\sim 102^\circ$  magnetic longitude), whereas the western (upward) field-aligned current (FAC) was between GML and NUR ( $78^\circ - 102^\circ$  magnetic longitude). Unfortunately, the station at KVI ( $96^\circ$  magnetic longitude) was not operational. The IMAGE array indicates a westward electrojet centred at latitudes equatorward of Tromsø. The ion flow at Tromsø was eastward (equivalent to a westward electrojet) from 2018 UT. Following the first Pi2 pulsation of this expansion phase at 2006 UT, there was a rapid increase in westward flow to larger than  $1 \text{ km s}^{-1}$ , at 2013 UT, but the ion flow had then turned eastward by 2015 UT. Thus Tromsø is likely to have been located poleward of the electrojet centre and possibly close to the downward FAC for the second expansion phase onset, but then east of this FAC for the following intensifications. For the last three intensifications, the western FAC was west of GML ( $78^\circ$  magnetic longitude), while the electrojet remained centred equatorward of Tromsø. The ion flow was eastward. Thus, we expect Tromsø to have been located within the substorm current wedge during these intensifications.

We begin our comparison with previous estimates of conductances by considering the growth phase values. Kirkwood *et al.* (1988) noted that in the diffuse aurora associated with the growth phase,  $\Sigma_H$  was typically between 2 and 15 S,  $\Sigma_P$  between 1 and 8 S and the ratio  $R$  between 1.6 and 2.0. The growth phase discussed above had values which were typically less than these, in particular  $\Sigma_H$  reached a value of only 7.5 S and the ratio  $R$  was typically less than 1. Unlike Kirkwood *et al.*, however, we have no direct evidence for the diffuse aurora in the radar beam during the growth phase. The values of  $\Sigma_H$  and  $\Sigma_P$  discussed earlier are higher than those during quiet periods during the extended run of CP-1 later in the campaign. We therefore believe that these values are related to particle precipitation. Other estimates of the growth phase conductances include 9 S for  $\Sigma_P$  (Mishin *et al.*, 1986), based upon a modified model of Spiro *et al.* (1982). Assuming that the higher values of  $\Sigma_H$  and  $\Sigma_P$  during the

growth phase are associated with particle precipitation, we can estimate the average energies of the precipitating electrons (*Robinson et al., 1987*). Assuming a Maxwellian electron distribution, the mean energy for values of  $R$  between 0.5 and 1 is typically between 1 keV and 2 keV (*Robinson et al., 1987*).

The peak values for  $\Sigma_H$  and  $\Sigma_p$  during the first expansion phase may have been associated with discrete auroral forms but the values for  $\Sigma_H$  are lower than those reported by Kirkwood et al. for discrete auroral forms at expansion phase onset, which were typically larger than 30 S. It is only during the later intensifications of the second expansion phase that  $\Sigma_H$  began to reach values similar to those associated with discrete arcs as well as expansion phase diffuse aurora of 15 - 30 S reported by *Kirkwood et al. (1988)*. Furthermore, we appear to have lower values of  $R$ , which may be due to the larger range of altitudes over which we have integrated the conductivity since there is a significant contribution to  $\Sigma_p$  at altitudes between 160 and 200 km. A comparison of  $\Sigma_p$  over the altitude range 86 - 200 km with  $\Sigma_p$  over the range 86 - 150 km, similar to that employed by *Kirkwood et al. (1988)* indicates the former is on average over the whole interval 20% higher than the latter. This does not fully account for the lower values of  $R$  reported here. We believe it is necessary to integrate up to altitudes of 200 km in order to gain a complete picture of the behaviour of  $\Sigma_p$ . The location of the break up region was most likely to have been west of Tromsø at these times based upon the current wedge identification. Therefore it is likely that these values are not associated with the WTS, but possibly with the auroral bulge. Values of  $R$  up to 2.5 indicate average particle energies associated with these conductances of 8 keV. Finally, the recovery phase has the peak value of  $R$  of 3.3 which is consistent with mean energies of  $> 10$  keV.

The simultaneous measurements of the electric field and Hall conductivity allows us to compute the Hall current density during the interval. Following *Lühr et al. (1994)* we use the expression

$$J_H = E_F \Sigma_H$$

where  $E_F$  is the electric field perpendicular to the magnetic field in the F region,  $\Sigma_H$  is the Hall conductivity integrated over the 86 to 200 km altitude range. The Hall current density for the interval 18 - 22 UT derived from the above relationship is given in Figure 5. The peak value in the Hall current density of  $2.66 \text{ A m}^{-1}$  occurred at 2139 UT coincident with the peak in Hall conductance of 76.5 S (note that the electric field was  $38.4 \text{ mV m}^{-1}$ ). The current density reached values larger than  $1 \text{ A m}^{-1}$  in the latter part of the expansion phase and the early part of



the recovery phase.

Close inspection of Figure 5 illustrates that there were peaks in the Hall current density which occurred close to the times of the Pi2 pulsations. At 1936 UT, the peak current density of  $264 \text{ mA m}^{-1}$ , was a result of the large peak in electric field close to  $50 \text{ mV m}^{-1}$  (Figure 4). The current densities following this peak were higher than those before the Pi2 pulsation but were due to an enhanced  $\Sigma_H$ . The peak in current density at 2006 UT was caused by a peak in conductance ( $17.5 \text{ S}$ ) rather than the electric field which remained between 20 and  $30 \text{ mV m}^{-1}$ . The Pi2 pulsation at 2018 UT was associated with a gradual rise in current density which was a result of an increase in  $\Sigma_H$  from  $3 \text{ S}$  at 2012 UT to  $44.5 \text{ S}$  at 2020 UT. The peak current density of  $851 \text{ mA m}^{-1}$  occurred at 2021 UT when  $\Sigma_H$  was starting to decrease and the electric field starting to increase. Another gradual rise in current density followed the Pi2 at 2042 UT. This was again associated with a gradual increase in  $\Sigma_H$  rather than in the electric field. The peak current density at 2048 UT of  $1875 \text{ mA m}^{-1}$  was due to a  $\Sigma_H$  of  $57.5 \text{ S}$ . The next two Pi2 pulsations at 2151 UT and 2100 UT, however, were followed by peaks in current density caused by the electric field rather than  $\Sigma_H$ . In fact,  $\Sigma_H$  decreased from between 40 and  $50 \text{ S}$  at 2051 UT to  $20 \text{ S}$  at 2100 UT whilst the electric field peaked at values of  $46.3 \text{ mV m}^{-1}$  at 2054 UT and  $44.5 \text{ mV m}^{-1}$  at 2102 UT. The final Pi2 pulsation was associated with a small peak in current density which was a result of an increase in the conductance.

There were a number of other peaks in the current density (Figure 5), particularly following the final Pi2 pulsation. Most of these were due to the electric field variation rather than the conductance although, as mentioned earlier, the highest current density was related to the largest  $\Sigma_H$ . The significance of choosing the peaks close to the Pi2 pulsations is that these times relate to changes in the tail associated with substorm expansion phases. The peak current densities are much larger than the AMIE estimates in the pre-midnight sector from substorm activity later in the SUNDIAL interval (*Lu et al., 1995*). The largest current density estimated in this later interval was of order  $625 \text{ A m}^{-1}$  at the time of the second peak in the AE index during the expansion phase (*Lu et al., 1995*). Thus it seems in both cases the current density was at its largest in the late expansion phase or early recovery phase in the pre-midnight sector.

We do not attempt here to relate the current density measured at EISCAT with the ground magnetic perturbations. One major problem with such a study is the limited area over which the radar measurements were made compared with the relatively large area over which the magnetometer averages. Furthermore, without any E-region measurements of ion velocity, it is not possible to estimate the effect of neutral winds on the currents (*Kirkwood et al., 1988*).

We note, however, that the peak current density at 2139 UT of  $2.66 \text{ A m}^{-1}$  flowing in the E-region would result in a magnetic perturbation on the ground of  $\sim 500 \text{ nT}$  which is similar to the overall perturbation measured by SOR at 2138 UT (the minimum in the X component).

## 5. Conclusions.

In summary, the simultaneous measurements of electric field and height integrated Hall and Pedersen conductivities during an interval of substorm activity have been presented. The measurements were made in the pre-midnight sector and in the region of the substorm associated westward electrojet. Peak values in  $\Sigma_H$  and  $\Sigma_P$  did not occur until well into the expansion phase or early in the recovery phase of the substorm. The ratio of the two conductances also changed during the interval, from less than 1 during the growth phase, to of order 1 during the early expansion phase to greater than 2 during the late expansion phase and recovery phase. Thus the average energy of the particles which caused the enhanced conductances increased during the substorm from less than 1 keV to  $\sim 10 \text{ keV}$ .

Peak values of  $\Sigma_H$  and  $\Sigma_P$  were 76.5 S and 40 S, respectively, during the recovery phase in the case of  $\Sigma_H$  and an earlier expansion phase in the case of  $\Sigma_P$ . The peak value in  $\Sigma_H$  also lead to the peak value in the Hall current density of  $2.66 \text{ A m}^{-1}$ , which was also coincident with the minimum X perturbation at SOR. The Hall current density peaked at or near the times of the Pi2 pulsations used to identify substorm expansion phases and intensifications. The peaks, however, were a result of the electric field on some occasions and  $\Sigma_H$  on others. The work demonstrates that localised Hall currents can often be larger than the average values but with the correct conductivity model magnetic field perturbations can be inverted to get correct current densities in the ionosphere. Further work is necessary to investigate the spatial extent of the large values of conductance.

## Acknowledgements.

We would like to thank the members of the UK campaign team for running the EISCAT radar during this interval. EISCAT is supported by the Suomen Akatemia (Finland), the Centre National de la Recherche Scientifique (France), the Max-Planck-Gesellschaft (Germany), the Norges Almenvitenskapelige Forskingsråd (Norway) the Naturveterskapliga Forskningsrådet (Sweden) and the Science and Engineering Research Council (United Kingdom). We would also like to thank Dr. David Orr for provision of SAMNET data, Dr. H. Lühr for provision of IMAGE data and Dr. Geoff Reeves for provision of Los Alamos National Laboratory particle data.

## References.

- Baumjohann, W., R.J. Pellinen, H.J. Opgenoorth and E. Nielsen, Joint two-dimensional observations of ground magnetic and ionosphere electric fields associated with local auroral break-ups, *Planet. Space. Sci.*, **29**, 431 - 447, 1981.
- Belian, R.D., D.N. Baker, E.W. Hones, P.R. Higbie, S.J. Bame and J.R. Ashbridge, Timing of energetic proton enhancements relative to magnetospheric substorm activity and its implication for substorm theories, *J. Geophys. Res.*, **86**, 1415 - 1421, 1981.
- Brekke, A., J.R. Doupnik and P.M. Banks, Incoherent scatter measurements of E region conductivities and currents in the auroral zone, *J. Geophys. Res.*, **79**, 3773, - 3790, 1974.
- Brekke, A., C. Hall and T.L. Hansen, Auroral ionospheric conductances during disturbed conditions, *Annal. Geophys.*, **7**, 269 - 280, 1989.
- Davies, J.A., M. Lester, B. Jenkins and R.J. Moffett, Dayside ion frictional heating: EISCAT observations and comparison with model results, *J. Atmos. Terr. Phys.*, **57**, 775 - 793, 1995.
- Emery, B.A., A.D. Richmond, H.W. Kroehl, C.D. Wells, J.M. Ruohoniemi, M. Lester, D.J. Knipp, F.J. Rich, J.C. Foster, O. de la Beaujarière, C. Senior, L.M. Shier, J.F. McKee and S. Maeda, Electric potential patterns deduced for the SUNDIAL period of September 23-26, 1986, *Ann. Geophys.*, **8**, 399 - 408, 1990.
- Farrugia, C.J., M.P. Freeman, L.F. Burlaga, R.P. Lepping and K. Takahashi, The earth's magnetosphere under continued forcing: substorm activity during the passage of an interplanetary magnetic field, *J. Geophys. Res.*, **98**, 7657 - 7671, 1993.
- Fuller-Rowell, T.J. and D.S. Evans, Height integrated Pedersen and Hall conductivity patterns inferred from the TIROS-NOAA satellite data, *J. Geophys. Res.*, **92**, 7606 - 7618, 1987.
- Hedin, A.E., MSIS-86 thermospheric model, *J. Geophys. Res.*, **92**, 4649 - 4662, 1987.
- Kamide, Y. and J.F. Vickrey, Relative contribution of ionospheric conductivity and electric field to the auroral electrojets, *J. Geophys. Res.*, **88**, 7989 - 7996, 1983.

Kirkwood, S., H. Opgenoorth and J.S. Murphree, Ionospheric conductivities, electric fields and currents associated with auroral substorms measured by the EISCAT radar, *Planet. Space Sci.*, **36**, 1359 - 1380, 1988.

Knipp, D.J., A.D. Richmond, G. Crowley, O. de la Beaujardière, E. Friis-Christensen, D.S. Evans, J.C. Foster, I.W. McCrea, F.J. Rich and J.A. Waldock, Electrodynamics patterns for September 19, 1984, *J. Geophys. Res.*, **94**, 16913 - 16923, 1989.

Lanchester B.S., K.U. Kaila and I.W. McCrea, Relationship between large horizontal electric fields and auroral arc elements, *J. Geophys. Res.*, In Press, 1995.

Lanzerotti, L.J., C.G. MacLennan and M.F. Robbins, Proton drift echoes in the magnetosphere, *J. Geophys. Res.*, **76**, 259 - 263, 1971.

Lester, M., M.P. Freeman, D.J. Southwood, J.A. Waldock and H.J. Singer, A Study of the Relationship Between Interplanetary Parameters and Large Displacements of the Nightside Polar Cap Boundary, *J. Geophys. Res.*, **95**, 21,133 - 21,145, 1990.

Lester, M., O. de la Beaujardiere, J.C. Foster, M.P. Freeman, H. Lühr, J.M. Ruohoniemi and W. Swider, The response of the large scale ionospheric convection pattern to changes in the IMF and substorms: results from the SUNDIAL 1987 campaign, *Ann. Geophys.*, **11**, 5567 - 571, 1993.

Lu, G., B.A. Emery, A. Rodger, M. Lester, J. Taylor, D.S. Evans, J.M. Ruohoniemi, W.F. Denig, O. de la Beaujardiere, R.A. Frahm, J. D. Winningham and D.L. Chennete, High latitude ionospheric electrodynamics as determined by the AMIE technique for the conjunctive SUNDIAL/ATLAS-1/GEM period of March 28-29 1992, *J. Geophys. Res.*, Submitted, 1995.

Lühr, H., The IMAGE Magnetometer network, *STEP International Newsletter*, **4** (10), 4 - 6, 1994.

Lühr, H., S. Thurey and N. Klockner, The EISCAT magnetometer cross. Operational aspects - first results, *Geophys. Surv.*, **6**, 305 - 315, 1984.

Lühr, H., H. Geisler and K. Schlegel, Current density models of the eastward electrojet derived from ground-based magnetic field and radar measurements, *J. Atmos. Terr. Phys.*, **56**, 81 - 91, 1994.

Lui, A.T.Y., A synthesis of magnetospheric substorms, *J. Geophys. Res.*, **96**, 1849, 1991.

McCrea, I.W., M. Lester, T.R. Robinson, N.M. Wade and T.B. Jones, On the identification and occurrence of ion frictional heating events in the high-latitude ionosphere, *J. Atmos. Terr. Phys.*, **53**, 587 - 597, 1991.

McPherron, R.L., C.T. Russell and M.P. Aubry, Satellite studies of magnetospheric substorms on August 15, 1968, 9, Phenomenological model for substorms, *J. Geophys. Res.*, **78**, 3131, 1973.

Mishin, V.M., S.B. Lunyushkin, D. Sh. Shiripov and W. Baumjohann, A new method for generating instantaneous ionospheric conductivity models using ground-based magnetic data, *Planet. Space Sci.*, **34**, 713, 1986.

Opgenoorth, H.J., R.J. Pellinen, W. Baumjohann, E. Nielsen, G. Marklund and L. Eliasson, Three-dimensional current flow and particle precipitation in a westward travelling surge (observed during the Barium-GEOS rocket experiment), *J. Geophys. Res.*, **88**, 3138 - 3152, 1983.

Reeves, G.D., R.D. Belian and T.A. Fritz, Numerical tracing of energetic particle drifts in a model magnetosphere, *J. Geophys. Res.*, **96**, 13997 - 14008, 1991.

Richmond, A.D. and Y. Kamide, Mapping electrodynamic features of the high-latitude ionosphere from localised observations: Technique, *J. Geophys. Res.*, **93**, 5741 - 5759, 1988.

Robinson, R.M., R.R. Vondrak, K. Miller, T. Dabbs and D. Hardy, On calculating ionospheric conductances from the flux and energy of precipitating particles, *J. Geophys. Res.*, **92**, 2565 - 2569, 1987.

Rostoker, G., S.-I. Akasofu, J. Foster, R.A. Greenwald, Y. Kamide, K. Kawasaki, A.T.Y. Lui, R.L. McPherron and C.T. Russell, Magnetospheric substorms - definition and signatures, *J. Geophys. Res.*, **85**, 1663, 1980.

Spiro, R.W., P.H. Reiff and L.J. Maher, Jr., Precipitating electron energy flux and auroral zone conductances - an empirical model, *J. Geophys. Res.*, **87**, 8215 - 8227, 1982.

Szuszczewicz, E.P., D. Torr, P. Wilkinson, P. Richards, R. Roble, G. Lu, D. Evans, S. Pulinets, B.M. Reddy, M. Abdu, M. Lester, K. Igarashi, P. Jiao, P. Blanchard and J. Joselyn, F-Region climatology during the SUNDIAL/ATLAS-1 campaign of March 1992: prevailing conditions and model-measurement comparisons, *J. Geophys. Res.*, this issue, 1995.

Torr, M.R., The scientific objectives of the ATLAS-1 shuttle mission, *Geophys. Res. Letts.*, **20**, 487 - 490, 1993.

Williams, P.J.S., T.S. Viridi, S.W.H. Cowley and M. Lester, Short-lived bursts of plasma velocity in the auroral zone. I. Observational evidence from radar measurements, *J. Atmos. Terr. Phys.*, **52**, 421 - 430, 1990.

Williams, P.J.S., R.V. Lewis, T.S. Viridi, M. Lester and E. Nielsen, Plasma Flow Bursts in the Auroral Electrojets, *Ann. Geophys.*, **10**, 835-848, 1992.

Yeoman, T.K., D.K. Milling and D. Orr, Pi2 polarisation patterns on the UK Sub-Auroral Magnetometer Network (SAMNET), *Planet. Space Sci.*, **38**, 589 - 602, 1990.

Yeoman, T.K., M.P. Freeman, G.D. Reeves, M. Lester and D. Orr, A Comparison of Mid-Latitude Pi2 Pulsations and Geostationary Orbit Particle Injections as Substorm Indicators, *J. Geophys. Res.*, **99**, 4085 - 4093, 1994.

## Figure Captions.

**Figure 1.** The X (North-South) Component of the magnetic field measured at selected stations from the IMAGE magnetometer array for the interval 1800 - 2400 UT on March 27 1992. The dashed vertical lines represent the times of Pi2 Pulsations identified in the SAMNET data (not shown).

**Figure 2.** In the top panel the Pedersen (solid line) and Hall (dotted line) Conductances are plotted as a function of UT from 1800 to 2200 UT. The lower panel shows the ratio of Hall to Pedersen conductance for the same interval. The dashed vertical lines in each panel represent the times of the Pi2 pulsations.

**Figure 3.** In the upper panel the Hall Conductance is plotted as a function of the Pedersen Conductance for the interval 1800 - 2000 UT. The dashed line represents Hall conductance equalling Pedersen Conductance. The full line represents the best fit linear function with the relationship at the top of the panel together with the correlation coefficient. The lower panel is the same but for the interval 2000 - 2200 UT. Note the difference in scale for the Hall Conductance in this panel.

**Figure 4.** In the upper panel the electric field measured by EISCAT is plotted for the interval 1800 - 2200 UT. In the lower panel the Hall Conductance is plotted for the same time. The dashed vertical lines in each panel represent the times of the Pi2 pulsations.

**Figure 5.** The Hall Current Density for the interval 1800 - 2200 UT. The dashed vertical lines in each panel represent the times of the Pi2 pulsations.

**TABLE 1.**

INTERVAL UT	MEAN			RANGE		
	$\Sigma_H$ (S)	$\Sigma_P$ (S)	R	$\Sigma_H$ (S)	$\Sigma_P$ (S)	R
1936-2005	9.6	9.3	1.02	3.4-29.5	4.2-25.0	0.63-1.61
2006-2017	7.8	7.7	1.02	3.2-18.0	4.1-18.0	0.74-1.82
2018-2042	21.1	15.6	1.32	9.3-44.5	7.9-27.0	1.00-1.65
2043-2130	40.6	20.2	1.99	16.5-70.5	12.0-33.5	1.25-2.50



27 March 1992 X Component

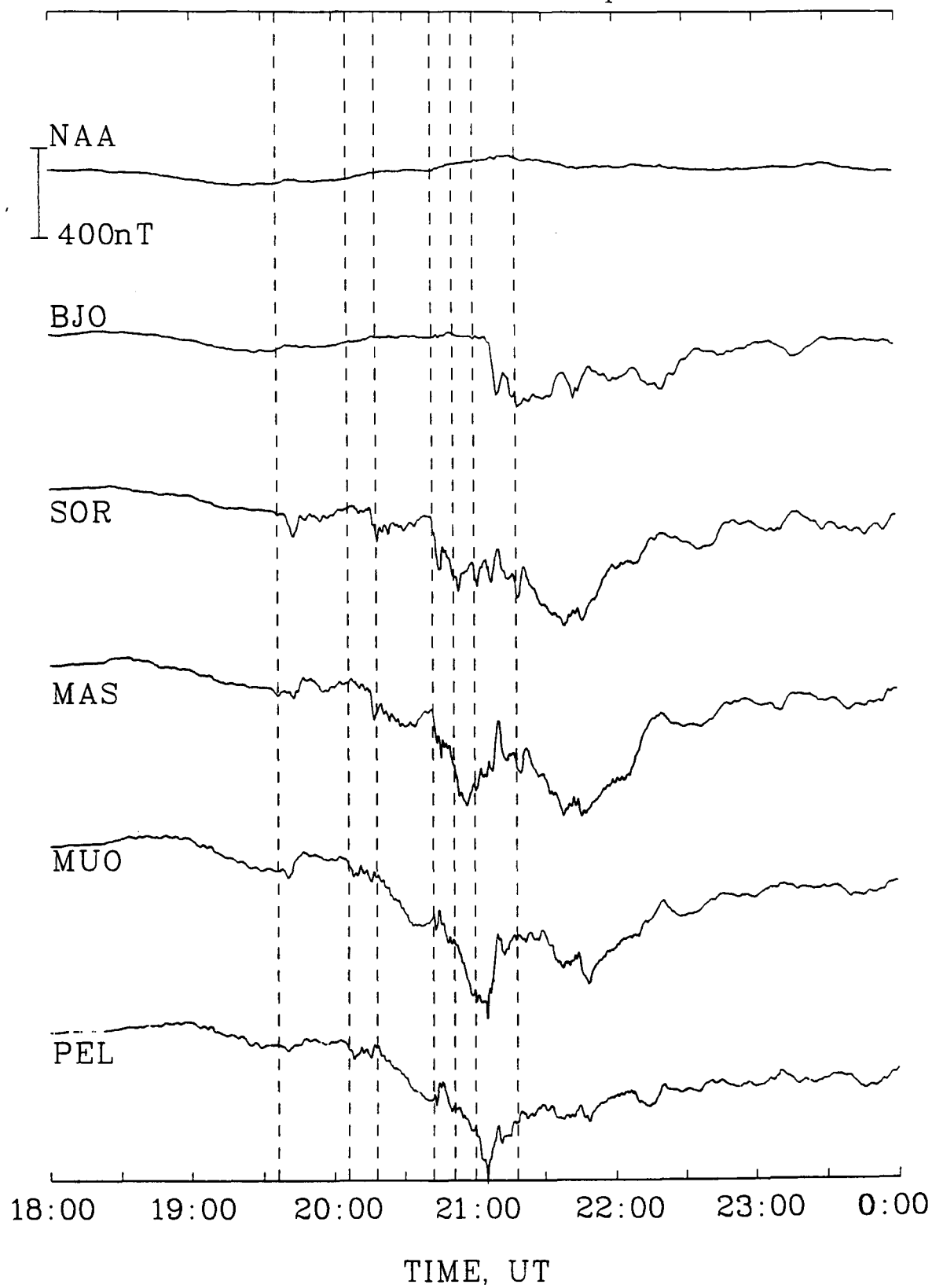


FIGURE 1.

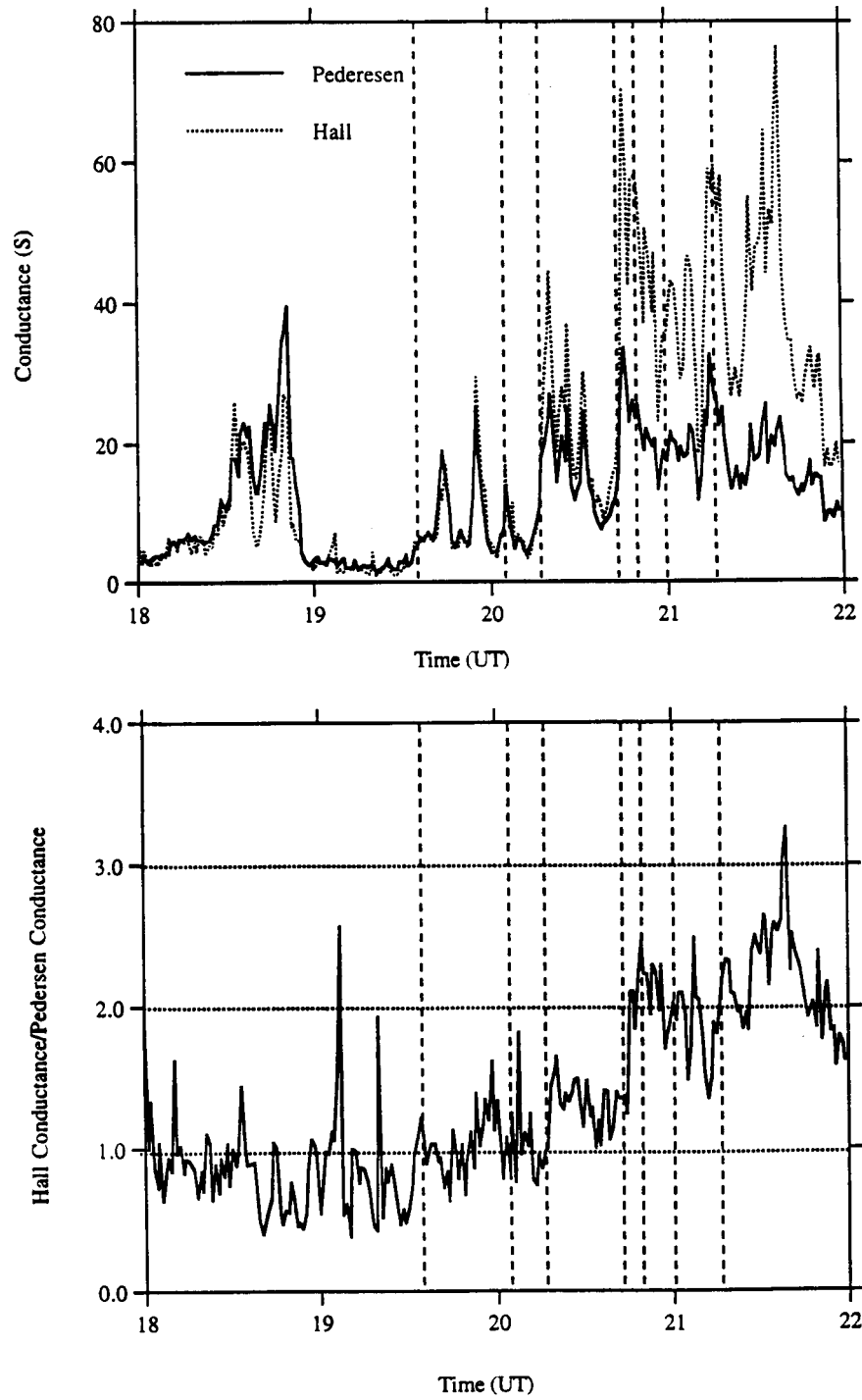


FIGURE 2.

SP-UK-ATLAS 27/3/92

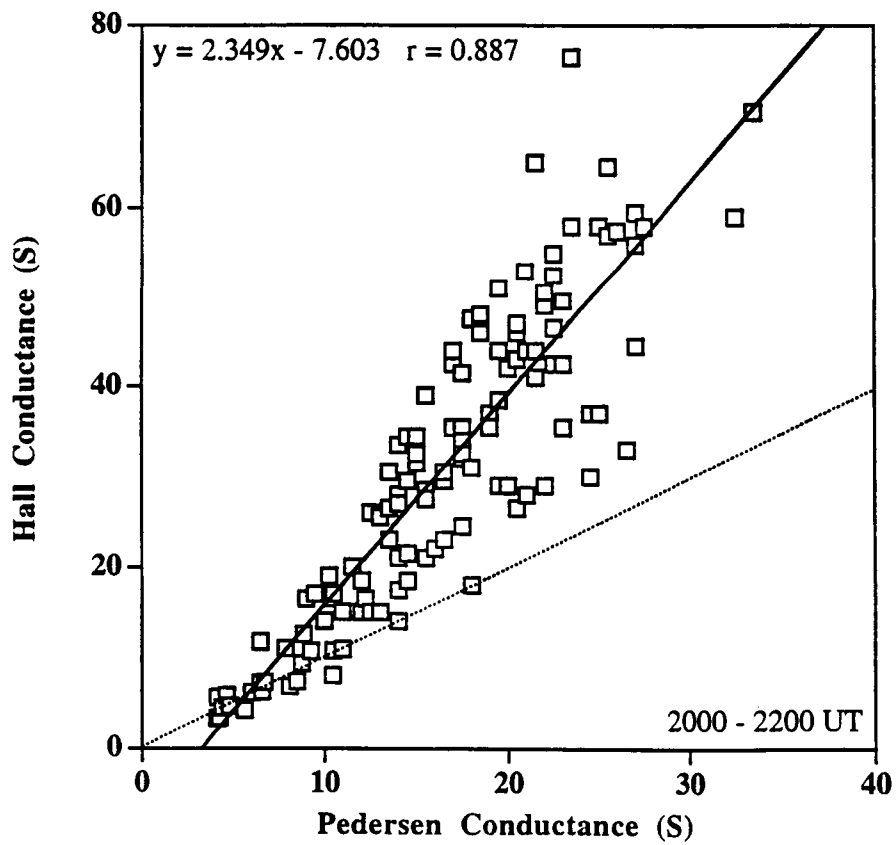
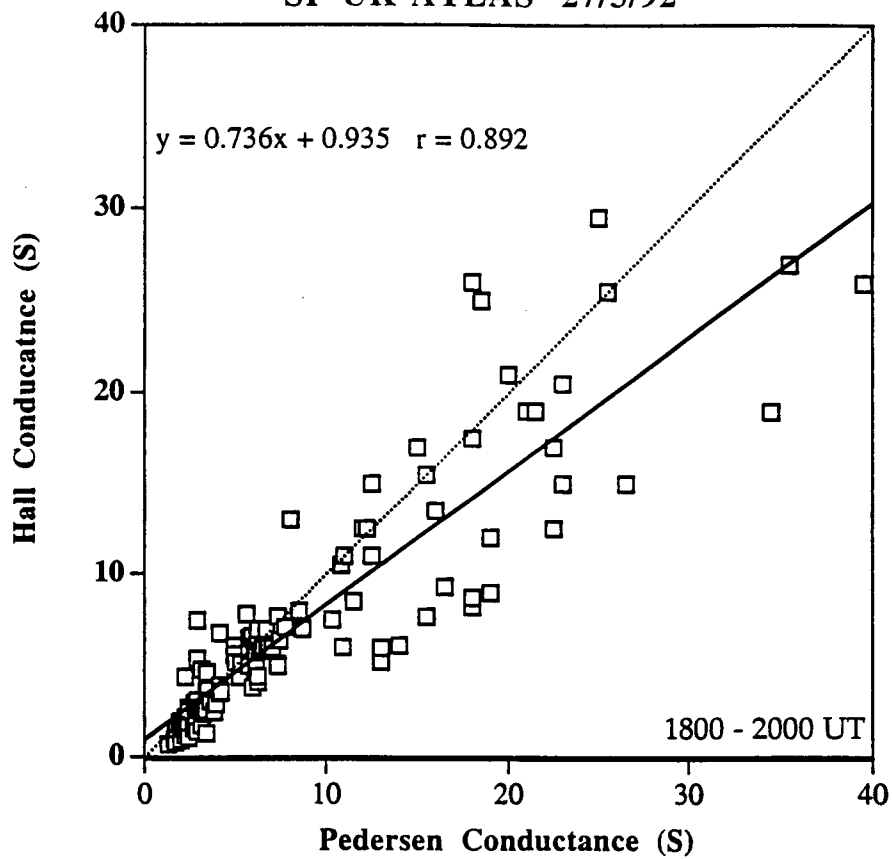


FIGURE 3.

March 27 1992 SP-UK-EISCAT

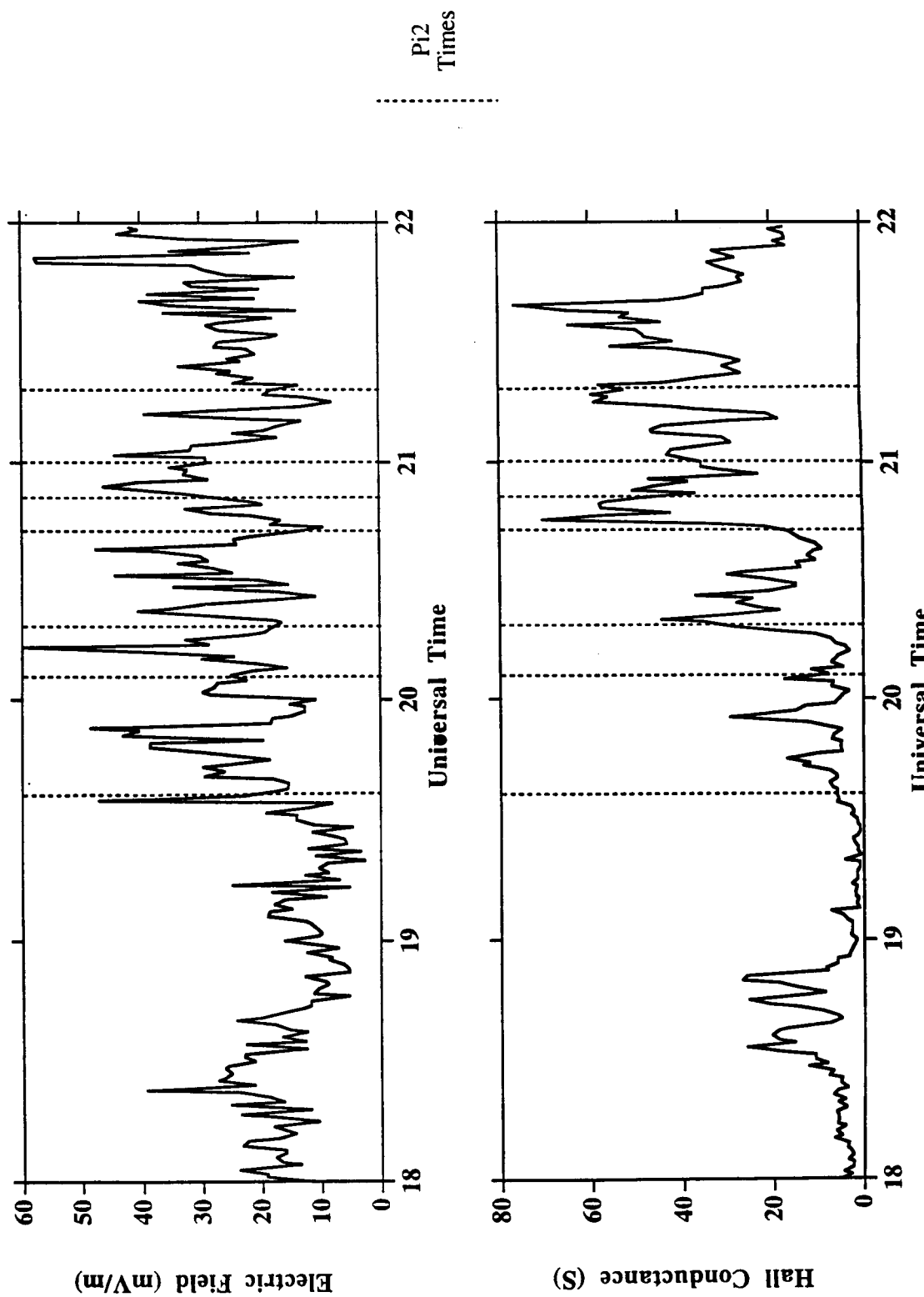


FIGURE 4.

SP-UK-ATLAS 27/3/1992

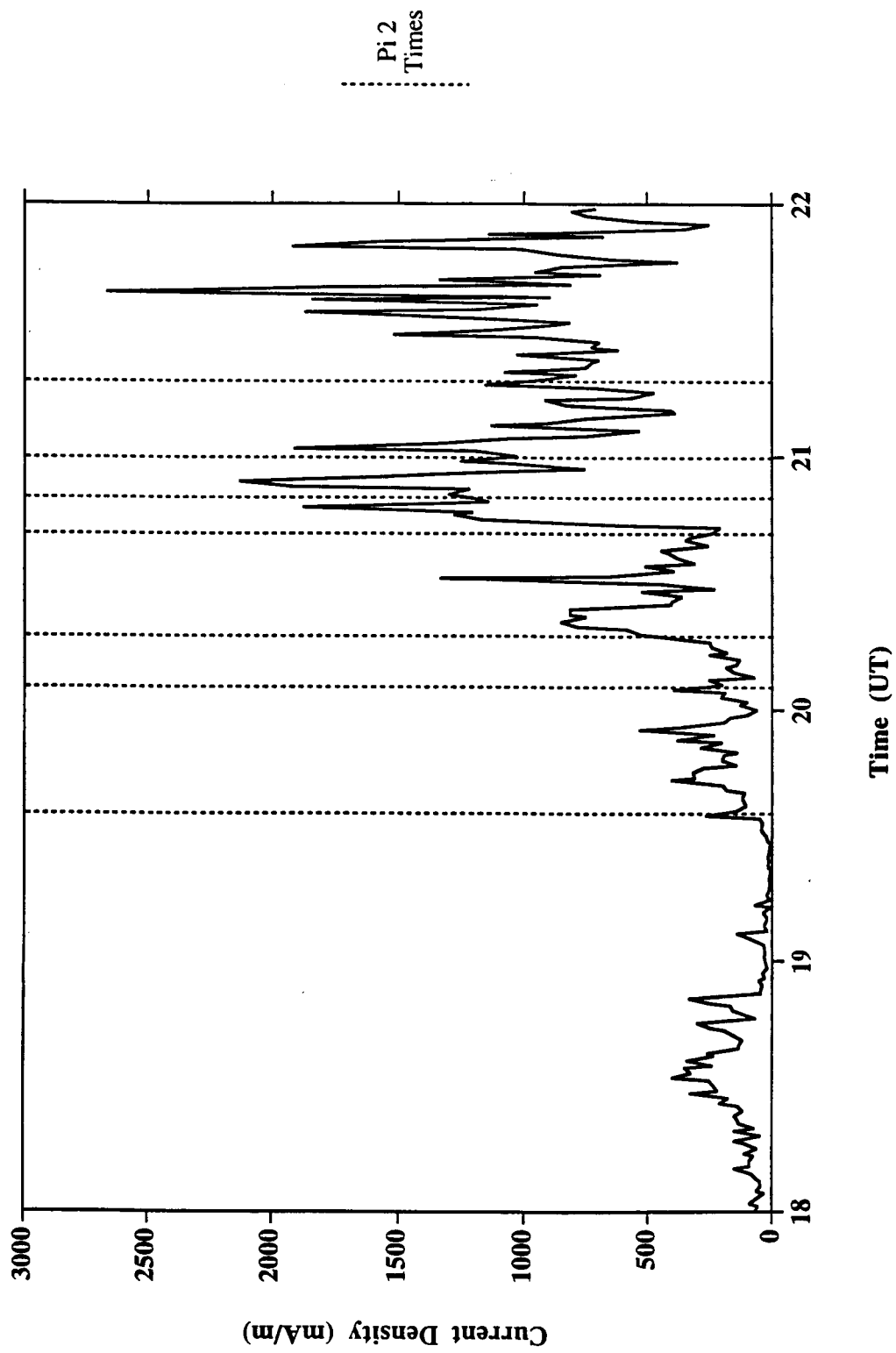


FIGURE 5.

**The Study of the Ionospheric Variability Within the  
Euro-Asian Sector During the  
ATLAS-1/SUNDIAL Mission**

**S.A. Pulinets, K.F. Yudakhin, D. Evans and M. Lester**

**THE STUDY OF THE IONOSPHERIC VARIABILITY WITHIN  
THE EURO-ASIAN SECTOR DURING  
THE SUNDIAL/ATLAS-1 MISSION**

**S. A. Pulinets and K. F. Yudakhin**

**Institute of Terrestrial Magnetism, Ionosphere and Radiowave Propagation,  
Russian Academy of Science, (IZMIRAN), Troitsk, Russia**

**D. Evans**

**NOAA/SEL, Boulder, Colorado**

**M. Lester**

**Department of Physics and Astronomy, University of Leicester, Leicester, U.K.**

**Short title: Ionospheric variability during SUNDIAL/ATLAS-1 mission**

**Author Address List:**

**Dave Evans, NOAA/SEL, 325 Broadway, Boulder, CO 80303**

**E-mail: [devans@sel.noaa.gov](mailto:devans@sel.noaa.gov)**

**Mark Lester, Radio and Space Plasma Physics, Department of Physics and Astronomy,  
University of Leicester, Leicester LE1 7RH, U.K.**

**Tel: 0116 252 3580, Fax: 0116 252 3555, E-mail: [mle@ion.le.ac.uk](mailto:mle@ion.le.ac.uk)**

**Sergei Pulinets, IZMIRAN, Troitsk, Moscow Region, 142092, Russia**

**Tel:007-095-3340919, Fax:007-095-3340124,**

**E-mail: [pulse@charley.izmiran.rssi.ru](mailto:pulse@charley.izmiran.rssi.ru)**

**Konstantin Yudakhin, IZMIRAN, Troitsk, Moscow Region, 142092, Russia**

**Tel:007-095-3340919, Fax:007-095-3340124,**

**E-mail: [pulse@charley.izmiran.rssi.ru](mailto:pulse@charley.izmiran.rssi.ru)**

### Abstract

In order to quantify, and to identify possible origins of, sub-auroral ionospheric variability during periods of moderate geomagnetic activity, ionospheric observations taken during the SUNDIAL/ATLAS-1 campaign (24 March to 2 April) from 10 ionospheric stations were analyzed in conjunction with observations from EISCAT, geomagnetic observations from magnetometer networks in Scandinavia and the United Kingdom, and auroral particle energy input observations from the NOAA-12 satellite. The network of ionospheric stations spanned longitudes from 13° E to 90° E but were relatively confined in geomagnetic latitudes so that longitudinal and local time dependencies in ionospheric variability are more clearly exposed. The ionospheric observations were analyzed in terms of both  $DfoF2$ , the difference between the hourly value of  $foF2$  at a given station and the monthly median  $foF2$  for that hour, and a new daily variability index  $AfoF2$ . The analysis using both parameters demonstrated an apparent longitudinal variation in ionospheric variability with a reversal at about 55° E longitude from a negative to a positive phase in the departure of ionospheric conditions from their mean values. An analysis of these ionospheric data in conjunction with the NOAA/TIROS estimates of power deposition by auroral particles demonstrated a significant local time dependence in mid-latitude ionospheric responses to auroral activity. This dependence may arise from the pre- to post-midnight asymmetry in high latitude convection electric fields.

### 1. Introduction

The day to day ionospheric variability is the point of concern of modern ionospheric physics [Gulyaeva et al., 1990]. The problem usually is regarded within the frames of “quiet/disturbed” ionosphere concept. This means that we need concerted definition of “quiet” and “disturbed” conditions. In the most cases level of disturbance is determined basing on the value of global geomagnetic 3-hour  $K_p$  index. In relation to the ionosphere this approach seems to fail because for the same values of  $K_p$  we could observe different levels of ionospheric activity. So we need for some different means to determine ionospheric activity or variability. Now the new ways of the ionosphere quietness determination are under elaboration [Gulyaeva et al., 1995]. Regardless the determination usually “quiet” implies the regular behavior of the ionosphere which could be described by regular



daily, seasonal and solar cycle variations. Recently the formulation of regular behavior of the ionosphere was named “climatology” [Szuszczewicz, 1995]. The regular variations could be described by different ionospheric models, either empirical or theoretical [Bilitza et al., 1992, Schunk and Szuszczewicz, 1988].

The opposite case is strongly disturbed ionosphere as a consequence of geomagnetic storms [Gonzales et al., 1994]. As a point of strong interest the state of ionosphere during development of geomagnetic storm was extensively studied and can be described now even by first principle models [Fuller-Rowell et al., 1994].

But more often we encounter the more complex case of unstable ionosphere as a result of consequent substorms with different time delay as is the case for our study. There exist models of high latitude convection driven by electric fields [Heppner and Maynard, 1987; Holt et al., 1987; Foster, 1993], but all of them examine more or less deterministic cases with isolated clear storm\substorm development (SC, main phase, recovery phase) without chaotic factor when one can observe multiple turnings of  $B_z$  during the short period of time, i.e. consequence of disturbances without recovery. The role of the IMF  $B_z$  polarity changes, where the “event” of changing polarity is determined by the Hapgood et al. [1991] procedure, was studied by Tulunay [1994]. Some people look for a regular component in ionospheric variability as a periodic variations [Lastovicka and Mlch, 1994a; 1994b]. Even from the few listed references it is clear, that a lot of sources of the ionospheric variability, especially at disturbed conditions with multiple magnetic storms or substorms, make very difficult formulation or modeling of the ionosphere behaviour. Sometimes we are able to find the direct cause effect relation between magnetosphere events and ionosphere parameters variations but deterministic approach fails in the complex conditions as we have for the SUNDIAL/ATLAS-1 period.

The way out from the difficult situation is usually looked in the building of some empirical relations based on the standard indices of geomagnetic activity, i.e.  $K_p$ ,  $A_p$ ,  $D_{st}$ , AE, etc. As examples of such approach we could cite the empirical model of the main trough position [Kohnlein and Raitt, 1977; Karpachev et al., 1995] or recent improvements of the IRI [Kishcha, 1995].

The cited models of the ionospheric trough were based on the satellite data with good and uniform spatial resolution, what is very important for the global

variability study. The ground-based ionospheric measurements give good temporal resolution but the generalization of the results depends in a great extent from the spatial stations distribution. If we have more or less dense network of the ionospheric stations we can try to analyze the spatial distribution of ionospheric variability. The network of ionospheric stations in Russia gives possibility to look on longitudinal behavior of the ionospheric variability, because many stations fall into the same latitudinal range (within  $15^\circ$ ). This in some cases permits the neglect of latitudinal variations. To complete the data set we used, in addition to Russian stations, the data from Juliusruh ionospheric station (Germany), that made possible to analyze the ionospheric data in longitudinal sector  $13^\circ$ -  $90^\circ$  during period of SUNDIAL/ATLAS-1 Mission 24.03-02.04.92 [Szuszczewicz et al., 1996]. The stations' geographical distribution is shown on Fig. 1 and all parameters of ground-based ionospheric data are presented in Table 1. Note that 7 from 10 stations fall into interval  $6^\circ$  of invariant geomagnetic latitude. The most northern Arkhangelsk station falls into region of main ionospheric trough, and the most southern, Tashkent, showed no high latitude influence at all for given level of geomagnetic activity. The same situation was observed at Australian-Japanese sector during SUNDIAL/ATLAS-1 period [Wilkinson et al., 1996].

To find some new approaches to the ionospheric variability we analyzed two new indices proposed recently. One of them, based on the vertical sounding data, was proposed by Gulyaeva et al., [1990]. Our choice was directed by two considerations: a) the index, based on the critical frequency values, should contain information about the ionospheric variability by definition; b) it does not include the indices of geomagnetic activity and hence could be used as independent means for ionospheric variability estimation. The second index we analyzed, is based on the satellite particle precipitation data described in [Foster et al., 1986]. Taking into account that the most of the ionospheric stations in our consideration are situated at sub-auroral zone, this index may give us new approach for the ionospheric variability prediction at least for given latitudes.

The geophysical and ionospheric conditions for the entire month of March 1992 were analyzed basing on data of Moscow and Juliusruh stations, and then more detailed analysis was applied to all stations data within the period 24.03-31.03.

To identify the difference between the global and local activity we used the data from NOAA/TIROS satellite on the particle precipitation activity and EISCAT measurements of electron density and temperature for the given period.

## 2. Geophysical conditions and ionospheric variations in March, 1992.

The March 1992 period could be characterized as a moderately disturbed . We have only few days in March (14, 19, 20) when activity (in  $K_p$ ) does not reach 3 (see Fig. 2 a)<sup>1</sup>. But these quiet days are surrounded by the periods with higher activity, so, taking into account the relaxation time of the ionosphere, there are no really quiet periods in March. From another point of view no severe storms were observed in March:  $K_p$  does not exceeds 5. It looks like a sequence of moderate disturbances without relaxation, especially during SUNDILA/ATLAS-1 period, which is expressed by the bold line on the X-axes of every panel of Fig. 2. One can observe three maxima of geomagnetic activity within the SUNDILA/ATLAS-1 period, which are clearly seen in the  $A_p$  variations: 9-11.03, 17.03, and 21-24.03. The  $D_{st}$  variations analysis supports our conclusion about March activity (see lowest panel in Fig. 2). All month presents itself as a sequence of storms and substorms without relaxation with 3 main maxima: 01.03, 17.03 and 21.03, which could be regarded as moderate storms by classification of Gonzales et al. [1994], when  $D_{st}$  exceeded -50 nT. Period between 09 and 13 of March is not so expressed as in  $A_p$  index: it looks like a wide minimum with small storm on 09 of March. Ionospheric activity within the SUNDIAL/ATLAS-1 interval is connected with the storm recovery phase with onset of the storm on 21.03 and subsequent substorms. The substorm occurrence with 100% probability (after Kamide et al. [1977]) could be determined by the  $B_z$  southward turnings, when the value of the 1-hour averaged  $B_z$  exceeds -3 nT. After 23 of March (by the IMP-8 data) the southward turnings of  $B_z$  were observed at least 8 times, with magnitude exceeding -5 nT. We should mention that the global activity, expressed in  $D_{st}$  and partly in  $A_p$  variations, was accompanied by the local activity in European sector. The analysis of local activity was based on the EISCAT data and the data from two

---

<sup>1</sup> For convenience in comparison with other indices the  $K_p$  and  $A_p$  indices are presented in the figure in reversed form.

magnetometer networks: IMAGE in Northern Scandinavia and SAMNET in the UK and Scandinavia [Lester et al., 1996]. This analysis has shown that during SUNDIAL/ATLAS-1 period substorms in European sector were observed every day twice: near 19h30m UT and near 00h UT. In this regard we will attempt to analyze the ionospheric data from the point of view of the global, as well as local activity taking into account the longitudinal variations. We will concentrate mainly on the density variations in the maximum of F2 layer from two points of view: this parameter is most sensitive to any geophysical changes, especially to the geomagnetic activity and can change even by orders of magnitude, whilst the heights of the different ionospheric layers could change no more than two times under the same conditions. The second reason is based on the poor correlation in variability of different ionospheric parameters [Kouris et al., 1994]. That's why, by including into analysis of other ionospheric parameters we risk only overload the paper instead of clarify the situation.

The monthly  $f_oF2$  variations for Moscow and Juliusruh stations are presented in Fig. 3. Hourly values of the critical frequency  $f_oF2$  (triangles) and monthly median (continuous line) are shown in the upper part of every panel, and the lower part of every panel shows the percentage deviation of  $f_oF2$  from the monthly median. The percentage instead of simple difference is used to express relative changes especially during early morning hours when the absolute value of  $f_oF2$  (and consequently  $\Delta f_oF2$ ) is small. We cannot observe the direct relationship between  $K_p$  and  $A_p$  variations and ionospheric parameters variations. For example, negative variations of  $f_oF2$  on 05.03 and 06.03 are the same as on 18.03, nevertheless the  $A_p$  on 17.03 two times larger than 05.03 and 3 times larger than on 06.03. At the same time from presented ionospheric data we can characterize all March as highly disturbed especially looking on Juliusruh data. The very strong daily variations with amplitude more than 30% for both negative and positive deviations are observed practically every day. But we should note two main differences between the Moscow and Juliusruh data. One can clearly observe the long-term modulation of Juliusruh data with period corresponding to the  $A_p$  index variation but it is not so remarkable in Moscow data. From the other hand the SUNDIAL/ATLAS-1 period in Moscow data differ from other part of March by long term negative variations, which for other part of March are observed only near midnight and are short term. In Juliusruh data the SUNDIAL/ATLAS-1 period does

not differ from the other part of March. Even more, the 09.03-11.03 variations at Juliusruh are more remarkable than during last decade of March. But from the both sets of data we can conclude that for SUNDIAL/ATLAS-1 period predominantly negative phase in  $f_oF2$  variations is the characteristic that reflects the storm development as a reaction on interplanetary conditions change shown by  $D_{st}$  (see Fig. 2 c). Comparing the  $D_{st}$  variations and  $\Delta f_oF2$  for Moscow and Juliusruh we could mention that slight positive trend in  $D_{st}$ , especially 25-27 of March is reflected in  $\Delta f_oF2$  variations.

It seems that explanation of the difference between the Moscow and Juliusruh data could be find in local substorm activity. Sporadic precipitation events due to field aligned electric fields having thin structure of order 10-100 km could be responsible for the observed differences at stations separated by  $24^\circ$  of the longitude [Evans, 1974; Chiu and Schulz, 1978; Ijima and Potemra, 1978].

### 3. Ionospheric variability index and global ionospheric activity.

Many application tasks connected with the knowledge of the near earth space characteristics, such as "Space weather program", demand from the existing models more predictability and more promptitude. Existing models of the ionosphere, as theoretical so empirical, need for calculations a lot of input parameters (or measurements). Very often this input parameters are not available or could be available after a long delay as happens with some geophysical indices (for example  $D_{st}$  and AE). The real time control of near-space should be based on the self-consistent sets of measurements which could give prompt estimations of the observed variations. Regarding the ionospheric variability, it is interesting to find some indices based on the ionospheric data themselves. We examined the ionospheric variability index proposed by Gulyaeva et al., [1990]. The index is calculated as a half of difference between the maximal and minimal values of  $f_oF2$  for a given day:

$$Af_oF2 = 1/2(f_oF2_{max} - f_oF2_{min})$$

The  $f_oF2$  parameter was selected due to its high sensitivity in comparison with other ionospheric parameters, what was discussed above.

We calculated the  $Af_oF2$  index for Moscow station for March 1992. The results of calculation are presented in Fig. 2 b (open circles). One can clearly see that calculated index reflects very well the main features of  $D_{st}$  shown in Fig 2 c,

especially the storm events on 16 and 21 of March. The calculated correlation between the  $Af_0F2$  and  $D_{st}$  was of order 0.7 for all month of March. But comparison of the  $Af_0F2$  index variations with  $A_p$  does not give such good correlation as it is observed for the  $D_{st}$  index.  $Af_0F2$  does not reflect the deep variations of  $A_p$  for the first part of March till 20.03. The visual observation is supported by the statistical estimations: cross-correlation coefficients for  $K_p$  and  $A_p$  does not exceed 0.2 and 0.3 respectively. The deep discussion about the physical meaning and difference between different geophysical indices one can find in [Gonzales et al., 1994], and more information about correlation between the different indices with more statistics in [Saba et al., 1994]. The comparison described above helps us to understand the physical sense of the derived  $Af_0F2$  index. It reflects the ring current influence on the middle latitude and subauroral ionosphere during the magnetic storm development. The ring current effect consist in suppression of daily variations of the critical frequency. Naturally this conclusion should be supported by statistical study for given and other ionospheric stations for different levels of solar and geomagnetic activity what will be done in the further work.

The indices of geomagnetic activity are produced from selected magnetic observatories data, which register the variations of magnetic field, practically the final product of the magnetospheric storms and substorms development. Basing the ionospheric data analysis on them, we are always outside the cause-effect chain of physical processes connected with the ionospheric variability. It is always interesting to find the direct relation between the observed variation of the parameter under study and its physical source. That's why we tried to look how the precipitating particles at the auroral latitudes relate to the observed variations of ionospheric peak density. The regular monitoring of energetic particle precipitation is provided by DMSP and NOAA/TIROS satellites. Data from NOAA/TIROS satellite were analyzed for the given period of SUNDIAL/ATLAS-1 campaign.

#### 4. NOAA/TIROS index and ionospheric variations

Foster et al., [1986] proposed to use the energetic particles flows precipitating in auroral zone and registered onboard the low orbiting satellites for estimation of energy input into the ionosphere. They constructed the special index characterizing this input by integration the particle flow energy during every pass

of the satellite over the auroral regions in both Northern and Southern hemispheres.

We compared these data with variations of the ionosphere peak density. The raw satellite data for SUNDIAL/ATLAS-1 period are shown in Fig. 2 in the upper right angle of the lowest panel. Following the same logic as for  $A_p$  and  $K_p$  presentation, the index is shown in figure in the reversed form. To be able distinguish between more quiet period (basing on  $D_{st}$  data) and disturbed recovery phase after 21 of March we used more wide interval of the NOAA/TIROS data than the SUNDIAL/ATLAS-1 period, beginning from the end of March, 17. One could observe the high similarity of particle flux variations with  $D_{st}$  index shown on the same panel, with one difference: the  $D_{st}$  index has less high frequency variability. But this similarity was very deceptive. The cross-correlation analysis have shown very unusual relation between them: the hourly values of  $D_{st}$  and NOAA/TIROS index do not correlate at all: the cross-correlation coefficient equals practically zero. At the same time the averaged daily values of the same indices have correlation coefficient 0.9 for all SUNDIAL/ATLAS-1 period. This, for the first view, strange difference could be explained as follows: the short time-scale variations of the  $D_{st}$  and NOAA/TIROS indices reflect different processes. The  $D_{st}$  reflects the process of injection of the energetic particles from the tail into the inner magnetosphere, where they move at the trapped trajectories at the shells lower than  $L = 4$ . The NOAA/TIROS index reflects the streams of energetic particles precipitating at latitudes sufficiently higher than  $L = 4$ . But the averaged values of the both indices express the dynamics of the energy transport from the solar wind into the magnetosphere and hence should have practically the same shape.

The daily averaged NOAA/TIROS index was compared with the  $Af_0F2$  and results of comparison are shown in the middle panel of the Fig.2. The averaged NOAA/TIROS index again is reversed for comparison and is shown in the figure by the filled circles. One can observe very similar shape of the  $Af_0F2$  and  $A_p$  indices variations, which is expressed numerically by the correlation coefficient of order 0.7 for all SUNDIAL/ATLAS-1 period. Taking into account the poor correlation of  $Af_0F2$  with  $K_p$  and  $A_p$  indices which include in their variations the local activity at subauroral latitudes, we can again put forward assumption that  $Af_0F2$  index reflects more the global storm activity than the local one. The difference between the  $Af_0F2$  and NOAA/ TIROS indices for 17-20 of March period implies conclusion

that the  $Af_0F2$  index is connected more with  $D_{st}$  variations than the particle precipitation within the auroral zone and correlation between  $Af_0F2$  and NOAA/TIROS indices has the same sense as between the  $D_{st}$  and NOAA/TIROS indices.

We should indicate the limitation of the proposed NOAA/TIROS index, derived from the fact, that the satellite pass over auroral latitudes takes only few minutes. The next pass over the same latitudes will take place after delay of order 90-100 minutes (one satellite full rotation orbit duration). So the data present the regular samples with gaps in measurements more than one hour. It means that in our calculations of the index we suppose that the level of particle activity does not change substantially between passes, which may not necessarily be true, especially regarding the local substorm activity. Nevertheless, the proposed index could be extremely useful from the point of view of its promptitude and simple physical meaning. Its relation to the ionospheric variability expressed in the form of deviation from the mean values of the critical frequency will be discussed lower.

### **5. Longitudinal variations during SUNDIAL/ATLAS-1 mission.**

We analyzed the data of vertical sounding collected from ten ionospheric stations situated within the longitudinal sector from 13° to 90° E. One can find the parameters of the used data base in Table 1, and map of stations geographical distribution in Fig. 1. Taking into account the discussed above possibility for the longitudinal variations study with the help of a given chain of stations, we could pay less attention to the latitudinal variations in comparison with longitudinal ones. For calculating of the  $f_0F2$  deviations we used not the monthly medians but averaged hourly values of the critical frequency for the period of 24.03-31.03. The time-longitude distribution of the critical frequency deviations  $\Delta f_0F2$ , expressed in percents, is demonstrated in Fig. 4 in the form of the 2-D plot. The longitude is put along the X-axis, and time is shown along the Y-axis from top to bottom. The deviations of critical frequency are expressed by color (the scale is shown by the right side of the plot). Local midnight position is shown by the bold white lines. One can observe the high variability of the ionosphere during SUNDIAL/ATLAS-1 period: for the most of stations  $\Delta f_0F2$  reach and sometimes exceeds  $\pm 40\%$ . One can observe several positive extremes (sharp increasing of the peak density), especially in the evening, March 27 at the western part of the chain. They could be attributed to the local strong precipitation events. One of them, observed by the



Arkhangelsk station, is marked by the bold black arrow in the Fig. 4. The beam relaxation within the auroral ionosphere was studied by many authors but the most systematic approach one can find in the books of Mishin et al. [1989, 1990]. The precipitating beams of accelerated electrons intrude into the upper ionosphere and cause many effects, namely: rising of the electron temperature within the upper ionosphere, increased ionization of the F and E-layers, formation of the thin layers of enhanced ionization on the height of 100-120 km due to wave particle interactions, pulsating aurora, etc. Such events are often observed by the EISCAT facility. One can find several examples of EISCAT registration of such precipitation events in [Wahlund and Opgenoorth, 1989] for the heights lower than 250 km. But we should keep in mind that during its way through the upper ionosphere the beam produces increased ionization not only within the E-layer but within the F-layer as well. To show that it is the case we looked for EISCAT data for the period of SUNDIAL/ATLAS-1 Mission, [Lester, 1993]. Fortunately there were EISCAT measurements during the precipitation event on 27 of March and results are presented in Fig. 5. The EISCAT facility data (electron density and temperature) are shown in the upper panel of the Fig. 5, and  $\Delta f_oF2$  daily variation for Arkhangelsk station in the middle panel of the Fig. 5. The Kiruna magnetic observatory data are presented in the bottom panel of the Fig. 5. It is clearly seen from the figure that the positive variations during morning and afternoon hours (especially sharp increasing of the electron density after 16 h UT) are connected with increased precipitation registered by EISCAT, and the peak near 19 h UT is connected with particles penetration up to 100 km height. The positive variations are observed during 27 of March on all western stations of the chain, but the pronounced peaks near 19 h UT are observed only at Arkhangelsk and Leningrad as most northward stations, close to the main trough. From the magnetometer data we see the local substorm development. So, we can classify the observed peak of increased ionization as a local substorm development. It was mentioned above that usually substorms are provoked by the southward turnings of the vertical component of IMF. We tried schematically show in the Fig. 4 by the open triangles on the left vertical axis the time position of the  $B_z$  southward turnings with amplitude higher than - 3 nT and obtained very close correspondence for the most of events, with the positive variations, mainly in the western part of the chain. Unfortunately, the IMP  $B_z$  component data are not continuous for the

SUNDIAL/ATLAS-1 period but even several shown examples give hope that such presentation of the ionospheric data in some extent make possible to reconstruct the interplanetary magnetic field behaviour

Except the local events discussed above one can observe the more large scale variations as in time, so in longitude within the given range of longitudes. The most pronounced effects are:

- a)** periodic changing of the positive and negative deviations of the critical frequency with period of approximately 5 days (one can observe two minima of this variation on 25 and 30 of March in the western part of the chain);
- b)** approximately 32 h difference between development of the minimum and maximum of critical frequency deviation on the western and eastern edges of the chain. The most pronounced effect one can see in the positive variation development on 26-28 of March. It starts at afternoon, 26 of March, at the eastern edge of the chain and moves to the west reaching the western edge of the chain at the evening of March, 28;
- c)** positive variations observed practically at all stations near local midnight;
- d)** existence of some longitudinal border near  $55^{\circ}$  E longitude when the phase of the critical frequency deviation changes its sign, it looks like the  $180^{\circ}$  phase shift between the different longitude zones.

One can conclude that the Fig. 4 represents a very complex combination of temporal and longitude variations, observed during sequence of substorms within the storm recovery phase. Among many variations described above it seems that the main feature of the observed picture is the change of the phase difference in variations on western and eastern stations occurred between 26 and 27 of March. We connect this effect with the change of all geophysical indices slope exactly within these two days.

We made attempt to separate the daily and longitudinal variations by two cross-sections of our data. We selected the values of critical frequency deviations for two given local time values: midnight and noon, and studied the dynamics of their longitudinal distribution within SUNDIAL/ATLAS-1 period. The results are presented in Fig. 6. The night-time longitudinal distributions (upper panel of Fig. 6) demonstrate the gradual density increasing at all longitudes (except low latitude Tashkent station,  $69^{\circ}$  E) after 26 of March. The local precipitation event is

observed on 31 of March at 60° E. For local noon time the longitudinal distribution is more complex. Except the local precipitation events discussed above, one can observe the longitudinal movement of the border between the positive and negative variations within the SUNDIAL/ATLAS-1 interval from west to east. It is very slow motion (the longitudinal velocity could be estimated as 50° a week). Probably this change in phase of the critical frequency deviation on different longitudes reflects the slow changes of interplanetary space conditions. But for such conclusions the special spectral analysis of different geophysical indices is necessary.

To find the position of the increased disturbances within SUNDIAL/ATLAS-1 period the ionospheric  $Af_oF2$  index was used. As it was done for the Moscow station, the variability indices  $Af_oF2$ , (see section 3), were calculated for other stations of the chain. Their distribution versus time and longitude (the index itself is shown by color) is presented in Fig. 7. As it was discussed in section 3, the  $Af_oF2$  drop indicates increasing of the disturbance. One can see three structures indicating the increased disturbance.

The most pronounced is vertical structure corresponding to position of the Arkhangelsk station. It reflects the fact of the stations' close position to the main trough (during disturbances it falls inside the trough) So this structure is connected more with the latitudinal position of the station than with longitudinal variations.

The second one is horizontal (along longitude) structure observed on 27-28 of March, to East from 50° E. Due to sufficiently large longitudinal distance between station the mapping procedure can not integrate between the stations, so the longitudinal disturbance is seen as several maxima corresponding to the stations longitudinal positions. This disturbance corresponds to the changing of critical frequency deviations phase between the eastern and western stations of the chain observed in the Fig. 4.

And the third disturbed structure is observed in the bottom left corner of the picture, what corresponds to period of 29-31 of March and western part of the ionospheric stations chain.

We have discussed higher the morphological characteristics of longitudinal snap-shorts built for the critical frequency deviations and the ionospheric index  $Af_oF2$ . This new visualization technique of the ionospheric data discovered a lot of new features of the ionospheric variability and made more obvious different

disturbances associated with geomagnetic activity. Instead of mixture of variations caused by different sources now we are able to distinguish such effects like precipitation events, local substorms connected with short southward  $B_z$  turnings, global ionospheric variation as periodic (5 days variations), so connected with global storm events. The ionospheric variations, systematized by the cause effect, later could be used for these cause identification, i.e. promptitude estimation of different solar-geomagnetic conditions. For example, comparing the positive variations in the western part of the chain with the temporal positions of the, we can suppose in absence of IMP-8 data that on 29.03 the southward  $B_z$  turning had place too. It makes investigator more independent from different geomagnetic indices in the cases when the quick reaction is necessary.

## **6. The particle precipitation and ionospheric variability**

It is well known that the geomagnetic  $K_p$  and  $A_p$  indices are the mixture of the local substorm activity and global geomagnetic storm expression [Gonzales et al., 1994]. They are calculated, basing on the geomagnetic data collected from the observatories falling into the  $50^\circ - 63^\circ$  of geomagnetic latitude range. Hence, they include as ring current effects, so the auroral activity effects. The ionospheric stations under consideration in present paper fall in the same geomagnetic latitude range. We presented higher the visualization technique which give possibility separate some of them. But it is interesting to find the direct information, what part of the ionospheric variability at subauroral latitudes is conditioned by the auroral activity. From this point of view it is interesting to look on the relation between the variations of particle precipitation fluxes within the auroral zone and ionospheric variability. In our analysis the information about auroral particle precipitation processes is presented by the NOAA/TIROS index discussed above, and ionospheric variability is expressed in percentage deviation of the critical frequency  $\Delta f_oF_2$  at the longitudinal chain of ionospheric stations within the Euro-Asian sector of longitudes.

To find the cause-effect relationships between the energy input into the auroral ionosphere in the form of precipitating particle fluxes and ionospheric density variations the cross-correlation analysis was made between the NOAA/TIROS index variations and the  $\Delta f_oF_2$  for every of station from the chain. We looked not only to the cross correlation coefficient magnitude but more on the

phase relation between the variations which is more convincing in this regard. Cross-correlation functions were calculated for all 10 stations. They are presented in Fig. 8. One can conclude from the figure that the direct phase relation between the precipitating electron fluxes and variations of  $f_oF_2$  exist. It is very important to note that the revealed result shows not only the similarity of the time behavior of the both processes but the cause-effect relation. The  $0.5 \pm 0.6$  value of cross-correlation function shows that to this extent the variations of  $f_oF_2$  are determined by the particle precipitation, and that the remaining variations are determined by the other factors. The time shift shows the time delay between the cause and effect processes (or the time shift between them). It is interesting to note that the half wave period of the cross-correlation function is of order of 16 hours what corresponds to the longitudinal positive disturbance movement determined by the Fig. 4 analysis which equals to 32 hours. The most striking fact is that effect is stable in relation to the local time, not UT because the cross-correlation functions for all stations were calculated in relation to the local time, and they practically overlap, nevertheless the essential shift in their UT (longitudinal) positions. It means that energy into ionosphere within the auroral zone is transported corresponding to local time and it should exist the phase shift in development of global storm in relation to the longitudinal position of the station.

The dependence on the local time not the universal time again attract our attention to the role of the high latitude electric field of magnetospheric convection penetrating into the middle latitudes. This field spatially depends on UT but not on LT. Near local midnight we have changing of the electric field direction in such a way that its zonal component directed westward in pre-midnight sector and eastward in postmidnight sector. Such electric field distribution, very similar to our Fig. 8 was obtained by Wang [1981] basing on the data from Millstone Hill radar. This fact give us possibility to explain the changing of the  $\Delta f_oF_2$  sign in Fig. 4 as a result of electric field configuration. We did not make measurements of the electric fields in present investigation but we use the results of the previous experiments with similar results and model calculations made in similar conditions. The physical mechanisms of substorms on the subauroral latitudes explaining the asymmetry in the development of substorm in pre-midnight and post-midnight sectors of the local time, formation of the narrow localized trough of ionization in the evening sector, formation of the step-structured ionosphere in the morning sector are

described in [Deminov and Shubin, 1987 and 1988]. One of the main features of the described mechanism is the dependence of the substorm development in the ionosphere on the local time (positive and negative phases, delay time from SC).

These calculations support our experimental result: one can see from Fig. 4 that the phase shift from positive to negative variations usually happens close to the white lines showing the local midnight time.

## 7. Conclusion

The ionospheric variability was analyzed for period of SUNDIAL/ATLAS-1 mission (24.03-31.03 1992) on the longitudinal chain of mid-latitude - sub-auroral ionospheric stations in European-West Asian sector (13°- 90° E), using the satellite (NOAA/TIROS) data for precipitating particles on auroral latitudes and EISCAT radar data. This period was characterized by sequence of substorms with moderate geomagnetic activity (mean  $K_p \sim 3.5+$ ) within the geomagnetic storm recovering phase.

The study was directed to the improvement of the promptitude of the ionospheric data analysis from the point of view of the ionospheric variability. For this purpose two recently introduced indices were analyzed: the ionospheric variability index of Gulyaeva et al. [1990] and NOAA/TIROS satellite particle precipitation index [Foster et al., 1986]. They were selected by the following reasons: the first one relates on the ionospheric data themselves and its calculation does not depend on the time of appearing of any geomagnetic index; the second one has clear physical meaning - it estimates the energy release within the auroral ionosphere during geo-magnetically active periods and give possibility for separation of auroral effects from the effects within the inner magnetosphere. The cross-correlation study was carried out for different combination of indices. In addition to known information about relation of different geomagnetic indices [Saba et al., 1994; Gonzales et al., 1994] it was shown that ionospheric variability  $Af_2F2$  index has good correlation with  $D_{st}$  index and poor correlation with  $K_p$  and  $A_p$  geomagnetic indices. We regard as very interesting and intriguing result that high frequency components of  $D_{st}$  and NOAA/TIROS indices practically do not correlate, but their daily averages have correlation near 0.9.

We proposed the new visualization technique for analysis of temporal and longitudinal variations. Longitudinal variations on the chain of sub-auroral

ionospheric stations show very complex character but this technique and comparison with other geophysical parameters (geomagnetic indices,  $B_z$  southward turnings, local time particle precipitation events) gave possibility to separate different types of ionospheric variability: local events, local substorm activity, periodic (5 days) variations, global reaction on the geomagnetic activity. In some cases the direct cause-effect relations were found.

The study of the storm development on the local time was carried out. The existence of such dependence was shown by two factors: the symmetry of the correlation functions between the particle precipitation (NOAA/TIROS index) and ionospheric variability in relation to the local time for all ionospheric stations of the chain and the change from positive to the negative variations of critical frequency near the local midnight. This experimental result is supported by the theoretical considerations relating to the role of the magnetospheric convection electric field, which changes its direction near the local midnight [Deminov and Shubin, 1988].

## References

- Bilitsa, D., K. Rawer, L. Bosny and T. Gulyaeva, International reference ionosphere - past, present and future: I. Electron density, *Adv. Space Res.*, **13**, No 3, p. (3)3-(3)13, 1992.
- Chiu Y.T., and M. Schulz, Self-consistent particle and parallel electrostatic field distribution in the magnetospheric-ionospheric auroral region, *J. Geophys. Res.*, **83**, pp.629-642, 1978
- Deminov M.G., and V.N.Shubin, Subauroral ionosphere dynamics in disturbed conditions, *Geomagnetism and Aeronomy*, **27**, No 3, pp. 398-403, 1987
- Deminov M.G., and V.N.Shubin, The electric fields effects in the night-time subauroral F-region, *Geomagnetism and Aeronomy*, **28**, No 2, pp. 319-321, 1988
- Evans D.S., Precipitating electron fluxes formed by a magnetic field aligned potential difference, *J. Geophys. Res.*, **79**, pp.2853-2858, 1974
- Foster, J.C., J.M. Hoit, R.G. Musgrove, and D.S. Evans, Ionospheric convection associated with discrete levels of particle precipitation, *Geophys. Res. Lett.*, **13**, 656, 1986
- Foster J.C., Storm time plasma transport at middle and high latitudes, *J. Geophys. Res.*, **98**, No A2, pp.1675-1689, 1993
- Fuller-Rowell T.J., M.V. Codrescu, R.J. Moffet, and S. Quegan, Response of the thermosphere and ionosphere to geomagnetic storms, *J. Geophys. Res.*, **99**, No A3, pp.3879-3892, 1994
- Gonzales W.D., J.A.Joselyn, Y.Kamide, H.W. Kroehl, G.Rostoker, B.D.Tsurutani and V.M.Vasyliunas, What is a geomagnetic storm? , *J. Geophys. Res.*, **90**, No A4, pp.5771-5792, 1994
- Gulyaeva T.L., M. Mosert de Gonzalez, S.M.Radicella and B.Zolezi, Spatial and temporal variability of the ionosphere during solar minima, *Adv. Space Res.*, **10**, No 11, p. (11)31-(11)34, 1990.
- Gulyaeva T.L., K.Barbatsi, J.Boska, G. de Francesci, S.S.Kouris, S.Moraitis, S.Pulinets, S.M.Radicella, I.Stanislawski, Th.Xenos and M.-L.Zhang, Definition of Disturbance and quietness with topside ionosonde data, *Adv. Space Res.*, **16**, No.1, pp. (1)43-(1)46, 1995



- Hapgood M.A., M.Lockwood, G.A.Bowe, D.M. Willis and Y.K.Tulunay, Variability of the interplanetary medium at 1 a.u. over 24 years: 1963-1986, *Planet. Space Sci.*, **39**, pp.411-424, 1991
- Heppner J.P, and N.c.Maynard, Empirical high latitude electric field models, *J. Geophys. Res.*, **92**, pp. 4467-4489, 1987
- Holt J.M., R.H. Wand, J.V.Evans, and W.L. Oliver, Empirical models for the plasma convection at high latitudes from Millstone Hill observations, *J. Geophys. Res.*, **92**, pp. 203-212, 1987
- Ijima T, and T.A. Potemra, Large-scale characteristics of field-aligned currents associated with substorms, *J. Geophys. Res.*, **83**, pp.559-615, 1978
- Kamide Y., P.D.Perrault, S.-I.Akasofu, and J.D.Winningham, Dependence of substorm occurrence probability on the interplanetary magnetic field and on the size of the auroral oval, *J. Geophys. Res.*, **82**, 5521, 1977
- Karpachev A.T., M.G. Deminov and V.V.Afonin, Model of the mid-latitude ionospheric trough on the base of Cosmos-900 and Intercosmos-19 satellites data, *J.A.T.P.*, in press, 1995
- Kishcha P., Indices and updating procedures for modeling of ionospheric disturbances, *Adv. Space Res.*, **16**, No 1, pp. (1)55-(1)64, 1995
- Kohnlein W. and W.J.Raitt, Position of the mid-latitude trough in the topside ionosphere as deduced from ESRO 4 observations, *Planet.Space Sci.*, **25**, (5/6), pp. 600-602, 1977
- Kouris S.S., K. Barabtsi, T.D.Xenos and Bruno Zolesi, Correlations in daily deviations from the median of  $f_oF_2$ ,  $M(3000)$  and  $h'F$ , *Annali di Geofis.*, **XXXVII**, No 2, pp.175-185, 1994
- Lastovicka J, and P. Mlch, Planetary wave range periodicities ( $\approx$  2-20 days) in  $f_oF_2$ -occurrence, relation to mesosphere, application in predictions, in Numerical mapping and modelling and their applications to PRIME, COST238/PRIME Workshop Proceedings, Eindhoven, The Netherlands, pp.95-102, 1994
- Lastovicka J, and P. Mlch, Variability in the period of 2-20 days and its usability in forecasting, in Development and testing of an electron density height profile model for PRIME, COST238/PRIME Workshop Proceedings, El Arenosillo, Spain, pp.157-164, 1994

- Lester M., J.A.Davies, H.Luhr and T.S.Virdi, High latitude Hall and Pedersen conductances during substorm activity in the SUNDIAL/ATLAS-1 campaign, *J.Geophys. Res.* 1996, this issue
- Mishin E.V., Yu.Ya.Ruzhin, V.A.Telegin, Interaction of the electron fluxes with the ionospheric plasma, Leningrad, Gidrometeoizdat, 1989, (in Russian)
- Mishin E.V., A.A.Trukhan and G.V.Khazanov, Suprathermal plasma effects within the ionosphere, Moscow, Nauka, 1990 (in Russian)
- Saba M, W.D.Gonzales, and A.L.C.Gonzales, Relationships between the  $D_{st}$ ,  $ap$ , and AE indices, *Adv. Space Res.*, **15**, (1)232 (1)236, 1994
- Schunk, R.W., and E.P.Szuszcwicz, First principle and empirical modeling of the global-scale ionosphere, *Ann. Geophys.*, **6**, 19-26, 1988
- Szuszcwicz E.P. et al. Sundial/ ATLAS-1 results Annual report to NASA, 1993.
- Szuszcwicz E.P., Advances in ionospheric physics: roles, relevance and predictions in the system of solar-terrestrial plasmas, U.S. National Quadrennial Rpt. To the IUGG, *Reviews of Geophysics, Supplement*, 721, 1995
- Szuszcwicz E.P., D.Torr, P.Wilkinson, P.Richards, R.Roble, B.Emery, G.Lu, M.Abdu, D.Evans, R.Hanbaba, K.Igarashi, P.Jiao, M.Lester, S.Pulinets, B.M.Reddy, P.Blanchard, K.Miller, J.Joselyn, F-region climatology during the SUNDIAL/ATLAS-1 campaign of March 1992: Model-Measurement comparisons and cause-effect relationships, *J. Geophys. Res.*, 1996, this issue
- Tulunay Y.K., Interplanetary magnetic field and its possible effects on the mid-latitude ionosphere II, *Annali di Geofis.*, **XXXVII**, No2, pp.193-200, 1994
- Wahlund J.-E., and H.J. Opgenoorth, Observation of thin auroral ionization layers by EISCAT in connection with pulsating aurora, *J. Geophys. Res.*, **94**, No A12, pp. 17,223-17,233, 1989
- Wang R.H., A model representation of the ionospheric electric field over Millstone Hill ( $\lambda = 56^\circ$ ), *J. Geophys. Res.*, **86**, No A7, pp. 5801-5808, 1981
- Wilkinson P., P.Richards, K.Igarashi, Ionospheric climatology and weather in the Australian-Japanese sector during the SUNDIAL/ ATLAS-1 campaign, *J. Geophys. Res.*, this issue, 1996

**Table 1. Parameters of Ionospheric Data Base Used in Analysis**

No	Station name	Station code	Longitude (E)	Latitude (N)	L	ILAT	UT	Period of data available	Data set
1	Juliusruh	JUL	13.3	54.6	2.6	51.2	1H	01.03-30.04	All
2	Kalinigrad	KGD	20.62	54.7	2.6	51.4	1H	24.03-08.04	$f_oF_2$ , M3000
3	Leningrad.	LGD	30.7	59.95	3.3	56.0	2H	24.03-31.03	All
4	Moscow	MSK	37.3	55.5	2.6	51.5	2H	01.03-30.04	All
5	Arkhangelsk	ARK	40.5	64.5	4.1	60.3	3H	24.03-31.03	$f_oF_2$
6	Sverdlovsk	SVR	61.1	56.7	2.7	52.6	4H	24.03-31.03	All
7	Tashkent	TAS	69.0	41.3	1.5	37.2	4H	24.03-02.04	All
8	Karaganda	KRG	73.1	49.8	2	45.8	5H	24.03-31.03	All
9	Novosibirsk	NVS	83.2	54.6	2.4	50.5	6H	24.03-31.03	All
10	Podkamennaya Tunguska	PKT	90.0	61.6	3.3	57.3	6H	24.03-02.04	All

• Now Sankt-Petersburg

\*\* Now Ekaterinburg

## Figure captions

Fig. 1. Map of geographical locations of the ionospheric stations within the Euro-Asian sector of longitudes, data of which are used in present analysis

Fig. 2. Geophysical conditions for March 1992

♦ **-top panel:** upper continuous curve - 3-hour  $K_p$  geomagnetic activity index  
lower curve - closed circles - daily  $A_p$  index of geomagnetic activity

♦ **- middle panel:** open circles - daily index of ionospheric variability  
 $Af_0F2$  closed circles - reversed mean daily values of NOAA/TIROS index

♦ **c - bottom panel:** upper plot - reversed NOAA/TIROS data  
lower plot -  $D_{st}$  index

The SUNDIAL/ATLAS-1 period is highlighted by the thick line in the right bottom part of every panel

Fig. 3. Upper plot of every panel - monthly variations of the critical frequency  $f_0F2$  (triangles) and monthly median (continuous curve)  
Lower plot of every panel -  $\Delta f_0F2$  variations in percents

Upper panel - Moscow data

Lower panel - Juliusruh data

Fig. 4. Dynamics of  $\Delta f_0F2$  (%) variations for SUNDIAL/ATLAS-1 in Euro-Asian sector. The  $\Delta f_0F2$  magnitude is shown by color. The time

southward turnings by IMP-8 data are shown at the vertical axis by open triangles. The bold black arrow in the figure indicates the precipitation event registered at Arkhangelsk station.

Fig. 5. **Top panel** - Variations of electron density and temperature on the heights 90 - 270 km by the data of Tromsø IS radar for evening hours of 27.03.92

**Middle panel** -  $\Delta f_oF2$  variations at Arkhangelsk ionospheric station on 27.03.92

**Bottom panel** - Magnetogram (horizontal component) at Kiruna observatory on 27.03.92

Fig. 6. Upper panel - longitudinal distributions for local midnight values of  $\Delta f_oF2$  for SUNDIAL/ATLAS-1 period.

Bottom panel - longitudinal distributions for local noon values of  $\Delta f_oF2$  SUNDIAL/ATLAS-1 period.

Fig. 7. Dynamics of the ionospheric variability index  $Af_oF2$  calculated for every station under analysis for period of SUNDIAL/ATLAS-1 campaign. The index value is shown by color.

Fig. 8. Cross-correlation functions between the critical frequency deviations and NOAA/TIROS index for period of SUNDIAL/ATLAS-1 interval calculated for every ionospheric stations from the longitudinal chain

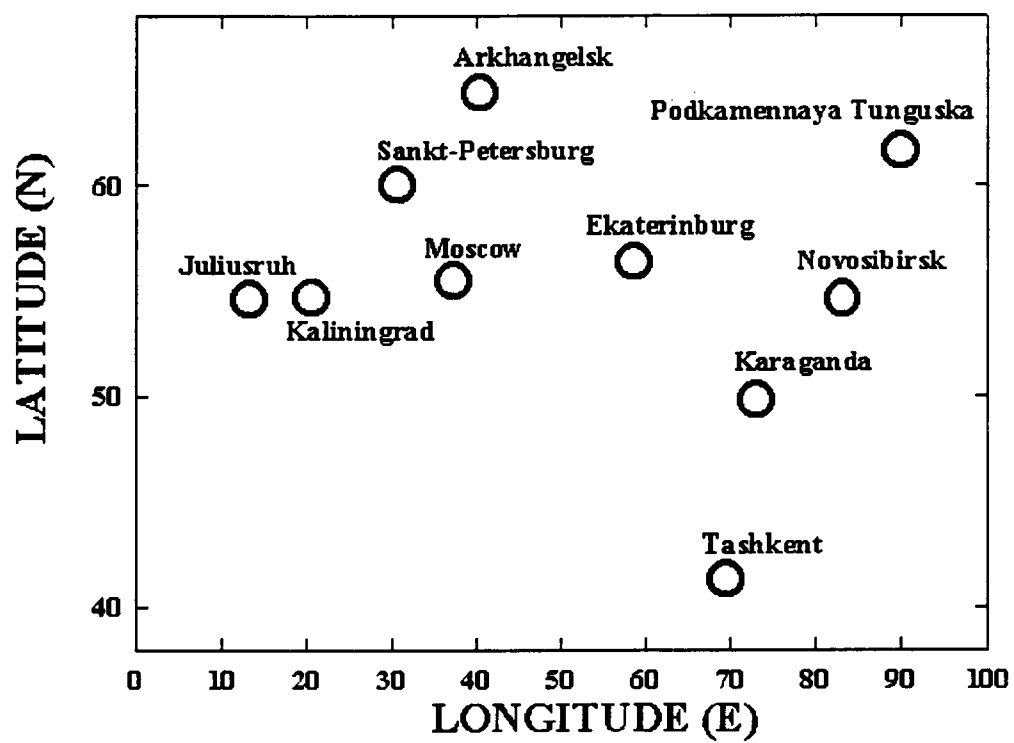


Fig. 1

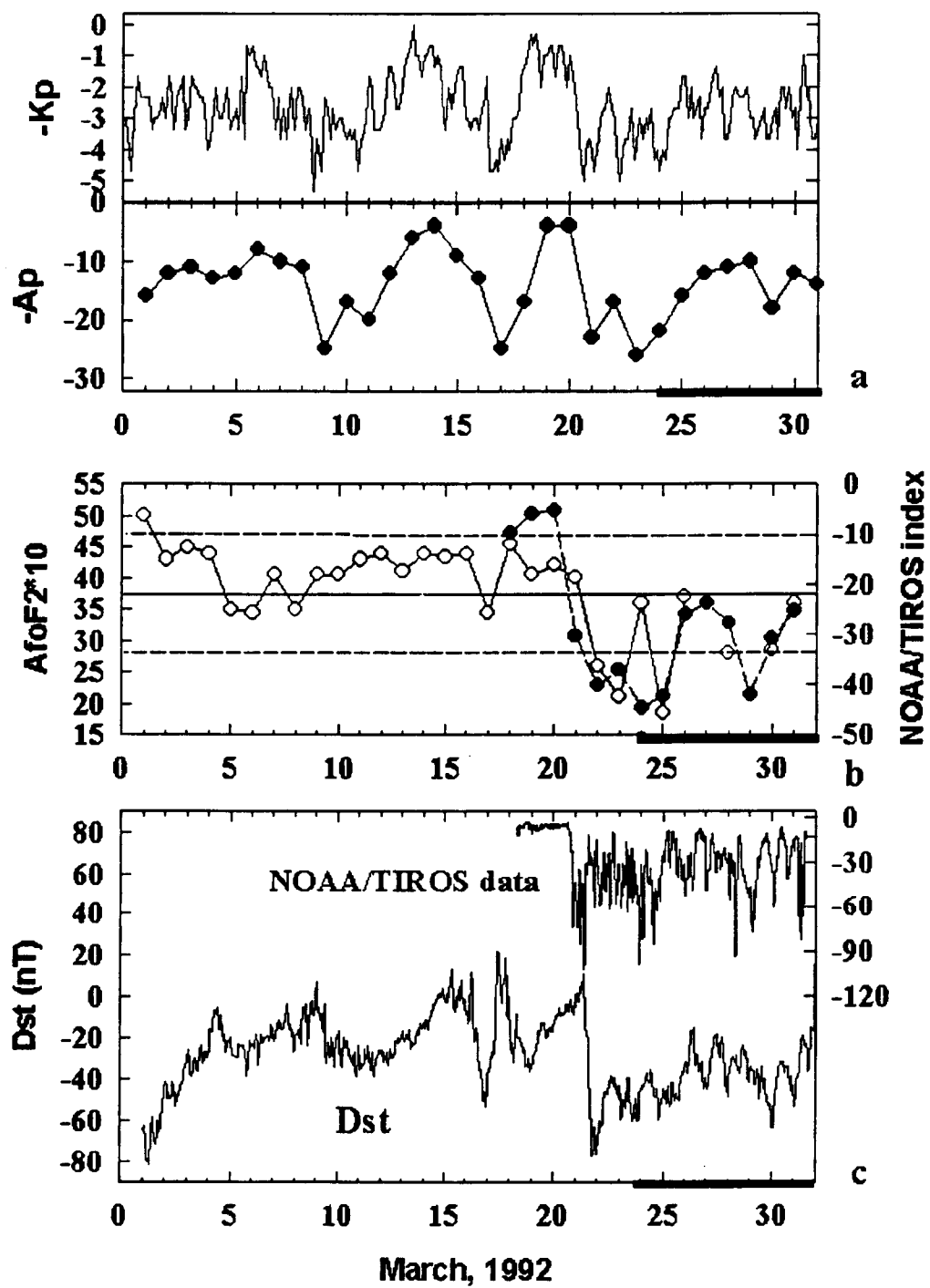
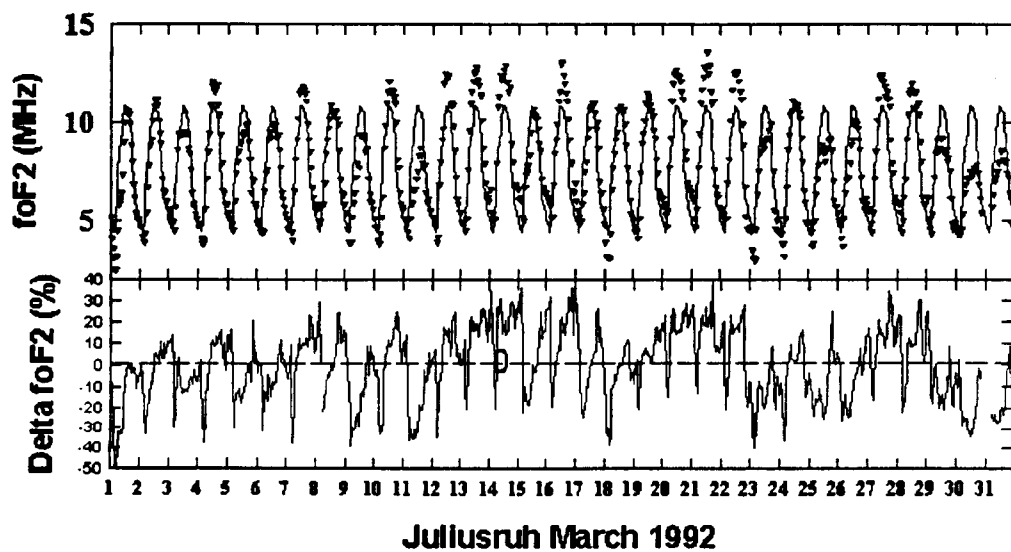
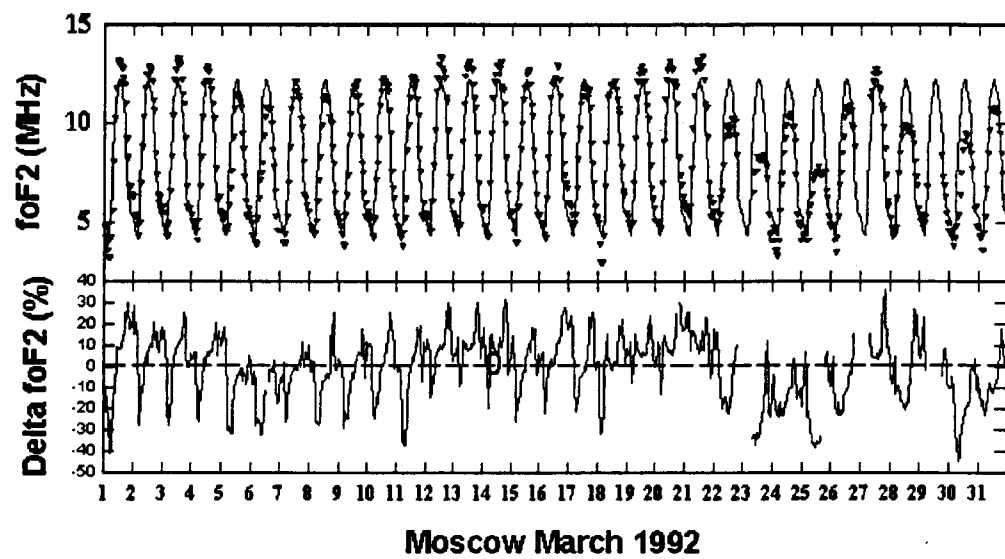
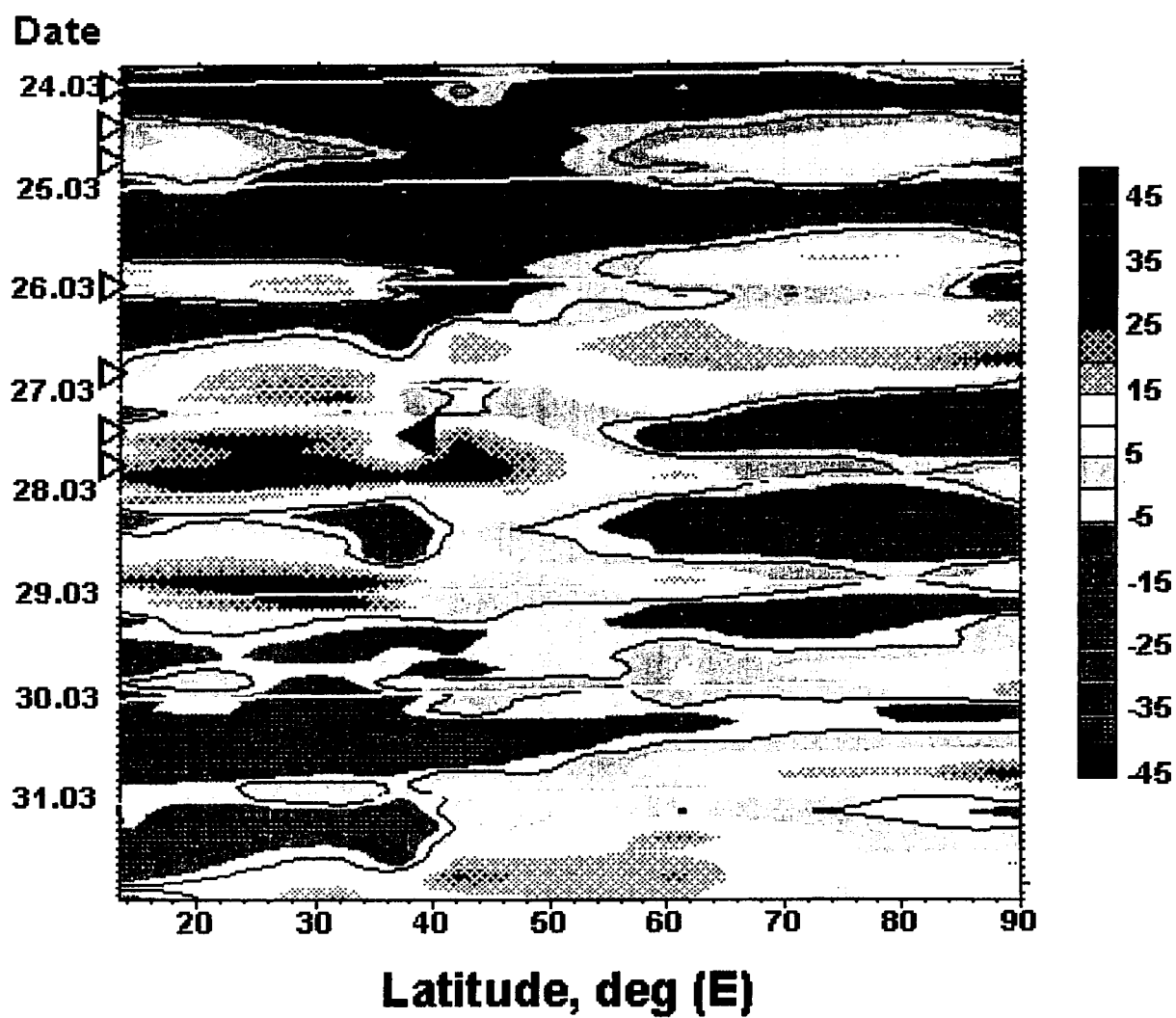


Fig. 2



**Fig. 3**





**Fig. 4**



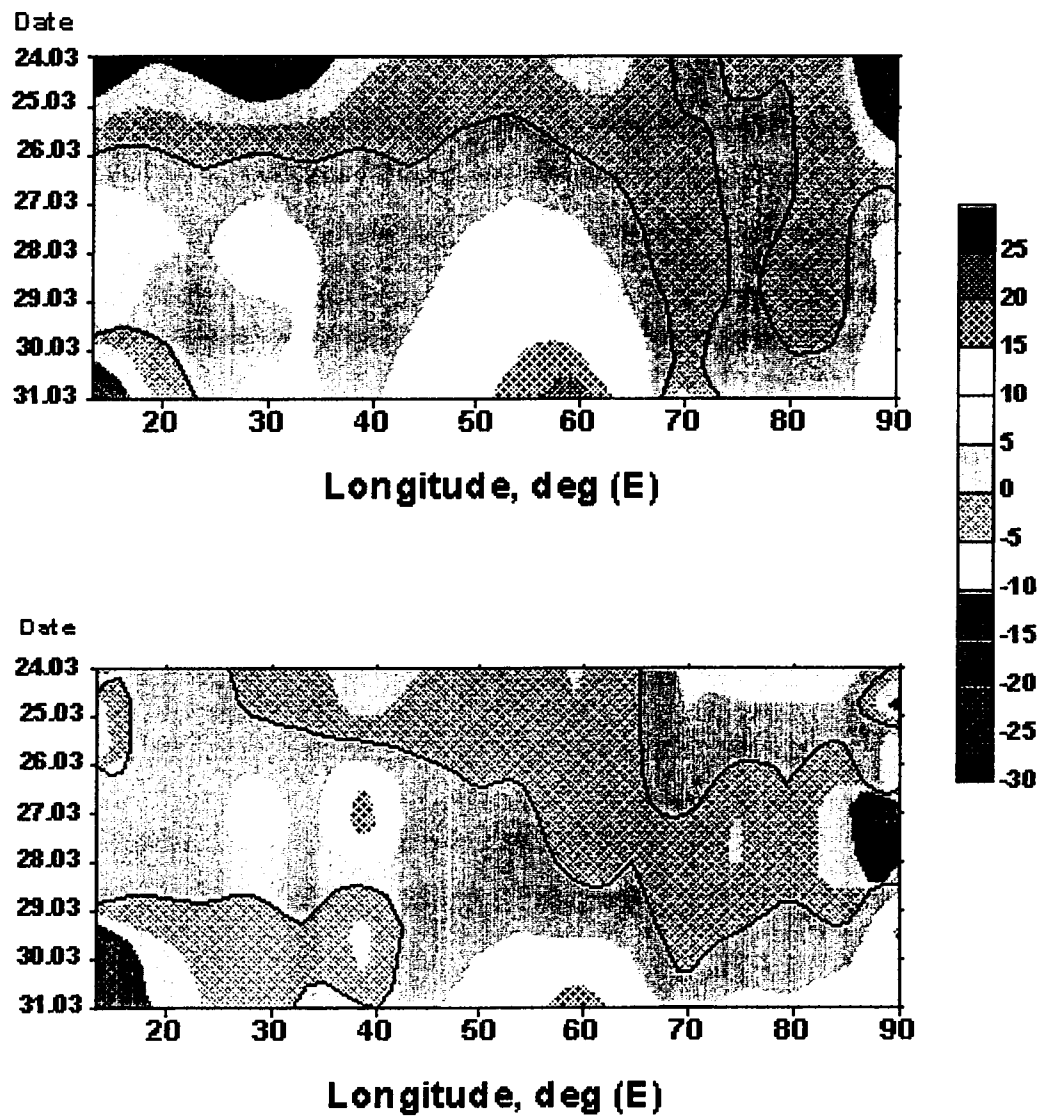


Fig.6

Date

24.03

25.03

26.03

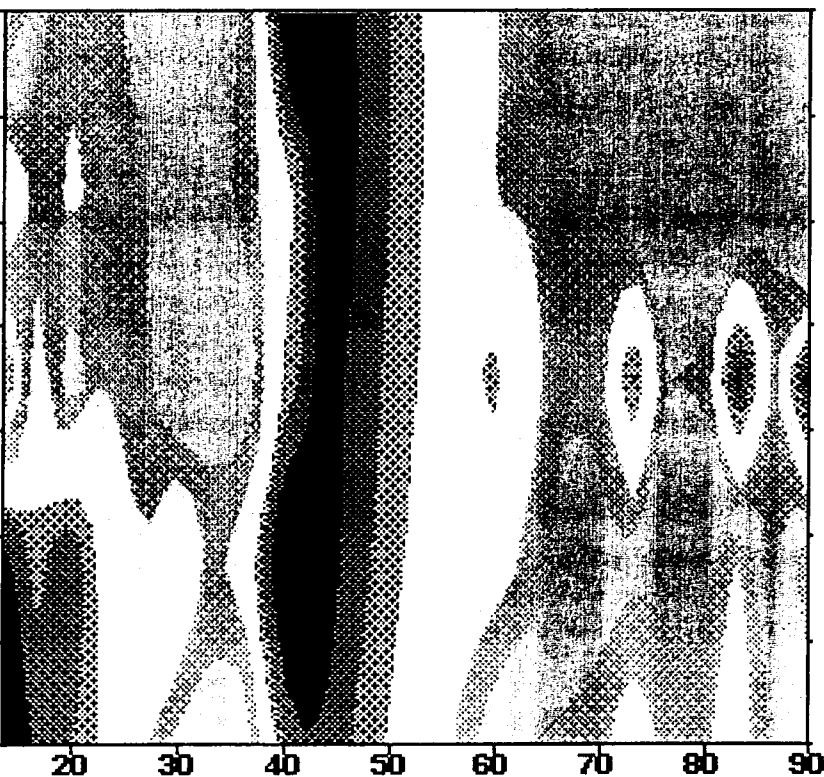
27.03

28.03

29.03

30.03

31.03



AfoF2

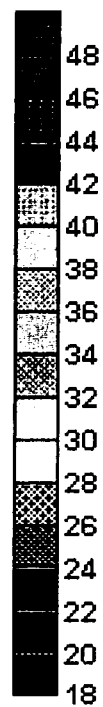


**Fig. 7**

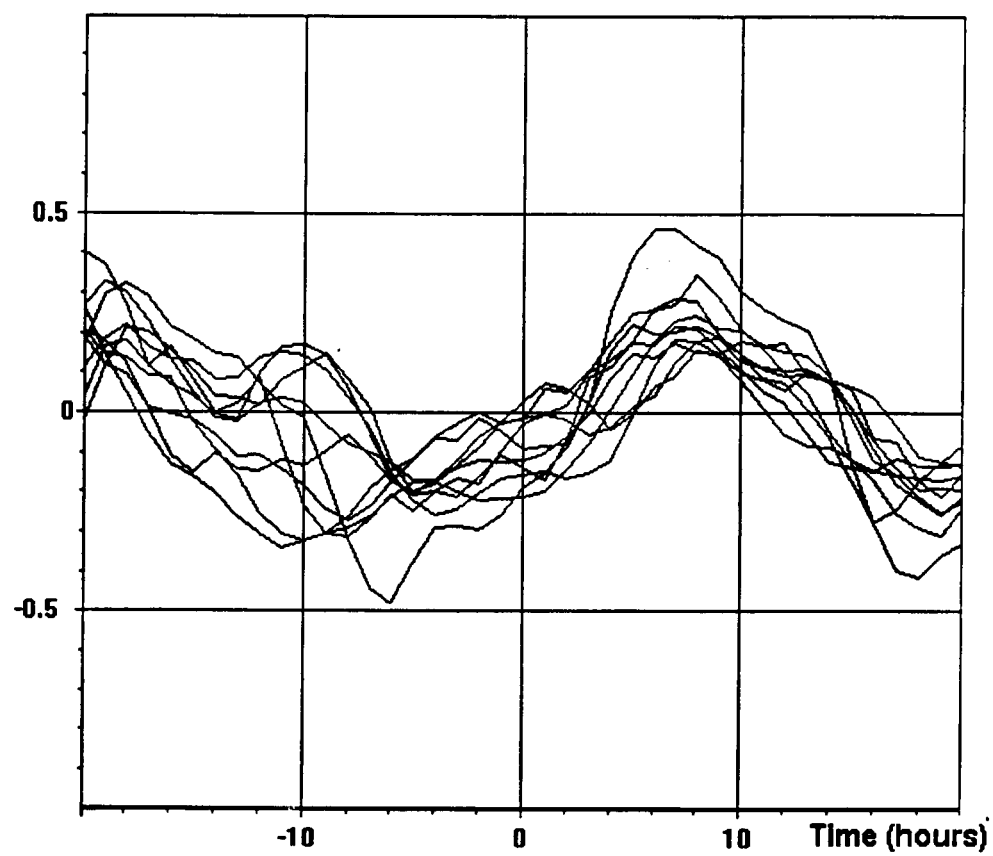


**Fig. 8**

**Zonal/Meridional Wind and Disturbance Dynamo Electric  
Field Control of the Low Latitude Ionosphere based on  
the SUNDIAL/ATLAS-1 Campaign**

**M.A. Abdu, J.H.A. Sobral, P. Richards, Marta M. de Gonzalez, Y.N. Huang,  
B.M. Reddy, K. Cheng, and I.S. Batista**

## **Zonal/Meridional Wind and Disturbance Dynamo Electric Field Control of the Low Latitude Ionosphere based on the SUNDIAL/ATLAS-1 Campaign**

M. A. Abdu (1), J. H. A. Sobral (1), P. Richards(2), Marta M. de Gonzalez(3), Y. N. Huang(4), B. M. Reddy(5), K. Cheng(6), E. ~~Pr~~ **Szuszczewicz**(7), I. S. Batista(1)

(1) Instituto Nacional de Pesquisas Espaciais. INPE. São José dos Campos, Brazil;

(2) Center for Space Plasma and Aeronomic Research. Univ. Alabama in Huntsville, USA;

(3) Complejo Astronomico El Leoncito, San Juan, Argentina;

(4) Directorate General of Telecommunication, MTC, Republic of China;

(5) National Physical Laboratory, New Delhi, India;

(6) Lunping Observatory, TTI, MTC, Republic of China;

(7) Science Application Int'l Corporation (SAIC), McLean Va., USA.

### **Abstract:**

We present an evaluation of global scale equatorial- and low- latitude ionospheric disturbances in response to the weak-to-moderate disturbed conditions that marked the SUNDIAL/ATLAS-1 12-day campaign of 22 March - 02 April 1992. Ionosonde data from South American and Indian-Asian longitudes are analysed to examine first the climatological (the average) pattern of the critical F region parameters (the layer peak density and height) in comparison with the empirical International Reference Ionosphere (IRI) model, and then to characterize the day-to-day variabilities aiming at identifying potential causal contributions from either disturbance zonal and meridional winds or magnetospheric and disturbance dynamo electric fields. Included in this analysis are data from South American midlatitude locations which are used to determine meridional winds using an adaptation of the servo analysis technique in the Field Line Integrated Plasma (FLIP) model. We have made an assessment of the causal mechanism of the day-to-day variabilities as arising from latitude dependent disturbance meridional winds, and from electric fields produced by disturbance zonal winds and disturbance dynamo. While the contribution from disturbance meridional winds decreases from mid- to equatorial latitude, that of the electric fields maximizes around the equator. It is found that there are two time intervals of maximum ionospheric variability resulting from the weak-moderate magnetospheric disturbance conditions that prevailed during the campaign: one near the evening/postsunset hours and the other in the post midnight-sunrise hours over low latitudes. At midlatitudes a broad maximum of the response occurs from pre midnight to morning hours. We provide a comparison of results for the South American and Indian-Asian longitudes and a

discussion of the competing roles of the disturbance zonal and meridional winds, and magnetospheric and disturbance dynamo electric fields as a function of latitude.

## 1. Introduction

Ionospheric climatology reflects the response of the ionospheric-thermospheric system to a quasi steady input of solar, magnetospheric, and lower atmospheric energy. Day-to-day variabilities (weather) are produced by fluctuations in these inputs resulting in perturbation electric fields and thermospheric winds and ultimately in fluctuating E- and F-layer heights and densities. Equatorial-to-low latitude ionospheric responses to magnetospheric disturbances has received some attention in recent years for moderate to intense storm events and a tentative understanding of such cases in terms of a cause-effect relationship seems to be emerging (see for example, Forbes, 1989; Fesen et al., 1989; Abdu et al., 1991; 1993; 1995a; Batista et al., 1991; Greenspan et al., 1991; Huang and Cheng, 1993; Fuller-Rowell et al., 1994; Fejer et al., 1995). In the case of the more frequent and weaker disturbances of magnetospheric origin, the low latitude ionospheric response remains almost undefinable. This is also true of the widely observed variabilities in the "quiet" time low latitude ionosphere. An example is the day-to-day variability in the intensity of the evening prereversal electric field (F layer vertical drift) enhancement that has direct implication on the equatorial spread F development conditions in the postsunset hours. In fact a major focus of current research is to achieve a better understanding of the causes of the observed day-to-day and seasonal variabilities in the equatorial spread-F phenomenon. Therefore it is important to investigate and identify the salient features of the variabilities of the low latitude ionosphere under "quiet" and weakly disturbed conditions if we are to identify them either as manifestations of the coupling process within the system or the response of the system to external forcing. The SUNDIAL-ATLAS-1 12-day campaign (22 March -2 April 1992) has provided an opportunity to examine some prominent global features of the day-to-day variability of the low latitude ionosphere, including causalities due to the competing roles of the electric field/zonal wind versus that of meridional wind as a function of latitude. The variabilities are presented and discussed with respect to the climatological (average) behavior of the ionosphere. Detailed discussion of the global climatology that prevailed during the campaign and comparisons with the specifications of the International Reference Ionosphere (IRI), and the predictions of first principle codes (Themosphere-Ionosphere General Circulation Model-TIGCM, and the Fieldline Integrated Plasma Model- FLIP) are carried out by Szuszczewicz et al. (1995, this issue).



The results presented in this paper are based on data from 6 ionosonde and 2 magnetometer stations distributed in the Indian-Asian and American longitude sectors as listed in Table-1.  $f_oF_2$ ,  $h'F$ , and  $hpF_2/hmF_2$  are analysed and the results are compared with the predictions from the IRI. (see for example, Bilitza et al., 1992) and the FLIP (Richards and Torr, 1988; Torr et al., 1990). The FLIP model has been run for the midlatitude stations Buenos Aires and Ushuaia to obtain the meridional winds over these stations to evaluate (by extrapolation) the possible effects of such winds on aspects of the climatology and the day-to-day variabilities of the ionosphere in the mid-to-equatorial latitude regions in the American sector. This approach is used because no model presently exists that could provide winds (from ionosonde data) for low latitude regions where the electric field effects dominate the ionospheric processes. The results for the American longitude sector are compared with those for the Indian-Asian longitudes.

The solar and geomagnetic activity conditions of the SUNDIAL-ATLAS-1 campaign are detailed in the paper by Szuszczewicz et al. (1995, this issue). Briefly, the period covered the recovery phase of a weak-to-moderate storm that had onset at about 2300 UT on 21 March, as indicated by the Dst values of Fig. 1 which was predominantly more positive than -50 nT with occasional decreases to values approaching -60 nT. The geomagnetic activity index, Kp also suggested weak-to-moderately disturbed conditions with values remaining generally less than 5 except for a few isolated periods. Using the local magnetograms in Brazil we conclude that the most disturbed intervals were the nights of 21-22, 23-24, and 29-30. This characterization was generally valid for the Asian sector as well.

## 2. F-Region Climatology

The climatological behavior of the F region, manifested by the average magnitudes of the critical parameters  $f_oF_2$  (the critical frequency representing the peak density  $NmF_2$  of the layer) and  $hpF_2$  (the height of the peak density) over the South American stations, Fortaleza, Cachoeira Paulista, Buenos Aires and Ushuaia, is presented in Fig. 2. We have used here the parameter  $hpF_2$ , instead of  $hmF_2$ , and it represents the height of the peak density for a parabolic approximation of the layer that is directly read from the ionograms (Piggot and Rawer, 1978). A comparative study by Batista et al. (1991a) of the  $hpF_2$  with the  $hmF_2$  from the true height POLAN code (Titheridge, 1985) has shown that for equinoctial night conditions the two values are practically the same, whereas during the day the  $hpF_2$  could be higher than  $hmF_2$  by up to 10 percent.  $f_oF_2$  and  $hmF_2$  obtained from the FLIP runs are also included in Fig. 2 for Buenos Aires and Ushuaia. With reference to Fig. 2 we will discuss the day-to-day variabilities and extend the results to Indian -Asian longitudes for which

the foF2 and hpF2 diurnal pattern are presented in Fig. 3. Our comparison here covers all local times but is restricted to a few stations in the South American and Indian - Asian longitudes. We note that there is very good general agreement between the observed mean and the predicted IRI values. But some notable differences are: (a) -The evening F-layer uplift (around 18-19 LT, Fig. 2, right panel) over Fortaleza produced by the prereversal enhancement electric field, and the corresponding postsunset resurgence of the equatorial ionization anomaly over Cachoeira Paulista (around 21-22 LT, Fig. 2, left panel) are not adequately represented by the IRI (see also, Abdu et al., 1995b); (b)- There is an indication that the postmidnight-morning hpF2 increases over Buenos Aires and Ushuaia and the corresponding (small) decrease of foF2 are not adequately represented by the IRI. We will show that such differences, however, are likely produced by equatorward meridional winds produced under the disturbed conditions that characterized the SUNDIAL-ATLAS campaign interval; (c)- The morning height increase over Fortaleza that appears as departure from the IRI representation is, in fact, in response to the disturbed conditions, but, as will be explained, it seems to be produced by disturbance dynamo electric field; (d)- Both the disturbance sources in (b) and (c) seem to be responsible for the morning height rise over Cachoeira Paulista; and (e)- The FLIP model results for hmF2 show excellent agreement with the observations over Ushuaia and Buenos Aires (except for its structured feature in morning hours over the latter site), whereas the foF2 values present some disagreement marked by low model values for night conditions over Buenos Aires and for noon-to-midnight conditions over Ushuaia.

### 3. Day-to-Day Variabilities

In Fig. 4 we present the hpF2 values for all the four stations for 30 March, a day which started with a short duration (5-6 hrs) Dst decrease to less than -60 nT (see Fig. 1). The following salient features may be noted. Over Fortaleza: (1)- there is a 60 km presunrise increase of the F layer height and there is (2)- a large uplift of the layer around sunset produced by the well-known evening prereversal enhancement electric field, which on this night was interrupted at 1915 LT by spread F. Over Cachoeira Paulista: (1) the amplitude of the presunrise height rise is larger than over Fortaleza and is in fact comparable to the diurnal maximum in hpF2; and (2) the evening height uplift is drastically reduced compared to that of Fortaleza. Over Buenos Aires the morning height rise tends to become the dominant feature of the diurnal pattern and over Ushuaia the morning height rise is the most dominant feature of the diurnal pattern. In fact the morning height rise over Ushuaia starts from near midnight and lasts to well after the sunrise. Thus there is a clear evidence here of a postmidnight-morning height enhancement and of a latitudinal dependence in its amplitude and duration (i.e., its amplitude and duration decrease with decreasing latitude from midlatitude to the

equator). By contrast the evening/sunset enhancement decreases rather rapidly with increasing latitude from the equator.

Fig. 5 presents superimposed daily plots, covering the campaign period, of the F layer height parameters,  $h_pF2$  and  $h'F$ , for the same four south American stations as in Fig. 4. All points mentioned above can be verified while presenting perspective of the day-to-day variability in the F-layer characteristics and their latitudinal dependence. The variability in the F-layer peak density parameter,  $foF2$ , is similar, being a consequence of the variability in the peak height. A separate figure on  $foF2$  is therefore not presented here. The sunset associated prereversal electric field enhancements seen as the F layer uplift that dominates the diurnal pattern over Fortaleza (in Fig. 5) seems to be better defined in F layer base height,  $h'F$ , rather than in peak height,  $h_pF2$ . (It is opportune to point out here that  $d(h'F)/dt$  is a better indicator of the evening electric field than is  $d(h_pF2)/dt$  because of the fact that the evening F layer lower boundary is better defined (under the condition of the steepening bottomside density gradient that develops at these times), and more accurately determined from ionograms, than is the peak height. Further, with the diffusion coefficient increasing exponentially with height, the layer peak height variation  $d(h_pF2)/dt$  has contribution from diffusion factor significantly more than in the  $d(h'F)/dt$ . There is a large day-to-day variability in the reversal time of the electric field, that is, in the local time of the evening maximum of the  $h'F$ . This is an indication of the variability in the intensity of the F layer dynamo electric field. The weaker (stronger) the F layer dynamo is the earlier (later) will be the reversal of the evening electric field. Since the F layer dynamo electric field intensity is dependent on the eastward thermospheric zonal wind (Rishbeth, 1981; Heelis et al., 1974; Farley et al., 1986; Batista et al., 1986) the observed variability of the evening  $h'F$  (and  $h_pF2$ ) is an indicator of a corresponding day-to-day variability in the amplitude of the thermospheric zonal wind. We will come back to this point.

Over Cachoeira Paulista the sunset height rise is rather small, but seems to be better defined in  $h'F$  than in  $h_pF2$ . There is a significant day-to-day variability in them that could be produced by zonal as well as meridional wind components. As expected, the sunset associated layer rise is totally absent over Buenos Aires and Ushuaia. At these latitudes prominent layer uplift occurs mainly during the near midnight to morning hours. We will show that these uplifts are produced by equatorward neutral winds.

The main point to note at this stage is that the F-layer height rise and its variability decrease equatorward, a trend that can be clearly verified by comparing the plots for Ushuaia, Buenos Aires,

Cachoeira Paulista, and Fortaleza (if we exclude from the latter two stations the curves specially identified with circles, stars, etc., for reasons to be explained soon). We may note further from a comparison of the data between Cachoeira Paulista and Fortaleza that on the specially identified days the morning layer rise is significantly larger over the latter location than expected solely from response to an equatorward wind. In fact, the layer rise produced by a meridional wind ( $U$ ) which is dip angle dependent, as  $U \cos I \sin I$ , is expected to be a factor 2.5 less over Fortaleza than over Cachoeira Paulista. However, the observed height rises are significantly larger which could possibly be caused by a disturbance dynamo electric field considering the varying degree of moderately disturbed intervals (Fig. 1) that characterized these days.

Fig. 6 shows the  $h'F$  variations on 4 days (24 -27 March) over Waltair and the  $h'F$  and  $h_pF_2$  for the entire campaign period over Chung Li, in the Indian-Asian longitude sector. Here, again, the dominating role of electric field in the evening hours near the equator (Waltair) and that of meridional wind in the midnight - morning hours over low latitude (Chung-Li) can be noted, in complete agreement with the results from the American longitude sector. The  $h'F$  increase during the presunrise hours over Waltair could be arising from meridional wind as well as possibly from disturbance dynamo electric field as mentioned in the case of Fortaleza.

#### 4. Discussion

Our main focus in this paper has been on the day-to-day variabilities that dominated the postsunset and presunrise periods over the low latitude ionosphere, and aspects of their coupling with midlatitudes. We will now examine the roles of the zonal and meridional winds and that of the disturbance dynamo electric field in these variabilities.

##### 4.1 Role of the Zonal Wind

We have noted that the most outstanding feature of the F-layer height characteristics over Fortaleza is the evening electric field enhancement manifested as a large uplift of the layer seen both in  $h'F$  and  $h_pF_2$ . This is the well-known prereversal enhancement of the vertical drift (zonal electric field) amply documented in the literature based on radar data (Woodman, 1970; Fejer et al., 1991), on ionosonde data (Abdu et al., 1981; Batista et al., 1986), on hf Doppler observations (Balan et al., 1992), and theoretically explained as produced by the F-layer dynamo (Rishbeth, 1971; Heelis et al., 1974; Farley et al., 1986; Batista et al., 1986; Crain et al., 1993). Briefly, the evening equatorial zonal wind (which is eastward) interacts with the longitudinal E layer conductivity gradient that

develops across the sunset terminator. This creates a certain negative charge accumulation at the day-to-night boundary which produces an electric field that is eastward (westward) on the dayside (nightside) of the terminator. Theoretical calculations show that the local time of the maximum of the prereversal enhancement electric field is dependent upon the time at which the steepest longitudinal gradient in conductivity occurs, while the strength of the electric field, that is, the amplitude of the vertical drift, is strongly dependent on the neutral wind velocity (Abdu et al., 1995a; Batista et al., 1986).

It is, therefore, reasonable to attribute the day-to-day variability in the vertical drift/zonal electric field enhancement amplitude, to the day-to-day variability in the zonal wind values. In fact, the variabilities in the evening vertical drift/zonal electric field could arise from different sources: (a) disturbance magnetospheric electric field that penetrate to the low latitude ionosphere, associated with substorm onset/recovery and asymmetric/Dst ring current developments (see for example, Fejer et al., 1990; Abdu et al., 1993, 1995a; Sastri et al., 1992; Tanaka, 1986; Somayajulu et al., 1991), (b) disturbance dynamo electric field associated with disturbances in the global thermospheric circulation driven by storm energy deposition in the high latitude thermosphere (Blanc and Richmond, 1980; Fejer et al., 1983, 1995); (c) The disturbance zonal and meridional winds associated with item "b" interacting locally with ambient thermospheric winds in the equatorial region. Since the entire campaign interval was characterised by the recovery phase of a storm of weak-to-moderate intensity we may consider the item "a" above as having contributed partially to the observed variabilities. The contributions from items "b" and "c" to the day-to-day variability in the evening electric field enhancement may be assessed as follows. The prereversal enhancement amplitude in the vertical drift ( $V_z$ )/eastward electric field shows a nearly linear positive dependence on the F10.7 flux (Fejer et al., 1991). For example, a 10 percent change in the solar flux could cause nearly 10 percent change in  $V_z$  (see, Fig. 3 of Fejer et al., 1991). The maximum variation in the F10.7 flux values was around 10 percent with respect to the mean value (182 flux units) during the campaign period (Solar-Geophysical Data Prompt Report, no. 574-Part I, NOAA, US Department of Commerce, June 1992). However, the variability in the  $V_z$  (as judged from the slope of the  $h'F/hpF_2$  curves near 18-19 LT in Fig. 5) is significantly higher than 10 percent which implies that causes other than the variability in F10.7 flux could be responsible for the observed variabilities in  $V_z$ . Another source of disturbance zonal wind arises from changing energy input at high latitudes that disturbs the global thermospheric circulation producing a westward wind in the equatorial latitudes (Blanc and Richmond, 1980). The westward wind interacting with the normal eastward wind would cause a reduced net eastward wind velocity which in turn could decrease the intensity of the evening electric field enhancement, as described in Abdu

et al. (1995a). These considerations suggest (although we have not shown quantitatively) that the day-to-day variability in the evening electric field could have a significant contribution from variability in the disturbance zonal winds besides that from disturbance electric fields. It appears that modest variations in the high latitude energy inputs, as expected for the weak-to-moderate disturbance of the campaign period, could produce variability in the equatorial zonal wind system since magnetospherically disturbed conditions prevailed for several hours prior to the local evenings (Abdu et al., 1995a) on many days of the campaign.

On the other hand, magnetospheric disturbances in the form of substorms or asymmetric ring current developments occurring in the dusk sector could produce penetration eastward electric fields causing enhanced uplift of the layer (Abdu et al., 1995a). In fact the larger evening uplift of the layer observed on 24 and 30 March in Figs. 5 and 8, accompanied by slightly higher slope of the h'F curve (that is, higher vertical drift) could be attributed to a disturbance electric field of this type associated with some degree of magnetic disturbances developing at these times as verified in the local magnetograms (not shown here). The enhanced vertical uplift of the equatorial F layer on these two days seems to have produced EIA enhancements in the postsunset hours. This can be verified from the foF2 plots over Cachoeira Paulista in Fig. 8 (see also, Abdu et al., 1995a).

Therefore, any explanation on the causes of the observed variabilities in the prereversal electric field enhancement should take into consideration if an associated magnetic disturbance developed just before (at closeby local times), and/or if such disturbances prevailed for several hours prior to, the dusk. Because of the weak-to-moderate nature of the disturbance condition, that characterized the SUNDIAL/ATLAS-1 campaign, unambiguous identification of a cause-effect relationship is difficult with respect to the different disturbance sources mentioned above.

#### ***4.2 Role of the Meridional Wind***

The meridional wind contribution to ionospheric heights as a function of latitude is indicated by the F2 peak height variations in Fig. 5. At midlatitudes the hmF2/hpF2 variation is a strong function of the meridional wind. We have calculated the meridional wind for Ushuaia and Buenos Aires following the method of Miller et al. (1986) that utilizes Richards/Torr ionospheric model (Young et al., 1980 a,b; Richards and Torr, 1985; Richards, 1991). These results for all individual days are plotted in Fig. 7. Over Ushuaia the winds are generally poleward (positive values) for most part of the day, and equatorward from near midnight to approximately 08 LT in the morning. From around 20 LT to midnight the meridional winds blow in both the directions in varying degrees on different

days. Day-to-day variabilities are significantly more pronounced in the equatorward wind, that dominates from midnight to morning hours, than in the poleward wind. This might point to the variable intensities of the high latitude energy source that could be driving the equatorward disturbance winds at these hours. This is consistent with what is to be expected from the generally active nature of the ATLAS-1 period represented by the continuous negative Dst values (fluctuating around  $-50$  nT, in Fig. 1), variable Kp values, and the interhemispheric power and activity index from NOAA/TIROS satellite presented in Szuszczewicz et al. (1995, this issue). Over Buenos Aires the durations of the equatorward winds are more restricted in local time than over Ushuaia, with equally significant poleward winds also registered at these times. The amplitude of the day-to-day variability in the disturbance meridional winds, indicated by the difference between the extreme values of the winds during the morning-midnight local times, are however nearly the same at both the locations. In Fig. 7 we have plotted also the meridional winds for Ushuaia and Buenos Aires as specified by the HWM-90 model of Hedin et al. (1991). The wind local time patterns presented are for the magnetically quietest and the most disturbed days of the campaign, i.e., 2 April ( $A_p=4$ ) and 23 March ( $A_p=28$ ). The HWM-90 model winds show, in general, reasonably good agreement with the winds derived from the ionosonde data for both the locations. Main exceptions are the poleward winds around midday over Buenos Aires and the equatorward winds in the evening hours at both locations that the HWM-90 tends to overestimate. Higher magnetic activity produces higher equatorward winds in the HWM-90 mainly for night conditions. Such a dependence is present also in the deduced winds, but with slightly different local time dependence at the two locations. Also, the observed amplitude of the day-to-day variabilities in the meridional winds are significantly higher than predicted by the HWM-90.

Over Cachoeira Paulista which is at a lower latitude than Buenos Aires the determination of the meridional wind from ionosonde data is a complex task (and no model is yet available) due to the increasing role of the electric field at equatorial latitudes. However, a comparison of the  $h_p F_2/h'F$  patterns over Cachoeira Paulista and Fortaleza with those over Buenos Aires and Ushuaia (Fig. 5) vis-a-vis the meridional wind variations over the latter stations (Fig. 7) points to a diminishing trend in the amplitude of the meridional wind from midlatitudes towards the equator in the morning hours. Such a trend becomes clearer if we exclude from Fig. 5 the specially identified curves for reasons to be explained below. Thus the results of Figs. 5 and 7 clearly demonstrate the dominating role of meridional wind in the day-to-day variability of the night-sunrise sector midlatitude ionosphere that progressively diminishes towards the equator. Such variabilities seem to result, as mentioned before, from the fluctuating magnetic activity that characterized the SUNDIAL/ATLAS-1 campaign period. The fluctuating magnetic activity seems to have produced, (in the same morning

local time sector) over equatorial latitudes. as to be explained below, additional F-layer height increases which can be attributed to the action of disturbance dynamo electric field.

#### ***4.3 Disturbance Dynamo Electric Field***

The morning (02-06 LT) height rise over Fortaleza in Fig. 5 is significantly larger on some days represented by specially identified lines than on other days. Such events of height rises seem to be associated with prior increases in magnetic disturbances, of a few hours durations, (seen as Dst values decreasing to less than  $\sim -50$  nT, marked in Fig. 1) that were observed on some days. These days were identified as 22, 24, 25 and 30 March. The  $h_pF_2$ ,  $h'F$ , and  $foF_2$  over Fortaleza and Cachoeira Paulista, for these days are plotted in Fig. 8 together with the mean of the magnetically quietest days (26, 27, 28 March and 01, 02 April) of the campaign (see Fig. 1). It is quite evident from Fig. 8 that a morning height increase is practically absent over Fortaleza in the quietest day mean curve, and significant height increase both in  $h'F$  and  $h_pF_2$  are clearly present on the disturbed days during the post midnight-morning hours with maximum effect centered around 03-04 LT. (The increase centered around 05 LT observed in the quiet day average curve of Cachoeira Paulista could be produced by quiet time neutral wind). In a recent study on time-dependent responses of ionospheric electric fields to magnetospheric disturbances, Fejer and Scherliess (1995) have shown from statistical analysis of long term Jicamarca vertical drift data, that maximum vertical drift disturbances from disturbance dynamo electric field occurred within 5-6 h from the onset of an auroral substorm event represented by AE indices. The corresponding maximum upward drift (eastward electric field) was around 03-04 LT (see Fig. 2 of Fejer and Scherliess). We note that the maximum effect in  $h_pF_2$  and  $h'F$  over Fortaleza also corresponds to disturbances occurring in the same local time range, in Fig. 8. It is further interesting to note that the height disturbances (whose occurrence local times are indicated in the Dst plot of Fig. 1) are preceded by short duration Dst decreases (to  $< \sim -50$  nT). The amplitudes of these morning height increases over Fortaleza are comparable to, if not higher than, those observed during the same LT interval over Cachoeira Paulista. The existence of disturbance meridional (equatorward) winds as the cause of such height increases may be discarded due to the fact that the effect of an equatorward wind in lifting up the F2-layer peak height is a factor of  $\sim 2.5$  less over Fortaleza (with dip angle of  $-8^\circ$ ) than over Cachoeira Paulista (with dip angle of  $-28^\circ$ ). The cause of the observed height increases over Fortaleza may therefore be attributed to the presence of disturbance eastward electric field. The antecedence time of up to a few hours ( $\sim 5-6$  hours) observed with respect to the increases in the Dst values are in general agreement with the Jicamarca results of Fejer and Scherliess (1995). Thus the results of the Fig. 8 offer evidence, for the first time based on ionosonde data, of disturbance



dynamo eastward electric field manifestation in the equatorial ionosphere. The result for Cachoeira Paulista in the lower two panels of Fig. 8 is in general agreement with that of Fortaleza. However, the dissimilar temporal structures at the two locations suggest that height variations over the former location was modulated by disturbance meridional wind. The disturbance dynamo electric field manifestation at other local times are ambiguous in the present data. Partial inhibitions of equatorial electrojet current as seen in reduced amplitudes of diurnal ranges in the geomagnetic field horizontal component, with associated ionospheric and thermospheric signatures, have been attributed to disturbance dynamo westward electric fields by Sastri (1988) and Mazaudier and Venkateswaran (1990), respectively, for the Indian and African-European longitudes. The variabilities in the evening F layer uplift seen in Figs. 5 and 8 are likely to be produced more by the variabilities of the zonal wind and to some extent by magnetospheric disturbance electric field (as explained earlier) than by disturbance dynamo electric field. It is interesting to note that the foF2 values also show generally positive modifications as those of the heights at both the stations, in response to the disturbance dynamo electric field, as the foF2 results for Cachoeira Paulista show in Fig. 8.

## 5. Conclusions

In the present study we considered the climatology of the low latitude ionospheric F region over the American and Indian-Asian longitude sectors. A comparison of the observed averaged behavior with the IRI model representations showed that such climatological picture is indeed describable by the model in general, with some exceptions noted, especially in the case of the equatorial F layer heights at times of the evening electric field prereversal enhancement and the nighttime resurgence of the equatorial ionization anomaly. The main focus of the study, however, has been on the day-to-day variabilities of the ionosphere, with reference to its average behavior, during the 12-day campaign period that marked the recovery phase of a weak to moderate magnetic storm. The recovery phase in itself was marked by fluctuating magnetic indices. The identification, in terms of specific cause-effect relationship, of low latitude ionospheric response to weak-to-moderate intensity storm event, is a rather difficult task. We have, therefore, adopted an approach that focuses on salient features of the day-to-day variabilities observed during the campaign interval on global as well as regional scales. Some specific local-time and latitude-dependent characteristics attributable to disturbance zonal and meridional winds and to disturbance dynamo electric field have been identified. The main findings are the following. Under weak-to-moderately disturbed conditions (with Dst  $\sim$  -50 nT) the day-to-day variabilities of the equatorial- and low-latitude ionosphere are produced mainly in the evening/sunset sector and in the early morning hours. The

former observation is a manifestation of the variability in the electric field prereversal enhancement amplitude (that is, in the F layer uplift) mainly caused by corresponding variability in the equatorial zonal eastward winds and penetrating disturbance magnetospheric electric field. The effects in the early morning hours, manifested as height rises produced from disturbance dynamo electric field, occurs with a delay of a few hours with respect to an increase in magnetic disturbance (seen as Dst decreases). It may be pointed out that this is the first evidence from ionosonde data so far reported on disturbance dynamo electric field effects in the equatorial ionosphere. These effects decrease steadily going away from the equator, becoming indistinguishable at latitudes higher than that of Cachoeira Paulista ( $-28^\circ$  dip), close to the equatorial ionization anomaly (EIA) crest. At midlatitude locations the day-to-day variabilities arise from corresponding variabilities in the meridional neutral wind, the effect being dominant from premidnight to morning hours. We may note that the servo method of height analysis gives an effective meridional wind which under disturbed conditions could mean combined effect of winds and electric fields. However, the indications that the amplitude of the effect decreases towards equator (in a way consistent with the equatorward decreasing values of the geomagnetic dip angle) is a rather strong suggestion that the day-to-day variabilities are caused by disturbance meridional winds. The effect gets also restricted in local time towards the equator such that at the latitude of the EIA crest it is observed during post midnight-sunrise hours only. At equatorial latitudes (such as Fortaleza and Waltair) the effect from meridional wind is imperceptible as such, being significantly smaller than the disturbance dynamo electric field effect that seems to dominate the response features for these locations during presunrise hours. It may be remarked that in the morning hours no identifiable effect was observed from direct penetration magnetospheric electric field whose presence seems to characterize some cases of the response features in the evening hours. It is suggested that further studies should be pursued, involving larger data base, aiming at elucidating further the cause-effect relationships governing the low latitude ionospheric response to magnetic disturbances of weak -to- moderate intensity.

#### **Acknowledgments:**

This work has been supported by Fundo Nacional de Desenvolvimento Científico e Tecnológico under contract FINEP-537/CT. Two of us, M. A. Abdu and J. H. A. Sobral have received support from Conselho Nacional de Desenvolvimento Científico e Tecnológico under the grants CNPq 501956/91-3 and 521980/94.1. Part of the data reduction was carried out by Ms. Cristina S. Yamashita through a junior research fellowship from Fundação de Amparo à Pesquisa do Estado de São Paulo - FAPESP (grant no. 93/1258-6). SUNDIAL/ATLAS-1 workshops were supported by the

U.S National Science Foundation under Grant no. P. Richards acknowledges the support through NSF Grant no. ATM-9415620.

#### **References:**

- Abdu, M.A., J.A. Bittencourt and I.S. Batista. Magnetic declination control of the equatorial F-region dynamo electric field development and spread F. *J. Geophys. Res.*, 86, 11443-11446, 1981.
- Abdu, M.A., J.H.A. Sobral, E.R. de Paula and I.S. Batista, Magnetospheric disturbance effects on the equatorial ionization anomaly(EIA): An overview. *J. Atmos. Terr. Phys.*, 53, 8, 757-771, 1991.
- Abdu, M.A., G.O. Walker, B.M. Reddy, E.R. de Paula, J.H.A. Sobral, B.G. Fejer, and E.P. Szuszczewicz. Global scale equatorial anomaly(EIA) response to magnetospheric disturbances based on the May-June 1987 SUNDIAL- coordinated observations. *Ann. Geophysicae*, 11, 585-594, 1993.
- Abdu, M.A., I.S. Batista, G.O. Walker, J.H.A. Sobral, N.B. Trivedi, and E.R. de Paula. Equatorial ionospheric electric fields during magnetospheric disturbances: Local time/ longitude dependences from recent EITS campaigns. *J. Atmos. Terr. Phys.* in press, 1995a.
- Abdu, M.A., I.S. Batista, and J.R. de Souza. An overview of IRI-Observational data comparison in American (Brazilian) sector low latitude ionosphere. *Adv. Space Res.*, in press, 1995b.
- Balan, N., B. Jayachandran, R. Balachandran Nair, S.P. Namboothiri, G. J. Barley and P.B. Rao, HF Doppler observations of vector plasma drifts in the evening F-region at magnetic equators. *J. Atmos. Terr. Phys.* 54, 1554, 1992.
- Batista, I.S., M.A. Abdu, and J.A. Bittencourt. Equatorial F region vertical plasma drifts: seasonal and longitudinal asymmetries in the American sector. *J. Geophys. Res.*, 91, 12,055- 12,064, 1986.
- Batista, I.S., E.R. de Paula, M.A. Abdu and I.J. Kantor. Comparative study of ionogram F2 peak height from different techniques. *Geofísica Internacional*, 30, 249-252, 1991a.

- Batista, I.S., E.R. de Paula, M.A. Abdu, N.B. Trivedi, and M.E. Greenspan, Ionospheric effects of the March 13, 1989, magnetic storm at low and equatorial latitudes, *J. Geophys. Res.*, 96, 13,943-13,952, 1991b.
- Bilitza, D., K. Rawer, L. Bosny, and T. Gulaeva, International reference ionosphere - past, present, and future: I. Electron density, *Adv. Space Res.*, 13, 3-13, 1992.
- Blanc, M., and A.D. Richmond, The ionospheric disturbance dynamo, *J. Geophys. Res.*, 85, 1669-1686, 1980.
- Crain, D.J., R.A. Heelis, G.J. Bailey and A.D. Richmond, Low-latitude plasma drifts from a simulation of the global atmospheric dynamo, *J. Geophys. Res.*, 98, 6039-6046, 1993.
- Farley, D.T., E. Bonelli, B.G. Fejer, and M.F. Larsen, The pre reversal enhancement of the zonal electric field in the equatorial ionosphere, *J. Geophys. Res.*, 91, 13723- 13728, 1986.
- Fejer, B.G., M.F. Larsen, and D.T. Farley, Equatorial disturbance dynamo electric fields, *Geophys. Res. Lett.*, 10, 537- 540, 1983.
- Fejer, B.G., R.W. Spiro, R.A. Wolf, and J.C. Foster, Latitudinal variation of perturbation electric fields during magnetically disturbed periods: SUNDIAL observation and model results, *Ann. Geophysicae*, 8, 441- 454, 1990.
- Fejer, B.G., E.R. de Paula, S.A. Gonzalez, and R.F. Woodman, Average vertical and zonal F region plasma drifts over Jicamarca, *J. Geophys. Res.*, 96, 13,901-13,906, 1991.
- Fejer, B.G., and Ludger Scherliess, Time dependent response of equatorial ionospheric electric fields to magnetospheric disturbances, *J. Geophys. Res.*, in press, 1995.
- Fesen, C. G., G. Crowley, and R. G. Roble, Ionospheric effects at low latitudes during the March 22, 1979, geomagnetic storm, *J. Geophys. Res.*, 94, 5405- 5417, 1989.
- Forbes, J.M., Evidence for the equatorward penetration of electric fields, winds and composition effects in the Asian/ Pacific sector during the September 17-24, 1984 EITS interval, *J. Geophys. Res.*, 94, 16,999- 17,007, 1989.

- Foster, J.C., J.M. Holt, R.G. Musgrove, and D.S. Evans, Ionospheric convection associated with discrete levels of particle precipitation, *Geophys. Res., Lett.*, 13, 656-659, 1986.
- Fuller-Rowell, T.J., M. V. Codrescu, R.J. Moffet, and S. Quegan, Response of the thermosphere and ionosphere to geomagnetic storms, *J. Geophys. Res.* 99, 3893-3914, 1994.
- Greenspan, M.E., C. E. Rasmussen, W. J. Burke, and M.A. Abdu, Equatorial density depletions observed at 840 km during the great magnetic storm of March 1989, *J. Geophys. Res.*, 96, 13,931-13,942, 1991.
- Hedin, A.E., M.A. Biondi, R.G. Burnside, G. Hernandez, R.M. Johnson, T.L. Killeen, C. Mazaudier, J.W. Meriwether, J.E. Salah, R.J. Sica, R.W. Smith, N.W. Spencer, V.B. Wickwar, T.S. Verdi, Revised global model of thermospheric winds using satellite and ground based observations, *J. Geophys. Res.*, 96, 7657-7688, 1991.
- Heelis, R.A., P.C. Kendall, R.J. Moffet, D.W. Windle, and H. Rishbeth, Electrical coupling of the E- and F- regions and its effect on the F- region drifts and winds, *Planet. Space Sci.*, 22, 743-756, 1974.
- Huang Yinn-Nien, and K. Cheng, Ionospheric disturbances around East Asian region during the 20 October 1989 magnetic storm, *J. Atmos. Terr. Phys.*, 55, 1009- 1020, 1993.
- Mazaudier, C. and S.V. Venkateswaran, Delayed ionospheric effects of the geomagnetic storm of March 22, 1979 studied by the sixth coordinated data analysis workshop (CDAW- 6), *Ann. Geophys.* 8, 511-518, 1990.
- Miller, K.L., D.G. Torr, and P.G. Richards, Meridional winds in the thermosphere derived from measurement of F2 layer height, *J. Geophys. Res.*, 91, 4531-4535, 1986.
- Piggot, W.R., and K. Rawer, *URSI Handbook of ionogram interpretation and reduction*, US Department of Commerce, Report UAG-23A, WDCA, 1978.
- Richards, P.G., An improved algorithm for determining neutral winds from the height of the F2 peak electron density, *J. Geophys. Res.*, 96, 17839-17846, 1991.

Richards, P.G., and D.G. Torr. Seasonal, diurnal, and solar cyclical variation of the limiting H<sup>+</sup> flux in the earth's topside ionosphere. *J. Geophys. Res.* 90, 5261-5268, 1985.

Rishbeth, H., The F- region dynamo. *J. Atmos. Terr. Phys.*, 43, 387-392, 1981.

Sastri, J.H., Equatorial electric fields of ionospheric disturbance dynamo origin, *Ann. Geophys.* 6, 635-642, 1988.

Sastri, J.H., H.N.R. Rao, and K.B. Ramesh, Response of equatorial ionosphere to the transient of interplanetary magnetic cloud of January 13-15, 1967: Transient disturbances in the F Region. *Planet. Space Sci.*, 40, 519- 534, 1992.

Somayajulu, V.V., B.V. Krishna Murthy, and K.S.V. Subbarao. Response of night-time equatorial F region to magnetic disturbances, *J. Atmos. Terr. Phys.*, 10, 965- 976, 1991.

Szuszczewicz, F.P., D.Torr, P. Wilkinson, P. Richards, R. Roble, C. Lu, D. Evans, S. Pulinets, B.M. Reddy, M. A. Abdu, M. Lester, K. Igarashi, P. Jiao, P. Blanchard, and J. Joselin, F- Region climatology during the SUNDIAL/ATLAS-1 campaign of March 1992: Prevailing conditions and model-measurement comparisons, this issue, 1995.

Tanaka, T., Low-latitude ionospheric disturbances: Results for March 1979 and their global characteristics. *Geophys. Res.Lett.*, 13, 1399-1402, 1986.

Titheridge, J.E. Ionogram analysis with the generalised program POLAN, US Department of Commerce. Report UAG-93, WDCA, 1985.

Torr, M.R., D.G. Torr, P. G. Richards, and S.P. Yung, Mid- and low-latitude model of thermospheric emission 1.O+(2P) 7320 Å and N<sub>2</sub> (2P) 3371 Å, *J. Geophys. Res.*, 95, 21147-21168, 1990.

Woodman, R.F., Vertical velocities and east-west electric fields at the magnetic equator, *J. Geophys. Res.*, 75, 6249-6259, 1970.

Young, E.R., P.G. Richards, and D.G. Torr, A flux preserving method of coupling first and second order equations to simulate the flow of plasma between the protonosphere and the ionosphere. *J. Comput. Phys.*, 38, 141, 1980a.

Young, E.R., D.G. Torr, P.G. Richards, and A.F. Nagy, A computer simulation of the midlatitude plasmasphere and ionosphere. *Planet. Space Sci.*, 28, 881, 1980b.

### **Figure Captions:**

**Fig. 1 -** The Dst values from 22 March to 02 April 1992. The local time intervals indicated by filled rectangles represent those of F layer height increases over Fortaleza due to disturbance dynamo electric field on 22, 24, 25 and 30 March.

**Fig. 2 -** The average diurnal pattern of foF2 and hpF2 for Fortaleza, Cachoeira Paulista, Buenos Aires and Ushuaia (continuous lines) compared with their IRI specifications (circles). foF2 and hmF2 from the FLIP runs (stars) are included for Buenos Aires and Ushuaia.

**3 -** Average foF2 values for Waltair, and foF2 and hpF2 values for Chung Li compared to their IRI specifications.

**Fig. 4 -** hpF2 diurnal pattern on 30 March 1992 for Fortaleza, Cachoeira Paulista, Buenos Aires and Ushuaia. Solar terminator positions as a function of height are indicated by slant lines.

**Fig. 5 -** Superimposed plots of hpF2/h'F for the SUNDIAL-ATLAS-1 campaign interval for Fortaleza, Cachoeira Paulista, Buenos Aires and Ushuaia. The curves specially identified with circles, stars, triangles, etc., represent data on more disturbed 4 days of the campaign (22, 24, 25 and 30 March) when anomalous height increases were observed during the presunrise hours. The data for the remaining days are plotted in continuous lines.

**Fig. 6 -** Plots of hpF2/h'F as in Fig. 5 but for Waltair and Chung-Li.

**Fig. 7 -** Meridional winds (positive poleward) obtained using the servo method by Miller et al. (1986) based on the FLIP model that used the hpF2 values for Buenos Aires and Ushuaia, plotted for all days of the SUNDIAL-ATLAS 1 campaign. The Hedin HMW-90 model meridional winds

are shown for the two days of the lowest and highest  $A_p$  values, 2 April (stars) and 23 March (circles), respectively.

Fig. 8 -  $h'F$ ,  $h_pF_2$  and  $f_oF_2$  values for the relatively more disturbed days of the campaign (22, 24, 25, and 30 March), that is, the days for which the morning hours were preceded by Dst decreases (to  $<50\text{nT}$ ) of a few hour duration plotted together with the mean curves for magnetically quietest days of the campaign.

Table - 1

Station	Coordinates		
	Lat.( N)	Long.( E)	Dip angle
Fortaleza	- 4	322	-9
Cachoeira Paulista	- 22.6	315	-28
Buenos Aires	- 34.6	301.7	-36
Ushuaia	- 54.8	281.7	-50.2
Waltair	15.0	80.0	14.0
Chung Li	- 24.9	121.5	35.2



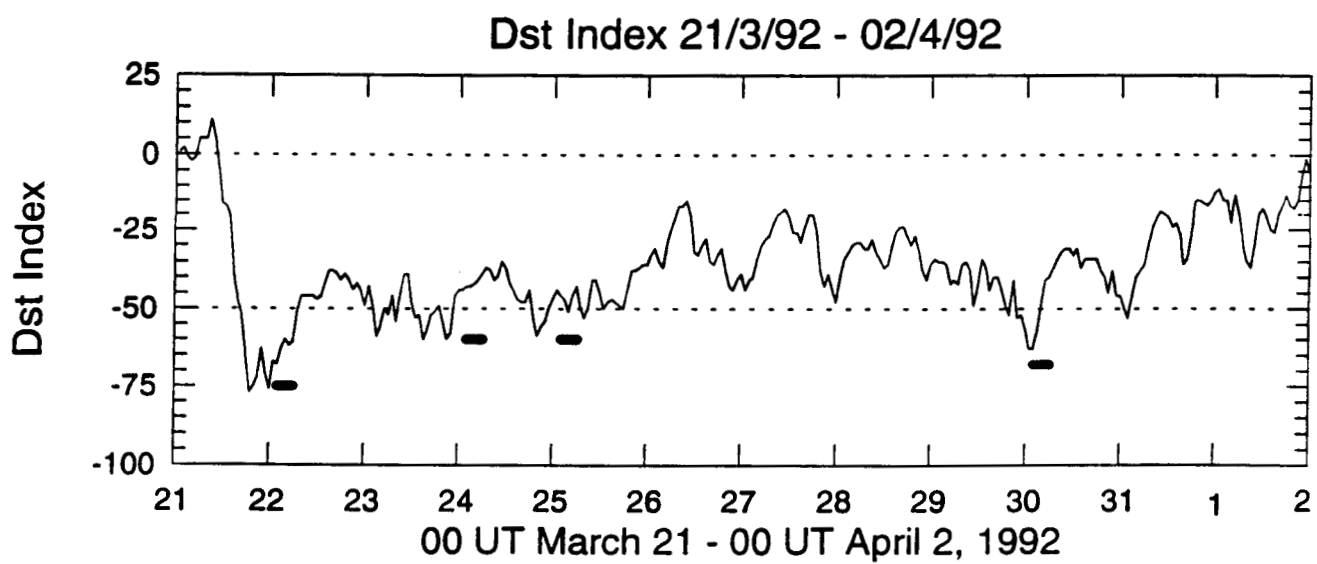
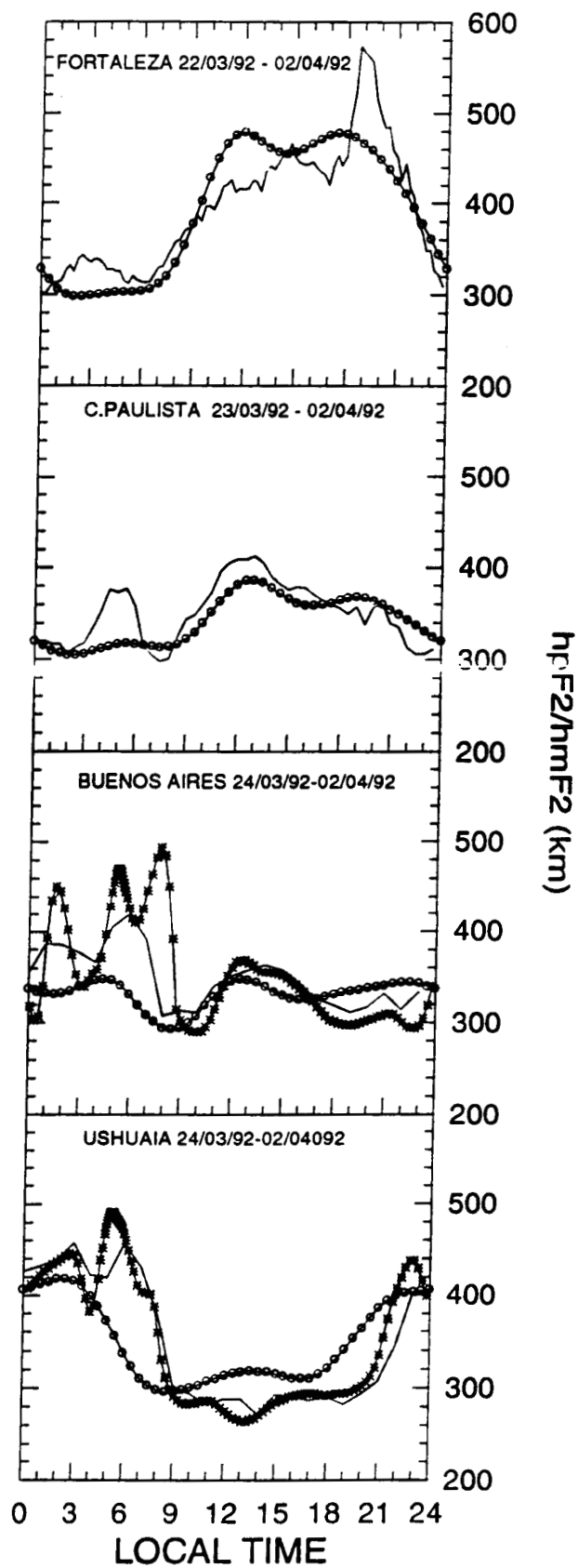
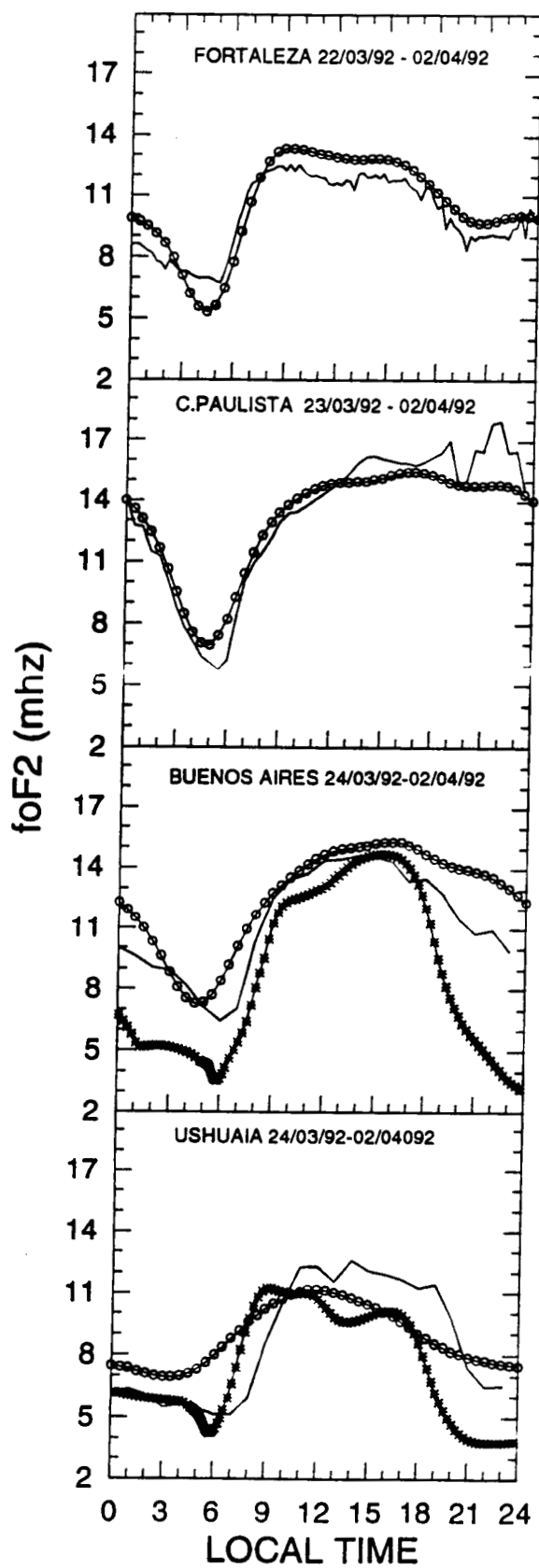


FIG. 01



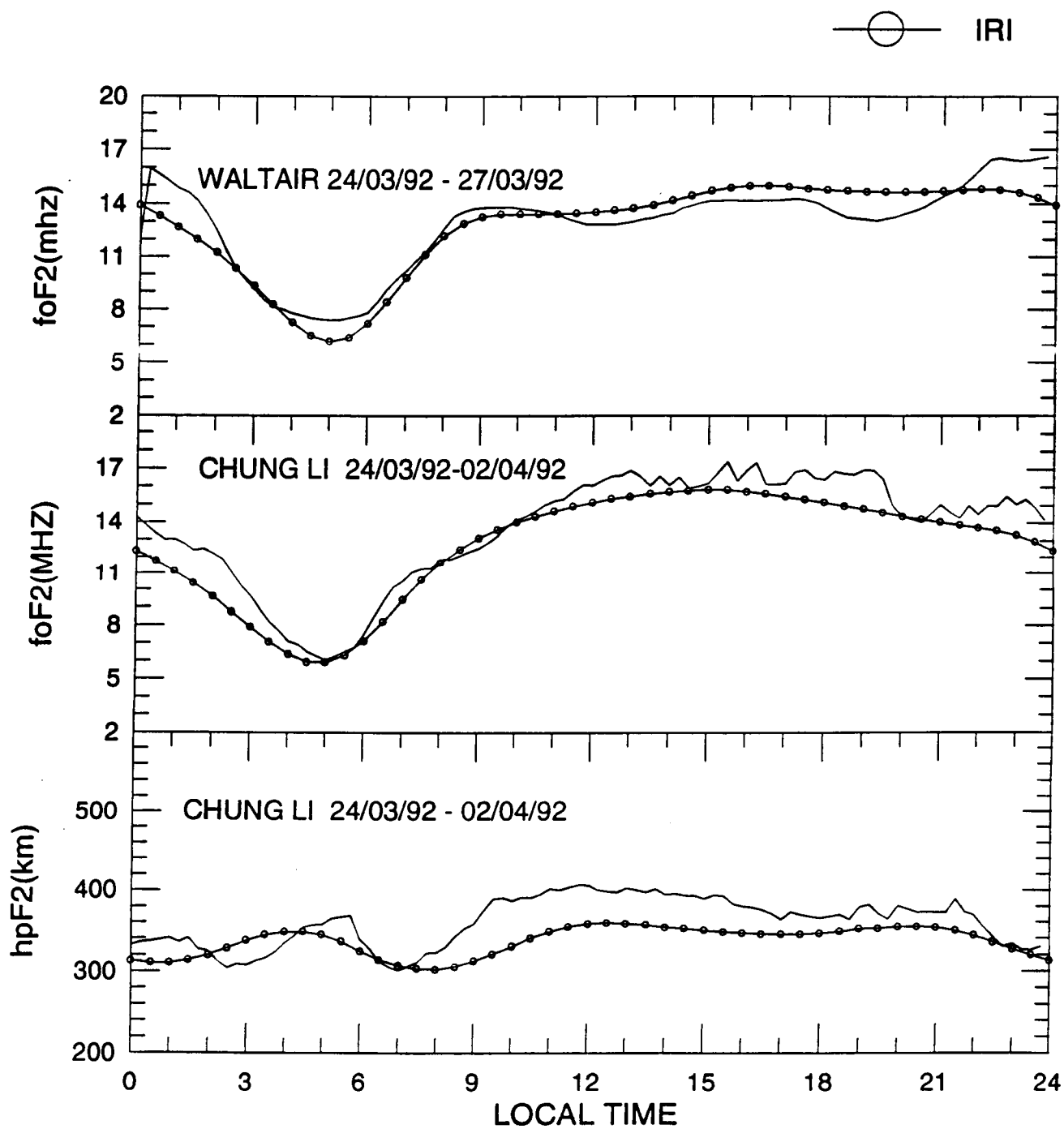
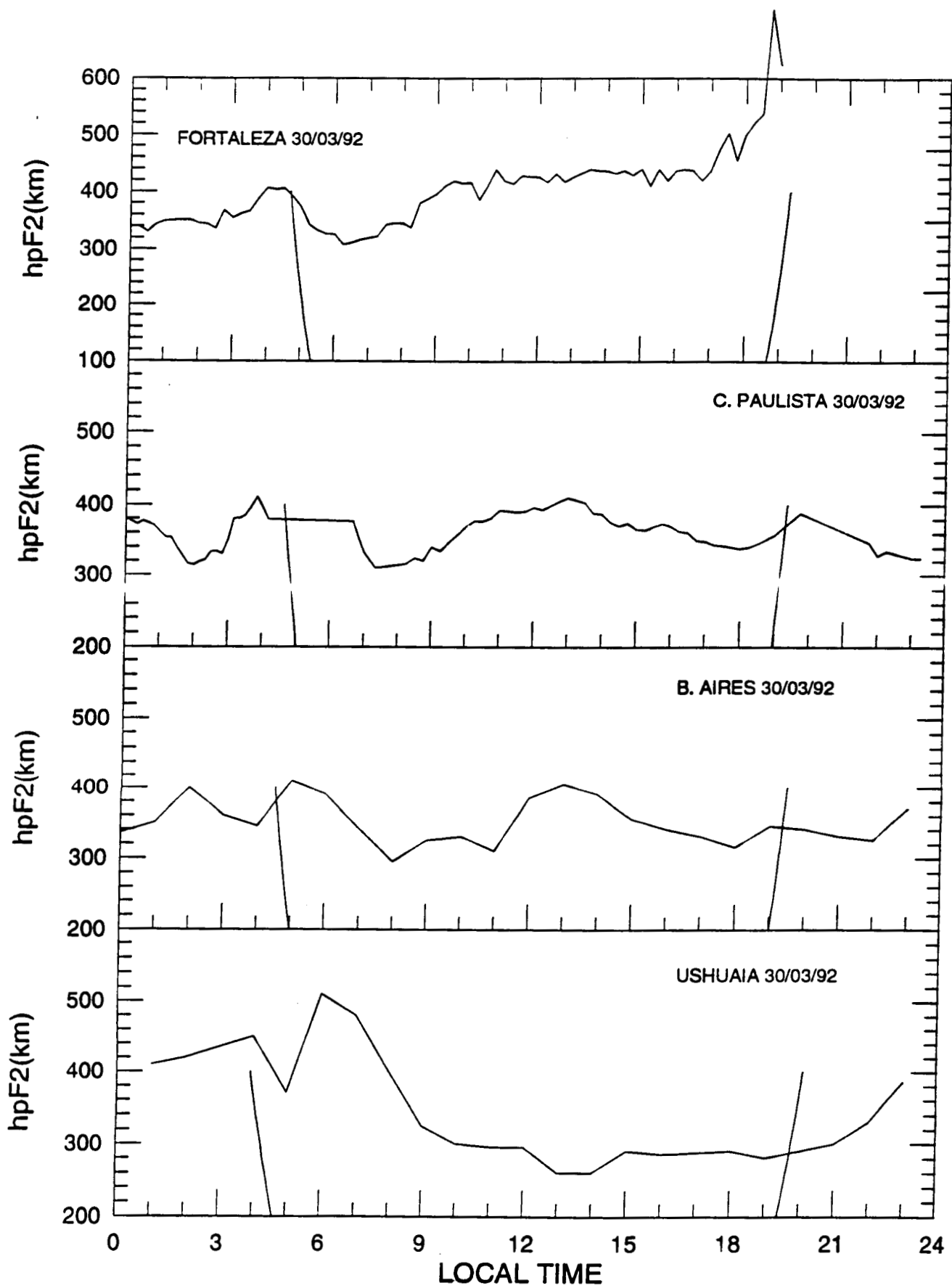


FIG. 03



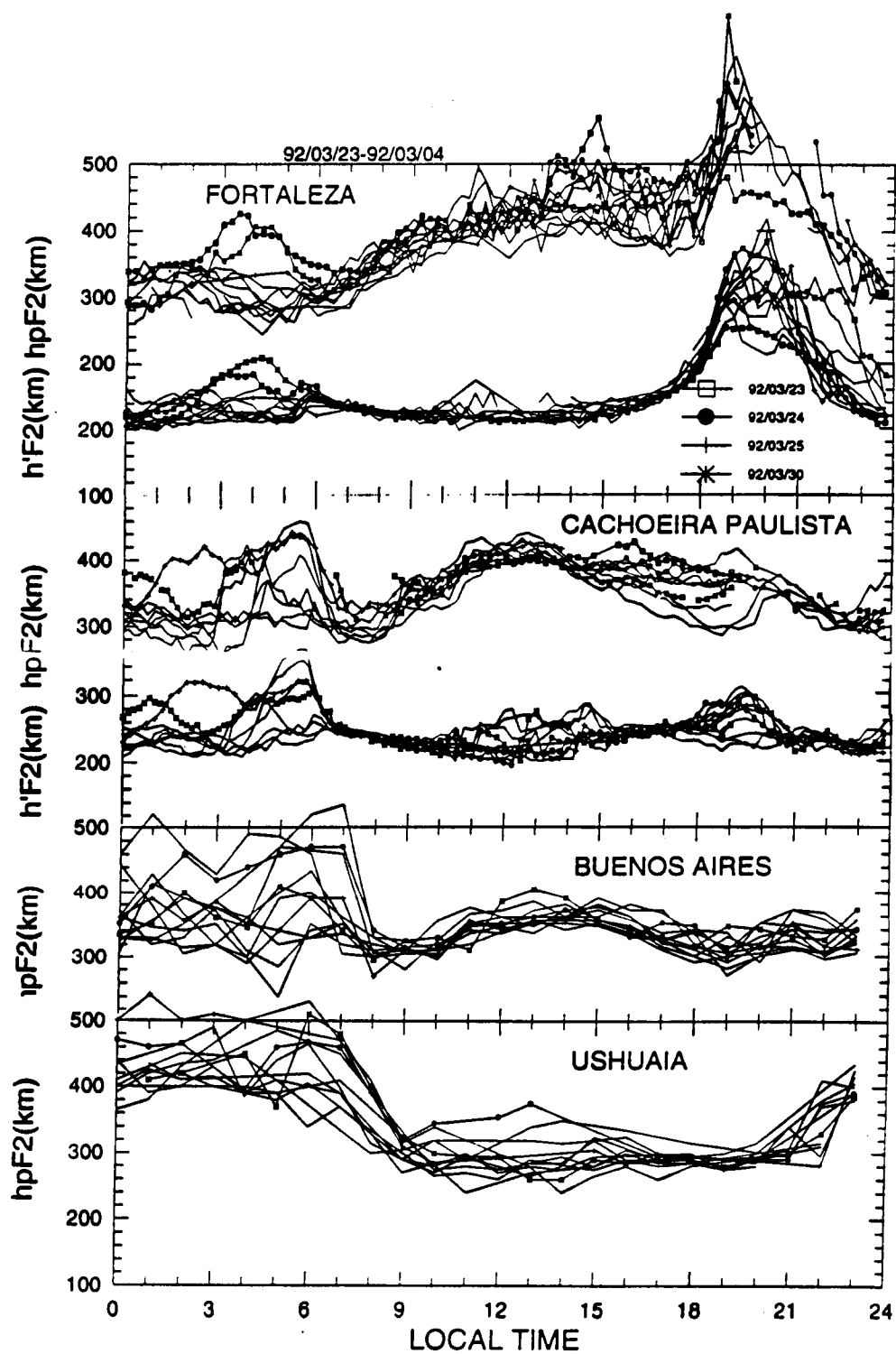
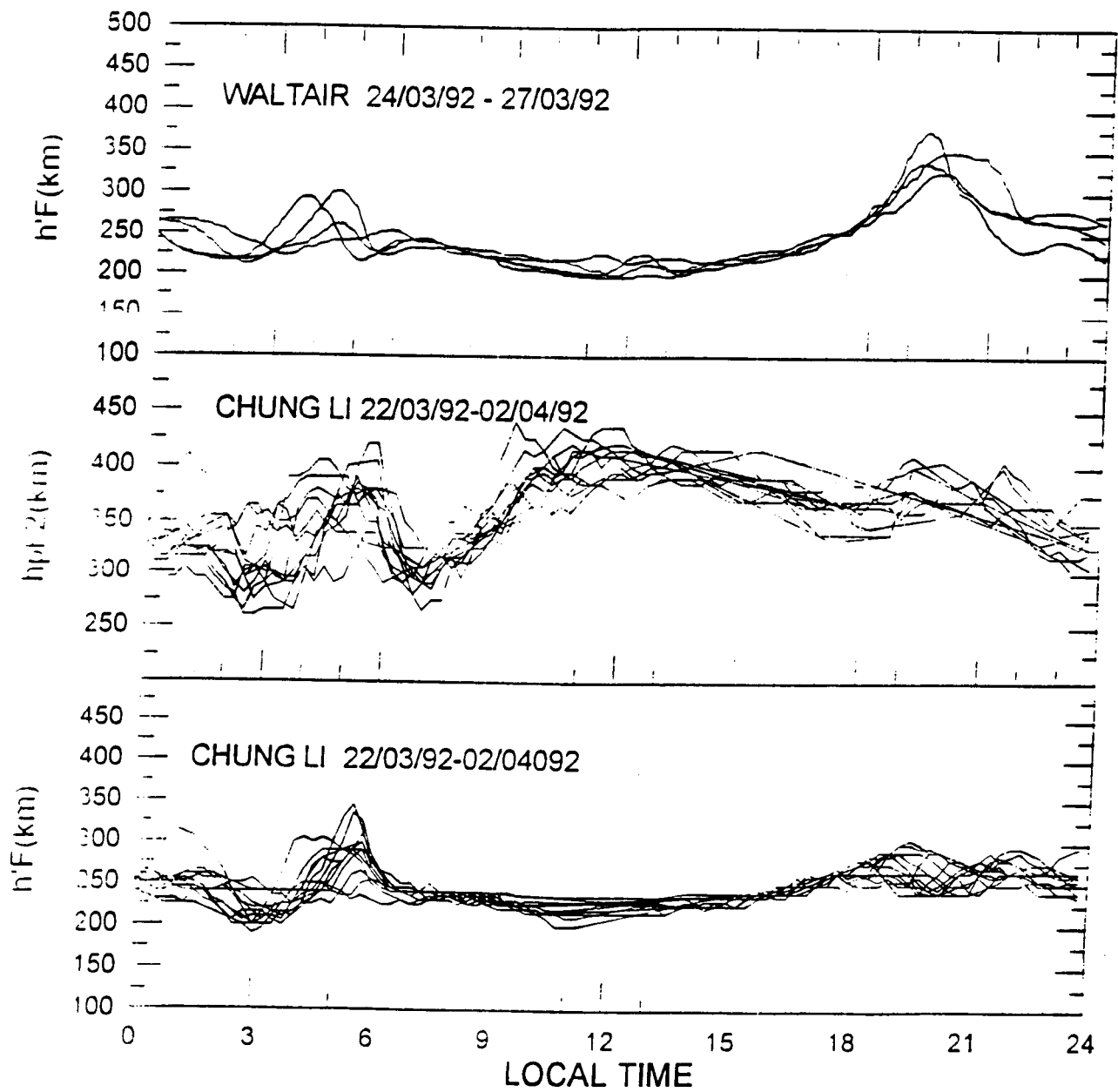


FIG. 05

Figura 6



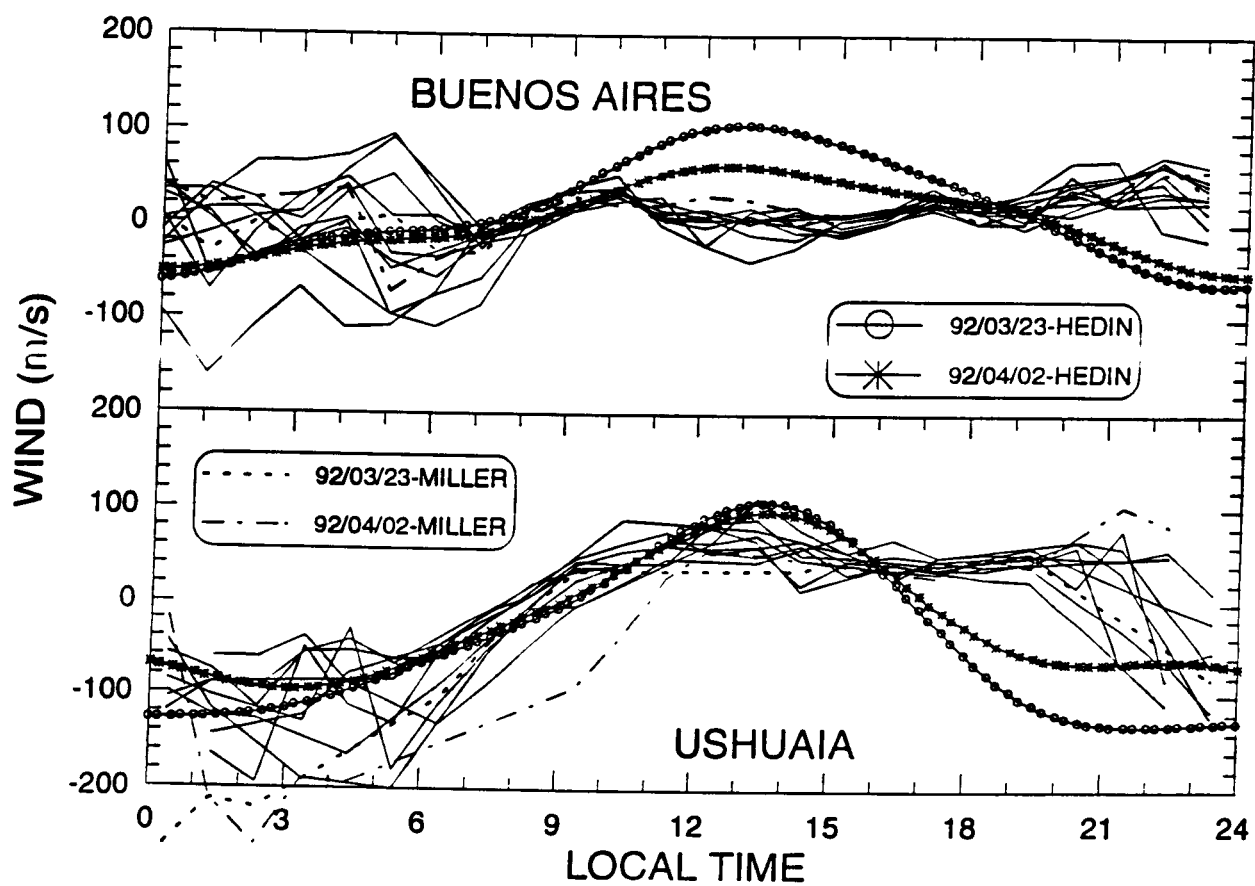


FIG. 07

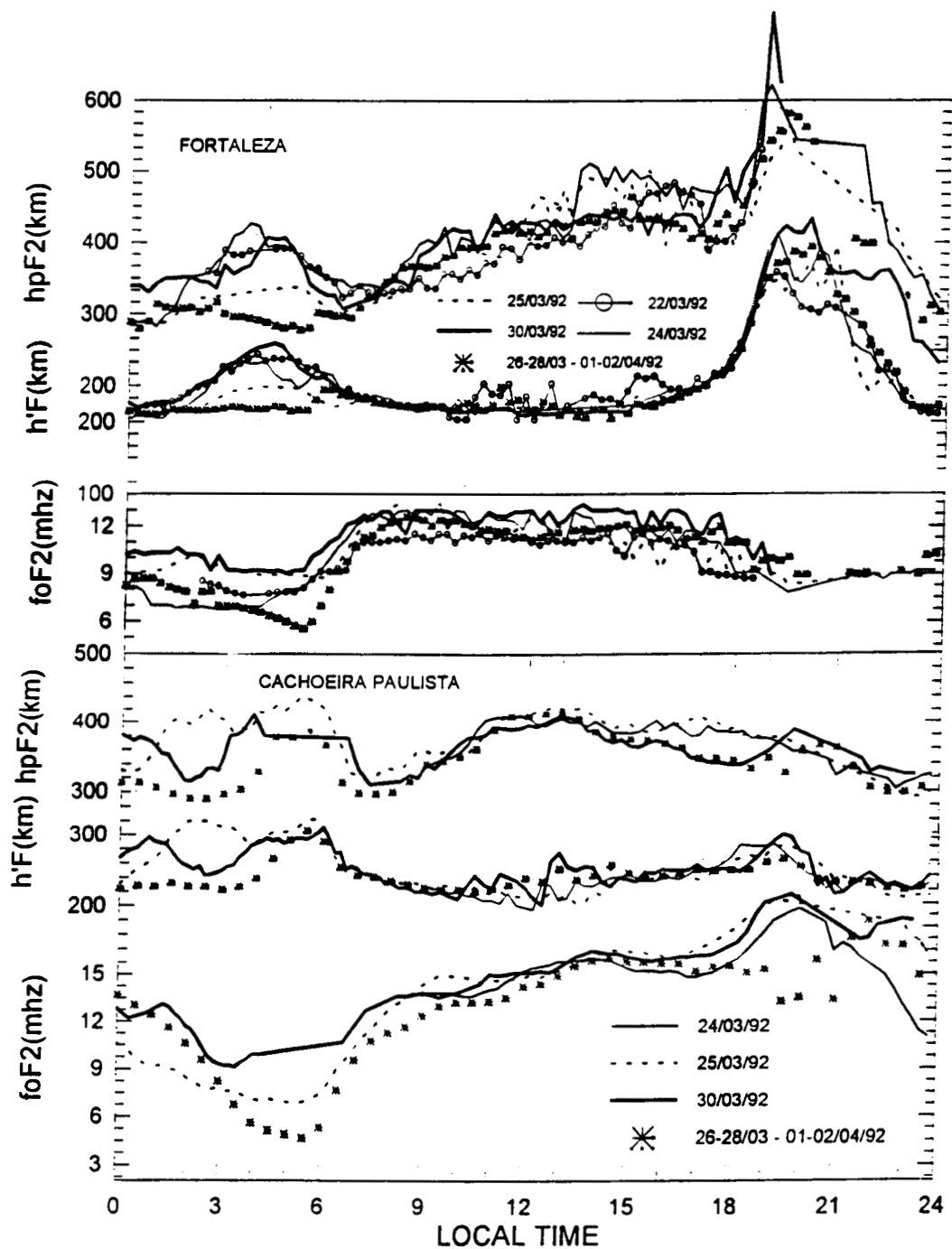


FIG. 08



**Ionospheric Climatology and Weather in the  
Australian - Japanese Sector during the  
SUNDIAL/ATLAS-1 Campaign**

**P.J. Wilkinson, P. Richards, K. Igarashi, and E.P. Szuszcwicz**

## **Ionospheric Climatology and Weather in the Australian - Japanese Sector during the SUNDIAL/ATLAS-1 Campaign.**

**P J Wilkinson**

IPS Radio and Space Services, P O Box 5606, West Chatswood, NSW 2057, AUSTRALIA

**P Richards**

University of Alabama, Huntsville, Alabama, USA

**K Igarashi**

Communications Research Laboratory, Tokyo, JAPAN

**E P Szuszczewicz**

Science Applications International Corporation, McLean, Virginia, USA

**Abstract.** The SUNDIAL/ATLAS-1 campaign took place during a period of high solar flux and moderate magnetic activity. For most days during the campaign the ionosphere over Australia and Japan was undisturbed. The International Reference Ionosphere (IRI), used with a suitable equivalent sunspot number, provided a good climatological description of the Australian and Japanese observations. The measured hmF2 was employed in the field line interhemispheric (FLIP) model to determine equivalent neutral winds and accurately reproduced the measured hmF2. With these winds, the daytime nmF2 was well reproduced in most cases although the measured nmF2 tended to peak before noon while the model nmF2 peaked 2-3 hours later at some locations. At night, the model nmF2 was typically lower than the measurements. The difference between the modelled and measured nighttime nmF2 worsened as the latitude decreased suggesting that the problem is not principally due to inadequate plasmaspheric fluxes. The equivalent winds from hmF2 were similar in amplitude to the winds from the HWM90 model but there were large differences in the phases. The two sets of winds show a similar decrease in amplitude with decreasing latitude. There appears to be a large longitudinal variation in the wind behaviour in the Australian sector. While the winds in eastern Australia show similar diurnal variations with daytime poleward winds and nighttime equatorward winds, the west coast winds were poleward most of the time. The differences in poleward winds are reflected in the much smaller changes in hmF2 in the west. The O<sup>+</sup> fluxes to and from the plasmasphere are generally larger than the H<sup>+</sup> fluxes for these solar maximum conditions. They show structure related to the neutral winds and hmF2. The O<sup>+</sup> flux variations are similar at most stations with upward fluxes during the day and very large downward O<sup>+</sup> fluxes at sunset followed by a rapid decay to small fluxes for most of the night. The H<sup>+</sup> flux behaviour is more complex with the west coast station (Mundaring) showing a classical, strong diurnal variation, upward during the day and downward at night. On the other hand, the H<sup>+</sup> fluxes are upward most of the time at Hobart on the east coast.

## **1. INTRODUCTION**

The ionosphere is constantly changing. Strong day-to-day and hour-to-hour variations can be superposed on the average diurnal, seasonal and solar cycle trends. While the latter are usually thought of as the ionospheric climatology, the day-to-day changes are the weather of the ionosphere.

These features are placed in context by figures 1A and 1B, showing the noon and midnight nmF2 values at the Tokyo (35.7°N 139.5°E) and Canberra (35.3°S 149.0°E) ionospheric observatories for four successive high solar activity years. Superposed over the data is a 30 day running mean. On average, the lowest noon electron densities (roughly  $3 \cdot 10^5$  to  $10^6$  cm<sup>-3</sup>) are seen in summer (June and July for Tokyo and December and January for Canberra) while the maximum noon electron densities ( $< 3 \cdot 10^6$  cm<sup>-3</sup>) are seen during the equinox, the March equinox being the highest of the two equinoxes for all four years of data for both locations. By contrast, there is no obvious equinoctial predominance in the midnight values. By 1993, the declining solar flux level effect is apparent. The ionosphere during high solar activity can vary over a much wider range of electron densities than during solar minimum, as is apparent in the figures. The 30 day running mean is different from one year to the next and there are obvious differences between both locations for both noon and midnight electron densities; only the trend in changing solar activity is similar. These trends are the ionospheric climatology and are the basis for empirical models. Large day-to-day variations, possibly associated with minor ionospheric storms, are present at all locations. Superposed on these are occasional large depressions in the noon nmF2, caused by ionospheric storms. These large, infrequent depressions usually exceed storm enhancements in electron density and also exceed in amplitude the day-to-day variations. The IRI won't match these at all. These changes are the severe weather systems of the ionospheric F region.

The simplest models for dealing with the ionosphere are empirical models. Considerable effort has been spent preparing statistical models [Schunk and Szuszczewicz, 1988] of the relevant ionospheric regions to make ionospheric climatological models. The International Reference Ionosphere (IRI), is such a model and it uses R12 (the twelve month smoothed sunspot number) to parameterise changes in solar activity.

The IRI does not take account of day-to-day variability in the ionosphere. Possibly an empirical model could allow for changes in magnetic activity by preparing stratified, climatological models indexed by the magnetic Ap index. This would allow categories of "weather" to be empirically modelled. An alternative approach, implemented for ionospheric applications such as radio propagation, supplements the climatological picture of the ionosphere with statistical bounds for the expected day-to-day variability. Bounds were developed by Davis and Groome, [1964] and are used in the ITU (International Telecommunication Union) HF prediction programs [CCIR, 1982] and Wilkinson [1995] has pointed out these are useful when modelling the ionosphere. However, to understand day-to-day variability a more complete picture must be developed using physical models.

Physical models that solve the continuity and momentum equations have advanced to the point where there is reasonable qualitative agreement between the calculated and observed F region behaviour. There are now several physical models of the ionosphere available [eg., Sojka and Schunk, 1985, Fuller-Rowell et. al., 1987, Roble et. al., 1988, Schunk and Szuszczewicz, 1988] which show varying levels of agreement between the observed and calculated F region behaviour. One of these models, the Field Line Interhemispheric Plasma (FLIP) model, was recently used to test current understanding of ionospheric behaviour at solar maximum, solstice conditions [Richards et. al. 1994]. Overall, the agreement between the measured and modelled nmF2 (the peak electron density of the F2 region) was found to be very good in the daytime, and less successful at night.

The SUNDIAL/ATLAS campaign [Torr and Sullivan, 1992; Torr 1993] took place during the March equinox (24 March to 4 April, 1992), after the peak of solar cycle 22 and just prior to a sharp drop in solar flux. Solar activity, measured by several indices was high (R12 was 108

and the Ottawa 10.7cm flux varied between 180 and 190 flux units during much of the campaign), and magnetic activity was unsettled-to-disturbed (magnetic activity measured by Ap lay between 12 and 18). These characteristics make the period suitable for exploring the application of ionospheric models to the equinox during periods of high solar activity.

The 10 day campaign took place close to a maximum in peak electron densities observed during solar cycle 22. While the twelve month, smoothed sunspot number for this period is 108, the F region electron densities are more typical of the high activity periods in 1990 and 1991, when a smoothed sunspot number of 145 was appropriate. This is apparent for both Canberra and Tokyo and complicates the problem of choosing a solar index to characterise the period for an empirical model such as the IRI.

In this paper, comparisons between FLIP and observations during high solar activity, using the IRI as a baseline prediction, are extended to equinoctial conditions for a chain of mid-latitude locations spanning  $\pm 45^\circ$  of latitude. Success and failure in modelling both the climatology and weather of the ionosphere are commented on.

## 2. THE DATA

The Japanese and Australian ionosonde networks form a latitudinal chain running from  $45^\circ\text{N}$  to the southern pole. A subset of these stations (Table 1) were used in this paper. At many sites observations were made every five minutes and the ionograms were manually scaled. In this paper, only nmF2 (the peak electron density of the F2 region) and hmF2 (the peak height of the F2 region) are used. The main advantage gained from more frequently sampled data is that it prevents major distortions in modelling occurring when data points are missing.

The nmF2 used here are recorded with ionosondes and calculated from the critical frequency, foF2, with good precision. For Canberra, the manual scaling error for foF2 is typically less than 0.1MHz, or 124 e/cc, 80% of the time [eg. *Wilkinson*, 1978].

The hmF2 is deduced from M(3000)F2 (the standard 3000km maximum useable frequency factor) using Dudeney's relationship [*Dudeney*, 1983]. While it is not easy to scale M(3000)F2 manually, 80% of the time this introduced an error of  $\pm 10\text{km}$  or less (equivalent to 0.06 units of M(3000)F2).

## 3. THE MODELS (IRI AND FLIP)

Two types of models are used in this paper: empirical ionospheric models represented by the IRI (International Reference Ionosphere), and physical ionospheric models represented by FLIP (Field Line Interhemispheric Plasma model).

The IRI calculates nmF2 using one of two sets of empirical coefficients. The older coefficients are the CCIR coefficients used in many HF prediction programs. The newer URSI coefficients appear marginally more accurate than the CCIR coefficients at well established data sites and are included with the IRI as a potentially useful improvement for the model.

The CCIR and URSI coefficients are used with the twelve month smoothed sunspot number, R12. An equivalent sunspot number, based on a data sample from the period of interest (eg. T index [*Caruana*, 1990], IF2 [*Minnis*, 1955]), could be used although this is not often done. This type of index is calculated using a set of calibration curves for nmF2 and R12 for a selected group of ionospheric stations. These calibration curves are used to calculate the value of R12 required to replicate a particular nmF2 observation. All the calculated R12 values can be pooled for a particular time period. The resulting index, an equivalent sunspot number, is

also called an ionospheric index. For the period of interest, the monthly T index of 156 is very similar to the level of R12 (145) that would be anticipated from inspection of figure 1, so an R12 of 150 was used with the IRI.

The FLIP model, developed over several years, is described in detail elsewhere [Richards and Torr, 1988, Torr *et al.* 1990, Szuszczewicz *et al.* this issue]. The main component of this one dimensional model calculates the plasma densities and temperatures along entire magnetic flux tubes from 80km in the northern hemisphere to 80km in the southern hemisphere. The continuity and momentum equations are solved for  $O^+$ ,  $H^+$  and  $He^+$  using the *St.-Maurice and Schunk* [1976] formulation for the topside ionosphere. Collisions between the neutrals and ions have been included in order to extend the equations into the E and F regions. The electron and ion temperatures are obtained by solving the energy equations [Schunk and Nagy 1978].

In order to simulate the ionosphere, FLIP requires three key inputs; the neutral atmospheric composition, the meridional component of the neutral wind, and the solar EUV flux. The neutral densities and temperatures are provided by the Mass Spectrometer and Incoherent Scatter (MSIS) model [Hedin, 1987] while the EUV flux is derived using the EUV flux model for aeronomic calculations (EUVAC) [Richards *et al.*, 1994]. The meridional winds are derived using the measured hmF2 following the methods of Miller *et al* [1986] and Richards [1991]. The aim is to use FLIP to model the day-to-day variability in the ionosphere.

#### 4. EFFECTS OF ERRORS IN M(3000)F2

Neutral winds have a profound influence on the structure of the ionosphere; causing large changes in the observed hmF2 and nmF2. These neutral winds are usually not observed directly and are difficult to model, but can be inferred from the observed hmF2 [Miller *et al.* 1986]. The Miller *et al.* [1986] method was modified by Richards [1991] to allow an ionospheric model to accept hmF2 as an input and convert it to a neutral wind so as to allow the model to faithfully reproduce variations in the observed hmF2. Even so, because of the sluggishness of the ionospheric response, the FLIP model will not follow unrealistically large excursions in hmF2, but rather will smooth out the variations.

All of the data used in this paper, and in most past papers by other workers, have been based on deriving hmF2 using manually scaled values of M(3000)F2. As pointed out earlier, scaling errors roughly correspond to a height error of  $\pm 10$ km. In addition, an extreme error of  $\pm 30$ km was introduced.

The hmF2 observations were presented to FLIP and the resulting modelled nmF2 (a heavy solid line) shown in figure 2, passes close to, and through, most of the observed nmF2 (open circles). Next, the hmF2 were presented to FLIP incremented and decremented by  $\pm 30$  km (the maximum error expected). These results are shown as short dashed lines bounding the nmF2 observations. In some cases, for instance between 36 and 48 hours, the range of the modelled nmF2 is large suggesting any bias in hmF2 resulting from the transformation from M(3000)F2 is smaller, and possibly a good bit smaller, than 30km.

Manual scaling errors in M(3000)F2 are random. However, to gain some impression about their effects, FLIP was again run with hmF2 incremented and decremented by 10km; an upper bound for 80% of scaling errors. The resulting nmF2 outputs are shown as thin lines which appear more or less symmetric about the normal FLIP output. For much of the period displayed, the FLIP output agrees with the observations within the 10km systematic error limits suggesting any offset in hmF2 may be smaller than 10km.

The large fluctuations in hmF2 (eg nighttime near 84 hours and 108 hours) do not produce similar large fluctuations in the FLIP nmF2. A check of the observations showed that these are periods when spread F was present and the scaled M(3000)F2 have rather larger errors than the 10km error just discussed. Thus FLIP responds to systematic changes in the input hmF2, as small as 10km, but larger, more rapidly varying input errors have no obvious effect.

It appears likely, from the comparisons in this section, that any persistent, systematic bias in the transformation used to calculate hmF2 is of the order of 10km or less. We have found that for time sampling less than or equal to 15 minutes, random noise on hmF2 has little effect on the calculated hmF2 or nmF2. Errors in M(3000)F2 should not impose a major limitation on modelling.

## 5. COMPARISON FOR THE AUSTRALIAN AND JAPANESE STATIONS

In figure 3, observations of nmF2 for a latitudinal chain of stations in the Australian (3A) and Japanese (3B) region are displayed as open circles together with nmF2 predictions from the IRI (a thin, solid line for the CCIR predictions and a thin broken line for the URSI predictions) and FLIP, a thick solid line. The figures show the observed nmF2 for several stations with latitude decreasing from the bottom of the figure, Hobart / Wakkanai, up to Vanimo / Okinawa, at the top of the figure. At the head of the figure is a needle chart of Kp showing that the entire SUNDIAL/ATLAS-1 campaign period was only moderately disturbed.

In the Australian region there is good consistency between data for successive days at each site. Of all the locations, Vanimo was the most variable. There are minor day-to-day changes in nmF2 at each station: at Hobart this is most evident during daylight hours, while for stations such as Vanimo, the pre-dawn minimum varies in depth.

The IRI is the baseline climatology prediction we seek to match. As figures 3A&B show, there is almost no difference between the two sets of coefficients. However, the CCIR F2 coefficients are widely available so it is relevant to comment on them. Any discrepancies between the predicted IRI nmF2 and observations are limitations of the CCIR coefficients and not a major deficiency of the IRI but for convenience the IRI is often referred to.

Even though R12=150 was used, during daytime the IRI nmF2 are too low at Hobart, Canberra and Mundaring (figure 3A), consistent with results in *Szuszcwicz et. al.* [this issue]. During nighttime, the IRI performed better, the predawn minimum being matched at all locations most nights. Although the data at Vanimo is patchy, it is evident agreement is good. The agreement between the post sunset IRI output and observed nmF2 for Darwin is more impressive because Darwin data were not available when the CCIR coefficients were constructed. Such agreement helps build confidence in the IRI. For the Australian region, the IRI, with adjusted R12, performed well during a period of high solar activity.

There is even better agreement between the IRI and the observations for the four Japanese stations (Figure 3B) than for the Australian region and there is almost no difference between the CCIR and URSI sets of coefficients supplied with the IRI.

The FLIP model performed well during the daytime [*Szuszcwicz et. al., this issue*] at most locations. As with the IRI, there are larger departures on some days at Hobart, but FLIP has outperformed the IRI here on most days, as well as at Canberra and Mundaring. Daytime agreement between FLIP and the observed nmF2 is best for Canberra, Mundaring, Norfolk and Yamagawa later in the campaign, although there is a tendency for the FLIP daytime maximum nmF2 to lag the observations by an hour or two at these and at the Japanese stations. This is most apparent at Canberra, Wakkanai and Tokyo. Darwin, Vanimo and Okinawa are matched

least well. During the daytime, the correct magnitude nmF2 is also obtained at the Japanese stations, but the peak in observed electron density occurs earlier than FLIP predicts. Although the magnitude of nmF2 is reasonable, the diurnal shape is modelled less well. FLIP performs better than the IRI, during daytime, for the higher latitude stations in the Australian network, and is roughly comparable to the IRI for the lower latitude stations.

FLIP was being adjusted using frequent hmF2 observations in order to match the day-to-day variations in nmF2. The nmF2 change from one day to the next by small amounts and FLIP tended to follow these changes, although with weaker modulation than the observations. In some cases, the matching is good; for instance, shortly before the end of day nine nmF2 is mildly depressed, compared to the previous days, and FLIP follows this reasonably well at Canberra but overcompensates at Hobart. The subsequent predawn minimum is more shallow at all locations, as FLIP predicts.

FLIP does not perform as well during nighttime; a common problem [eg. *Wilkinson et al*, 1988]. There are obvious failures to match the pre-dawn minimum in nmF2 for all locations and in some cases, eg. Norfolk Island, the mismatch is apparent most days. On the other hand, there are some successes; for instance, the period mentioned above. FLIP is more successful with the Japanese stations, matching Yamagawa and Okinawa reasonably well. Tokyo, like Norfolk Island, is mismatched on most nights.

At Darwin, the electron density does not initially decay as rapidly as it does at the higher latitude stations, such as Canberra, and FLIP fails to follow this feature which is also present at Townsville and Norfolk Is. Obviously, this is a persistent feature because the IRI models it well.

The observed hmF2 (dots) for the Australian stations are shown in figure 4 together with the FLIP output (heavy line) and the IRI (thin line). The IRI matches the observations at all locations; Mundaring being the poorest match. Although FLIP matches even better, often tracking small fluctuations in hmF2, this is expected as the model has been tuned to match hmF2. Since travelling disturbances may affect M(3000)F2, and hence hmF2, it may possibly be better to smoothed hmF2 values passed to FLIP rather than use raw data. However, at this stage, there is no evidence that the higher sampling is detrimental.

In many cases FLIP has performed as well, or better than the IRI although there are significant nighttime problems. The equivalent winds from hmF2 and vertical ion fluxes used by FLIP in modelling nmF2 are discussed in the next two sections.

## 6. EQUIVALENT MERIDIONAL WINDS CALCULATED USING FLIP

The most important variable affecting the day-to-day behaviour of nmF2 at mid-latitudes is thought to be the meridional wind which modifies the ion densities above about 200km by changing the rate at which  $O^+$  ions diffuse downward under the influence of gravity. The most obvious effects are on the F2 peak density and the height at which the peak forms. Normally, the wind is poleward during the day, enhancing the downward diffusion towards a region of greater loss and reducing the peak electron density while lowering the layer peak height. At night, the wind is normally equatorward, inhibiting downward diffusion, raising the layer peak height and thereby maintaining the nighttime layer peak electron density.

Using *Miller et al.* [1986], FLIP calculates an equivalent meridional wind using the hmF2. These winds form an output of FLIP shown in figure 5A and 5B. To help assess whether the calculated winds are reasonable, they are compared with an empirical model, the Horizontal Wind Model (HWM90) based on satellite "in situ" and Fabry-Perot wind measurements

together with ground based Fabry-Perot and radar data [Hedin *et al* 1988, 1991]. The HWM90 gives some guidance on climatological wind fields although little data for the Australian region was used in the model.

Although the algorithm of Richards [1991] is very effective for reproducing the details of the measured hmF2, the calculated winds are often too large near dawn. One reason for this is the low electron density near dawn in the model allows chemical processes to rival the dynamics in importance. Unreasonably large poleward winds are often needed to overcome this chemical effect in order to lower hmF2 as quickly as observed. For this reason, the winds presented in this section were calculated using the method of Miller *et al.* [1986] which is not so greatly affected by this problem. At other times the methods agree well.

At most locations, the magnitude of the equivalent meridional winds from hmF2 (called hmF2 winds here) agree with the HWM90 but often disagree in direction. Both HWM90 and hmF2 winds show a decrease in amplitude with decreasing latitude. There are some obvious discrepancies. At Hobart, Wakkanai and Tokyo the HWM90 daytime poleward winds are larger than the hmF2 winds. At Mundaring, the HWM90 nighttime equatorward winds appear to be 180° out of phase with the hmF2 winds for nearly all the observation period. A similar tendency appears at Norfolk and Townsville, although both the winds from HWM90 and hmF2 are small. While Mundaring and Canberra have similar latitudes, the equivalent wind behaviour is very different with Mundaring winds being poleward most of the time. This is a reflection of the much lower hmF2 at Mundaring. In contrast, the hmF2 winds at Norfolk Island are very similar to those seen at Canberra.

What conclusions can be drawn about the modelled nmF2 based on the FLIP and HWM90 winds?

If the HWM90 daytime winds were used in FLIP the modelled nmF2 would be decreased and no longer match the observations. A similar result is found for most locations. This result is consistent with Titheridge [1993] who found the daytime HWM90 winds were too large by almost a factor of two at solar maximum.

The agreement between hmF2 winds at Hobart nighttime is mixed. During the early part of the campaign the hmF2 winds are greater than the HWM90 winds, which appear shifted in time with respect to the hmF2 winds. However, agreement between the modelled and observed nmF2 is good. Later (the fifth day) the nighttime hmF2 winds agree, but the nmF2 disagree which is inconsistent since a decrease in the equatorward winds should decrease nmF2. During the next two nights, the two wind models agree reasonably well and FLIP nmF2 agree well with observations, suggesting day-to-day variability is not easily modelled by changing only the winds. The nighttime problem may be due to a 10-20 km bias in the measured hmF2, but it might just as well be a problem with the MSIS neutral densities or some other factor.

Canberra daytime HWM90 winds peak sharply, just prior to midday, while the hmF2 winds have a flatter response. Since, for much of the campaign, observed and modelled daytime nmF2 at Canberra agree, the HWM90 winds appear inconsistent with the observations. The largest nmF2 departures occur on the last four days (figure 4A) when the hmF2 winds show the nighttime equatorward winds suppressed for the first two days and then strongly enhanced.

Daytime observed and modelled nmF2 agree well at the other Australian locations, but nighttime agreement becomes progressively poorer as latitude decreases. It seems possible that an increased equatorward wind could improve these results. As an example, during the brief disturbed period (ninth day) there is a sharp nighttime increase in hmF2 at Hobart, Canberra, Norfolk and Townsville. The resultant hmF2 wind has increased equatorward speed



compared to earlier days, as shown in figure 4A, and coincides with a good match in nmF2, suggesting a wind of this magnitude is required to improve the present model results at night. At all locations this is roughly equivalent to doubling the present HMW90 winds, which are already larger than the hmF2 winds at night.

## 7. ION FLUXES CALCULATED BY FLIP

At the beginning of the simulation using FLIP, the protonospheric flux tubes were about half full and were allowed to fill up as the simulation proceeded. The shorter flux tubes (e.g. Darwin, Townsville) fill up in about a day while the longer flux tubes (e.g. Hobart) may take several days. As a result, the upward fluxes, that fill the flux tubes, should decrease with time while the downward fluxes, that maintain the nighttime ionosphere, should increase. However, the neutral wind can also have a large effect on the fluxes. Some of the differences in flux variations between stations can be attributed to neutral wind differences. After a few days, all flux tubes will have close to the physically maximum downflow at night to support the ionosphere. Interestingly, at some stations, the model actually does more poorly at night as time progresses. This suggests that there is some other explanation for the low model densities at night. The fact that the model nmF2 agrees well with the data at Hobart but the problem worsens towards low latitudes also suggests that the nighttime problem is not related to plasmaspheric fluxes because there is only a small plasmaspheric ion reservoir at low latitudes.

The  $O^+$  and  $H^+$  fluxes passing through the 1500km level are shown in Figure 5A&B for the Australian and Japanese stations. Fluxes into and out of the protonosphere can have an effect on nmF2 and hmF2 [Bailey *et. al.*, 1978], so it is worth considering how FLIP deals with these fluxes. Generally, there is an outward flow of  $O^+$  and  $H^+$  during the daytime and an inward flow during the night. For the Australian locations, near sunset, there is a regular, sharp increase in the inward  $O^+$  flux associated with the thermal collapse that begins with the conjugate sunset in FLIP and intensifies at layer sunset, lasting for one to two hours, while equilibrium is established. There is no obvious comparable effect on  $H^+$  at Hobart and Canberra, but Norfolk and Townsville show an inflow of  $H^+$  at sunset. Generally, for the Australian region, the fluxes of  $O^+$  and  $H^+$  are similar in magnitude but with small differences in detail.

The  $H^+$  flux at Mundaring, and to a lesser extent Darwin, is different from the other locations, having a strong diurnal modulation, with large inward fluxes of  $H^+$  during the nighttime matched by similar outflows during the daytime. The larger nighttime downward fluxes at Mundaring appear to be related to the poleward neutral winds that persist for most of the time at this station. However, these larger ion fluxes are still insufficient to preserve the nighttime nmF2 at Mundaring. At Darwin, the  $O^+$  flux is significantly larger than  $H^+$ , but otherwise follows it closely in form.

The Japanese stations of Wakkanai and Tokyo, while showing the same general behaviour, differ in detail from the Australian region. Unlike the Australian stations, the  $O^+$  and  $H^+$  fluxes are more similar in amplitude, and are more variable. Both show very similar inflows at sunset and sharp increases in outflow at sunrise. It appears the two species are more closely coupled in FLIP in the Japanese region than for the Australian region. For the southern hemisphere, sunrise occurs a little earlier in the northern hemisphere (half hour).

While there are small day-to-day changes in the fluxes, there is little obvious correspondence between these and the modelled and observed nmF2. The agreement in form between several stations (Hobart, Canberra, Norfolk and Townsville) and the good repetition of the structure on successive days at the same station is encouraging. It does not appear that these fluxes are

likely to help explain any failures to match nmF2 [see also *Szuszciewicz et. al.* this issue], but they do offer an insight into the operation of FLIP and can, potentially, signify occasions when results are inconsistent.

## 8. SUMMARY AND CONCLUSION

Ionospheric climatology in the Australian and Japanese regions during an equinoctial, high solar activity period is described well by the IRI. The best agreement comes about by using an equivalent sunspot number, rather than the recommended twelve month smoothed sunspot number, R12. Quite likely, this practice is adopted informally already, but here its desirability is stressed. Retrospective ionospheric indices, such as IF2 and T, are readily available and should be used with the IRI rather than R12. There are occasions when this approach is particularly useful. For instance, the process can be extended to include shorter time duration indices (for instance, daily and regional indices) to mimic some of the daily variations in the ionosphere. However, the main limitation of IRI is that it is driven by a single number producing the best average result for the entire globe. By contrast, to be truly predictive, the FLIP model will need a much improved wind or hmF2 model.

Ionospheric weather, or day-to-day changes in the ionosphere, can only be understood within the framework of a physical model, such as FLIP. In this paper, hmF2 data were used with FLIP to model the daily changes in nmF2 through the influence of winds. FLIP was found to match the observed nmF2 reasonably well, although the day-to-day changes were not matched exactly. Nighttime agreement was more evasive. Furthermore, it appears that there are some problems in our fundamental understanding of ionospheric controls that still need to be resolved. Since some persistent climatological features of the ionosphere are still not modelled well. For both Australian and Japanese locations, the daytime maximum in nmF2 modelled by FLIP lagged the observed maximum by two or more hours. The cause is speculative. It may be due to minor errors in the MSIS compositions used by FLIP. The nighttime minimum in nmF2 was not modelled correctly by FLIP. At most locations, many days were poorly modelled in the pre-dawn period, although ironically there were successes on the disturbed days. The failures appear to be associated with an increase in nmF2, which is more apparent at the low latitude stations (eg. Darwin, in particular). *Titheridge* [1993], states that modelling the quiet, mid-latitude ionosphere should be adequate given suitable neutral wind models. Since the neutral winds have been calculated indirectly using hmF2, presumably this source of error has been minimised. However, at night, it appeared a better match would be obtained using the HWM90 winds rather than hmF2.

One possible source of error is the transformation of M(3000)F2 into hmF2. Scaling errors were explored using several runs of FLIP. These runs suggested that a large scale bias error in hmF2, if it existed, would significantly reduce the agreement already found for nmF2. Also [Richards *et. al.*, 1994] such offsets result in distortion of the electron density profile below the F region peak. These results are taken to imply that errors in the conversion to hmF2 are likely to be small and probably there is no bias present

The meridional winds predicted by FLIP show mixed agreement with the HWM90 winds. During daytime, at Hobart and Wakkanai, the HWM90 winds appear too large; a result that is consistent with *Titheridge* [1993]. In fact, the results here also support *Titheridge's* assertion that the daytime shape of the HWM90 winds is incorrect in the Australia-Japan sector. This problem is not surprising because there was very little data in this region for the construction of the HWM90 model [*Hedin et al.*, 1991].

The IRI has proven to be a good climatological model of the ionosphere and the FLIP model, while not being as successful, is nevertheless producing good agreement for much of the data investigated. In the longer term, physical models, such as FLIP, will be needed to understand and model day-to-day variability in the ionosphere. Their improvement will be increased by further comparisons of this nature, defining areas of common disagreement, and also areas where modelling is successful.

## REFERENCES

- Bailey G. J., R. J. Moffett and J. A. Murphy, Interhemispheric flow of thermal plasma in a closed magnetic flux tube at mid-latitudes under solar minimum conditions, *Planet. Space Sci.*, 26, 753, 1978.
- Caruana, J., The IPS Monthly T index, *Solar Terrestrial Predictions Workshop Proceedings, US Department of Commerce, NOAA, Boulder, USA*, 1990
- CCIR, 1982, CCIR atlas of ionospheric characteristics. Propagation in Ionised Media, *Recommendations and Reports of CCIR, Report 340-4 vol. VI* Geneva: Int. Telecommun. Union.
- Davis R. M. and N. L. Groome, Variations of the 3000km MUF in time and space, *NBS Report 8498*, US Department of Commerce, 1964.
- Dudeney J. R., The accuracy of simple methods for determining the height of the maximum electron concentration of the F2-layer from scaled ionospheric characteristics, *J. atmos. terr Phys.*, 45, 629, 1983.
- Fuller-Rowell, T. J. Interactions between neutral thermospheric composition and the polar ionosphere using a coupled ionosphere-thermosphere model, *J. Geophys. Res.*, 92, 7744, 1987.
- Hedin, A. E., MSIS-86 thermosphere model, *J. Geophys. Res.*, 92 4649, 1987.
- Hedin, A. E., N. W. Spencer and T. L. Killeen, Empirical global model of the upper thermosphere winds based on Atmosphere and Dynamics Explorer satellite data, *J. Geophys. Res.*, 93, 9959, 1988.
- Hedin, A. E., M. A. Biondi, R. G. Burnside, G. Hernandez, R. M. Johnson, T. L. Killeen, C. Mazaudier, J. W. Meriwether, J. E. Salah, R. J. Sica, R. W. Smith, N. W. Spencer, V. B. Wickwar and T. S. Virdi, Revised global model of thermospheric winds using satellite and ground-based observations, *J. Geophys. Res.*, 96, 7657, 1991.
- Miller K. L., D. G. Torr and P. G. Richards, Meridional winds in the thermosphere derived from measurements of F2 layer height, *J. Geophys. Res.*, 91, 4531, 1986.
- Minnis C. M., A new index of solar activity based on ionospheric measurements, *J. atmos. terr. Phys.*, 7, 310, 1955.
- Richards, P. G. and D. G. Torr, Ratio of photoelectron to EUV ionisation rates for aeronomic studies, *J. Geophys. Res.*, 93, 4060, 1988.
- Richards, P. G., An improved algorithm for determining neutral winds from the height of the F2 peak electron density, *J. Geophys. Res.*, 96, 17,839 1991.
- Richards P. G., D. G. Torr, B. W. Reinisch, R. R. Gamache and P. J. Wilkinson, F2 peak electron density at Millstone Hill and Hobart: Comparison of theory and measurements at solar maximum, *J. Geophys. Res.*, 99, 15,005, 1994.

Roble, R. G., E. C. Ridley, A. D. Richmond and R. E. Dickinson, A coupled thermosphere/ionosphere general circulation model, *Geophys. Res. Lett.*, 15, 1325, 1988.

Schunk, R. W. and A. F. Nagy Electron temperatures in the F region of the ionosphere: Theory and observations, *Rev. Geophys.*, 16, 355, 1978.

Schunk R. W. and E. P. Szuszczewicz, First-principle and empirical modelling of the global-scale ionosphere", *Annales Geophysicae*, 6, 19-30, 1988.

Sojka, J. J. and R. W. Schunk, A theoretical study of the global F-region for June solstice, solar maximum and low magnetic activity, *J. Geophys. Res.*, 90, 5285, 1985.

St-Maurice, J-P., and R. W. Schunk, Diffusion and heat flow equations for the mid-latitude topside ionosphere, *Planet. Space Sci.*, 25, 907, 1976.

Titheridge J. TE., Atmospheric winds calculated from diurnal changes in the mid-latitude ionosphere, *J. atmos. terr. Phys.*, 55, 1637, 1993.

Torr, M. R., D. G. Torr, P. G. Richards and S. P. Yung, Mid- and low-latitude model of thermospheric emissions,  $1, O^+(^2P)$  7320Å and  $N_2(^2P)$  3371Å, *J. Geophys. Res.*, 95, 21,147 1990.

Torr M. R. and K. D. Sullivan, "The ATLAS-1 Shuttle Mission", *EOS*, 73, 105, 1992.

Torr M. R., "The scientific objectives of the ATLAS-1 Shuttle mission", *Geophys. Res. Lett.*, 20, 487-490, March 1993.

Wilkinson P. J., Scaling errors in ionospheric characteristics, *Ionosonde Network Advisory Group Bulletin*, 27, WDC-A for STP, US Department of Commerce, NOAA, Boulder, USA, 20, 1978.

Wilkinson P. J., R. Schunk, R. Hanbaba and H. Mori, "Interhemispheric comparison of SUNDIAL F-region data with global scale ionospheric models", *Annales Geophysicae*, 6, 31-38, 1988.

Wilkinson P. J., Predicability of ionospheric variations for quiet and disturbed conditions, *J. atmos. terr. Phys.* [accepted], 1995.

Szczuszczewicz et al 1995 (this issue) [added here on double spaced typescript sent to JGR.]

Table 1: Stations used in this study

Station name	latitude (north +ve)	longitude (east +ve)	L shell
Wakkanai	45.4	141.7	1.55
Tokyo	35.7	139.5	1.22
Yamagawa	31.2	130.6	1.12
Okinawa	26.3	127.8	1.04
Vanimu	-2.7	141.0	0.98
Darwin	-12.5	131.0	1.09
Townsville	-19.6	146.9	1.25
Norfolk Island	-29.0	168.0	1.49
Mundaring	-32.0	116.2	1.89
Canberra	-35.3	149.0	2.00
Hobart	-43.0	147.3	2.87

## FIGURE CAPTIONS

### Figure 1A

The noon nmF2 at Tokyo, for four years (1990, 1991, 1992, 1993) during the maximum activity and declining phase of solar cycle 22 show clearly the large variability in the ionosphere both diurnally and seasonally. A 30 day running mean is superposed on the daily observations to make the seasonal variations clearer.

### Figure 1B

The noon and midnight nmF2 for Canberra further highlight the variability, showing the spatial differences and similarities (March equinox), as well as highlighting the range of diurnal changes that occur.

### Figure 2

The nmF2 output from the FLIP model (thick filled line) are compared, with Canberra nmF2 measurements (open circles) for a segment of the campaign period. Also shown as potential error margins are the nmF2 modelled by reducing and increasing the hmF2 supplied to FLIP by  $\pm 30\text{km}$  (thin dashed line),  $\pm 10\text{km}$  (thin filled line).

### Figure 3A and 3B

The F region peak electron density, nmF2, (open circles) for the Australian ionosonde network, 3A, and the Japanese ionosonde network, 3B, is compared with the FLIP output (thick, filled line) for hourly samples, for the campaign period. For comparison, the IRI predictions of the peak electron density using the CCIR coefficients (thin, filled line), and the URSI coefficients (thin dashed line) are shown.

### Figure 4

The F region peak height, hmF2, (dots) for the Australian region is compared with the FLIP output (thick, filled line) for hourly samples, for the campaign period. For comparison, the IRI prediction of the peak height (thin, filled line) is also shown as well as FLIP output for more frequent sampling (thick, dashed line). Similar results were found for the Japanese stations.

### Figure 5A and 5B

The equivalent meridional wind (thick filled line) calculated using hmF2 from the Australian (5A) and Japanese (5A) ionosonde networks is displayed together with the HWM90 meridional wind (dashed line). For guidance, the  $0\text{m sec}^{-1}$  line has been displayed as a thin filled line and nighttime is shown as a horizontal line. The winds are positive polewards for both hemispheres and time is displayed as UT. Vertical lines mark the end of a UT day.

### Figure 6A and 6B

The  $\text{O}^+$  (thin line) and  $\text{H}^+$  (thick line) fluxes into the ionosphere calculated by FLIP are shown for the Australian ionosonde network (6A) and Japanese ionosonde network (6B). Positive fluxes are out of the ionosphere and the zero flux is plotted as a baseline. Nighttime is shown as a horizontal line. The fluxes are calculated at a height of roughly 1450 to 1500km except for Yamagawa (1165km), Okinawa (738km) and Vanimo (642km). These last three stations are equatorial sites.

Figure 1A: Tokyo Noon/midnight nmF2 for four high activity years

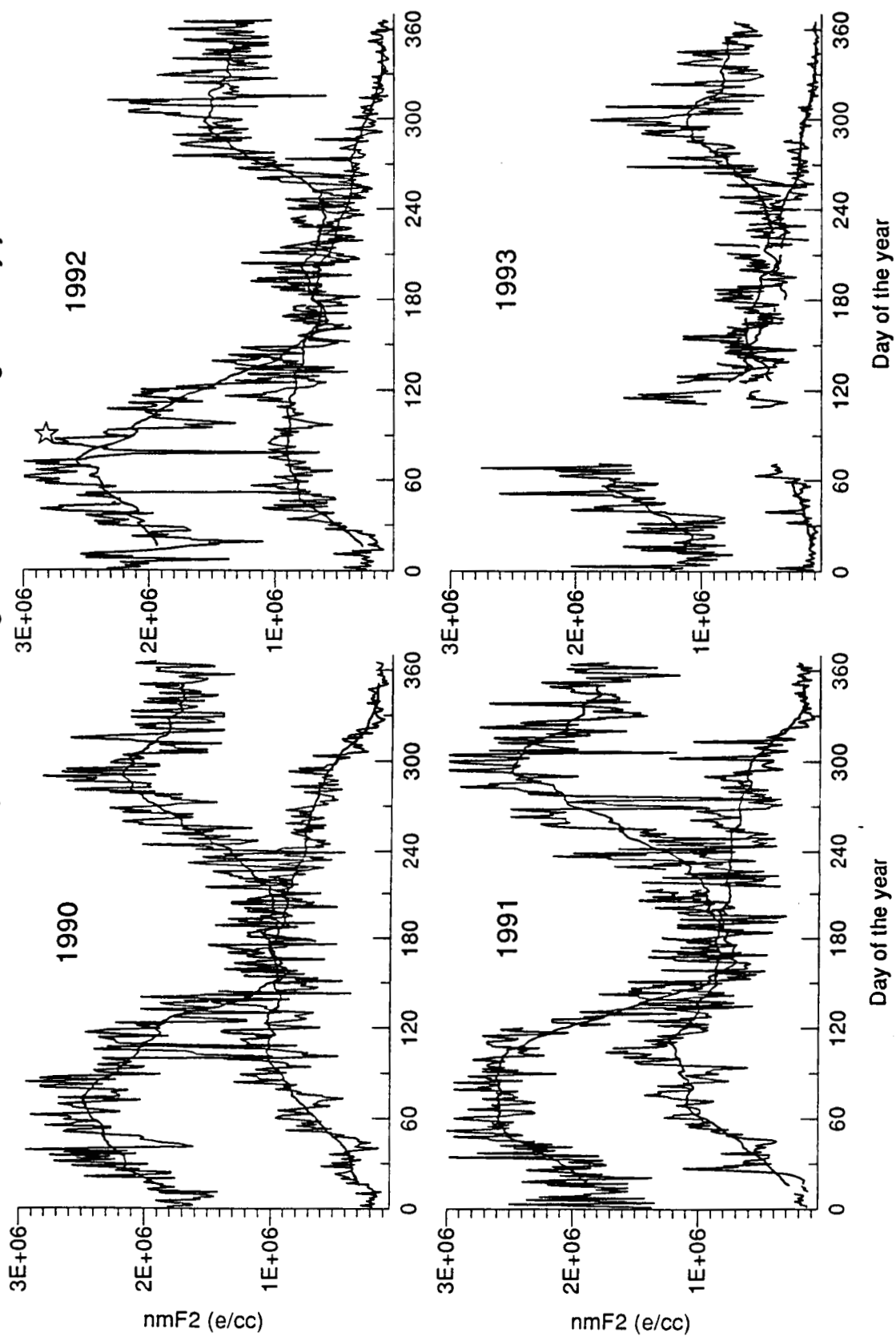


Figure 1B: Canberra Noon/midnight nmF2 for four high activity years

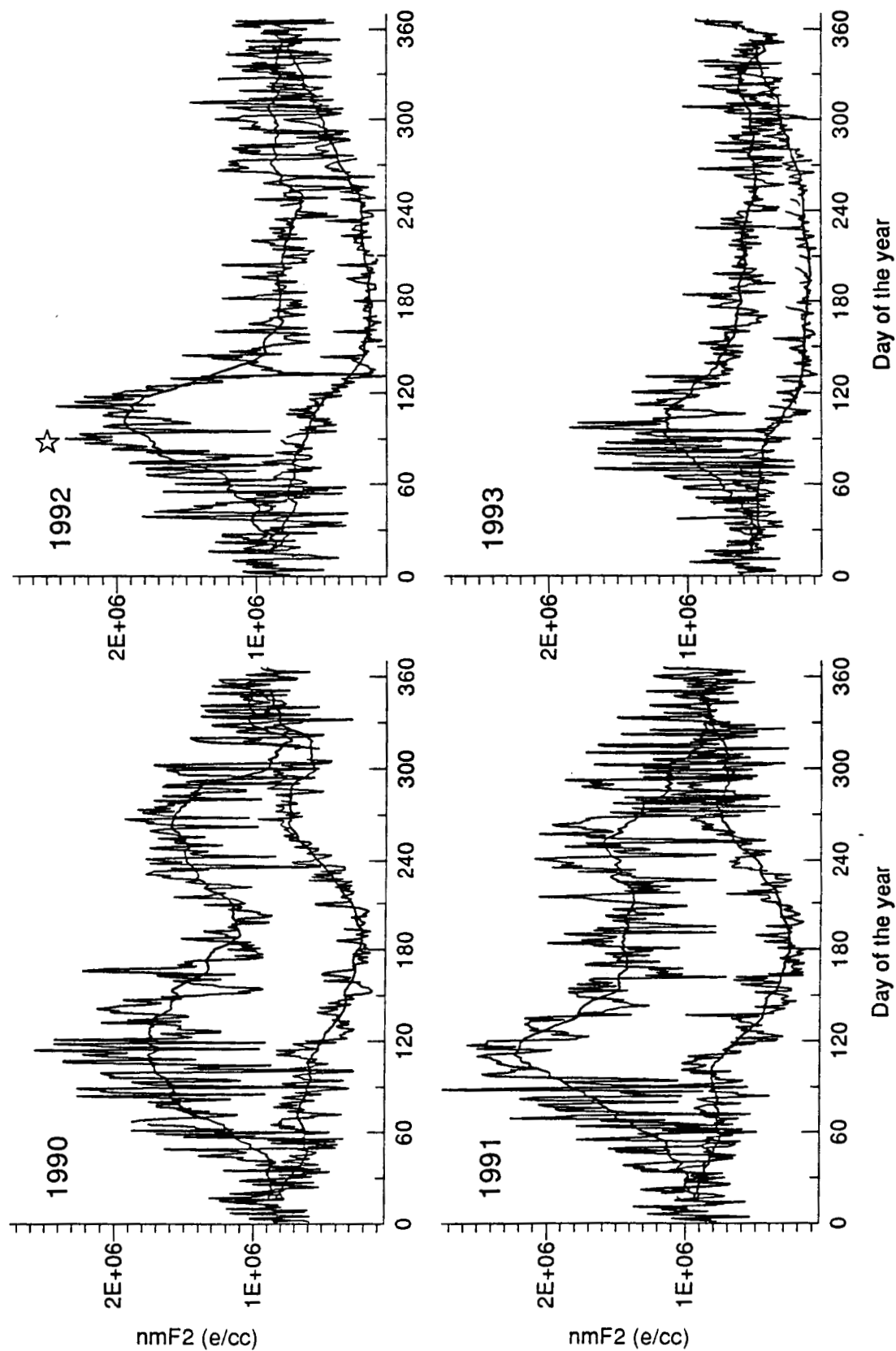




Figure 2. Error estimate based on varying the input F region peak heights.

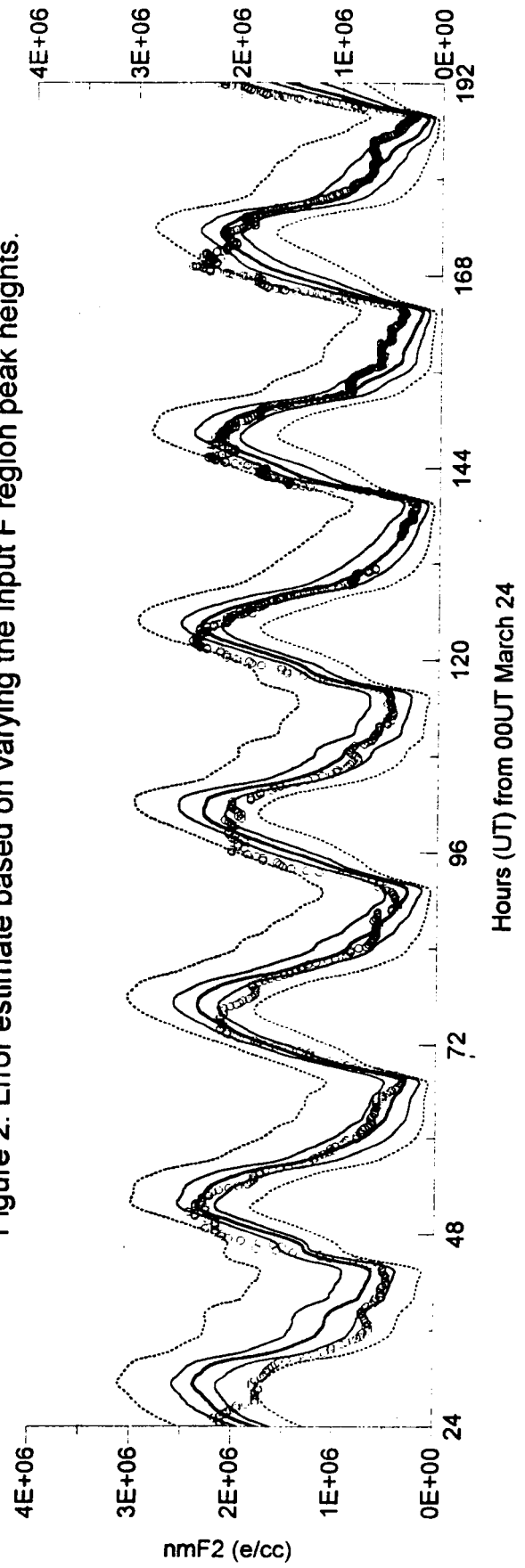


Figure 3A. Australian nmF2 compared with FLIP/IRI

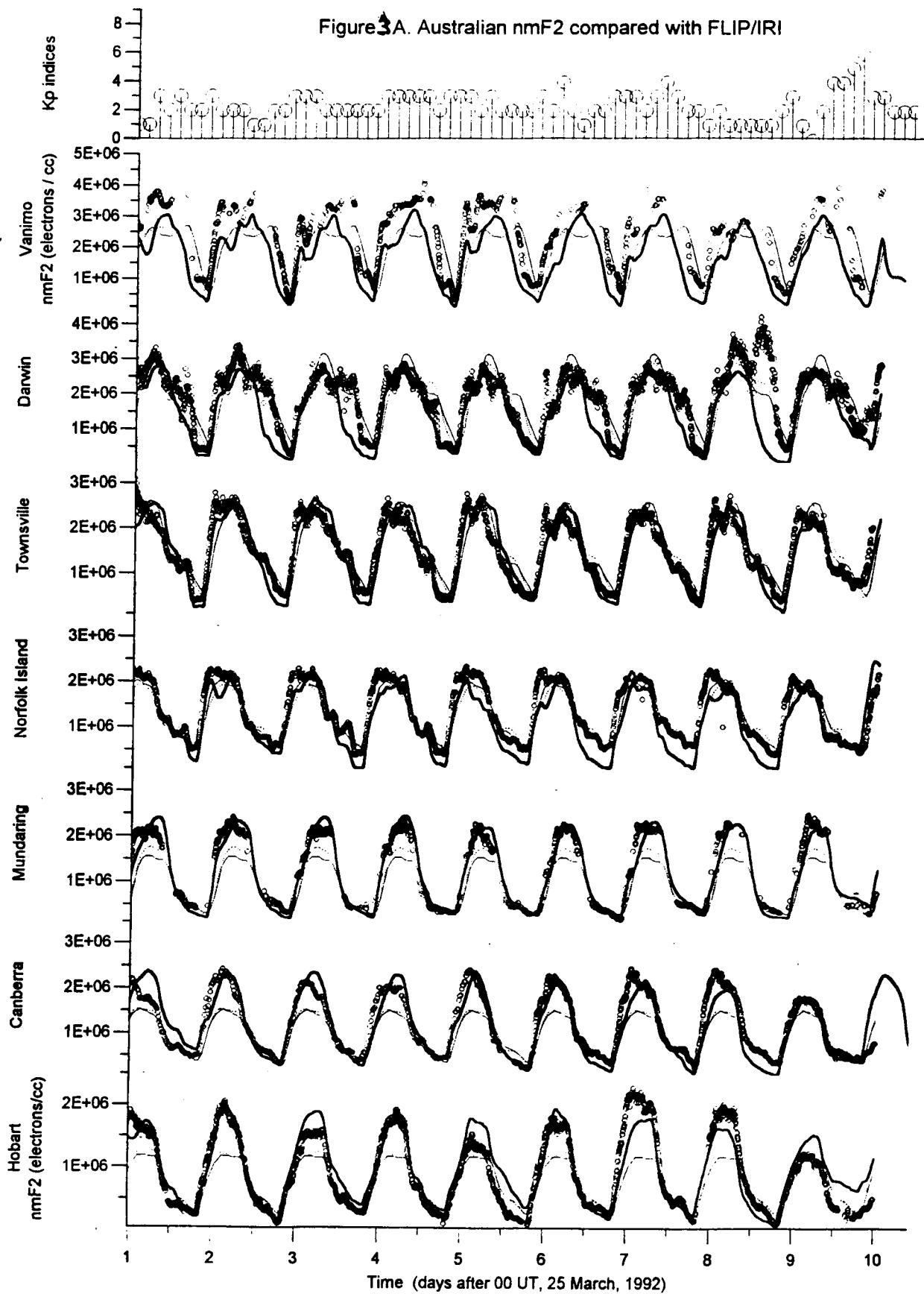


Figure 3B. Observed nmF2 compared with FLIP output  
for the Japanese stations

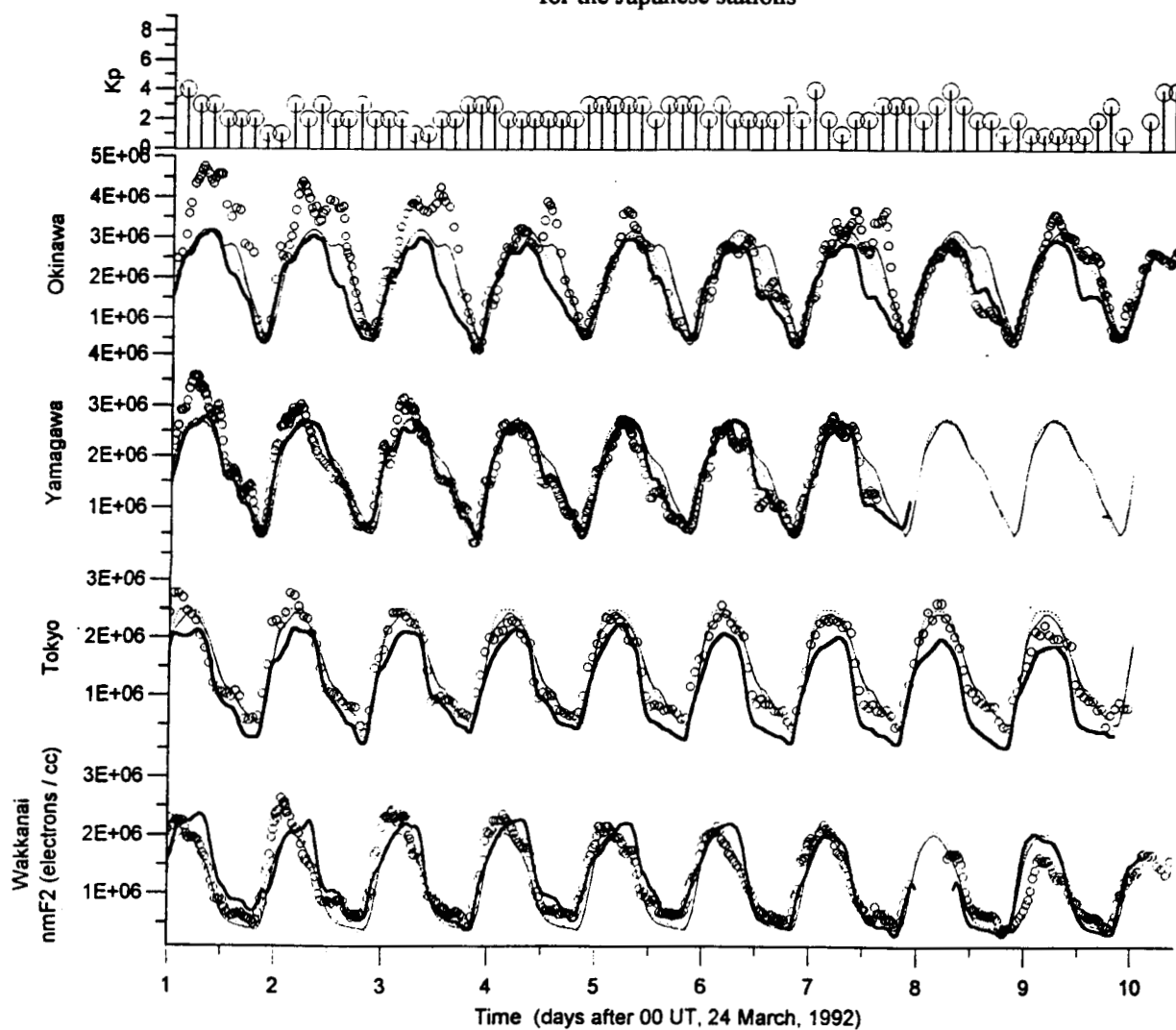


Figure 4. Australian hmF2 compared with FLIP / IRI

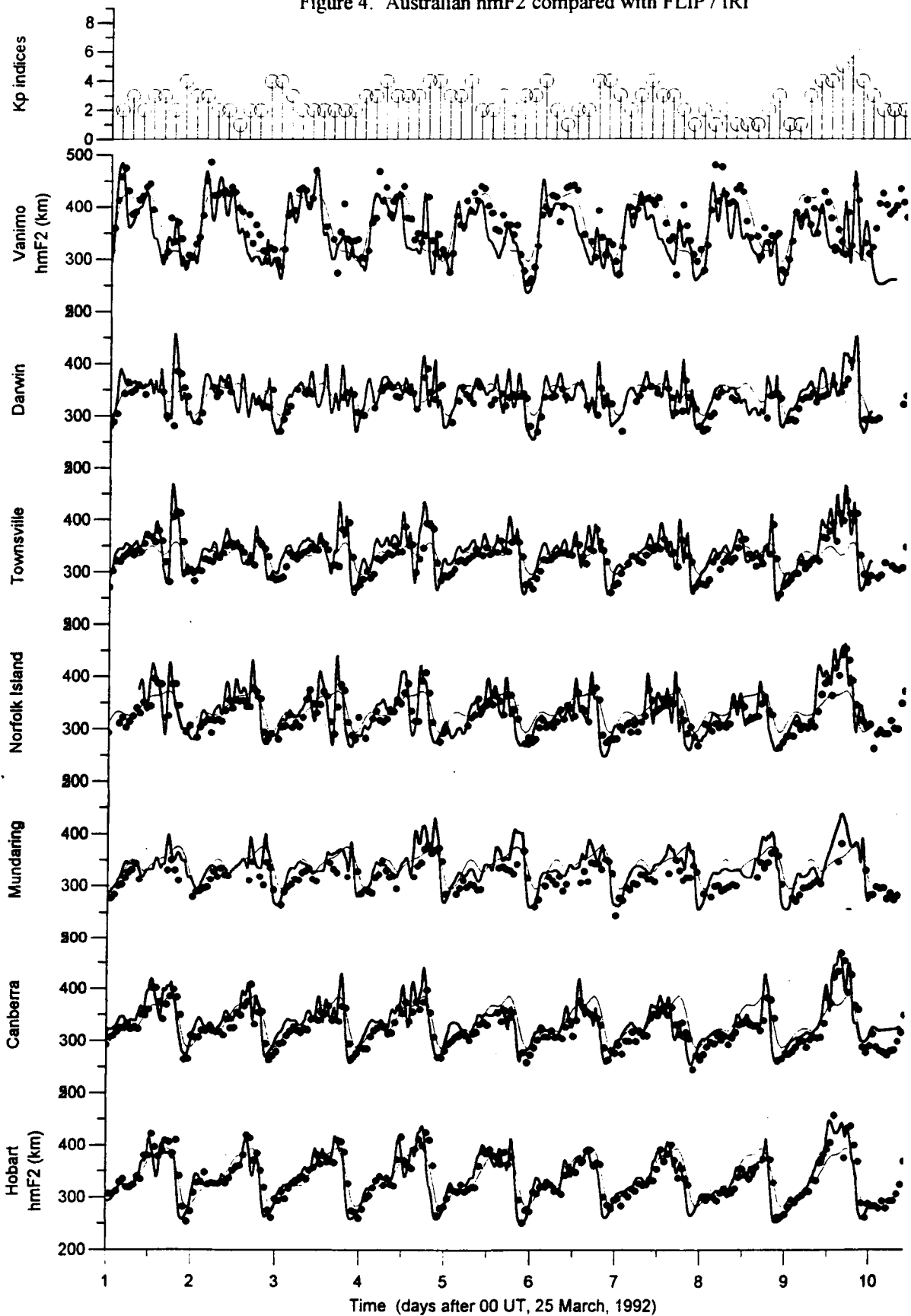


Figure 5A. Meridional winds in the Australian region:  
a comparison of HWM90 (dashed line) and hmF2 derived winds (filled line).

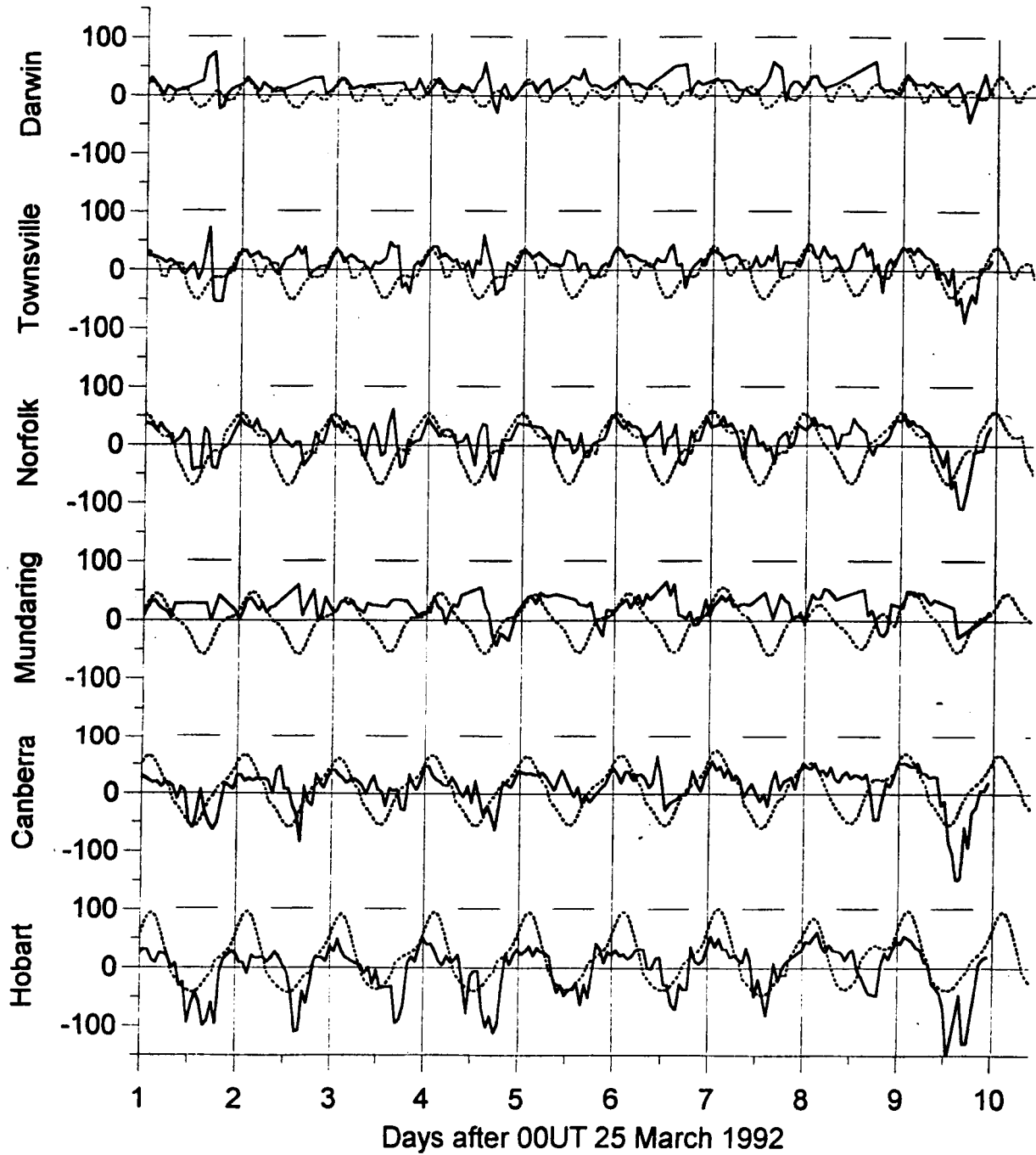


Figure 5B. Meridional winds in the Japanese region.

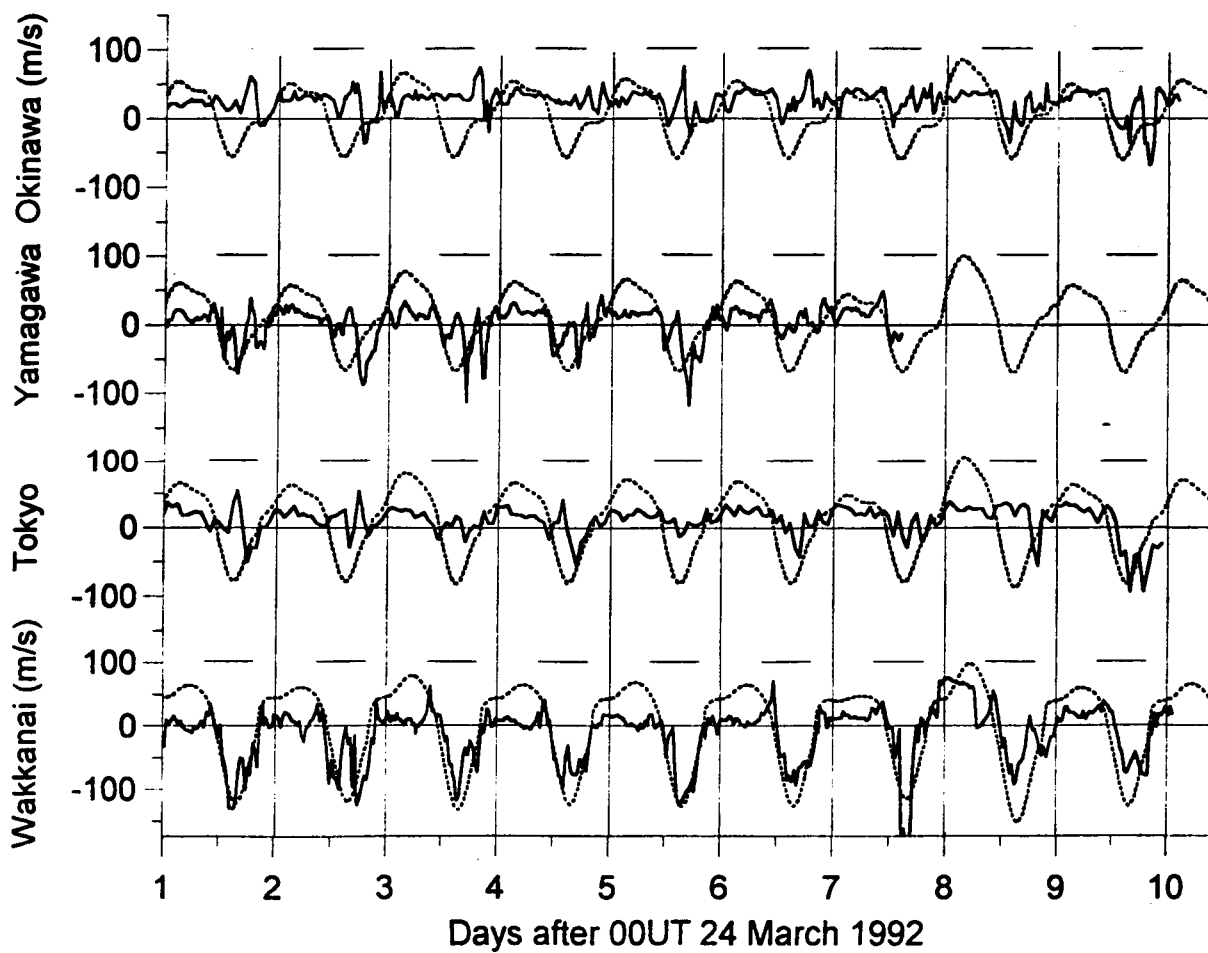


Figure 6A. H<sup>+</sup> (thick line) / O<sup>+</sup> (thin line) fluxes in the Australian region.  
(horizontal line marks night)

